Durham E-Theses

The role of viscous deformation mechanisms in controlling fault weakening during the propagation of earthquakes.

POZZI, GIACOMO

How to cite:

POZZI, GIACOMO (2019) *The role of viscous deformation mechanisms in controlling fault weakening during the propagation of earthquakes.*, Durham theses, Durham University. Available at Durham E-Theses Online: http://etheses.dur.ac.uk/13079/

Use policy

The role of viscous deformation mechanisms in controlling fault weakening during the propagation of earthquakes.

Giacomo Pozzi

Thesis submitted in partial fulfilment of the
requirements for the degree of Doctor of Philosophy

Department of Earth Sciences, University of Durham

2019

The role of viscous deformation mechanisms in controlling fault weakening during the propagation of earthquakes.

By Giacomo Pozzi

Abstract

Faults become transiently weak during the propagation of earthquakes. Fast, efficient lubrication of the sliding portion of seismic faults promotes slip acceleration, rupture propagation and radiation of potentially hazardous waves. Indeed, laboratory experiments show that fault materials dramatically weaken when sheared at seismic velocities (> 0.1 m s^{-1}). Several thermally-activated mechanisms, triggered by shear heating, have been proposed to explain the coseismic weakening of faults. However, a unifying law describing the thermal weakening observed for different rock types is still lacking.

We explored this problematic by performing friction experiments in a rotary shear apparatus on powders of a range of rock-forming minerals (calcite, dolomite, anhydrite, sodium chloride and olivine), at seismic velocities up to v = 1.4 m s^{-1} and normal stresses up to σ_n = 25 MPa.

When the experimental fault is weak, sheared gouges consistently develop a well-defined, porosity-free principal slip zone (PSZ) with finite thickness (a few tens of micrometres). PSZ is composed of fine-grained (< 5 µm) crystalline aggregates, which display textures typical of sub-solidus viscous flow. These are similar to those found in natural ultramylonites of ductile, aseismic shear zones active in the lower crust.

Calcite experiments were explored in-detail through the monitoring of acoustic emissions and with further microstructural analysis, which integrated SEM EBSD technique and TEM imaging. We show that, at dynamic conditions, thermally-activated viscous mechanisms (e.g. grainsize sensitive and insensitive creep) compete with brittle processes in controlling fault strength.

We also show that local temperatures attained during seismic slip control the strength of simulated faults according to an Arrhenius-type law. Our results demonstrate that coseismic lubrication of faults is operated by viscous processes, which can be described by are general, material-dependent Arrhenius-type constitutive equation. Therefore, our essay offers a unifying approach to the quantification of the dynamic strength of faults and to numerical modelling of earthquakes.

ii

The role of viscous deformation mechanisms in controlling fault weakening during the propagation of earthquakes.

Author: Giacomo Pozzi

A thesis submitted in partial fulfilment of the requirements for the degree of Doctor of Philosophy at Durham University

Department of Earth Sciences, University of Durham

2019

I declare that this thesis, which I submit for the degree of Doctor of Philosophy at Durham University, is my own work and not substantially the same as any which has previously been submitted at this or any other university.

"Lapidum natura restat, hoc est praecipua morum insania, etiam ut gemmae cum sucinis atque crystallinis murrinisque sileantur. Omnia namque, quae usque ad hoc volumen tractavimus, hominum genita causa videri possunt: montes natura sibi fecerat ut quasdam compages telluris visceribus densandis, simul ad fluminum impetus domandos fluctusque frangendos ac minime quietas partes coercendas durissima sui materia. Caedimus hos trahimusque nulla alia quam deliciarum causa, quos transcendisse quoque mirum fuit."

Naturalis Historia, Book XXXVI, by Pliny the Elder

Acknowledgments

Table of contents

x

1.   Introduction

1.1. Faults and localisation of brittle deformation in the upper crust.

In our dynamic planet rocks deform through geologic history, changing Earth's deep interior as well as its outermost face. The upper crust is dominated by a brittle behaviour, where processes such as fracturing and rigid body rotation produce permanent deformation (e.g. Scholz, 2002). The foremost expression of such behaviour is the complex network of faults that populate the crust at different scales in a self-similar fashion. Faults are – using a rough description – relatively narrow, tabular zones that localise brittle deformation and across which a sharp velocity gradient can be measured (Twiss and Moores, 2007). This definition, however, does not convey the complexity and variability of their structural and textural properties, which are factors intimately entwined with their macroscopic kinematic behaviour.

Faults – or better fault zones – are in fact heterogeneous bodies whose structure evolves with depth and across their width. In a well-established but simplistic model, fault displacement is mainly accommodated within the fault core (or cores, Fig. 1.1), which contains thin (up to a few cm) principal slip zones (e.g. Chester *et al.*, 1993; Wibberley *et al.*, 2008; Faulkner *et al.*, 2010). The fault core is often surrounded by an outer brecciated rock volume, the damage zone, with variable extension. The amount of total slip accommodated in the damage zone is relatively small compared to that in the fault core, and the intensity of damage decreases in the damage zone as one moves away from the fault core, towards the protolith (Fig. 1.1).

The fault core consists of a thin zone – when compared to the whole thickness of the fault zone – composed by heavily damaged rocks such as cataclasites, ultracataclasites and fault gouges (pulverized rock; e.g. Sibson, 1977). To a close inspection, most of the slip appears to be accommodated in narrower zones within the core. Observations made on exhumed seismogenic faults (De Paola *et al.*, 2008; Smith *et al.*, 2011; Fondriest *et al.*, 2012; Bullock *et al.*, 2014), on ruptures that reached the surface during recent
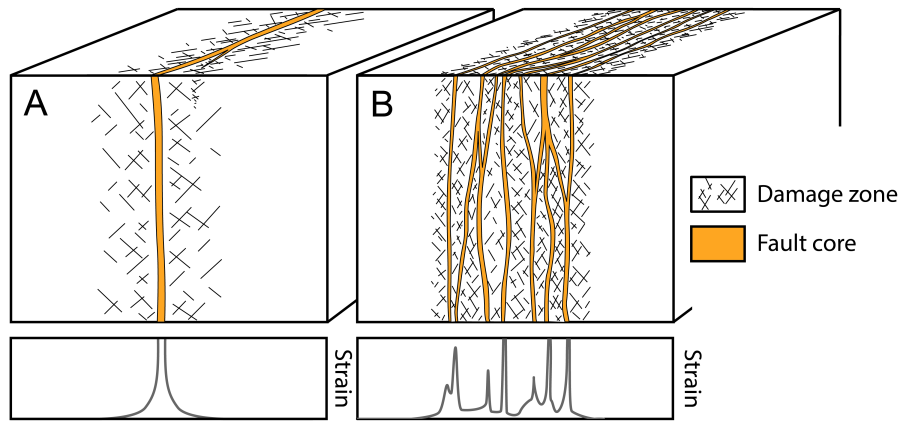
Fig. 1.1 | Cross-sectional view of: A) a simple fault displaying single fault core and damage zone; B) complex fault zone composed by multiple fault cores accommodating different amounts of displacement and extended damage zone. Below each drawing, a qualitative distribution of strain measured across the fault. Redrawn after Faulkner et al. (2010).

earthquakes (Lockner *et al.*, 2000; Noda and Shimamoto, 2005; Lin *et al.*, 2015) and on core samples recovered by drilling of active seismogenic faults (Chester *et al.*, 2013) showed extreme strain localisation along slip surfaces or within a principal slip zone (PSZ), whose thickness is in the range of few centimetres or millimetres (Chester and Chester, 1998; Rockwell and Ben- Zion, 2007; Faulkner *et al.*, 2010). Collettini *et al.* (2014) showed that in some carbonate-bearing exhumed faults the PSZ corresponds to a continuous layer with thickness < 300 μm, hosting submicrometric particles that are organized in thin sublayers (Fig. 1.2).
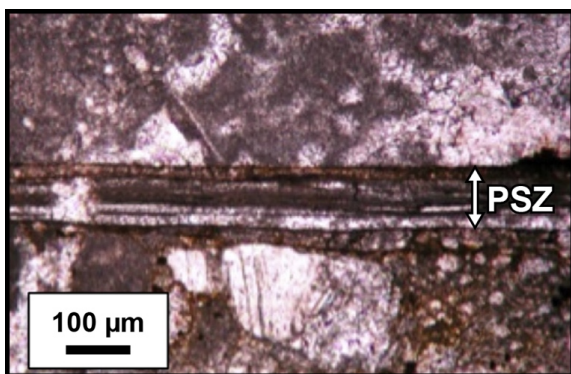
Fig. 1.2 | Cross section showing a thin principal slip zone (PSZ) of the Monte Maggio fault. The PSZ is composed by multiple layers with straight boundaries. Image modified after Collettini et al. (2014).

2

1.2. Faults are weak during earthquakes

The strength of the upper crust is assumed to be controlled by critically stressed faults, whose strength is, in most cases, approximated by the Coulomb frictional-failure criterion (Mogi, 1972; Sibson, 1977; Byerlee, 1978; Townend and Zoback, 2000). The criterion links shear stress across the fault (τ, acting parallel to displacement vector) with the normal stress (σ_n, acting perpendicular to the fault boundaries) through the coefficient of friction $\mu = \tau/\sigma_n$. Byerlee (1978) reported with his experimental work that, at high normal stresses, μ is in the range of 0.6 - 0.9 (Fig. 1.3A), and is generally independent of the lithology, with the only exception of some phyllosilicate minerals (e.g. ilite/smectite).
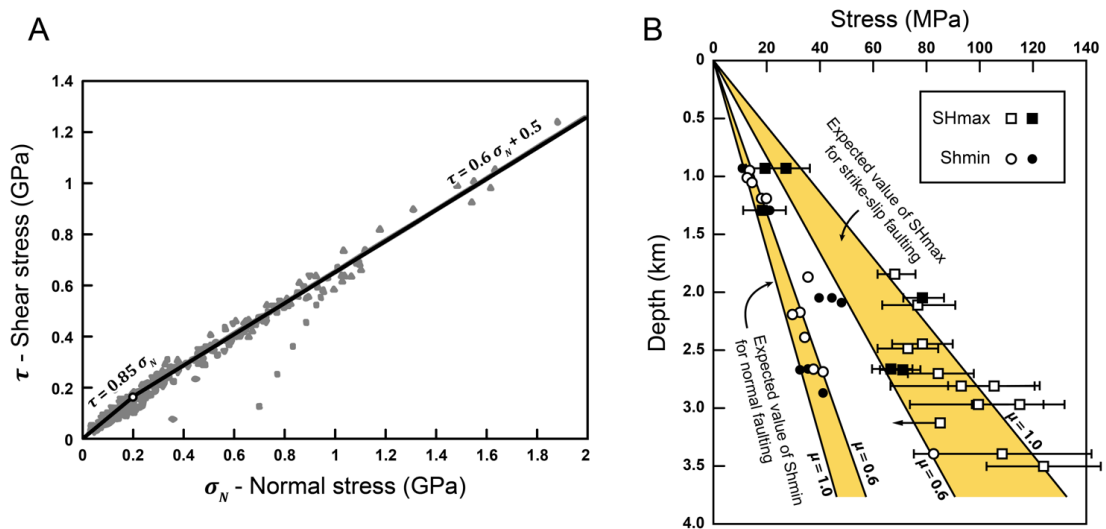
Fig. 1.3 | *A) Frictional response of a wide variety of rock types. Shear stress is plotted as a function of normal stress at the maximum friction recorded during experiments. Data points cluster along two lines, whose slope is the friction coefficient. Byerlee's friction coefficients are comprised between 0.6 and 0.9. Redrawn after Byerlee (1978). B) Magnitude of least principal horizontal stress (Shmin, circles) and estimates of maximum horizontal principal stress (SHmax, squares) from borehole data. Shaded areas show the theoretical magnitudes according to Byerlee's law friction coefficients (between 0.6 and 1.0). The graph shows that the stress in-situ measurements (orientation and magnitude) within boreholes indicate friction coefficients consistent with Byerlee's law. Redrawn after Zoback and Healy (1992).*

In-situ stress measurements in deep boreholes (Fig. 1.3B) suggest that the strength of the crust is controlled by faults, whose frictional strength is consistent with those values predicted by Byerlee's rule (Hickman, 1991; Zoback and Healy, 1992; Townend and Zoback, 2000). However, the evidences are mostly limited to local measures at static conditions within the stable continental crust, which may not necessarily be representative of in-situ conditions in active large faults.

Faults, however, are dynamic bodies that deform inhomogeneously through time, either by aseismic creep or during paroxysmal events, such as earthquakes. Furthermore, seismic slip is believed to be the principal mechanism that accommodates large deformations in the upper crust (e.g. Chester and Chester, 1998). The question whether the dynamic frictional strength of faults – which slide at seismic slip velocities of metre per seconds – is well represented by Byerlee's rule raises spontaneously. In fact, Byerlee's friction coefficients have been derived in laboratory experiments performed at slip rates orders of magnitude lower than those expected for earthquakes ($v \sim 1$ m/s, e.g. Heaton, 1990). If these friction coefficients ($\mu > 0.6$) were maintained during seismic slip they would result in large thermal anomalies, given the efficient energy dissipation into heat by shear heating. However, heat flows measured on major seismogenic faults, like the S. Andreas fault, are not anomalous at all (e.g. Brune *et al.*, 1969 and references therein). Also, large shear heating should result in very high co-seismic temperatures in narrow principal slip zone (up to a few cm, Chester et al., 1993), well above the melting temperatures of most fault rocks (e.g. Rice 2006), which should produce large volumes of pseudotachylites. Although psedutachylites are indeed observed along some faults, there is a general lack of geologic evidence about their association to large, seismic faults. A possible explanation for such observations is that faults are, in fact, dynamically weak, with an estimated friction coefficient as low as 0.2 (e.g. Lachenbruch, 1980; Hickman, 1991; Chester *et al.*, 1993).

The advent and evolution of rotary shear apparatuses made possible to reproduce seismic conditions in laboratory experiments, i.e. high slip velocity in the ms^{-1} range and large amounts of slip, comparable to co-seismic slip of moderate large earthquakes > 1m. Numerous experimental studies show that the measured friction coefficients of

4
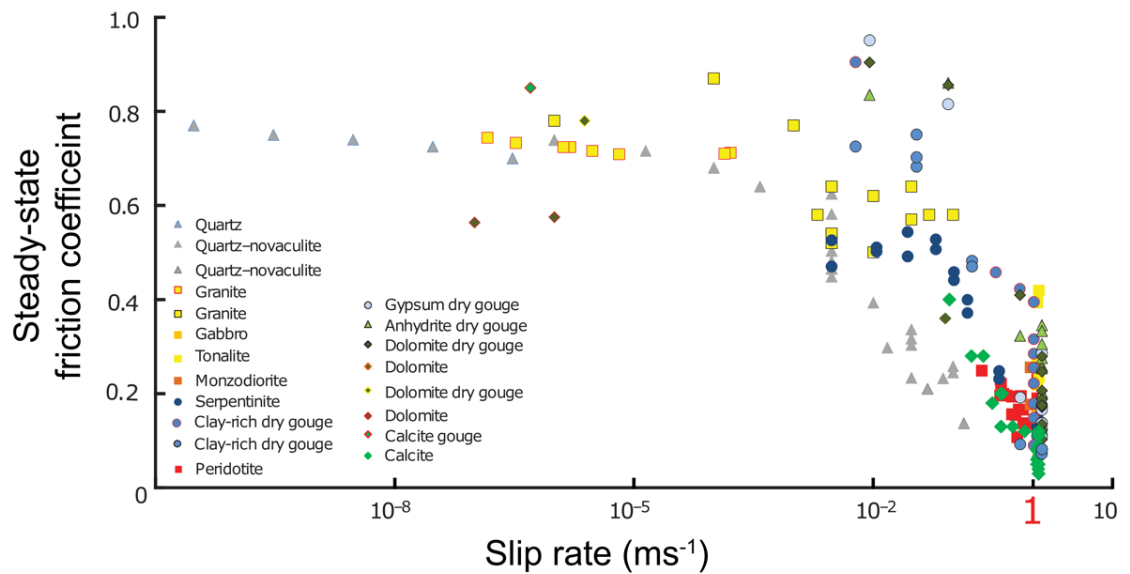
***Fig. 1.4 |** Comprehensive plot of steady-state friction values vs slip rate obtained from experiments performed on different rock and rock powder types (refs. in Di Toro et al. 2011). Remarkably, friction coefficients are substantially reduced when approaching seismic slip rates (~ 1 ms⁻¹ and above). Modified after Di Toro et al. (2011).*

both cohesive and incohesive rocks significantly reduce (< 0.2), when seismic velocities are approached, independently of the rock composition (Fig. 1.4; Di Toro *et al.* 2011).

The microstructural study of samples produced in numerous high velocity (>1m/s) shear experiments reveals that, when the fault is weak, most of the total fault displacement is accommodated within narrow slip zones, which are comparable to those found in natural fault cores (e.g. Han *et al.*, 2010; De Paola *et al.*, 2011b; Fondriest *et al.*, 2013; Smith *et al.*, 2013, 2015). This suggests that strain localisation might be the key to the understanding of fault lubrication during earthquake propagation.

By assuming seismic slip rates, localised slip and a constant friction coefficient in the Byerlee's range, the simple result for non-adiabatic heating gives temperatures far exceeding those required for the onset of melting of crustal rocks (Rice, 2006). Given the scarce evidence in the geologic record of pervasive frictional melting in natural

faults, a mechanism able to reduce fault strength had to be invoked in order to explain the preservation of such thin microstructures. Therefore, if strain localisation is associated to seismic activity, it is reasonable to assume that dynamic weakening mechanisms must lubricate seismic faults, and that such mechanisms are likely to have a thermal origin (Rice, 2006). Bizzarri and Cocco (2006a, 2006b) showed in their models that the temperature increase in a localised slip zone is predominantly controlled by the slip zone thickness rather than by the amount of slip. Furthermore, recent work modelling coseismic fault weakening not only acknowledges the prime role of shear localisation (e.g. Platt *et al.*, 2014; Rice *et al.*, 2014), but also physically demonstrate that the thermally activated mechanisms have a positive feedback in reducing the slip zone thickness.

1.3. Weakening mechanisms

Earthquakes nucleate and propagate different settings but fault weakening seems to occur regardless of the rock type (Di Toro *et al.*, 2011). However, a satisfactory, unifying theory on the processes and mechanisms that lead to the dynamic evolution of friction is still missing. In fact, several different dynamic weakening mechanisms (which are in turn dependent on the rock type) have been proposed by various authors: melt lubrication (e.g. Nielsen *et al.*, 2008), silica-gel lubrication (e.g. Di Toro *et al.*, 2004), flash heating (e.g. Goldsby and Tullis, 2011), thermal decomposition (e.g. Han *et al.*, 2010), thermal pressurization (e.g. Rempel and Rice, 2006), nanopowder lubrication (e.g. Reches and Lockner, 2010), nanograin superplasticity (e.g. Green *et al.* 2015; De Paola *et al.*, 2015) and flash weakening triggered by fast-moving dislocations (Spagnuolo *et al.*, 2015). Most of these mechanisms are thermal-activated, and the main ones are briefly described in the following text.

1.3.1. Melt lubrication

Frictional melt, found in nature as pseudotachylytes (Fig. 1.5), is one of the few

unambiguous indicators of seismic slip along natural faults (Sibson, 1975; Spray, 1987, 1993, 2010). While Scholz (2002) suggests that the high viscosity of an anhydrous melt would retain a considerable shear resistance, recent laboratory experiments (Hirose and Shimamoto, 2005; Di Toro *et al.*, 2006a, 2006b) seem to validate it as an efficient lubrication mechanism. Nielsen *et al.* (2008) proposed a complete physical model of this process. They showed that the dynamic strength of the experimental fault at steady state conditions is described by:

$$\tau_{ss} = \sigma_n^{0.25} \left(\frac{A}{\sqrt{R}}\right) \sqrt{\left[log\left(2\frac{v}{W}\right)\right]\frac{W}{v}} \quad (1.1)$$

where σ_n is the normal stress, v is the slip rate, R is the radius of contact area (solid core cylinders), A is a dimensional normalizing factor and W is a characteristic rate. This formula holds as long as the melt is continuously produced and is free to migrate outside the slipping patch of the fault (the experimental contact between the two sliding rock
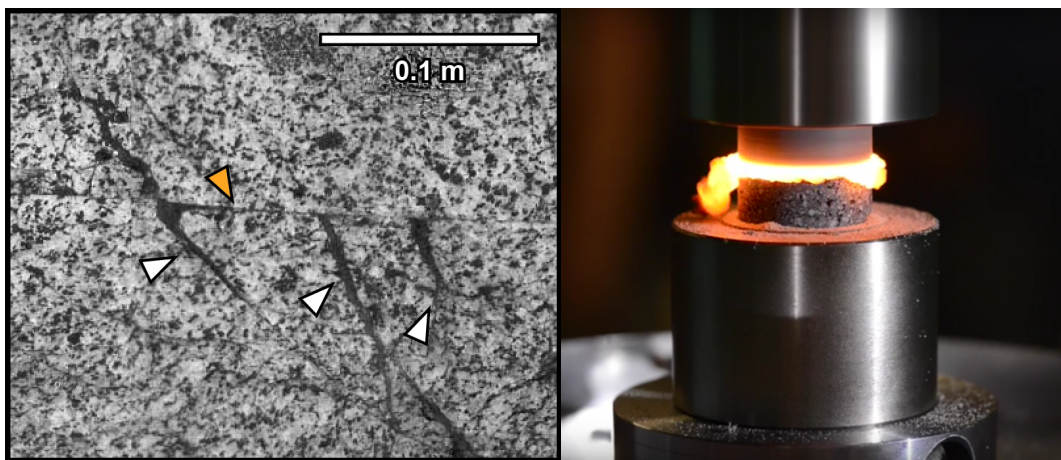
Fig. 1.5 | On the left, natural frictional melt, i.e. pseudotachylytes, cropping out in the tonalites of the Adamello pluton, Italian Alps. Wing cracks filled with the pseudotachylyte (white arrows) branch-out from the principal slip zone (shear sense: top to the right) decorated by the same material (yellow arrow). On the right, frictional melting observed in high velocity rotary shear experiment on andesite. Experiments performed at University of Liverpool Experimental Volcanology Laboratory, by J. E. Kendrick.

cylinders). At these conditions, a stable thermal profile is maintained in the thin layer of melt. The melt viscosity, hidden in the formula, follows an Arrhenius-type dependency on temperature.

Although generation of pseudotachylytes is generally believed to be hindered in presence of fluids by the effect of thermal pressurization (Sibson, 1973, 2003; Rempel and Rice, 2006; Rice, 2006), Bestmann *et al.* (2016) reported about natural evidence of coexisting pseudotachylytes and coseismically instantaneous quartz healing, which would suggest efficient fluid overpressure dissipation.

1.3.2. Flash heating

Flash heating is not a mechanism of weakening itself but rather a thermomechanical analysis of the frictional heating at the asperity scale, which has been first described for metals (e.g. Bowden and Thomas, 1954; Archard, 1959). According to flash heating models, bulk weakening is achieved by the weakening of the small-scale contact asperities, where melting and other weakening mechanisms are triggered due to the high normal stresses and temperatures attained. Rice (1999) linked a critical weakening velocity v_w to the dimension of asperities d (Fig. 1.6A) by defining a critical contact age $\theta_w = d/v_w$ (or alternatively $\theta_w = d_w/v$, by considering a critical dimension of asperities d_w at a fixed slip rate v). The critical age is controlled by the balance between simple one-directional heat conduction and the rate of production of shear-generated heat, which is given by

$$\theta_w = \frac{\pi \kappa}{v^2} \left[\frac{\rho c\, \Delta T}{\tau_c} \right]^2 \quad (1.2)$$

where v is the slip rate, κ is the thermal diffusivity, ρc is the volumetric heat capacity, ΔT is the temperature rise and τ_c is the shear resistance of contact junctions, which is a material property. ΔT is defined by the difference between a weakening temperature T_w, which can be the temperature of melting or of an hypothetically instantaneous transformation to a weaker phase, and the starting temperature T_f at which τ_c is defined.

8

If θ_w is greater than the maximum age of the asperity ($\theta_{max} = d/v$) then no weakening occurs and the friction coefficient has Byerlee's values (μ_0 =0.8). Vice versa, if $\theta_w < \theta_{max}$, flash heating is efficient and the asperity has no strength as described by Rice (1999) or better, with a refined model by Beeler *et al.* (2008), the residual friction coefficient at the asperity μ_w is small but not negligible, and the bulk friction coefficient can be predicted by the equation

$$\mu = (\mu_0 - \mu_w)\frac{v_0}{v} + \mu_w \quad (1.3)$$

where v_0 is the threshold velocity of weakening and $v_0 = d/\theta_0$, where θ_0 is the time necessary to weaken the asperity at that speed. The friction coefficients predicted by Eqn. 1.3 are presented in the graph of Fig. 1.6B.

Flash heating has been proven to predict satisfactorily the frictional weakening of silicate rocks at seismic slip rates (Beeler *et al.*, 2008; Goldsby and Tullis, 2011) and the slip-pulse (Heaton, 1990) rupture behaviour of earthquakes. A model of flash heating for carbonate-bearing faults has been proposed by Spagnuolo *et al.* (2015), which
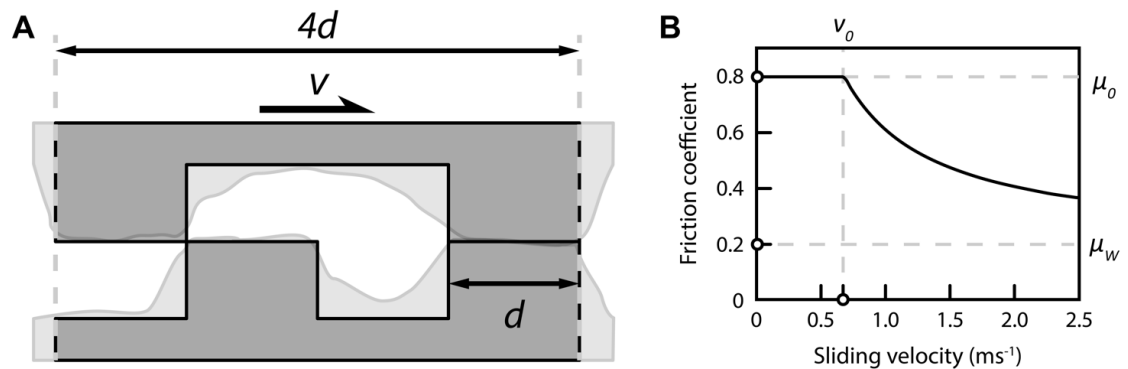
Fig. 1.6 | A) Simplified array of square contacts with dimension d shown in cross section. The unit cell (bounded by dashed lines) has length of 4d and is assumed to be repeated an infinite number of times along the sliding surface. The contact area is independent of the displacement so that, if the slip velocity v is constant, the age of the asperity is constant. Redrawn after Beeler et al. (2008). B) Steady state behaviour of the modified Rice model for flash weakening (Eqn. 1.3), with μ_0 = 0.8 and μ_w = 0.2. redrawn after Beeler et al. (2008).

involves fast moving dislocations. In this case, either grain-dependent plasticity or the formation of patches of amorphous carbon has been proposed as the lubricating mechanisms. Flash heating has been also described in serpentine after laboratory evidences of dehydration, amorphisation and crystallisation of anhydrous phases (Hirose and Bystricky, 2007; Viti and Hirose, 2010).

Although flash heating predictions find a good fit with the laboratory experiments, it is important to note that the original model and theory applies to bare rubbing surfaces and the effects and implications of wear products, such as gouges, have not been included in current studies in order to simplify the physical treatise (Rice, 2006; Beeler, Tullis and Goldsby, 2008; Goldsby and Tullis, 2011). Rempel (2006) extended the model of Rice (2006) to flash heating in gouges limited to a thin, but finite, shear zone. Assuming an array of contacts, the effective weakening velocity (v_w) is controlled by the product between the nominal local weakening slip rate and the number of contacts mobilised across the gouge (N_c) which is about 10-20 (Brantut and Platt, 2017):

$$v_{w,gouge}(T) = v_w(T)N_c \quad (1.4)$$

1.3.3. *Thermal pressurization and thermal decomposition.*

Fluid pressurisation has been invoked as an important lubrication mechanism by several authors since four decades ago (Sibson, 1973). It is modelled at its basis as the direct effect of shear heating in rising the pore pressure, owing to the commonly assumed low-permeability of the fault core material (and described by the Darcy's law). Hence, the generation of fluid overpressure can lower the effective normal stress, which results in lower frictional resistance regardless of the initial friction coefficient (Lachenbruch, 1980; Mase and Smith, 1984; Bizzarri and Cocco, 2006; Rempel and Rice, 2006; Rice, 2006)

$$\tau = \mu(\sigma_n - p) \quad (1.5)$$

where ($\sigma_n - p$) is the Terzaghi effective stress, σ_n is the normal load and p is the pore

fluid pressure. Bizzarri and Cocco (2006) modelled thermal pressurisation showing that strain localisation controls the temperature rise and, even in presence of fluids (see Ch. 1.3.2), melting temperatures are achieved if the shear zone is sufficiently thin. Rempel (2006) suggests that increasing damage promotes changes in the permeability and thermal poroelastic behaviour of the slip zone and surrounding host rock. This may increase the fault strength due to pore pressure dissipation and consistently reduce the slip distance required to achieve melting temperatures.

Fluids may also be released by temperature-controlled reactions such as dehydration (Hirose and Bystricky, 2007; Brantut *et al.*, 2008, 2011; Viti and Hirose, 2010) or decarbonation (Han *et al.*, 2007; Sulem and Famin, 2009; De Paola *et al.*, 2011a; De Paola *et al.*, 2011b; Collettini *et al.*, 2013; Smith *et al.*, 2013; Mitchell *et al.*, 2015), which may then be pressurised and lead to the same lubrication mechanism driven by pore overpressure. These processes, addressed as thermal decomposition, may also produce crystalline (Han *et al.*, 2010; Viti and Hirose, 2010) or amorphous phases (De Paola *et al.*, 2015) that possibly change the frictional behaviour of the shear zone. For example, nanograin production by decomposition can promote higher porosity and thus hinder thermal pressurisation mechanisms (Han *et al.*, 2010).

1.3.4. *Powder lubrication and nanograin superplasticity*

The scientific community is currently rising its awareness on nanoscale materials and processes related to earthquakes. In particular, numerous works put their emphasis on nanopowder materials (loose or sintered) that are commonly found in natural faults and laboratory friction experiments (Chester *et al.*, 2005; Wilson *et al.*, 2005; Sammis and Ben-Zion, 2008; Han *et al.*, 2010; Viti and Hirose, 2010; Tisato *et al.*, 2012; Verberne *et al.*, 2013; De Paola *et al.*, 2015; Green *et al.*, 2015). Such materials do not follow the fractal distribution of grain sizes produced by mechanical grinding (e.g. Sammis and King, 2007). Thus, it is argued that abundant nanosized gouges are produced during highly energetic events, the earthquakes.

It is known that friction laws at the nanoscale generally deviate from the macroscale

behaviour, but a satisfactory theory on this challenging research topic is still lacking (Mo *et al.*, 2009). Consequently, powder lubrication has been invoked as a weakening mechanism only owing to experimental observations, and it is not yet physically constrained (Han *et al*., 2010; Reches and Lockner, 2010). For instance, Han *et al.* (2010) performed shear experiments on non-cohesive and cohesive carbonates and observed strong weakening at seismic velocities (~1.3 m/s) coupled with evidences of thermal decomposition. Since strain localisation occurred into a layer of a porous aggregate of nanoparticles (< 1 μm), they assumed that the generic weakening mechanism was nanopowder lubrication, after excluding thermal pressurisation (high porosity) and flash heating (low velocity and temperatures). As reported in the previous chapter, localisation of strain in faults is strictly linked with brittle comminution and most of the seismogenic exhumed faults show an ultracataclastic core composed by ultra-fine grained gouges down to the nanometric scale (Chester *et al.*, 2005; Wilson *et al.*, 2005; Viti, 2011; Siman-Tov *et al.*, 2013). However, the origin of nanoparticles is problematic, and still matter of debate. The main proposed mechanisms are: (i) shock waves (Sammis and Ben-Zion, 2008; Spagnuolo *et al.*, 2015), (ii) thermal decomposition (Han *et al.*, 2007; Han *et al.*, 2010; De Paola *et al.*, 2011b), (iii) brittle failure after plastic twinning (Siman-Tov *et al.*, 2013) and intracrystalline plasticity (De Paola et al., 2015). Laboratory shear experiments on gouges and rubbing bare rock surfaces showed an efficient production of thin layers of nanogouge, even at subseismic slip rates (Wilson *et al.*, 2005; Han *et al.*, 2010; Reches and Lockner, 2010; Viti and Hirose, 2010; Tisato *et al.*, 2012; Verberne *et al.*, 2013a,b). This efficiency seems to be validated by Wilson *et al.* (2005), who argued that formation and weakening of new nanogouge is required after each seismic slip events in experimental faults, due to rapid gouge ageing (regain of strength).

More recently, some authors proposed nanograin grain boundary sliding (GBS) as a weakening mechanism in calcite (Verberne *et al.*, 2014; De Paola *et al.*, 2015; Green *et al.*, 2015; Siman-Tov *et al.*, 2015). They observed the formation of low-porosity slip zones composed by equant nanoscale grains with low dislocation densities and no preferred orientation, as well as highly reflective slip surfaces (SS). This mechanism will be discussed with more detail in the next chapter.

1.4. Previous work on high velocity experiments in carbonates

"Fault mirrors" or "mirror like surfaces" (MSs, introduced in the previous chapter) are highly reflective smooth surfaces commonly found in natural exhumed faults (Fig. 1.7). They occur in faults in different lithologies, even in unconventional ones like pure tourmaline (Viti *et al.*, 2016) or magnetite (Tarling *et al.*, 2018), and have been long found in carbonate-hosted faults (e.g. Hancock and Barka, 1987; Jackson and McKenzie, 1999). Most authors link the formation of MSs to seismic activity where high velocity slip on principal slip surfaces would promote high temperatures causing smearing and sintering (densification and grain growth) of nanograin layers (e.g. Siman-Tov *et al.*, 2013). Therefore, it has then been proposed that MSs may represent a microstructural

Fig. 1.7 | *Mirror-like surface on a strike-slip fault in brecciated Eocene limestone, Kfar Giladi quarry, Israel (Siman-tov et al., 2013).*

proxy for past seismic activity in carbonate-hosted fault zones (Fondriest *et al.*, 2013; Siman-Tov *et al.*, 2013; Smith *et al.*, 2013). No pseudotachylytes – which is regarded as the only non-ambiguous evidence of seismic slip in natural faults – are found in carbonate terrains. In fact, carbonates thermally decompose to oxides plus CO_2 rather than melting, if CO_2 can escape from the system (calcite decomposes at 720-900°C at room pressure; Deer *et al.* 1992; Han *et al.* 2007).

MSs indeed form in experimental faults sheared at seismic velocities and several authors tried to link the MSs microstructure to the observed mechanical weakening (e.g., Smith *et al.*, 2013, 2015; Siman-Tov *et al.*, 2015; Green *et al.*, 2015; De Paola *et al.*, 2015). However, patchy MSs are frequently observed also in low velocity experiments and some authors have therefore questioned their reliability as seismic markers (e.g. Verberne *et al.*, 2013; Tesei *et al.*, 2017).

Extensive experimental work has been carried out on the study of the frictional properties of carbonates, and a few mechanisms have been proposed to explain the observed dynamic weakening of experimental carbonate-bearing faults. Amongst the mechanisms proposed, two main different case scenarios can be identified, depending on whether the suggested weakening mechanisms are triggered and operate along the main sliding surfaces (rubbing surfaces) or within a principal slip zone of finite thickness (viscous flow). The most common interpretation is that MSs are principal slip surfaces, where seismic slip ($v > 0.1$ ms^{-1}) promotes thermally activated processes such as flash heating (Smith *et al.*, 2015) or by thermal runaway at dynamic asperities (Siman-Tov *et al.*, 2015). In support to these models, there is also evidence of temperature-activated crystal plasticity in the immediately adjacent rock volumes, which show ultramylonite-like texture (Smith *et al.*, 2015). The most favoured interpretation by previous authors is that these volumes are regions of low strain that are heated passively by the shear heating generated during seismic sliding along the main slip surfaces.

Other authors (De Paola *et al.*, 2015; Green *et al.*, 2015) found that these volumes adjacent to the MSs have remarkable textural affinity with those shown by metals and ceramics displaying superplastic behaviour (Chandra, 2001). Such textures are known to occur when deformation is accommodated by diffusion-assisted grain boundary sliding

14

(GBS, e.g. Ashby and Verrall, 1973). Therefore, these authors suggested that grainsize-sensitive creep mechanisms, occurring in a narrow (<100-µm-thick), ultrafine-grained shear zone, can cause coseismic weakening (Green *et al.*, 2015; De Paola *et al.*, 2015). De Paola *et al.* (2015) suggested that existing flow laws for GBS in calcite, obtained at low strain rates (10^{-3} s^{-1}) and larger grain sizes (3 µm; Schmid *et al.*, 1977), can predict the low shear stress measured at the temperatures, high strain rates (> $10^2 s^{-1}$) and nano-grainsize (< 100 µm) conditions attained during their experiments. These findings suggest that even at very high strain rates (> 10^2 s^{-1}), viscous flow of calcite can be an efficient fault lubricant.

1.5. Project rationale

1.5.1. Understanding the weakening mechanisms. Why does it matter?

Earthquakes have a strong impact on the anthroposphere. It is worth to remember the recent events that caused uncountable casualties and that shook so intensely the international awareness on the topic. For example, the 2015 Gorkha earthquake in Nepal (intercontinental collisional boundary, e.g. A vouac *et al.*, 2015), the 2016-2017 Central Apennines sequence of Italy (back-arc extension, e.g Tinti *et al.*, 2016) and the 2011 Tohoku-Oki earthquake (subduction zone, e.g. Ide *et al.*, 2011). The latter surprised the scientific community by rupturing a shallow patch of the fault which was thought to be creeping or, in other words, stable. Noda and Lapusta (2013) proposed with their model that the rupture propagation in aseismic patches, generally treated as "barriers", is possible and it is dominated by the effect of dynamic weakening. This concept becomes clear when the energy budget of earthquakes is taken in account. The energy radiated during an earthquake is equal to the difference between the potential energy change (i.e. the elastic energy released with the stress drop) and the dissipated energy, which is the mechanical work done on the fault (Scholz, 2002; Rivera and Kanamori, 2005; Kanamori and Rivera, 2006). Any reduction in the friction coefficient, due to weakening, makes slip propagation processes more efficient as it reduces the dissipated energy in the slipping part of the fault. This allows more energy to be spent for further

rupture propagation rather than in dissipative processes. Even though radiated energy can be constrained by inversion of seismological data from natural earthquakes, there is still an open debate about what is the best method to constrain it (e.g., Abercrombie *et al.*, 2013; Nielsen *et al.*, 2016). Therefore, understanding the mechanisms that control dynamic weakening – and possibly formulating rigorous governing equations – is key to the quantification and modelling of earthquakes.

1.5.2.   Earthquakes in carbonate rocks: constraints from calcite experimental faults.

Amongst the ones listed above, the 2016-2017 Central Apennine seismic sequence belongs to a populated category of recurrent, moderate to large (over 7 of moment magnitude scale), earthquakes. These have shallow hypocentres (up to 15 km) and propagate through thick sequences of sedimentary rocks, including a thick carbonate multilayer (e.g. Chiaraluce, 2012). Carbonate rocks are common worldwide, including the circum-Mediterranean mountain belts of the Apennines (Italy), the Hellenides-Dinarides (Balkan Peninsula), the Maghrebides (Algeria–Tunisia), Zagros (Iran) (Amato *et al.*, GRL

Fig. 1.8 | *On the left, view of Monte Vettore from the Piani di Castelluccio (looking towards east). Towards the top of the mountain is visible the scar left by the 6.0 magnitude Amatrice earthquake (August 2016), which ruptured to the surface. On the right, the small neighbouring town, Amatrice, annihilated by the event (photo property of L'Eco di San Gabriele).*

16

1998; Durand *et al.*, 1999, and references therein; Di Bucci & Mazzoli, 2003; Miller *et al.*, 2004; Burchfiel *et al.*, 2008). As these regions are densely populated, moderate to large earthquake events represent a severe and active hazard. Even moderate events were capable of widespread destruction and ruptures frequently broke to the surface (Fig. 1.8). Carbonates are therefore extremely relevant rocks for the study of nucleation and propagation of earthquakes.

1.5.3. Open questions and aim of the work.

Numerous publications are available in the scientific community addressing the weakening mechanisms during coseismic deformation in carbonate rocks. However, still different theoretical and conceptual viewpoints are offered to explain the collected experimental data and microstructural observations (e.g. Han *et al.*, 2010; De Paola *et al.*, 2015; Green *et al.*, 2015; Siman-Tov *et al.*, 2015; Smith, Nielsen and Di Toro, 2015). Therefore, I performed a systematic investigation of the processes controlling dynamic weakening in carbonates – using an integrated experimental and phenomenological approach – to build a comprehensive experimental and microstructural dataset. The main goal of my work was to use such constrained experimental and microstructural supporting evidence to formulate conceptual and theoretical frameworks of dynamic weakening processes in carbonates. The main aims of my research will be pursued throughout the chapters, building up evidences from multiple approaches and methodologies.

Chapter 3: The third chapter will focus on the experimental approach. High velocity experiments performed on a rotary shear apparatus will be used to investigate the weakening mechanisms in carbonate gouges. The method uses the integration of mechanical data with post-mortem microstructural analysis of samples. In particular, it will be investigated the relationship between mirror-like surfaces (see ch. 1.4), commonly regarded as principal slip surfaces, and well-defined principal slip zones. Their ubiquitous coexistence in natural and experimentally deformed rocks poses a puzzling

problem to the description of deformation processes. In fact, it is still poorly understood how strain is partitioned between the mirror-like surfaces and the nanoscale gouges in the principal slip zone and, hence, what is the role of mirror-like surfaces at dynamic conditions.

Chapter 3 will try answer to:

- What is/are the coseismic weakening mechanism/s in carbonate-hosted faults?

- What is the role played by mirror-like surfaces during coseismic deformation?

- How is deformation partitioned during seismic slip?

Chapter 4: The fourth chapter will present the results of acoustic emissions (AE) monitoring during similar experiments as those presented in Chapter 3. The technique has been rarely used to investigate deformation processes in rotary apparatuses at seismic velocities, almost no data exists for deformed rock powders. Therefore, still little is understood about the relationship between AE activity and deformation processes during propagation of experimental earthquakes. The approach has been made possible by a new custom-made acquisition system I developed, which is hosted within the sample assembly. Our results represent further, independent evidence, even if related to indirect type measurements, of the real-time dynamic evolution of deformation mechanisms throughout the weakening history. In this chapter, experiments performed on "unconventional" rock powders of sub-micron grainsize, the nano-gouges, will be also presented. Nano-gouges are believed to play a foremost role during coseismic weakening, but their behaviour is still poorly understood at such conditions (Ch. 1.3.4).

Chapter 4 will try answer to:

- How are deformation mechanisms evolving throughout the weakening history?

- What microstructural elements are active during deformation and when are they formed?

- What is the AE signature of experimental coseismic deformation in gouges?

18

Chapter 5: The fifth chapter will go into further microstructural investigation depth of experiments presented in Chapter 3. Electron backscattered technique, operated with a scanning electron microscope (SEM), will be used to document the evolution of textures and crystallographic orientation within critical regions of the inner fault architecture. Results will show for the first time the combined action of brittle and viscous deformation mechanisms at seismic strain rates and their impact on microstructures. In fact, little is still understood about the role that creep mechanisms play at high strain rates, where the influence of viscous processes is frequently neglected. Results will also be supported by microstructural analysis at the nano-scale using transmission electron microscope for imaging of intra-crystalline features.

Chapter 5 will try answer to:

- Can further, independent evidence be found about creep mechanisms controlling fault strength at high, seismic strain rates?

- What is the interplay of brittle and viscous mechanisms throughout the weakening history?

- What are the characteristic crystallographic textures of high velocity deformation processes?

Chapter 6: In the sixth chapter, we explore the problematic of finding a general, unifying characterisation of coseismic fault weakening. In fact, it appears that the dynamic weakening mechanisms proposed so far are dependent on the rock composition (Ch. 1.3), and each one is treated separately in literature using diverse constitutive equations. However, coseismic fault lubrication is ubiquitously observed in all terrains and is believed to be controlled by energetic balance between dissipative and conservative processes. By extending the experimental approach to materials other than calcite, we try to capture the behavioural similarity of their deformation processes in order to formulate a general, unifying theory.

2.   Methods

2.1.   High velocity shear experiments

2.1.1   Low to high velocity rotary shear apparatus.

The frictional properties of rock powders were tested using a Low to High Velocity Rotary shear apparatus (LHVR, Fig. 2.1, model MIS-233-1-77) built by the Marui & Co., Ltd Company (Osaka, Japan). Its functioning is similar to that of the apparatus first described by Shimamoto and Tsutsumi (1994; see also Hirose and Shimamoto, 2005). This machine allows to simulate the narrow principal slip zone of a fault at shallow crustal conditions (up to ~1 km in depth). The simulated fault is hosted within an annular chamber contained in the sample assembly (described in detail below). Due to the rotary configuration of the apparatus, it is possible to perform experiments with an arbitrary amount of slip.

The apparatus is housed in a rigid loading frame, made of assembled steel plates, and set up in a vertical configuration, secured to the floor by a base plate (Fig. 2.1 L). The machine has two vertical main shafts, on which is mounted the sample assembly. The upper one (Fig. 2.1 C) is connected through a gear box (Fig. 2.1 B) to an electric servo-controlled motor (Fig. 2.1 A), which has 11 kW power, 70 Nm rated torque and maximum revolution rate of 1500 rpm. The gear box reduces the revolution rate transferred from the motor to the main shaft using a system of clutches and reduction gears. Three speed-lines are allowed: high-speed (gear ratio 1:1), medium-speed (gear ratio 10^3:1) and low speed (gear ratio 10^6:1).

The machine speed is controlled by the operator with the control unit (Fig. 2.1 M) or by using an external function generator. The revolution rate and the cumulative rotation angle are measured by a tachometer and a pulse counter, respectively, mounted on the upper shaft. Measures are based on the pulses measured by a rotary encoder (Fig. 2.1 D) with a capacity of 3600 pulses per full rotation. The apparatus can accelerate to the maximum revolution rate (1500 rpm) in 0.277 – 0.351 s at normal stresses of 25 MPa

20

(for the hollow cylinder sample assembly; see Ch. 2.1.2), depending on the tested material (the numbers refer to calcite and olivine powders, respectively).

The sample assembly is mounted vertically in the apparatus (Fig. 2.1 E) so that the sample shear plane is parallel to the laboratory floor. The lower shaft (Fig. 2.1 F) is connected to a pneumatic cylinder (Fig. 2.1 K) that allows the application of the normal load to the sample by its vertical movement. The pneumatic piston (Bellofram type cylinder with an 82 mm stroke) is able to produce a maximum thrust of 10 kN. The axial load system is equipped with a high-precision air regulator to reduce and automatically correct the load fluctuation during the experiment. Axial load is measured using a thin compression load cell (Fig. 2.1 J) with a rated output of 2 mV/V ± 0.5%. Axial load cell resolution is ± 5 kN.
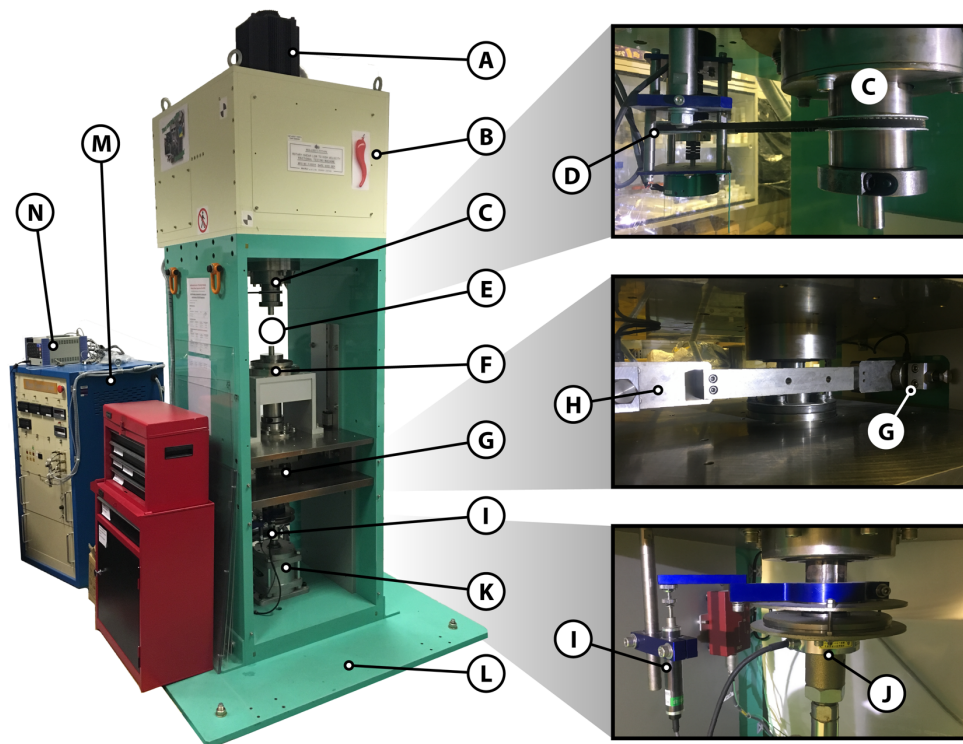
Fig. 2.1 | The high to low velocity rotary apparatus. A) servo motor; B) gear box; C) upper main shaft; D) rotary encoder; E) sample assembly location (not mounted); F) lower main shaft; G) torque gauge; H) torque bar; I) axial displacement gauge; J) compression load cell; K) pneumatic cylinder; L) base plate; M) control unit; N) acquisition system.

The axial displacement values attained during the experiments are measured using a high sensitivity displacement gauge (strain gauge type) with a capacity of 10 mm and rated output of 5 mV/V ± 0.1% (Fig. 2.1 I). Axial displacement resolution is ± 2 µm. Torque values attained during the experiments are measured by two compression load cells (strain gauge type, Fig. 2.1 G), which are activated by a torque bar (Fig. 2.1 H) fixed to the lower, main shaft. The load cell capacity is 1 kN, with a rated output of 2 mV/V ± 0.5%. Torque cell resolution is ± 0.5 N.

2.1.2   Sample assembly and sample preparation.

The sample assembly consists of two hollow cylinders (Fig. 2.2 A, external radius $r_e = 12.5$ mm and internal radius $r_i = 5.25$ mm) sandwiching a layer of gouge (Fig. 2.2 B, D). The cylinders are made of titanium-vanadium alloy (Ti-alloy, Ti90Al6V4; Yao et al., 2016), which is chosen as it has similar thermal properties (thermal condiuctivity of 5.8 Wm^{-1}K^{-1}) to common rocks. The base of each cylinder that is in contact with the gouge layer is machined with a crosshatch pattern of grooves (500 µm deep, Fig. 2.2 A), to force shear localisation within the gouge layer. A Teflon cylinder and a Teflon ring (Fig. 2.2 B), which is tightly fastened by a hose clip (Fig. 2.2 C), are mounted to prevent the internal and lateral extrusion of the gouge, respectively, during the experiments.

During the preparation, the Teflon gaskets are first mounted on the bottom cylinder producing an annular chamber where the gouge is poured in and levelled (Fig. 2.2 D). For experiments in micro-gouge (grainsize 63 – 90 µm), the standard material used in this work, exactly one gram of rock powder is used. In order to distribute the powder evenly, the cylinder is gently tapped and the thickness of the layer is measured with a calliper. This procedure grants reproducible thicknesses (when the same amount of powder is used) and allowed to minimise preparation artefacts, which could affect the quality and reproducibility of the mechanical data. The top cylinder is mounted directly on the sample holder located in the upper (dynamic) main shaft (Fig. 2.1 C) The cylinder is secured to the main shaft and axially aligned (±5 µm misalignment measured with a dial gauge) using a hydraulic mechanical lock.

Likewise, the assembled bottom cylinder is secured to the lower (static) main shaft (Fig. 2.1 F), which is connected to the gauges and the pneumatic cylinder. The lower column is then lifted until the top cylinder slides into the Teflon ring and touches the gouge. For reproducibility reasons, this operation is considered complete when an axial load of 0.35 kN is measured by the load cell. After this, the load is monitored, along with the axial displacement, and raised to target. The shear experiment can be started once the thickness of the sample is at equilibrium with the axial load.
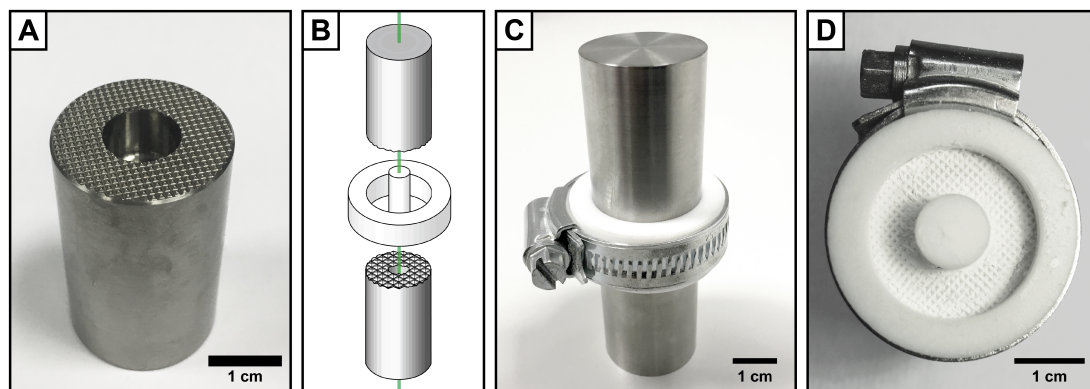
Fig. 2.2 | *Sample assembly: A) Hollow cylinder with grooved top; B) schematic representation of the mount; C) lateral view of the full sample assembly (not mounted on the apparatus); D) top view of the annular chamber containing calcite gouge (teeth marks are visible on top).*

2.1.3   Data logging, measured and calculated parameters

Velocity can be controlled either manually, using a four-digit code on the control panel, or using a digital function generator. All experiments were performed using the highest gear ratio supported by the motor. Rotations per minute (RPM) on the dynamic arm can be varied from 0 to 1500 changing the code from 0000 to 9999. The relation of RPM to code is linear. Velocity can be varied during the run, however, experiments reported in this work have been performed at constant target velocity (i.e. without changing the code). Alternatively, a digital function generator can be used to control the velocity of the apparatus and has been mainly employed to run experiments that

required control over the slip distance. The function generator (DF1906, NF Corporation) outputs a user-defined signal with a voltage range between 0 and 10 V DC. The apparatus responds linearly to the voltage producing up to 1500 RPM when 10 V are outputted. However, the function generator is not well-behaved over voltages of 9.5 V and delivers a maximum of 9.7 V. This means that each experiment performed at more than 1360 rpm had to be controlled manually. The function used for experiments is a simple box function (Fig. 2.2) with height linearly proportional to the target velocity.

The mechanical data outputted by the gauges is transferred to an acquisition system (EDX-100A, Kyowa Electronic Instruments CO LTD, Fig. 2.1 N) and recorded with the Dynamic Data Recording software, DCS-100A (Kyowa). Six channels are used to record values of time, cumulative rotation angle, angular velocity, axial load, torque and axial displacement. The sampling frequency varies depending on the type of experiment. Top speed runs have been recorded at 5 kHz. For each experiment, a CSV file containing the raw data is produced.

Given the cylindrical shape of the stainless steel cylinders, the slip slip rate (v) is variable across the sample radius. A reference radius (r_r) is chosen to calculate the mechanical properties of the material. For the hollow cylinder assembly, the reference radius is $r_r = (r_e + r_i)/2 \approx 8.33$ mm. Cross sectioning of deformed samples was always performed at this fixed distance from the rotating axis, to allow for a consistent interpretation of the microstructures.

The fundamental mechanical parameters are calculated according to the following equations (refer to Shimamoto and Tsutsumi, 1994, and Hirose and Shimamoto, 2005):

Tangential slip rate (ms^{-1}):

$$v(r_r) = 2\pi r_r R/60 \quad (2.1)$$

Where *R* is the revolution rate of the upper main shaft (in rpm). The tangential slip rate is calculated at the reference radius.

Displacement (m):

$$\delta(r_r) = v(r_r)t \qquad (2.2)$$

Where t is the time (s).

Normal stress (Pa):

$$\sigma_N = \frac{L_A}{\pi}(r_e{}^2 - r_i{}^2)^{-1} \qquad (2.3)$$

Where r_e and r_i are the external and inner radius (m) of the hollow cylinder, respectively, and L_A is the axial load (N).

Shear stress (Pa):

$$\tau = \frac{3\mathcal{T}}{2\pi}(r_e{}^3 - r_i{}^3)^{-1} \qquad (2.4)$$

Where $\mathcal{T}$ is the torque (Nm).

2.1.4   Experimental conditions and procedure of a standard experiment.

Before each run, the experiment is designed choosing: material, target velocity, pressure and total displacement (calculated at the reference radius). Once the sample assembly has been correctly mounted, the thickness of the specimen is monitored until it does not vary with time under the applied constant load (axial load of 0.35 kN), suggesting that sample axial compaction is completed. Then, the full axial load required for the experiment can be applied. The axial load is raised to target values using an air valve connected to the pneumatic piston. A maximum allowed axial load of 10 kN produces on the experimental fault a normal stress of σ_n = 25 MPa (when normalized over the contact area of the hollow cylinder), which corresponds to crustal depths (if a nominal lithostatic gradient of 27 MPa/km is assumed) of ~ 1 km. Most of the experiments were run at these conditions. The axial loading stage lasts for less than one minute as no variability in the loading path was observed to influence the mechanical

data at high velocities. This stage was recorded at low frequency to check reproducibility of the sample preparation and to test the initial loss of thickness. The experiment can start when no further axial displacement is measured in the following minutes.

Each run starts and stops with the input of the operator or the function generator. With the simple approach used in this work, the machine immediately accelerates to achieve target velocity as fast as possible (Fig. 2.3). The maximum acceleration depends on the sample assembly, the experimental conditions and the material used. For example, on the hollow cylinder assembly using calcite micro-gouge (material details are reported below), the angular acceleration at the maximum axial thrust (from 0 to 1550 rpm at 25 MPa) is ~862 rad s^{-2} (~5.05 ms^{-2} at the reference radius) At lower pressure (2.5 MPa) the acceleration is ~1200 rad s^{-2} (~7.04 ms^{-2} at the reference radius). After the stop signal is outputted, the column decelerates to stop with a slope that is steeper than the initial acceleration: ~1353 rad s^{-2} (~7.04 ms^{-2} at the reference radius). The velocity path in time has a trapezoid shape and shows small overshooting effects (< 1% of target v) at the end of the initial acceleration (Fig. 2.3).
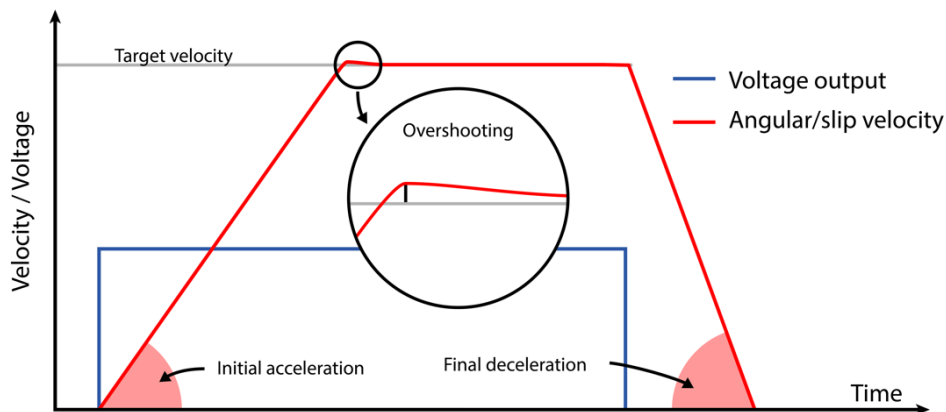
Fig. 2.3 | *Schematic diagram of the velocity profile measured during a generic experiment. The voltage output (either from the user-operated control unit or from the function generator) used to generate the velocity profile has the shape of a simple box function.*

2.2.   Microstructural analyses

2.2.1. Sample preparation for microstructural analysis

Samples are carefully recovered after each run for microstructural analysis. Due to the common formation of mirror-like surfaces (introduction), samples easily split along them when recovered from the metal cylinders. When this happens, it means that the full thickness of the deformed sample cannot be recovered, potentially undermining the full characterisation of the inner architecture of the slip zone. Therefore, the procedure was carried out as carefully as possible trying to preserve the entire thickness comprised between the metal cylinders. First, the outer Teflon ring is loosened and slid down one of the cylinders, while the sample is still mounted on the machine. The normal load is then removed slowly until the two cylinders separate. Most of the sample is generally preserved on the side still hosting the inner Teflon cylinder. After the removal from the machine, the sample is collected with tweezers and carefully stored. This method, when carried out successfully, provided excellent microstructural observations of the entire thickness of the deformed sample, including full imaging of the architecture of the entire slip zone.

The largest sample chips recovered after the experiments were mounted vertically using cyanoacrylate superglue in a cylindric mould and embedded in epoxy. A high viscosity resin was used in order to avoid further damage to the microstructures (like splitting along MSs by capillarity). Samples are arranged in the same relative position to allow recovery of cross-sections of the same representative area. One-inch pellets produced this way can host several chips and ease quicker analysis at the microscope (Fig. 2.4 A). Pellets were then machined with a grinder polisher using sand paper to expose a representative cross-section of the embedded chips (Fig. 2.4 B). The section is chosen at a distance equal to the reference radius (halfway between the sample contacts with the Teflon seals), parallel to the slip direction and perpendicular to the rotation plane (Fig. 2.4 C). This orientation is similar to the one classically used to analyse natural mylonites (e.g. Vernon, 2004). The cut surface was lapped with progressively finer diamond paste (6, 3, 1 and 0.25 µm). Each step required 5 to 10 minutes to be completed by the user (Fig. 2.4 B). Given the low hardness of the rocks analysed, longer

27

polishing sessions resulted in badly damaged surfaces.
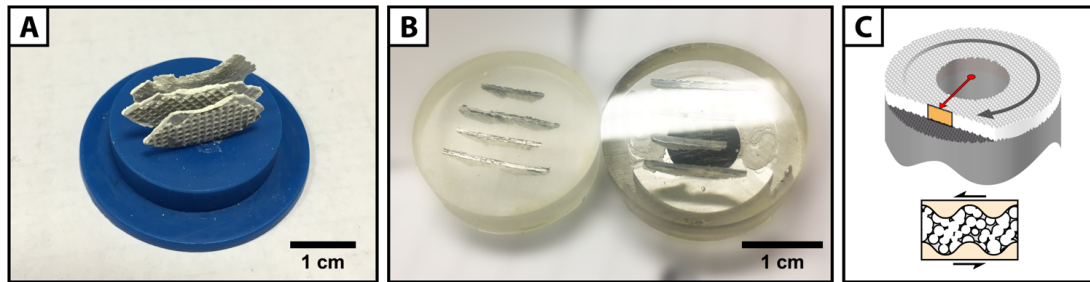
Fig. 2.4 | *Sample preparation: A) vertical mount of the sample chips on the mould base, prepared to be embedded in epoxy; B) sample chips embedded in epoxy and cut at the reference radius, before (left) and after (right) polishing; C) schematic of the position of the cross-sectional area used for microstructural analysis (orange area), the reference radius is represented by a red arrow.*

2.2.2. SEM and TEM imaging.

Microstructural analysis of cross-sections was carried with a FEI Helios Dual Beam Nanolab 600 scanning electron microscope (SEM) at the Department of Physics of Durham. Images were acquired in backscattered (BS) and forescattered (FS) modes. BS is operated using the through-the-lens acquisition system on samples coated with graphite. Due to the presence of ultrafine particles (< 100 nm) the coating thickness is kept as low as possible (< 30 nm). The advantage of BS is that, dealing with monomineralic gouges, it is possible to map qualitatively the porosity of the sample. At low magnifications, less porous areas will appear lighter in colour. This technique was used for relatively large-scale microstructures, to map fractures, individuate the epoxy (appears black) and, limitedly, imaging the grain boundaries. BS, though, is not suited to investigate well-polished areas with very low porosity, where tightly packed grains are non-resolvable. FS technique is used for detailed microstructures producing good contrast along the grain boundaries. The sample, however, requires special preparation. An additional polishing step using colloidal silica is used to produce extremely smooth

28

surfaces. FS is operated on uncoated specimens tilted at 70° using a 4 Quadrant KE Development FS imaging control detector.

FEI SEM was also used to prepare thin foils – carved with ion milling from specific locations of SEM-prepared samples – for transmission electron microscopy (TEM). Images were acquired on a JEOL 2100F FEG TEM at the Department of Physics of Durham using scanning (STEM) mode. STEM images allow to investigate the local and intra-crystalline nano-scale structure including features non resolvable with SEM imaging: e.g. microfractures, cavitation, dislocations and subgrains.

2.2.3. EBSD analysis.

The nature and evolution of grain crystallographic orientation patterns can be investigated using electron back scattered diffraction (EBSD) analysis. This can give important quantitative insights into the nature and evolution of grain scale mechanisms, which can then be related to the other microstructural observations and bulk mechanical data obtained during the experimental deformation of gouges. EBSD analysis is carried on uncoated cross sections polished as for SEM FD imaging and using the same tilted geometry (70°) and microscope. Data is collected with an Oxford Instruments Nordlys HKL detector (AZtec acquisition software, Oxford Instruments). EBSD data is elaborated using Channel5 to quantify the crystallographic orientation of grains in a chosen area. It can be visualised using orientation maps and pole figures, and used to perform misorientation analysis. The latter is used to quantify the overall distribution of crystal orientations and allows to inspect the geometric relationship between neighbouring grains.

2.3. Acoustic emissions recording.

Acoustic emissions were collected using a modified geometry of the sample assembly, the HexAPUS (Hexagonal Array of Piezoelectric acoUstic Sensors) unit (Fig. 2.5

29

A). The lower cylinder has been modified (Fig. 2.6 A) by the drilling of some vertical chambers (Fig. 2.6 D) to accommodate a built-in radial array of six acoustic sensors (Fig. 2.5 B). Each of the six vertical chambers hosts a sensor unit composed by a cylindrical piezoelectric transducer crystal (PI ceramic Pi255, 3×3 mm and 2.5 mm thick; Fig. 2.6 B) sandwiched by two copper disks (3 by 1 mm), all wrapped by heat-shrinking insulating tube (Fig. 2.6 C). The sensor is placed in contact with a copper disk that is also in direct contact with the bottom of the chamber (Fig. 2.6 D; close to the grooving) and kept in position by a Teflon disk, a steel spacer and a steel bolt (Fig. 2.6 E). Coaxial electric cables connected to each sensor pass through slits carved on the sides of the cylinder (Figs. 2.6 A, E and F).
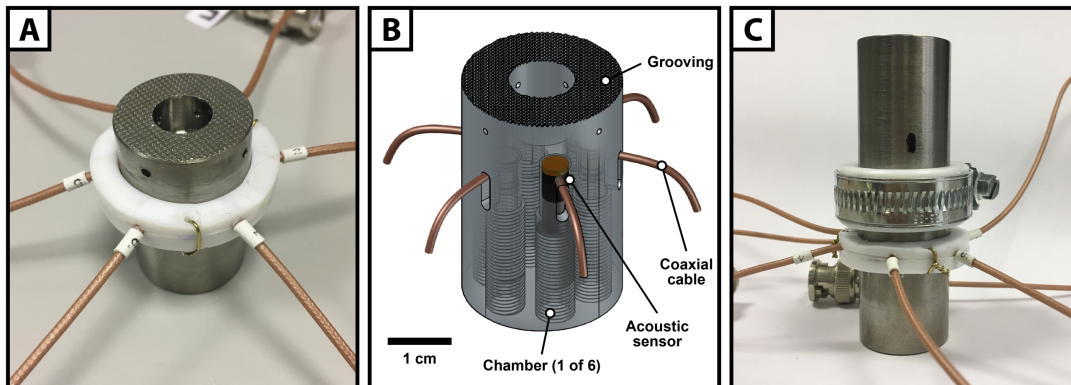
Fig. 2.5 | A) The HexAPUS: hollow cylinder modified to host an array of six piezoelectric sensors (connected to the cables protruding from the sides); B) schematic of the Hexapus; C) sample assembly fully mounted with HexAPUS at the bottom.

Acoustic emissions are monitored with a high frequency acquisitions system (up to 10 kHz) using the software InSite – Lab in continuous mode. The signal of each channel (measured in mV) is pre-amplified at 6 or 30 dB, corresponding to 4 and 31.6 times the original amplitude, respectively. The value was chosen depending on the material used. HexAPUS acoustic sensors have been calibrated using a Hsu-Nielsen source (lead-breaking test; Sause, 2011). Their sensibility band width is individuated between ~12 kHz and ~1 Mhz.

Machine noise has been tested running 12 experiments at different (1.4, 0.14, 0.014 and 0.0013 ms^{-1}) and normal stresses (2, 10 and 25 MPa) using Teflon sheets. No acoustic emissions were recorded during such experiments and the background noise during the run remained close to the static one.

The acquired voltage signal can be used to monitor in real time the activity of processes that emit acoustic waves such as fracturing. For example, a rough esteem of the vibrational energy dissipated is calculated with the hit count density in time. The qualitative activity of acoustic emissions is better visualised elaborating the raw signal with a fast fourier transform and then plotting the data into sonograms. Sonograms, or spectrograms, show the spectral signature (distribution of amplitudes with frequency) of the events through time. The technique is described in detail in chapter 4.
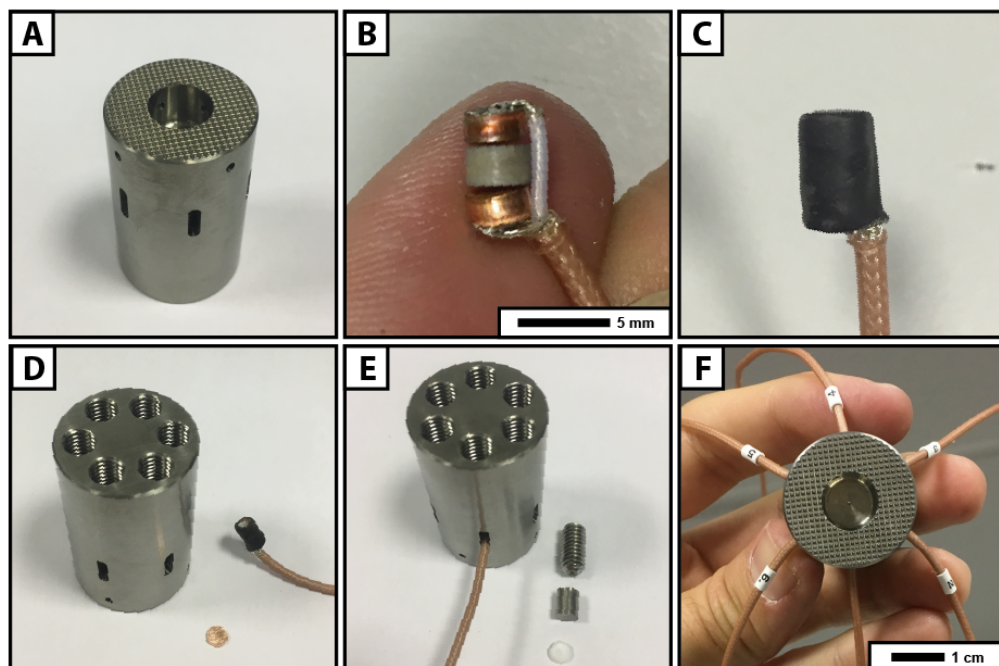
Fig. 2.6 | Preparation and mount of the piezoelectric sensors on the HexAPUS: A) modified hollow cylinder, on the sides are slits communicating with the inner chambers; B) sensor assembly consisting of two copper disks – connected to a coaxial cable – sandwiching a piezoelectric ceramic crystal; C) sensor wrapped by insulating rubber jacket; D) cylinder bottom showing the chambers, copper disk and assembled sensor; E) sensor mounted in the chamber, Teflon and steel spacers, and steel sealing bolt; F) fully assembled HexAPUS.

2.4. Temperature estimate in the principal slip zone during the experiments

During the experiment run it is not possible to directly measure the temperature with a probe, within the deforming layer and, particularly, within the actively slipping principal slip zone. A simple mono-dimensional equation for heat diffusion in a half space from a thin tabular source is utilised to estimate the temperature rise (ΔT) in the principal slip zone (PSZ; Carslaw and Jaeger, 1986; Rice, 2006) according to:

$$\Delta T(t) = \frac{1}{\rho c_P \sqrt{\pi \kappa}} \int_0^t \frac{\Phi(t')}{\sqrt{t-t'}} exp\left(-\frac{W^2}{4\kappa(t-t')}\right) dt' \quad (2.5)$$

where ρ is the density, c_P is the specific heat, κ is the thermal diffusivity, Φ is the heat flux, t is time and W is the PSZ thickness. This equation does not consider heat sinks apart from heat diffusion from the shear zone.

When the following relation is satisfied

$$W \ll 4\sqrt{(\kappa\delta/v)} \quad (2.6)$$

(where δ is the displacement and v is the slip rate) W is negligible compared to the length scale of heat diffusion and

$$exp\left(-\frac{W^2}{4\kappa(t-t')}\right) \approx 1 \quad (2.7)$$

In this case, non-adiabatic conditions can be assumed, and Eqn. 2.5 can be simplified to the following equation:

$$\Delta T(t) = \frac{1}{\rho c_P \sqrt{\pi \kappa}} \int_0^t \frac{\Phi(t')}{\sqrt{t-t'}} dt' \quad (2.8)$$

The heat flux radiating through one of the boundaries of the brittle shear band can be calculated according to (Rice, 2006):

$$\Phi(t) = \frac{\tau(t)v}{2} = \frac{\mu(t)\sigma_n v}{2} \quad (2.9)$$

where τ is the shear stress, σ_n is the normal stress and μ is the friction coefficient, to

32

obtain:

$$\Delta T = \frac{v}{2\rho c_P \sqrt{\pi\kappa}} \int_0^t \frac{\tau(t')}{\sqrt{t-t'}} dt' = \frac{\sigma_n v}{2\rho c_P \sqrt{\pi\kappa}} \int_0^t \frac{\mu(t')}{\sqrt{t-t'}} dt' \qquad (2.10)$$

Microstructural observations showing that the PSZs are usually thinner than 150 μm, allow us to assume that non-adiabatic conditions are representative of the thermal regime during the experiments. Hence, conditions expressed by Eq. 2.6 are always met in all of the experiments. It is important to note that the temperature rise calculated by Equation 6 is an upper estimate, as no other heat sinks are accounted for in it, apart from heat diffusion. In fact, as reported in the following chapters, we argue that all of the deformation energy in the deforming slip zone is dissipated as heat and neglecting heat sinks. For instance, in calcite gouges decarbonation reactions were not quantitatively significant. Temperature values obtained are used as a first approximation of the thermal conditions during the weakening process.

The thermal properties of materials used for the experiments is reported in table 2.1 below.

Rock	ρ	Density kg m^{-3}	c_p	Thermal Capacity J Kg^{-1} K^{-1}	κ	Thermal Diffusivity 10^{-6} m^2 s^{-1}
Anhydrite[A]		2950		721		2.5
Calcite[B]		2700		700		1.48
Dolomite[A]		2900		858		1.9
Sodium chloride[C]		2160		916		1.2
Olivine (Fo91)[D,E,F]		3340		1060		0.85

Table 2.1 |Thermal properties (determined at 300 K, see also Di Toro *et al.*, 2010) of rocks used in high-velocity experiments. References: A) Di Toro et al. (2011); B) De Paola et al. (2015, and references therein); C) Smith (1976); D) Xu et al. (2004); E) Clauser and Huenges (2013); F) Su et al. (2018).

3. Viscous flow controls fault strength during propagation of earthquakes in carbonate-hosted faults

3.1. Foreword

As discussed in the introductive chapter 1.4, coseismic weakening in carbonates is intimately linked to the formation of highly reflective smooth surfaces, known as "mirror-like surfaces" (MSs). Thus, our investigation of the weakening mechanisms found a natural beginning in the study of these microstructures, whose role played during the weakening of experimental carbonate faults at seismic slip rates is still debated (Fondriest et al., 2013; Siman-Tov et al., 2013; Smith et al., 2013), as it is still debated their interpretation in the field as seismic markers of natural faults (Verberne et al., 2013; Tesei et al., 2017). This chapter presents experimental results obtained using a rotary shear apparatus, which are integrated with microstructural observations, captured with the use of a scanning electron microscope. Our results led to propose a novel conceptual model of the weakening history of carbonate seismic faults – and its complex evolution of mechanisms – where MSs are (mutable) protagonists.

Details about the experimental methodological approach adopted, and about the apparatus used to obtain the experimental dataset, are reported in Chapter 2. The results and main findings of this chapter have also been published in Geology (Pozzi *et al.*, 2018), and a copy of the original Geology manuscript is included in the Appendix II.

3.2. Introduction

MSs have long been found and described along natural exhumed faults. More recently, it has been proposed that they may represent a possible microstructural proxy for past seismic activity in carbonate-hosted fault zones (Siman-Tov *et al.*, 2013). Several authors have since demonstrated that continuous MSs develop in carbonate gouges and rocks when sheared at seismic velocities (> 0.1 ms^{-1}) – in situations where frictional weakening is also observed – and have proposed different interpretations of their role in the weakening process (e.g., Smith *et al.*, 2013, 2015; Siman-Tov *et al.*, 2015; Green

et al., 2015; De Paola *et al.*, 2015). Other authors, however, have produced patchy MSs during lower velocity experiments (0.1 10 μms^{-1}), and therefore questioned their reliability as seismic markers (e.g., Verberne *et al.*, 2013). When dynamic fault weakening is observed, MSs are typically interpreted to be principal slip surfaces developed within and/or at the boundary of a slip zone. It has been argued that weakening during shear along the MSs can be driven by flash heating (Smith *et al.*, 2015) or by thermal runaway at dynamic asperities (Siman-Tov *et al.*, 2015). In support of these models, there is also evidence of temperature-activated crystal plasticity in the immediately adjacent rock volumes. Other authors have suggested that grainsize-sensitive creep mechanisms, occurring in a narrow (< 100 μm thick), ultrafine-grained shear zone, can cause coseismic weakening (Green *et al.*, 2015; De Paola *et al.*, 2015). However, the role played by MSs throughout the weakening history of carbonate gouges is still uncertain, as is the partitioning of strain between presumed sliding along MSs and bulk deformation by grain boundary sliding and/or crystal plasticity within the main slip zone. Here, we integrate mechanical data and microstructural observations to develop a new conceptual model concerning the role and significance of MSs throughout the weakening history of calcite gouges sheared at seismic velocities.

3.3. Methodology and results

3.3.1 Experimental conditions

We performed friction experiments on simulated calcite gouge (grain size: 63 - 90 μm) in a low-to-high-velocity rotary shear apparatus (De Paola et al., 2015; also described in Ch. 2.1.1). A sample assembly with two hollow cylinders made of a titanium-vanadium alloy (Ti-alloy, Ti$_{90}$Al$_6$V$_4$; Yao et al., 2016) was used to sandwich a layer of gouge (weight of 1 g and initial thickness ~1.4 mm), which was confined using a Teflon outer ring and an inner Teflon cylinder (see Ch. 2.1.2). All experiments were run at room temperature and humidity conditions, normal stress σ_n ~ 25 MPa and slip rates up to v = 1.4 ms^{-1}, calculated at the reference radius of ~8.9 mm. Experiments were arrested at different displacements (up to 1 m, for a duration <1 s) to analyse the evolution of

microstructures of samples throughout their weakening path.

3.3.2   Mechanical data: A four-stages weakening history

The mechanical data are summarised in Table 3.1 and the experimental results are plotted in Figs. 3.1, 3.2 and 3.3. However, experiments run at low velocities (v < 0.3 ms-1) frequently failed after a certain amount of slip due to gouge loss (shown by * in Table 3.1). For these experiments, only the reliable part of each run is plotted in Figs. 3.1 and 3.3 and its total displacement is reported in table 1.

Exp. #	v (ms^{-1})	δ (m)	δ_{tr} (cm)	σ_n (MPa)	τ_P (MPa)	τ_{ss} (MPa)	μ_{ss}	D_W (m)	α	T_W (°C)
VF 666		0.04								
VF 664		0.07								
VF 695		0.26								
VF 662	1.4	0.26	4.7	25.0	20.1	3.8	0.15	0.4	1E-11	751
VF 693		0.26								
VF 660		0.90								
VF 793		3.24								
VF 827	0.58	1.00	4.7	25.0	21.2	5.6	0.22	0.31	5E-9	735
VF 828	0.36	1.00	4.7	25.0	20.1	6.8	0.27	0.25	3E-8	604
VF 829*	0.25	0.60	4.7	25.0	20.0	~8.6	~0.34	~0.23	2E-6	487
VF 680		0.08								
VF 675		0.23								
VF 679*	0.14	0.26	6.4	25.0	21.4	~10.5	~0.42	~0.25	3E-5	474
VF 677*		0.29								
VF 676*		0.37								
VF 803*		0.39								
VF 834*	0.077	0.15	9	25.0	-	-	-	-	-	445
VF 831*	0.046	0.20	12	25.0	-	-	-	-	-	410
VF 833*	0.031	0.22	20	25.0	-	-	-	-	-	420
VF 672*		0.13								
VF 673*	0.014	0.18	27	25.0	-	-	-	-	-	334
VF 824*		0.32								
VF 670	0.0014	0.07	-	25.0	-	-	-	-	-	-
VF 823*		0.32								

Table 3.1 | *Compendium of mechanical data where v is the slip rate, δ is the total displacement for the reliable part of the experiment, δ$_{tr}$ is the displacement to the onset of weakening (stage II in experiments with v > 0.077 ms-1), σ$_n$ is the normal stress, τ$_P$ is the peak shear stress (end of stage I), τ$_{ss}$ is the shear stress at (quasi-) steady state conditions, μ$_{ss}$ is the friction coefficient at (quasi-) steady state conditions, D$_C$ is the weakening distance, α is a best-fit coefficient used in Eq. 3.1 and T$_W$ is the calculated PSZ bulk temperature at the onset of weakening (room T = 20°C).*

Shear stress curves have been fitted using the exponential decay equation (Fig. 3.1 B):

$$\tau_f = \tau_{SS} + (\tau_P - \tau_{SS})e^{\left[\frac{ln(\alpha)\delta}{D_W}\right]} \qquad (3.1)$$

where τ_f is the fitted shear stress, τ_{SS} and τ_P are the shear stress at steady state and peak conditions, respectively, α is a best fit coefficient, δ is the displacement and D_W is the slip weakening distance (modified after Mizoguchi *et al.*, 2007 and De Paola *et al.*, 2011b). D_W is calculated as the displacement required for the shear stress to decrease from τ_P by an amount equal to 95% of $(\tau_P\text{-}\tau_{SS})$. The values used in the calculation are reported in Table 3.1.

Dynamic weakening was observed in experiments run at v > 0.1 ms^{-1} (Fig. 3.1), in good agreement with values typical of seismic slip rates (Smith *et al.*, 2013). The evolution of strength of the experimental fault follows a characteristic weakening profile characterized by four distinct phases (Fig. 3.4). During Stage I, Byerlee's friction values of μ > 0.6 were attained, and slip-hardening up to peak values of μ = 0.9 is observed (Fig. 3.4). Experiments consistently showed the onset of weakening after an amount of slip of δ ~6.4 cm and δ ~4.7 cm for target velocities of *v* = 0.14 ms^{-1} and v $\geq$ 0.25 ms^{-1}, respectively (Stages I and II in Fig. 3.4). During Stage II, the material weakens in an exponential fashion to low, rate-dependent friction values, μ = 0.5 - 0.4 at *v* = 0.14 ms^{-1}, and μ = 0.2 - 0.15 at *v* = 1.4 ms^{-1} which then remain low throughout Stage III (Fig. 3.4). During Stage IV, material strengthens up to friction values μ = 0.4 - 0.5 upon deceleration of the motor to arrest (Fig. 3.4).

We use a simple mono-dimensional thermal diffusion model (Rice, 2006) to calculate the bulk temperature rise associated with the development of a thin slip zone (Ch. 2.4). Due to the high angular strains (γ >> 10) and strain rates (> 10^3) attained during the experiments, it is reasonable to assume that, to a first approximation, all of the deformation energy in the deforming slip zone is dissipated as heat (Hobbs and Ord, 2014, and references therein). The estimated temperature at the onset of weakening, T_w (beginning of Stage II) is rate-dependent, with T_w ~470 °C and T_w ~750 °C for *v* = 0.14 ms^{-1} and *v* = 1.4 ms^{-1}, respectively. Repeated runs show a consistent evolution in the
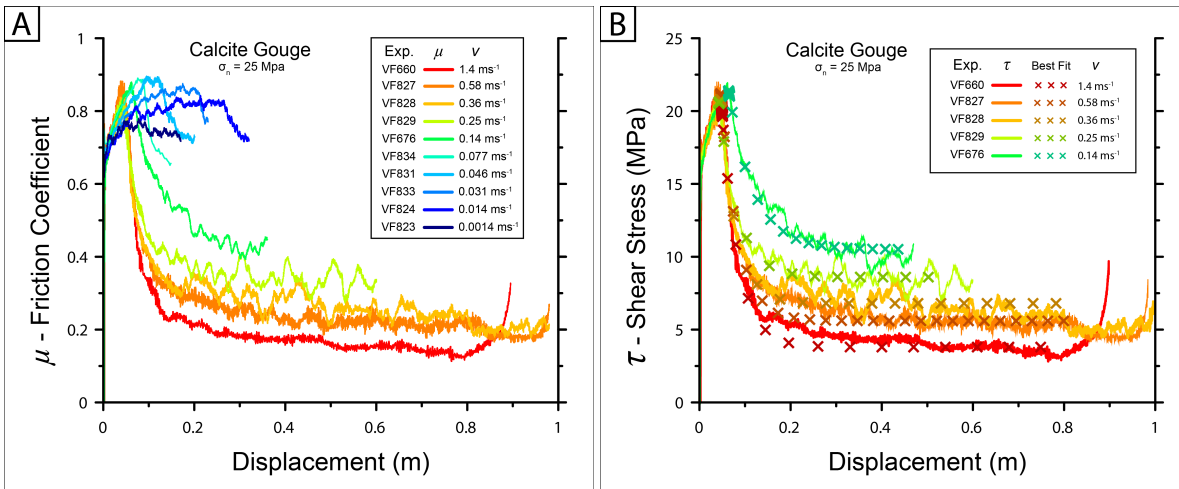
Figure 3.1 | *Representative friction coefficient (A) and shear stress (B) curves plotted over displacement for different velocities (with σn = 25 MPa). Best fit curves calculated with Equation 3.1 using the variables reported in Table 3.1 are plotted with X symbols in B). Onset of weakening and (quasi-) steady state (stage III) friction coefficient are clearly slip rate dependent.*
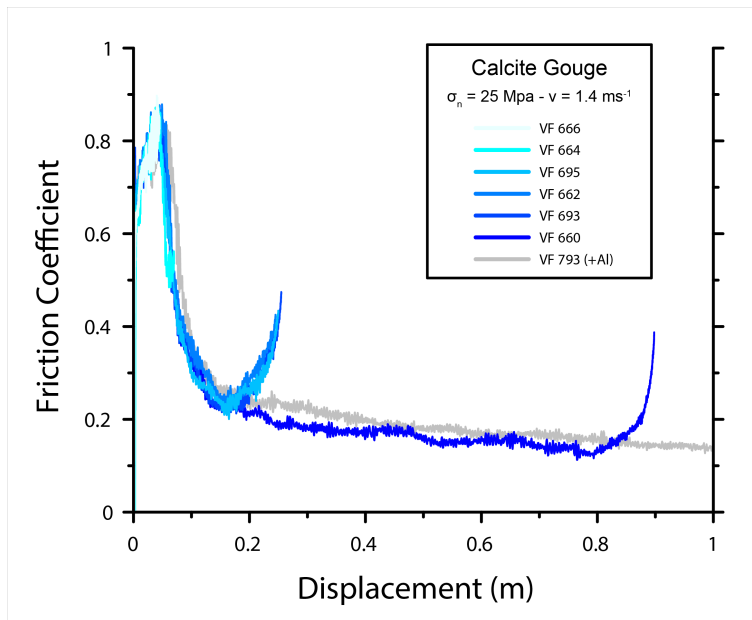
Figure 3.2 | *Friction coefficient curves plotted over displacement for experiments performed at slip rate of 1.4 ms^-1. VF_793 shows a slightly different behaviour due to the contamination with low amounts of Al_2O_3 powder, used as strain marker.*
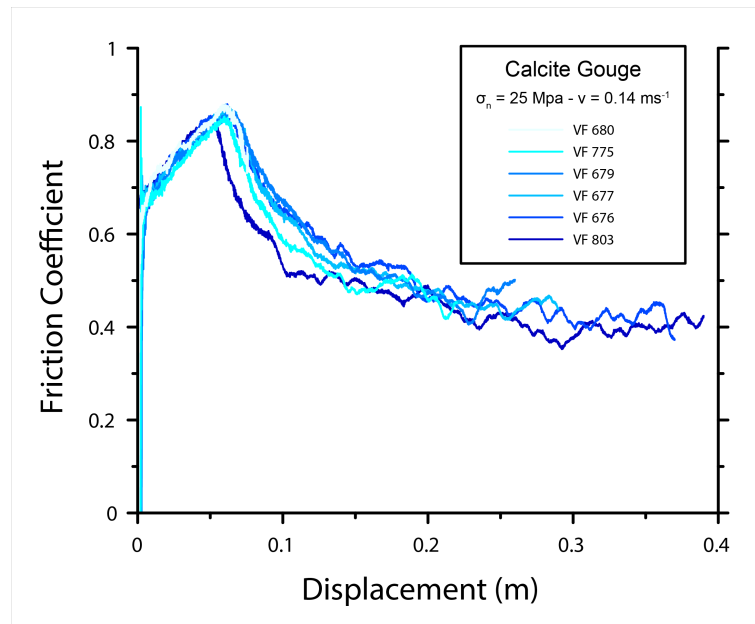
Figure 3.3 *| Friction coefficient curves plotted over displa-cement for experiments performed at slip rate of 0.14 ms⁻¹.*
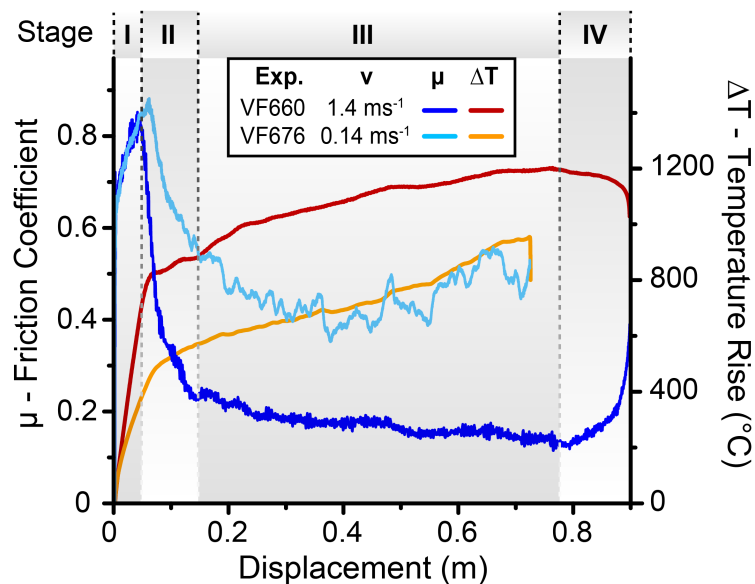
Figure 3.4 *| Mechanical data for two representative experiments (Exp., v = 1.4 ms⁻¹ and v = 0.14 ms⁻¹): friction coefficient (μ, shown in cold colours: light and dark blue) and estimated temperature rise (ΔT, shown in warm colours: orange and red) curves are plotted versus displacement. The four stages of friction evolution are highlighted by the shaded areas.*

mechanical data, proving good reproducibility of the experimental results (Figs. 3.2, 3.3).

Substantial axial shortening *(ΔW)* of the sample occurs during the application of the vertical, normal load. The amount of shortening depends on the normal load applied, and at σ_n = 25 MPa it is on average ~0.5 mm. This shortening is due to the reduction in porosity that occurs under static conditions, i.e. before any shear motion is imposed to the sample. For experiments performed at 1.4 ms^{-1}, after the onset of shearing, less than 0.2 mm of shortening occurs during Stage I (Fig. 3.5), mostly due to shear-induced compaction. The rate of axial shortening decreases through stage II, and up to 0.15 mm of additional shortening is recorded before the onset of Stage III. During Stage III and IV, the sample slowly shortens until the end of the experiment (1 m of slip), reducing its thickness by less than 0.1 mm.
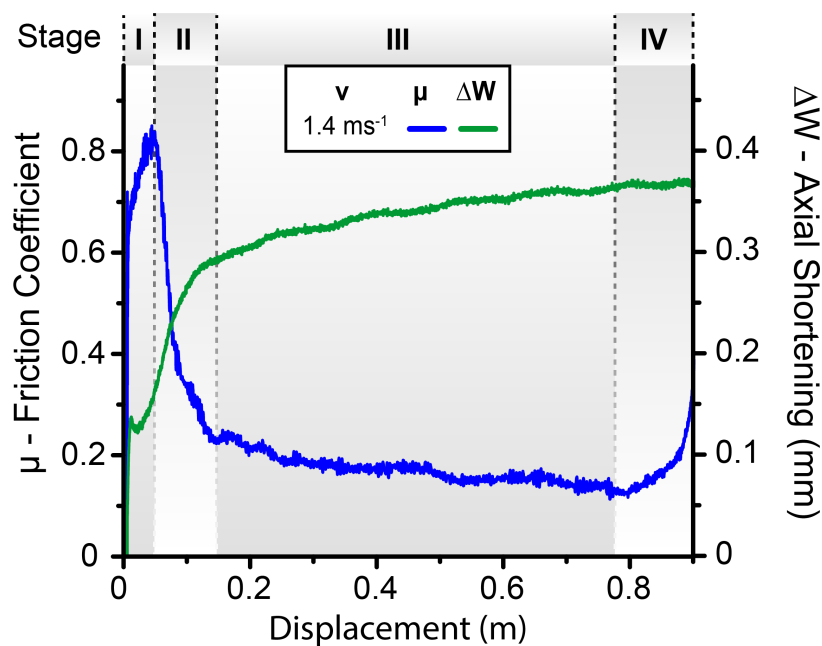
Figure 3.5 | *Representative axial shortening recorded for an experiment run at σn = 25 MPa and v = 1.4 ms^{-1} (VF660).*

3.4.   Microstructural observations

After the experiments, sample chips were carefully removed from the rotary assembly and embedded in epoxy to preserve the whole thickness of the gouge layer (Fig. 3.6). We used a FEI Helios Nanolab 600 electron microscope to acquire backscattered and forescattered electron images on polished cross-sections, which were cut parallel to the slip direction and perpendicular to the gouge layer boundaries, at the reference radius (~8.9 mm). The values of grain size and slip zone thickness reported here refer to samples sheared at $v = 1.4$ ms^{-1}.

Gouge samples recovered at the end of Stage I are porous, slightly cohesive, and show the effect of widespread brittle grain-size reduction (Fig. 3.6 A). During this stage, deformation is mostly accommodated by Riedel shears (R and R') and is within an ~100 µm thick Y-shear zone (Fig. 3.6 A), where extreme grain-size reduction occurs (down to a few tens of nanometers). Microstructures change during Stage II, from the onset of weakening, when the Y-shear zone evolves to a well-defined principal slip zone (PSZ) with sharp boundaries and inhomogeneous grain size, with larger clasts (<1 µm) dispersed within a finer-grained matrix (mean grain size ~100 nm; Figs. 3.6 B and C). Volumes of low-porosity sintered material, with thicknesses of ~20 µm, form outside the PSZ (Fig. 3.6 C) and their surfaces bound the PSZ, forming discontinuous MSs.

At the end of the transient stage of decay from peak to low friction values (Stage II) and throughout Stage III, the PSZ becomes a discrete, porosity-free volume of fine, polygonally recrystallized material with constant thickness (~30 µm; Figs. 3.6 D, 3.7 A and B). The internal structure of the PSZ shows fairly homogeneous grain size, triple junctions, and oblique foliation, marked by a shape-preferred orientation of the crystals, consistent with the overall (sinistral) sense of shear (Figs. 3.7 B and 3.8). This texture is similar to that observed in some natural (Bestmann *et al.*, 2000; Herwegh and Kunze, 2002) and experimental (Barnhoorn *et al.*, 2004) calcite ultramylonites. PSZ grain size increases from an average of ~300 nm (Fig. 3.8 C) at the beginning of Stage III to ~700 nm (Fig. 3.8 F) after ~0.75 m of slip.
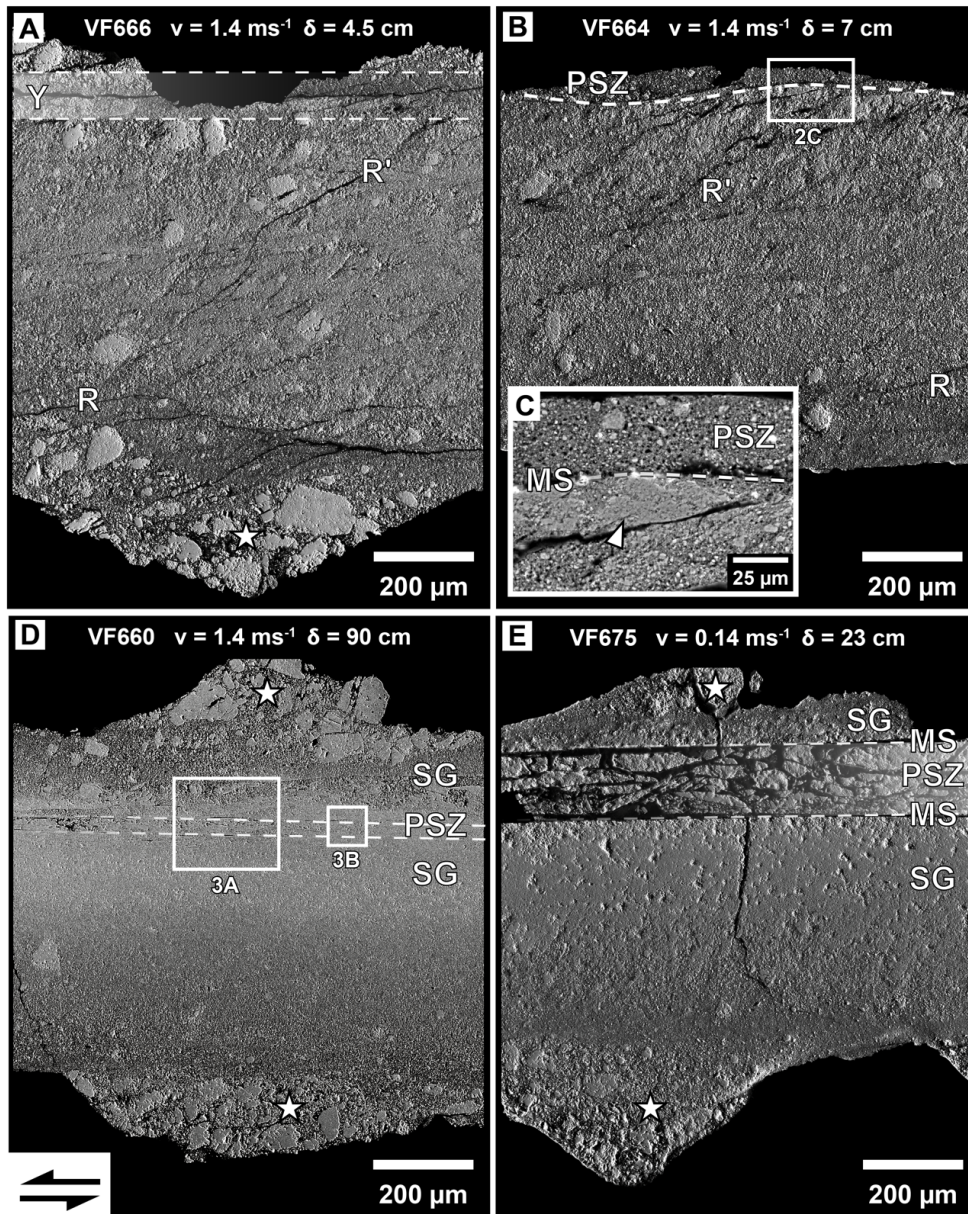
Figure 3.6 | *Backscattered electron images of sample cross sections obtained from the whole thickness of gouge layer (see the coarse-grained gouges filling the grooves machined on the top and bottom sample assembly cylinders, indicated with white stars) cut at the reference radius. Shear sense is top to the left. A) Stage I: diffuse and localized deformation with Riedel shear bands (R, R') and a horizontal Y shear band (Y). B) Stage II) well-developed principal slip zone (PSZ) with patchy recrystallized boundary ("mirror-like surface", MS). C) Close-up of area outlined in B. D, E) Stages III and IV) fully developed PSZ bounded by MSs and sintered deactivated layers (sintering gradient, SG) of experiments run at v = 1.4 ms^{-1} and v = 0.14 ms^{-1}, respectively. Stage IV damage in the PSZ is more evident in the lower-velocity experiment.*

The texture observed in proximity to, but outside, the PSZ is similar to that observed inside the PSZ, but shows an abrupt increase in grain size of approximately one order of magnitude (>1 μm; 3.7 B). Such marked grain-size decoupling produces sharp planar boundaries on either side of the PSZ: the MSs (figs. 3.7 B and 3.9). In the outer layers, away from and on both sides of the PSZ, porosity gradually increases as recrystallization becomes less pervasive, forming what we term here a 'sintering gradient' (SG; 3.6 D). In these regions, an array of relict subparallel MSs is observed (white lines in 3.7 A). The younger MSs are straight and smooth, and show a homogeneous grain size along them (Figs. 3.7 A and B). Another set of more irregular MSs is also observed (3.7 A), and interpreted to represent older MSs due to their similarity to the patchy ones formed during the early Stage II (Fig. 3.6 C). These are locally reworked and may truncate larger clasts (e.g., Fondriest *et al.*, 2013) during formation and localization of the early PSZ. During Stage IV, brittle dilatant fracturing occurs and appears to be consistently restricted to the PSZ (e.g., Fig. 3.6 E). It includes splitting along the MSs (exploited by epoxy during sample preparation; 3.7 B), which exposes shiny MSs visible in recovered samples (Fig. 3.9 A). These structures always unavoidably overprint — but do not obliterate — microstructures developed during Stage III. Similar to findings discussed by De Paola *et al.* (2015), our microstructural and mineralogical observations revealed that, during Stage III and IV, the PSZ is composed of crystalline calcite. This confirms that decarbonation reactions were not quantitatively significant during our experiments.

3.5.   Discussion

With its finite volume, parallel boundaries, and textural decoupling with the outer layers, we can reasonably assume that the PSZ corresponds to a zone of finite simple shear strain (inset of 3.7), where grainsize-sensitive processes are active (e.g., De Paola *et al.*, 2015; Green *et al.*, 2015). We define W_{PSZ} as the thickness of the PSZ, evolving throughout every stage of the weakening path. W_{PSZ} is constrained by microstructural observations (Figs. 3.6 and 3.7). We propose a conceptual model where W_{PSZ} is compared to a theoretical thickness W_T (Fig. 3.10 B), here defined as the minimum thickness, for a given velocity ($W_T = v/\dot{\gamma}_{max}$ where $\dot{\gamma}_{max}$ max is the maximum strain
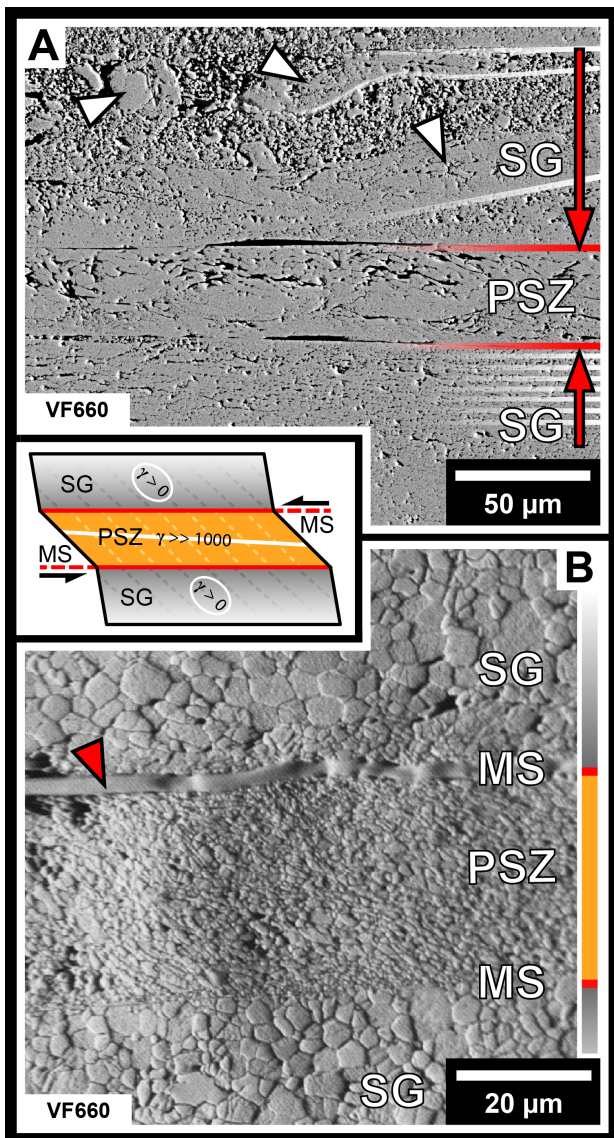
Figure 3.7 | Close-up scanning electron microscopy images of Stages III and IV principal slip zone (PSZ) cross sections (same sample as in Fig. 2D, v = 1.4 ms^{-1}, δ = 90 cm). A) Back-scattered electron image showing relict (highlighted with white lines) and the last active (red lines) "mirror-like surfaces" (MSs); white arrows indicate the older, irregular, reworked MSs; red arrows indicate direction of migration of the PSZ boundaries during localization. SG—sintering gradient.

B) Forescattered electron image of PSZ displaying oblique foliation, sharp grain-size transition at the boundaries, and MSs locally split and filled with epoxy during sample preparation (red arrow). Textures inside and outside the PSZ are clearly asymmetric with respect to MSs. In the inset, a schematic model of simple shear is compared to the microstructures. γ is the angular strain.

Figure 3.8 | *Grain size comparison between FSD images of sample VF662 and VF660. A) early stage III PSZ; B) close up of early stage III grains in the SG close to PSZ; C) close up of early stage III grains in the PSZ; D) stage III PSZ; E) close up of stage III grains in the SG close to PSZ; F) close up of stage III grains in the PSZ.*

45
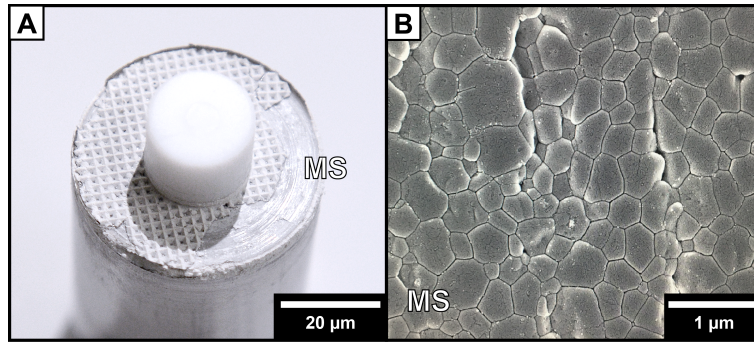
Figure 3.9 | *A) Sample of calcite gouge sheared at σ_n = 25 MPa and v = 1.4 ms^{-1} up to stage III (~1 m of slip), still mounted on the bottom cylinder after unloading and removal from the machine. Part of the sample (left hand side) has split revealing a shiny mirror-like surface (MS). Concentric grooves are visible on the MS. Successful recovery of the full sample thickness is possible where the imprint of the top cylinder (crosshatch pattern) is visible. B) Back scattered electron image of the MS.*

rate), of an ideal viscous shear zone deforming by grain-size-sensitive creep. W_T is therefore a function of grain size (*D*), temperature (*T*) and shear stress (*τ*), i.e. $W_T = f(D, T^{-1}, \tau^{-1})$ (derived from Eq. 3.2; Poirier, 1985).

During Stage I, brittle deformation, which is initially distributed within the entire gouge-layer thickness, localizes after a small amount of slip into a Y shear band (Figs. 3.6 A and 3.10 B). With increasing displacement, this band becomes a well-defined discrete PSZ, where extreme comminution (D << 1 μm) and increasing bulk temperature occur. Nanometric particles are formed in the PSZ, possibly by shock-like stress release processes (Sammis and Ben-Zion, 2008; Spagnuolo *et al.*, 2015) and brittle failure aided by intragranular crystal plasticity (Siman-Tov *et al.*, 2013; De Paola *et al.*, 2015). At this stage, the PSZ temperature is still relatively low (Fig. 3.10 C) and, consequently, W_T >> W_{PSZ} (Fig. 3.10 B), which means that the dominant strain rate is still controlled by brittle processes (e.g., Smith *et al.*, 2015). At the beginning of Stage II, as the temperature rises, we infer that the viscous strain rate increases and begins to compete with the brittle one, leading to a rapid decay in friction to the low friction values of Stage III (Figs. 3.10 B and C). During Stage II, the PSZ grain size homogenizes and porosity reduces due to
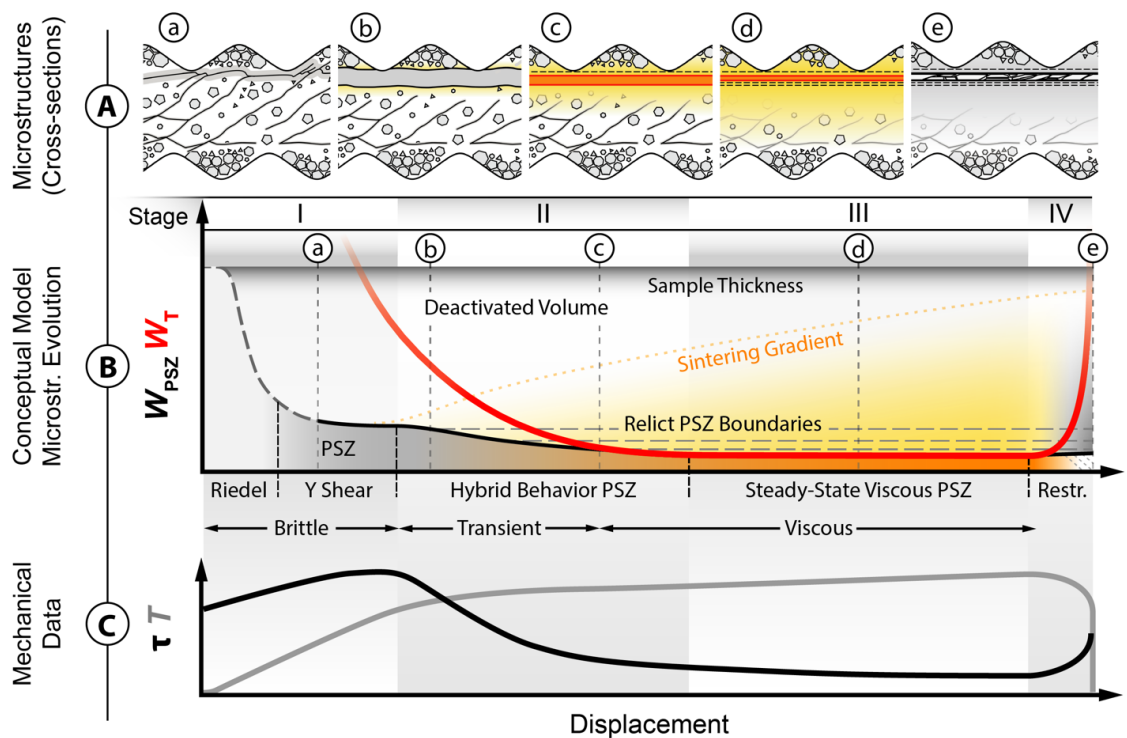
***Figure 3.10** | Graphical representation of the conceptual model with increasing displacement. A) Interpretation of microstructural evolution in the sample. B) Conceptual model comparing the thickness of the actively deforming volume (W_{PSZ}, PSZ - principal slip zone) with the theoretical thickness (W_T) and evolution of microstructures with increasing displacement. C) Schematics of shear stress (τ) and temperature (T) during experiments.*

plastic yielding of nanograins. The heat diffusing from the PSZ boundaries promotes grain-size growth in the outer regions on either side of the PSZ. During this stage, the PSZ becomes confined between two sharp sintered boundaries, and its thickness reduces as the temperature rises (migration of MSs; see below). When $W_T = W_{PSZ}$, the viscous strain rate becomes dominant, and at this point, the grain-size–sensitive creep controls the strength of the fault (Fig. 3.10 B). The increase in temperature due to viscous shear heating will decrease WT and can lead to further localization of the PSZ (Fig. 3.10 B), before the achievement of the low friction values of Stage III. As the PSZ narrows, the old boundaries are deactivated and are preserved as closely spaced planar discontinuities (relict MSs) in the coarse-grained sintered layer (3.7 A). A similar

microstructure has also been observed in natural faults (Tesei *et al.*, 2013; Collettini *et al.*, 2014). By Stage III, the PSZ has reached steadystate thickness and strain rate, with low, slowly evolving shear stress (viscosity) and grain size (Fig. 3.10 B). We interpret that the oblique foliation formed in the PSZ during Stage III is a steady-state foliation, achieved through cycles of passive rotation and resetting through dynamic recrystallization (e.g., Barnhoorn *et al.*, 2004, and references therein). Thus, it does not reflect the total strain in the PSZ.

Following the approach in De Paola *et al.* (2015), a general flow law for creep is used:

$$\dot{\gamma} = A^* \frac{\tau^n}{D^m} e^{\left(-\frac{H}{RT}\right)} \qquad (3.2)$$

where $\dot{\gamma}$ is the strain rate, A^* is the pre-exponential factor, τ is the shear stress, n the stress exponent, D is the grain size and b is the grain size exponent, H is the apparent activation energy for creep, R is the gas constant, T is the absolute temperature. Table 2 reports the variables used for the two different creep regimes (De Paola *et al.*, 2015 and references therein).

As discussed in detail in De Paola *et al.* (2015), the grainsize in the PSZ in the post-mortem microstructures is not fully representative of the dynamic values during deformation, due to grain growth by static recrystallization during the cooling stage after the experiment. Flow stress values were therefore calculated for a range of grain sizes (0.10 - 0.01 µm), which are equal or smaller than those observed in the PSZ. Our calculated flow stresses are of the same order of magnitude than those measured during the experiments run at 1 ms^{-1} and 0.14 ms^{-1} (Fig. 3.11 A and 3.11 B, respectively).

We propose that throughout Stages II and III, heat produced by shear heating within the PSZ diffuses into regions immediately adjacent to and outside the PSZ, where the strain rate is lower. The dissipated heat leads to the development of sintering gradients (SGs) by quasi-static grain growth and densification in the materials outside the PSZ. At the same time, viscous deformation maintains a homogeneous, nanometric grain size inside the PSZ. These interpretations are supported by our microstructural observations

Def. Mechanism	$A*$ (s^{-1} bar^{-n} μm^{m})	n	m	H (kcal mol^{-1})	R (kcal K^{1} mol^{-1})
Grain Boundary Sliding	$9.55*10^{4}$	1.7	3	51.0	
Dislocation Creep	$4.6*10^{-2}$	4.7	0	71.0	1.987 E-3

Table 3.2 | *Variable used in Eq. 3.2 to calculate the curves of Fig. 3.11.*

showing a sharp textural contrast between the material in the PSZ and that in the SG domains (3.7B). Therefore, the MSs evolve to become strain compatibility boundaries, separating a fine-grained, weak, viscously deforming PSZ (with > 10^{3}), from coarser-grained and sintered volumes. These are passively heated and deform slowly on both sides of the PSZ (also proposed by Kim *et al.*, 2010, and Smith *et al.*, 2015). If slip (and frictional heating) did localize on the MS, rather than inside the PSZ, the microstructural evidence of the temperature gradient (SG) would be symmetrical with respect to the MS, which it is not (3.7B). MSs are therefore not frictional sliding surfaces, as they are commonly interpreted, but instead, they mark sharp rheological contrasts between highly strained (PSZ) and much lower-strained (SG) regions. We interpret that grooves seen on the MSs parallel to slip direction, down to the nanometer scale (Fig. 3.9 A; De Paola *et al.*, 2015; Smith et. al, 2015), are corrugations of the PSZ boundary. We speculate that they may reflect small local variations in PSZ thickness, in a direction orthogonal to slip; i.e., they are not formed due to abrasive wear. This might be inherited from the irregularity of older MSs (3.7A), formed during Stage II, when the PSZ grain size was less homogeneous (Fig. 3.6C). During Stage IV, upon deceleration of the sample to arrest, the PSZ temperature drops, affecting its rheological behaviour (Fig. 3.10C). At this stage, the theoretical thickness is $W_{T} > W_{PSZ}$ (Fig. 3.10B). We interpret that the actively deforming PSZ, which is unable to thicken due to its now coarser-grained sintered boundaries, rapidly strengthens and eventually undergoes embrittlement and reworking (Figs. 3.6 D and E). Thermal cracking due to fast undercooling and damage during unloading may also enhance the splitting of the sample along pre-existing textural discontinuities, such as the MSs, which are then exposed in extracted samples (Fig. 3.9). During the fast (<1 s) cooling stage after the experiments, grain growth due to static recrystallization is very limited, both within and on either side of the PSZ (see De

Paola *et al.*, 2015).
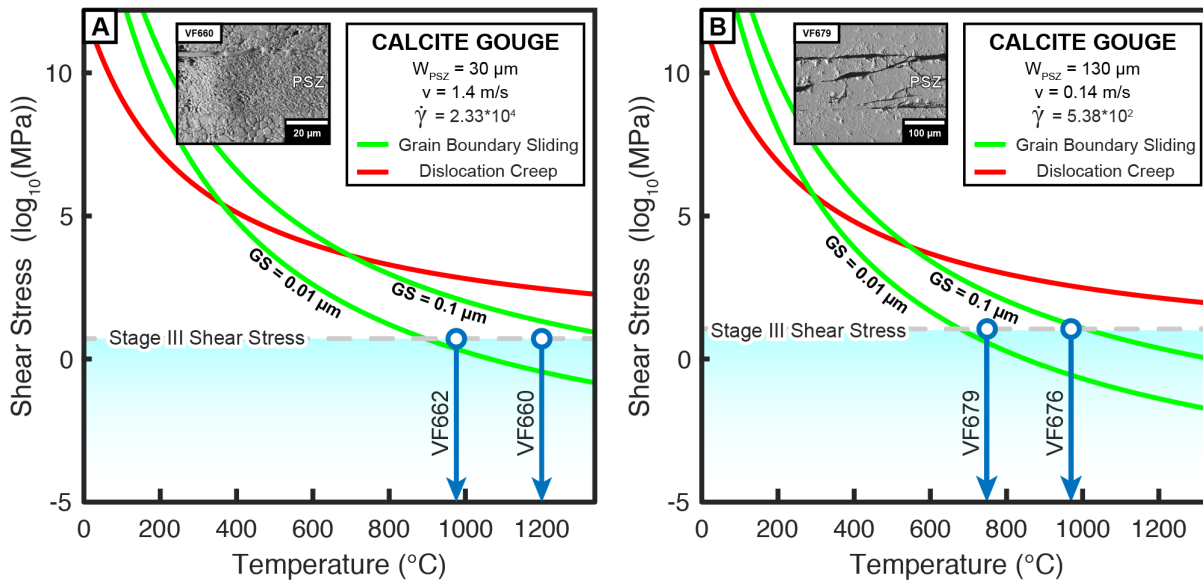
Figure 3.11 | *Predicted flow stress with temperature for grainsize sensitive grain boundary sliding (GBS, green curves) and dislocation creep (red curves), calculated using the data from experiments performed at v = 1.4 ms⁻¹ (A) and 0.14 ms⁻¹ (B). The flow stress of GBS, unlike in the case of dislocation creep, is affected by the grainsize. The flow stress and temperature measured for representative experiments are compatible with those predicted for GBS using a range of grainsize (GS) between 0.01 μm and 0.1 μm.*

3.6.   Conclusions

A simple conceptual model for coseismic weakening in calcite gouges is developed, integrating experimental data, microstructural analysis, and theoretical arguments. We propose that weakening is driven by thermally induced grainsize-sensitive mechanisms active within a PSZ, whose finite thickness is controlled by grain size, temperature, and shear stress. Careful recovery of the samples has allowed a quantitative characterization of the entire PSZ thickness, which is on the order of a few tens of microns, comparable to the thickness of those found in natural seismic faults in carbonates. According to our conceptual model, MSs mark rheological contrasts across which an extremely sharp

50

strain gradient is observed. They partition the deformation between the weak, viscously deforming PSZ and the stronger and sintered outer layers. Thus, our observations suggest that MSs are not frictional slip surfaces in the classical sense. Whether their preservation in natural carbonate-hosted fault zones remains indicative of past seismogenic behaviour is open to debate. However, seismic slip velocities and coincident shear heating make their formation more likely.

4. From brittle to viscous flow:
evidences from acoustic emissions monitoring

4.1. Acoustic emissions in rotary apparatus

In the previous chapter, microstructural observations have been integrated with mechanical data to reconstruct the weakening history of the experimental seismic faults. Temporal constraints of the fast-evolving processes occurring during the weakening history have been inferred by post-mortem microstructural observations, obtained from repeated runs arrested at different displacements. However, it must be noted that the transition from brittle to viscous behaviour in the sample occurs within a timeframe of less than a second. Furthermore, the sample always experiences an embrittlement phase at the end of each run, which causes some overprinting of microstructures. Overprinting of diachronous processes is unavoidable and microstructures from previous deformation stages must be carefully evaluated.

The monitoring of the acoustic emissions (AE) has been successfully employed to inspect the activity of brittle processes, both in the field and laboratory. AE are transient elastic waves produced during rapid release of energy during fracturing, and carry information about size, location and deformation mechanisms of the events (e.g. fracture mode). AE carry a characteristic frequency content - a spectral signature - where the peak frequency shows inverse dependency to the size of the fracture (Lockner, 1993; Ning *et al.*, 2014 and references therein):

$$\nu \sim \frac{V_i}{2l} \qquad (4.1)$$

where ν is the frequency, V_i is the wave speed and l is the length of the fracture. Therefore, AE recorded during mechanical experiments on samples with small dimensions, less than a few tens of centimetres, are generally found within frequencies on the order of kilo- and mega-Hertz (Lockner, 1993).

Several studies recorded AE for real-time study of dynamic faulting processes within triaxial rigs in laboratory. A few authors explored the transition between brittle and ductile deformation (e.g. Schubnel *et al.*, 2006), showing the aseismic (AE-silent) behaviour of the latter. The monitoring of AE may thus represent a non-invasive technique to obtain some independent evidence about the real time evolution of deformation mechanisms during the weakening history of seismic faults, which was reconstructed in the previous chapter from analyses on post-mortem samples.

However, some technical issues arise when applying conventional AE methodology in the setting of high-velocity experiments (Passelègue *et al.*, 2016). Usually, sensors can be mounted directly on the sample – generally a rock core – allowing for good coupling and low attenuation of the signal. During our experiments, incohesive gouges were used so that the direct coupling of the sensors with the deforming material was not possible. In this chapter we explore the potential of AE monitoring during high-velocity experiments in a rotary shear apparatus, using a novel sensor assembly applied for the first time to incohesive gouge.

4.2. Sample assembly for acoustic emissions recording

The sample assembly is the same used for the experiments reported in previous chapters, with the exception of the geometry of the lower cylinder, which was modified to host the AE sensors. This was replaced by a modified version, the HexAPUS (Hexagonal Array of Piezoelectric acoUstic Sensors) unit. HexAPUS consists of a standard hollow cylinder (Ch. 2.3) hosting a coaxial radial array of acoustic sensors. These are placed in chambers at ~11 mm below the grooved end of the cylinder and 8 mm from the rotation axis. Each sensor consists of a piezoelectric crystal (PI ceramic Pi255, modified lead zirconate titanate, diameter of 3mm and 2.5 mm thick) sandwiched between two thin copper disks (diameter of 3mm and 1 mm thick) and insulated by a rubber tube, tightened around the assembly. The axis of each sensor is parallel to the rotation axis, with the positive pole of the crystal oriented towards the top of the cylinder. Sensors are kept in place by bolts separated by a Teflon spacer, which insulates the lower end of the assembly.

Sensors are connected to two independent acquisition systems: Richter and Cecchi. The Richter system records in continuous mode at sampling rate of 10 MHz. The Cecchi system is instead used in trigger mode, and it allows the operator for a real-time overview on the activity of acoustic emissions during the experiments. The triggering voltage threshold has been calibrated depending on the ambient noise. Signal from the HexAPUS channels is pre-amplified with six separate units at 6 and 30 dB, depending on the powders sheared during the experiments (see details below). Data presented here are elaborated from the continuous recording of the Richter system.

Sensors response has been tested with a lead-breaking test, i.e. using a Hsu-Nielsen source (Sause, 2011). Fig. 4.1 reports the signature of Channel 3, used for data processing in this chapter. The averaged signature of low-energy collected during three experiments is reported along with the lead test curve (Fig. 4.1). These curves are produced using all events with amplitude up to 10% larger than the ambient noise.
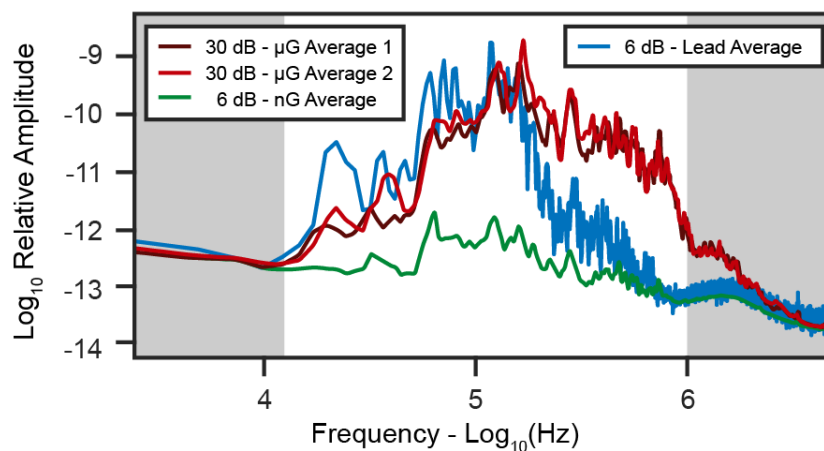
Fig 4.1 | *Resonance spectrum of the acoustic sensor (Channel 3). Blue curve is the spectral response from Hsu-Nielsen source (lead-breaking test) averaged from 4 tests. Green and red curves are the average of low-energy events (with amplitude 10% higher than the ambient noise) for three experiments in calcite nano-gouge and micro-gouge, respectively. The band width corresponding to the sensitivity of the sensor is individuated between 12 kHz and 1 MHz (between the shaded areas).*

54

The band width of sensor sensitivity is individuated between ~12 kHz (lowest frequency events detected) and ~1 Mhz, at the resonant frequency (related to the thickness) of the ceramic disk employed in the assembly. This band width corresponds to the resonance spectrum of the sensors.

Before investigations on rock powder samples, twelve shear experiments were performed using Teflon disks mounted in the sample assembly, to test the level of background noise due to the apparatus and sample assembly. Teflon deforms without emissions of AE and maintains low friction coefficients independently of the displacement accommodated by the sliding surface (Biswas and Vijayan, 1992). Tests were run combining different velocities (1.4, 0.14, 0.014 and 0.0013 ms^{-1}) and normal stresses (2, 10 and 25 MPa). No AE events were recorded in triggered mode, even using low voltage thresholds and high pre-amplification (30 dB). Therefore, the machine can be considered silent within the band width of the sensors, and AE recorded during experiments employing rock gouges must originate from the sample itself.

4.3.   Experimental procedure

Each experiment was run using 1 g of rock powder, using the same procedure described in Ch. 2.1.4. Two different materials were used: natural calcite micro-gouge (sieved between 63 and 90 μm), the same material described in the previous chapters, and calcite nano-gouge (mean grainsize ~ 200 nm), produced by the American Elements company. The choice was aimed to test differences in behaviour arising from textural variability (e.g. grain size of the initial material), especially during the initial stages of brittle deformation when grain size reduction is the dominant process.

The apparatus was operated in digital control using a function generator (Ch. 2.1.3). The device was set to supply a box-shaped pulse, where the height of the box in voltage is calibrated to a target slip velocity. Maximum working speed of the apparatus was limited to 1 ms^{-1} (at the reference radius) by the voltage supplied by the function generator (Ch. 2.1.3). The duration of the experiment was set such that the length of the box-shaped pulse corresponded to total slip distance of 1m, calibrated accounting

for the acceleration and deceleration of the apparatus. AE were recorded in continuous mode by the Richter system using eight channels simultaneously. Of the eight channels used, six were connected to the sensors of the HexAPUS, and two to high-resolution laser callipers (LK-H052, Keyence, Fig. 4.2). These were used to monitor the motion of targets mounted on the static and dynamic axial columns of the apparatus in order to synchronise the mechanical data with the AE records. Maximum normal load was limited to 20 MPa, due to the high values of torque required during the slip-hardening phases observed in nanogouges at low velocities, which were within the torque limitation of the motor (70 Nm).
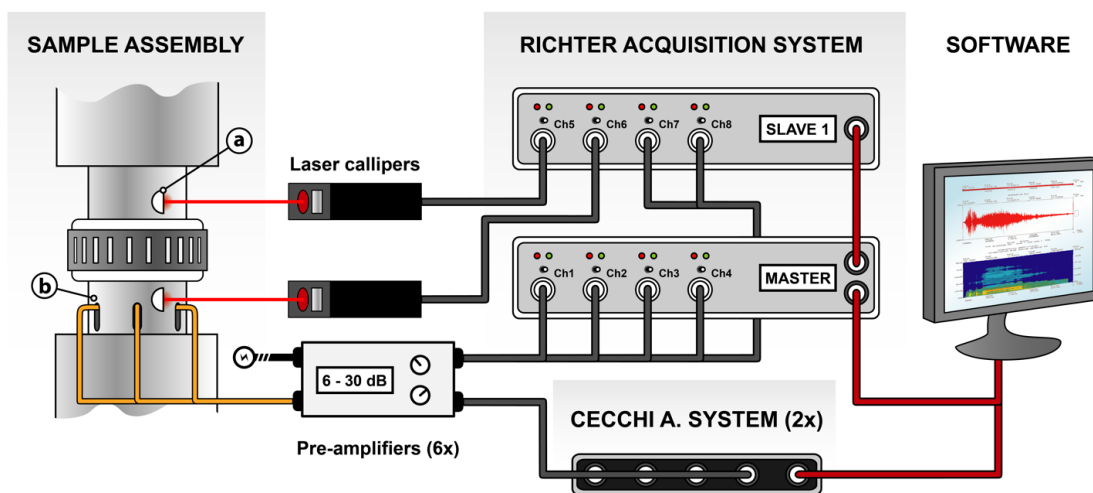
Fig 4.2 | Acquisition system assembly for the recording of acoustic emissions. The sample assembly includes top regular cylinder and lower HexAPUS cylinder (b). The displacement of the upper and lower main shafts is monitored using two high resolution callipers, which measure the distance of a target glued on the cylinders (a). The signal recorded by the six piezoelectric sensors hosted by the HexAPUS are pre-amplified using six independent amplifiers with a gain of 6 to 10 dB. Two units (Master and Slave1) of the Richter acquisition system record simultaneously 8 channels (6 acoustic sensors plus 2 laser callipers) at a frequency of 10 MHz in continuous mode. The Cecchi acquisition system, consisting of two units, is set to acquire in parallel with the Richter in triggered mode (6 acoustic sensors). Cecchi data is not treated here.

4.4. Results

Figure 4.3 shows the results of six experiments performed with micro- and nano-metric gouges, respectively, for three different velocities (1, 0.1 and 0.001 ms^{-1}) and σ_n = 20 MPa. Further details for each experiment are reported in Appendix I. Micro gouge experiments perform well at high velocities (1 ms^{-1}) - as seen in the previous chapters - while they tend to fail, after a certain amount of slip (Fig. 4.3), at sub-seismic velocities (v ≤ 0.1 ms^{-1}). For example, at the velocity of 0.001 ms^{-1}, uncharacteristic weakening trends are observed, which can be related to failure of the assembly through loss of gouge. In fact, the steady descending slope of fault friction corresponds to an increased rate of axial shortening of the sample, which is due to the loss of gouge through the space created between the cylinder and the damaged Teflon ring. The Teflon ring used to contain the gouges shows remarkable wear at subseismic velocities. Unreliable data are greyed-out in Fig. 4.3.

Conversely, nano-gouge experiments are successful for the entire range of slip rates used, and show stable shortening profiles after the initial slip-hardening phase, similar
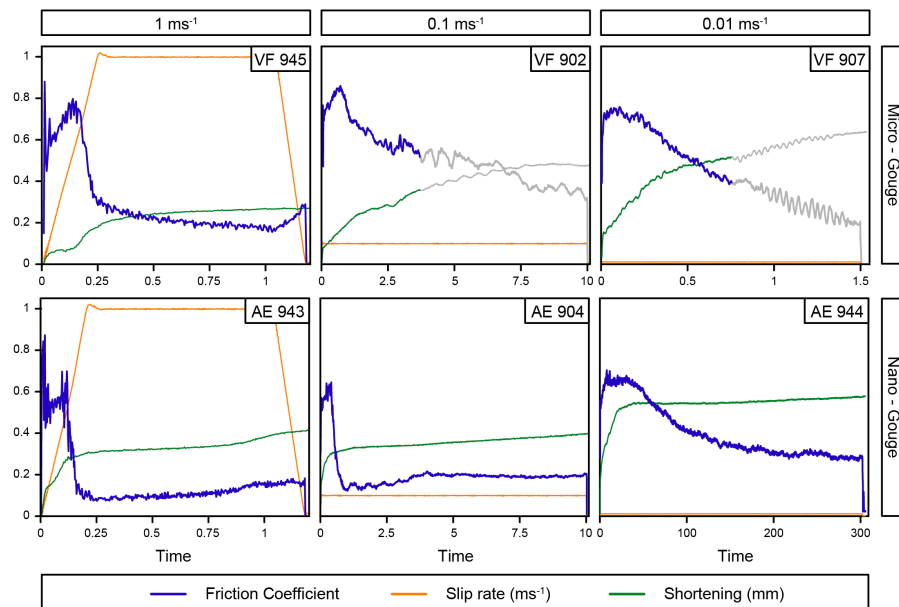
Fig 4.3 | *Mechanical data of the micro- and nano-gouge experiments. The vertical axis shows the values of each mechanical data plotted: friction coefficient (blue), slip rate (orange) and axial shortening (green).*

57

to the 1 ms^{-1} micro-gouge runs. Damage to the Teflon ring is strongly reduced during these experiments. At dynamic weakening conditions, minimum friction coefficients are lower than those achieved in micro-gouge experiments at the same velocity. Almost no re-strengthening is observed upon deceleration of the apparatus to arrest.

The focus of this chapter is set on the high-velocity experiments (v = 1 ms^{-1}), which are presented and discussed in the following paragraphs.

4.4.1. Micro-gouge

Micro-gouges produce a four-stage weakening history (Fig. 4.4 A), which has been described in detail in previous chapter (Ch. 3). Initial Stage I slip hardening, with friction values in the Byerlee's range (μ = 0.6 - 0.9), is followed by rapid, exponential decay of fault strength during the transient stage II (down to values of μ = 0.3). Low friction values attained at the end of the transient Stage II are observed to slowly decrease during Stage III (down to values of μ = 0.2), until deceleration of the apparatus to arrest during Stage IV, when the fault partially recovers its strength ($\mu \sim$ 0.3). Two major steps of sample compaction are interpreted at the beginning of Stage I and throughout stage II, from observed steeper gradients shown by the axial shortening data (Fig. 4.3).

The AE signal from the sample assembly (recorded with pre-amplification of 30 dB) shows a progressive increase in amplitude towards the end of Stage I (Fig. 4.4 A). Hit counting data show that the maximum activity of AE is recorded during Stage II and at the beginning of stage III, roughly coincident with the second step of axial shortening (Fig. 4.4 A). However, the amplitude of events throughout the run does not show substantial variability, and it is difficult to set an exact threshold value for the hit count. Discrete bursts of AE, with much larger amplitude (three times larger than those events recorded in Stages I to IV), are recorded for a protracted period immediately after the stop of the experiment (Fig. 4.4 A). This transient will still be referred to as Stage IV. This stage is also characterised by a rapid decrease of temperature of more than 400°C in less than a second.
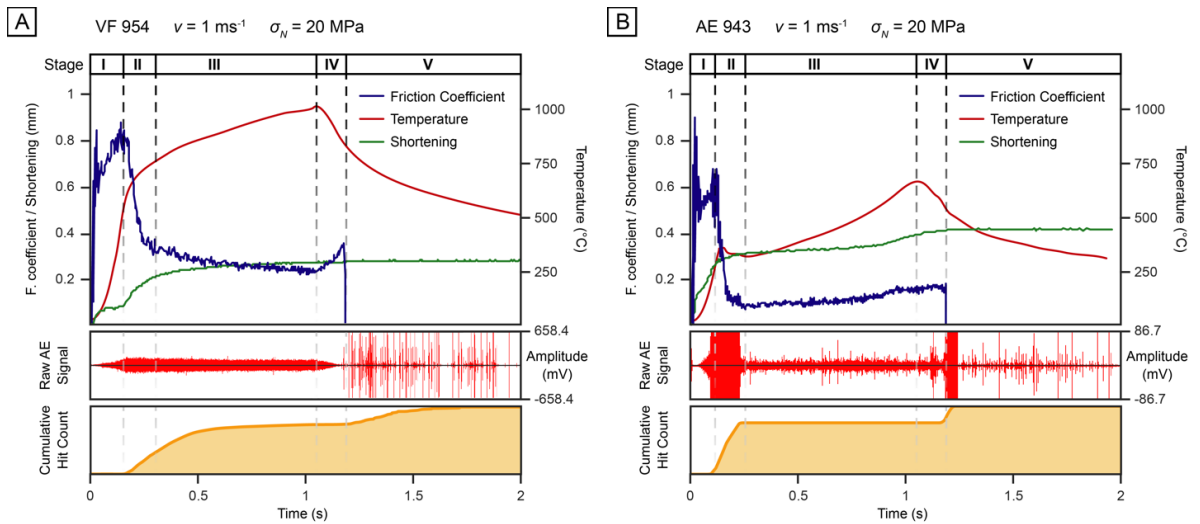
Fig. 4.4 | *Mechanical data, raw AE signal and hit count for the two selected experiments performed at v = 1 ms⁻¹ and σ_n = 20 MPa: A) micro-gouge, VF 945, and B) nano-gouge, AE 943.*

4.4.2. Nano-gouge

Nano-gouge experiments share a similar evolution with the micro-gouge ones (Fig. 4.4 B). During Stage I, the slip hardening phase is slightly shorter and shows lower friction coefficients (0.5 < μ < 0.8) than shown by the micro-gouge experiments. Axial shortening is mostly accommodated during this stage and rapidly stabilises throughout Stage II (Fig. 4.4 B). The fault strength rapidly drops to low friction values (μ ~ 0.1), which slowly rise throughout Stage III up to values of μ = 0.15 (Fig. 4.4 B). Some strengthening is observed at ~ 0.8 s in concomitance with additional compaction (Fig. 4.4 B). Almost no frictional re-strengthening typical of micro-gouge experiments is recorded during Stage IV.

Nano-gouge runs produced a better AE signal, with reduced amplitude of the continuous low-energy emissions at dynamic conditions and, thus, required less pre-amplification (only 6 dB). Differently from micro-gouges, AE activity seem evolving according to four stages – plus one (IV) – in good agreement with the four mechanical stages. Stage I is relatively silent with increasing emissions recorded towards the peak friction values. Large AE bursts are recorded during stage II, then quickly disappearing at the beginning of Stage III (Fig. 4.4 B). Most of the events occur during this transient, as shown by the cumulative hit counts (Fig. 4.4 B). Stage III is relatively quiet, with a

59

multitude of low-energy events and a few discrete events above ± 40 mV recorded. Some discrete, more energetic events are recorded during stage IV (Fig. 4.4 B).

Important AE activity follows the arrest of the sample prior to the disengagement of the loading column from the motor, substantially increasing the cumulative hit count (Fig. 4.4 B). This burst of events is concomitant with small adjustments of the column (non-zero velocity) before disengagement from the motor clutch. Discrete, large amplitude events are recorded during the cooling of the sample after the stop of the sample (Fig. 4.4 B), hence under static conditions (Stage V).

4.5. Frequency content and spectral signature

The raw AE data are processed to build spectrograms, which are computed with the use of consecutive Fourier transforms. The moving time window, used for the analysis, was chosen 2.5 times wider than that necessary to analyse events with the lowest frequency detected by the sensors. Successive windows overlap by 25%. The results are visualized in Figs. 4.5 and 4.7. Spectrograms show the frequency content of acoustic emissions through time, where the relative amplitude of events (for each characteristic frequency) is expressed using a colour gradient. Cold (green and blue) and warm (yellow) colours correspond to low and high relative amplitudes, respectively.

Sonograms can be sliced to obtain the spectral signature of single events in a selected time window. A Python routine was set up to select fifteen energetic events from each of the following stages: Stage I, Stage II, Stage III and IV together and Stage V. Selected events are evenly spaced within the cumulative hit count over an arbitrary threshold that was chosen depending on the average magnitude of events for each stage. For example, the threshold was set lower for events of Stage III in nano-gouges experiments. Timing of selected events is reported in Figs. 4.5 and 4.7 using coloured dots. The spectral signature of each selected event is plotted in Figs. 4.6 and 4.8 with the same colour code.

60

4.5.1. Micro-gouge

The analysis of the spectrogram obtained from the microgouge experiment shows that the average amplitude of AE increases during Stage I and II, and rapidly decreases during Stage IV (warm colours, Fig. 4.6). No clustering of the automatically selected events (between Stage I and Stage IV) suggests that the AE activity remains fairly homogeneous during each Stage. During each Stage, the frequency content is similar to the average signature of low-energy events (Fig. 4.6). This low-energy signature (events with up to 10% higher amplitude than the noise) is obtained with the same averaging method used during the AE sensor test (see Ch. 4.2 and Fig. 4.1). Stage V signal is instead discrete in time, with isolated bursts of AE showing much higher amplitude (Fig. 4.5). However, the frequency content is not dissimilar form the previous Stages (Fig. 4.6).

4.5.2. Nano-gouge

In the nano-gouge experiments spectrograms, the same five distinct Stages as described for the raw AE data have been identified (Fig. 4.7), each characterised by a peculiar AE activity. During Stage I, an increasing number of events (see the cumulative hit count) were recorded, with progressively higher amplitude (warmer colours in the spectrogram in Fig. 4.7), when the fault strength approaches peak values. The events with the highest amplitude are recorded at the beginning of Stage II, at the onset of weakening. The amplitude and number of events gradually diminishes towards Stage III. During Stage II, it is also observed a rapid evolution of the spectral signature of the selected events, with a rapid loss of the low-frequency content (< 200 kHz; Fig. 4.8). More than 70% of the cumulative hit count is recorded during Stage II (Fig. 4.7). At the end of Stage II, acoustic emissions experience a substantial drop. Only few events emerge during Stage III from the low-energy continuous AE background (grey curve, Fig. 4.8). Most of these events are clustered in proximity of the hardening step measured at 0.85 s.

Their spectral signature is similar to that of the averaged low-energy events, and only slightly higher in the frequency range between 50 and 250 kHz (Fig. 4.8). Only towards the end of Stage IV, isolated AE bursts are observed, with moderate amplitude (Fig. 4.7),
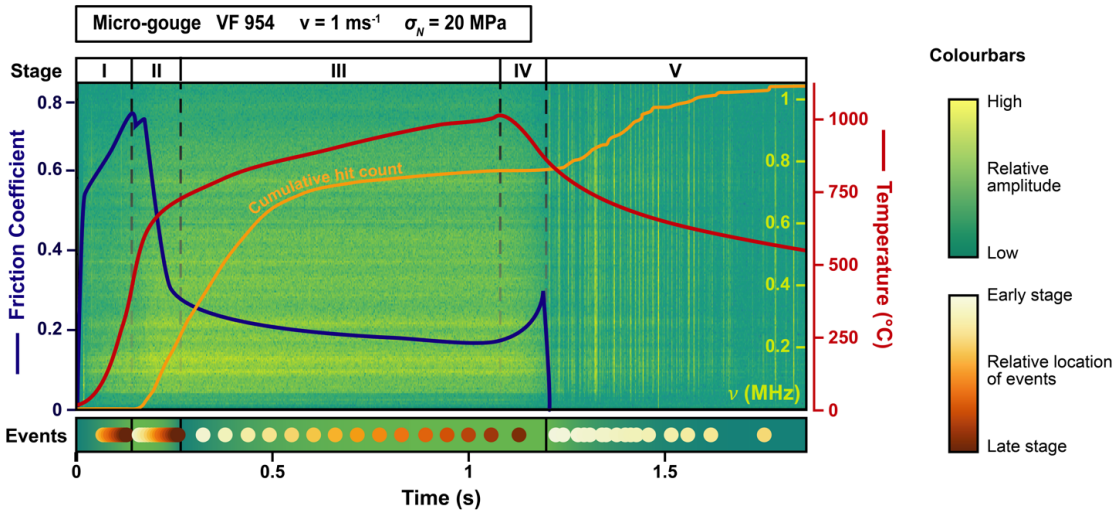
Fig 4.5 | *Spectrogram of micro-gouge experiment VF 945. The lower bar shows the location of events selected and plotted in Fig. 4.6.*
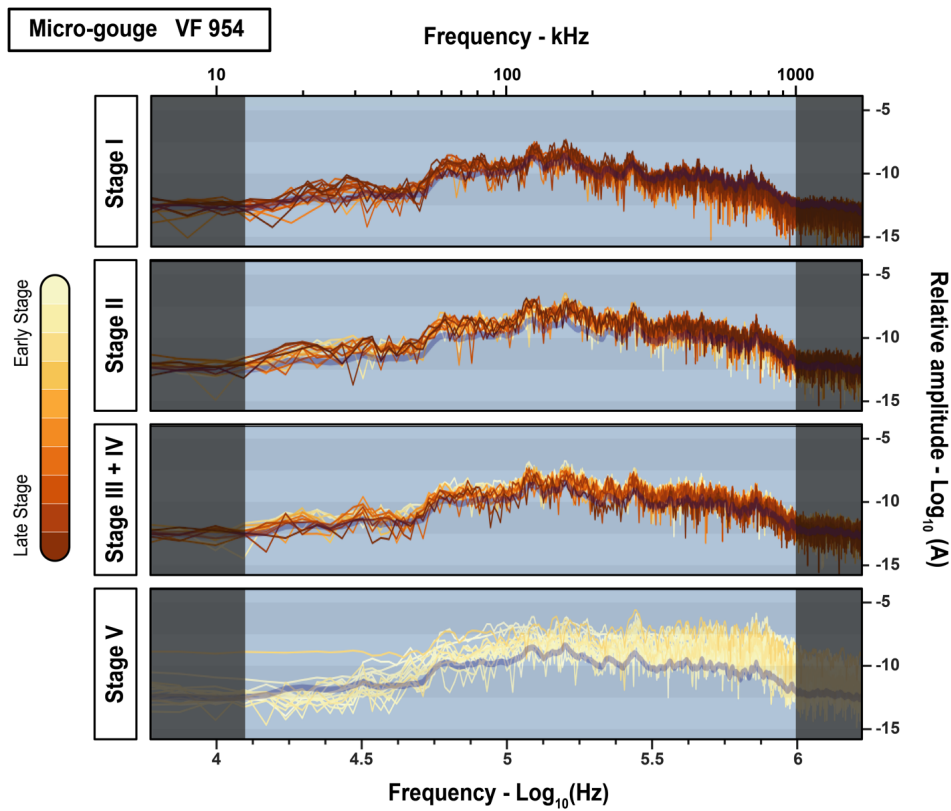
Fig 4.6 | *Spectral signature of selected energetic events of experiment VF 945. The color code shows the relative location of the events during each Stage: from early stage in white, to late stage in brown. Each diagram reports the average (grey bold line) of low-energy events (amplitude within 110% of the ambient noise).*
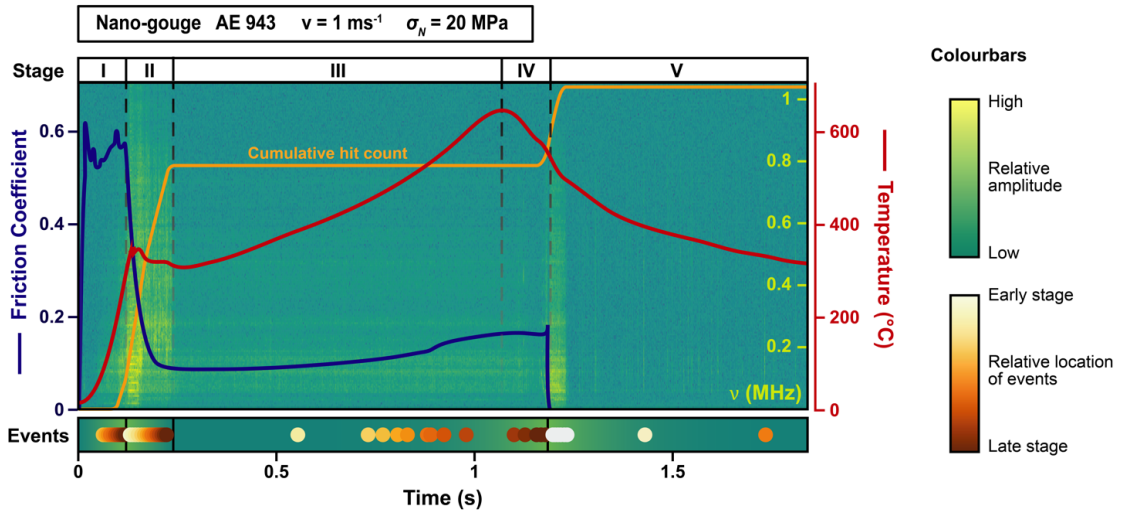
Fig 4.7 | *Spectrogram of micro-gouge experiment AE 943. The lower bar shows the location of events selected and plotted in Fig. 4.8.*
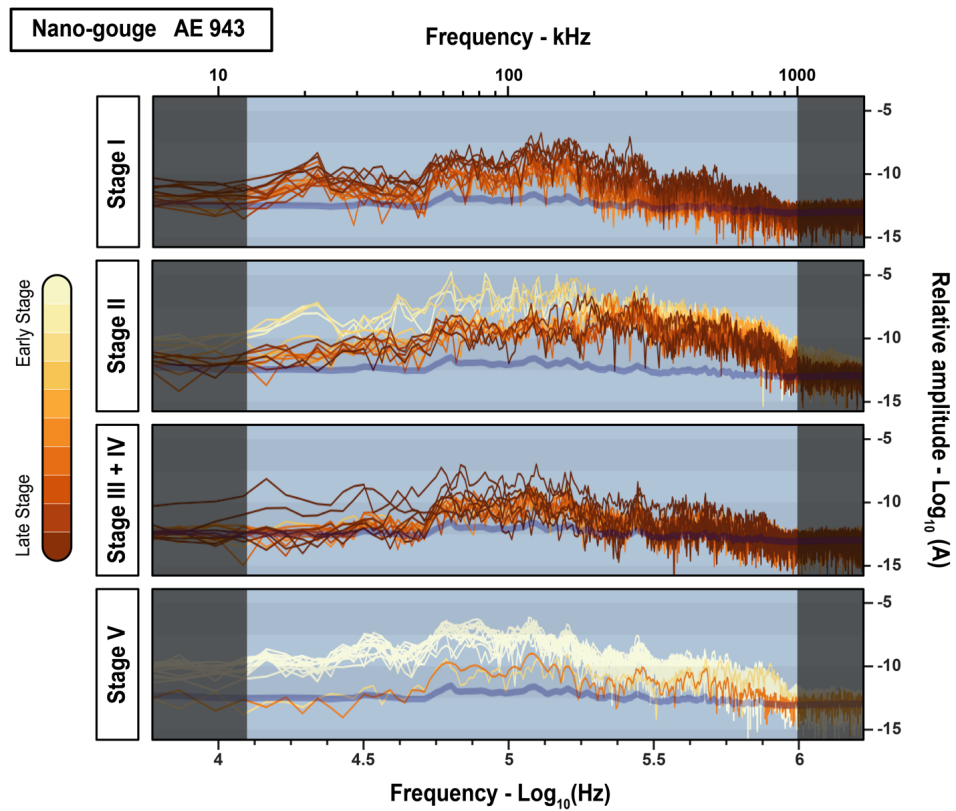
Fig 4.8 | *Spectral signature of selected energetic events of experiment AE 943. The color code shows the relative location of the events: early stage, white, to late stage, brown. Each diagram reports the average (grey bold line) of low-energy events (amplitude within 110% of the ambient noise).*

which have a spectral signature dominated by the low frequencies ($10 < \nu < 200$ kHz, Fig. 4.8). These emissions are similar to those recorded during the early Stage II, but have a lower amplitude at frequencies of $\nu > 300$ kHZ. Just after the stop of the sample, during early Stage V, a short transient with numerous AE is recorded. This is dominated by events with low frequency content, similar to those recorded during late Stage IV (Fig. 4.8). These events are recorded in correspondence of small adjustment of the column before disengagement from the motor clutch. Later events have low amplitude and are scattered in time. Their frequency content is most represented between values of 60 and 500 kHz.

4.6.   Comparative microstructures

It is evident that AE data differ substantially between micro- and nano-gouge experiments. Difference in the values of mechanical data, such as friction values, affects our temperature estimates as well. However, the two tested materials overall share the same weakening history comprising four Stages (I to IV), plus an additional Stage V highlighted by AE records, and due to static cooling of the sample after its arrest. Microstructural observations are therefore essential to further investigate the nature of the different AE response.

Unfortunately, the AE assembly makes the recovery of the entire thickness of the samples problematic (Fig. 4.10). In order to recover the full top to bottom sections of deformed samples for microstructural analyses, some additional experiments were run with the use of the standard sample assembly (Chapter 3). Furthermore, the fragile nature of nano-gouge aggregates deformed until Stage I and II, respectively, did not allow the preparation of sample for microstructural imaging. Samples deformed up to stage III, when the material is sintered at high temperatures, are more cohesive and could be prepared and used for microstructural analyses.

Here are presented the results of an experiment run with nano-gouge at σ_n = 25 MPa and v = 1.4 ms^{-1} so that microstructures can be directly compared with those already described in Chapter 3. Mechanical data of VF_660 (Fig 4.9 A) and AE_757 (Fig 4.9 B)

show comparable evolution with that of VF_954 (Fig. 4.4 A) and AE_943 (Fig. 4.3 B), respectively (both performed at σ_n = 20 MPa and v = 1 ms^{-1}). The following description focuses on the main microstructures of these two samples (Fig. 4.11), more extensively described in Chapter 3.

Both materials deformed to Stage III - and also experiencing Stage IV – produce cohesive rock chips that easily split revealing continuous, grooved and highly-reflective surfaces, known as mirror-like surfaces (MSs, Fig. 4.10; see also Ch. 3). These are typical
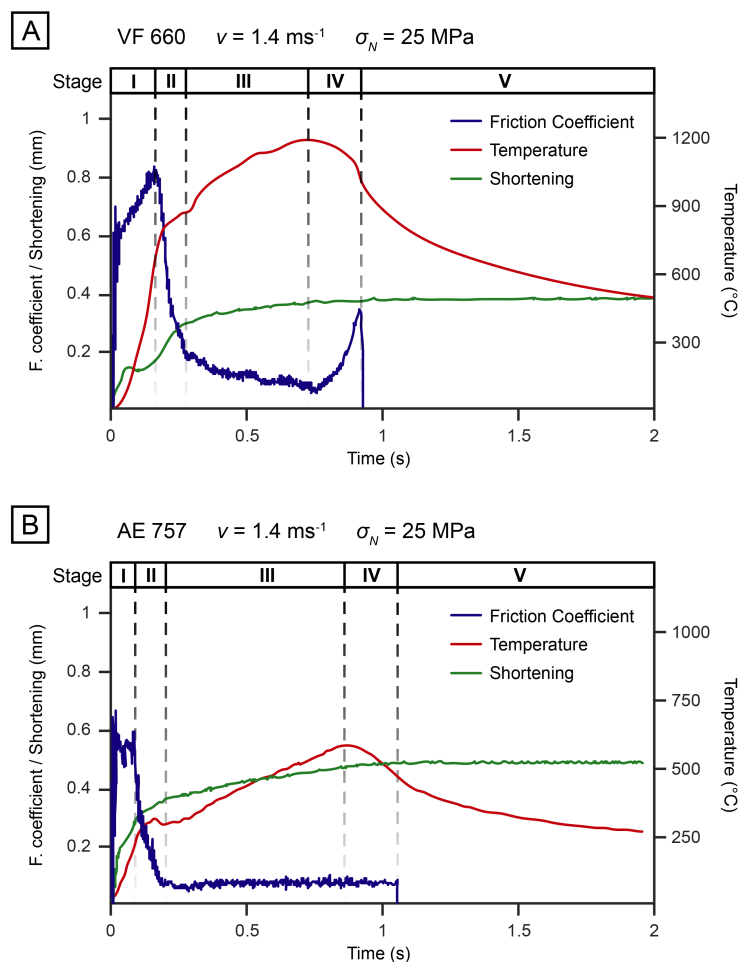
***Fig 4.9** | Mechanical data for the two selected experiments performed at v = 1.4 ms^{-1} and σ_n = 25 MPa: A) micro-gouge, VF 660, and B) nano-gouge, AE 757. Samples recovered from these experiments have been used for microstructural analysis.*
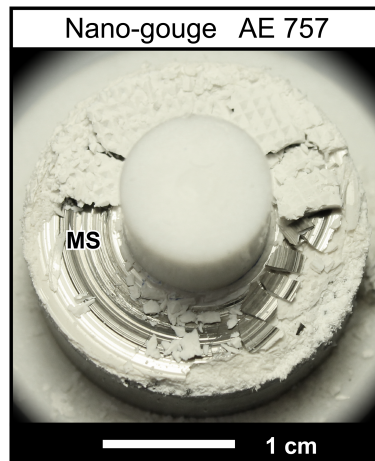
Fig 4.10 | Mirror-like surfaces (MS) well-exposed after the end of the experiment in nano-gouge (σ_n = 25 MPa and v = 1.4 ms^{-1}). No nano-gouge samples could be recovered preserving the full thickness due to the pervasive brittle damage along MSs.

microstructures that consistently develop in calcite samples sheared at seismic slip rates.

Cross-sections reveal that the micro- and nano-gouges share the same inner architecture and textures. In both materials, a PSZ develops (Figs. 4.11 A-B), which is composed by sub-micron tightly packed grains (Fig. 4.11 C-D), showing fairly homogeneous grain size, polygonal shapes and triple junctions. Micro-gouge PSZ is 30 μm thick and has a mean grainsize of 700 nm (Figs. 4.11 A, C). Nano-gouge PSZ is 20 μm thick, with mean grainsize of 300 nm (Figs. 4.11 B, D). The PSZs in both materials experienced some partial reworking by brittle processes (Figs. 4.11 E-F), most evident in nano-gouges where peak temperatures were lower. The most prominent brittle feature is the opening of fractures along mirror surfaces (Figs. 4.11 E-F), which are observed on both sides of the PSZ. This damage made impossible to recover the full thickness of the sample in the case of nano-gouges (Fig. 4.10). Just outside and on both sides of the PSZ – across the MS – some layers are observed with a similar recrystallized texture but with much coarser grain size (c.a. one order of magnitude larger than that in the PSZ). These layers extend away from the PSZ showing the progressive decrease of recrystallised grain size and increasing porosity, which defines a sintering gradient (SG). SG in nano-
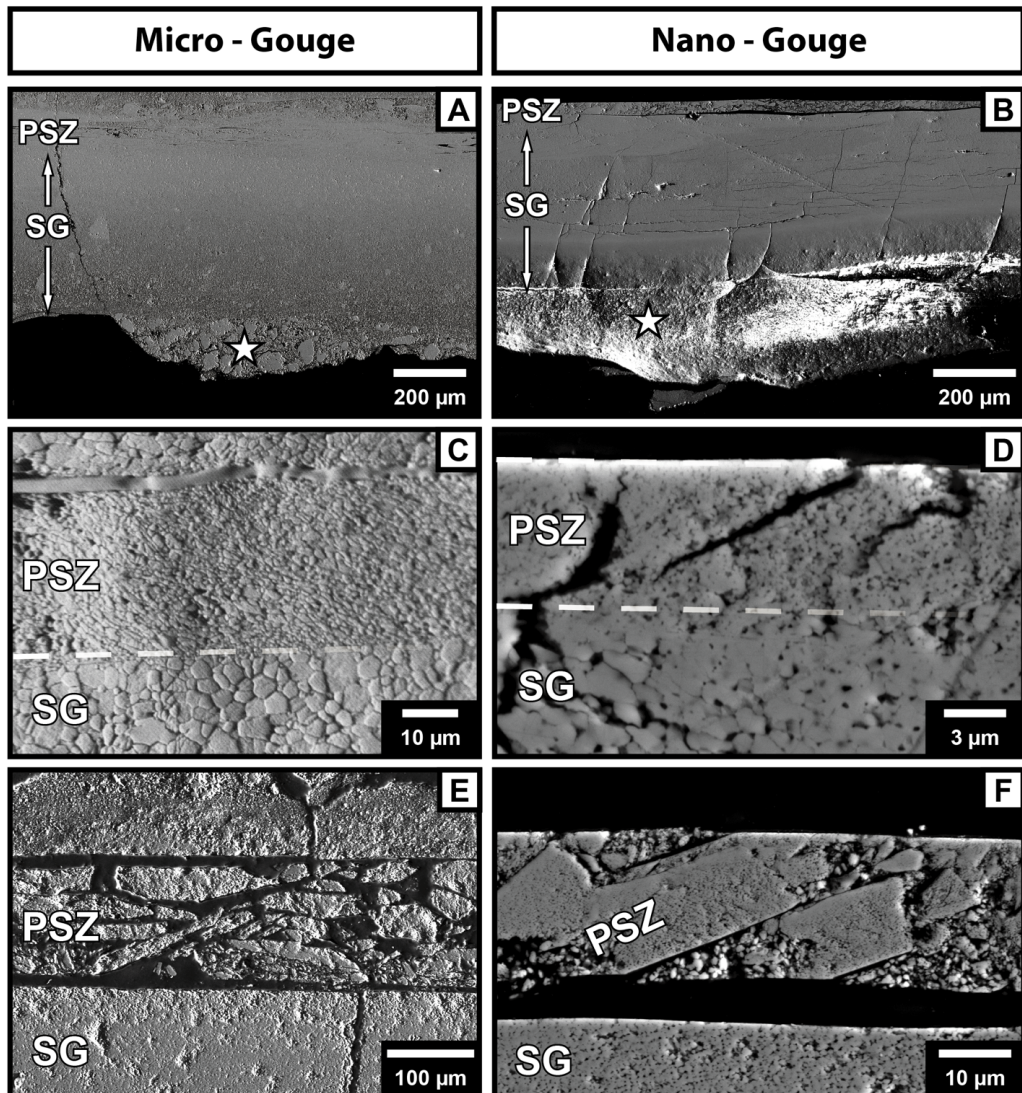
Fig 4.11 | *SEM images acquired with back- and forward-scattered (only C) technique of experiments selected for microstructural analysis: micro-gouge (VF 660 and VF 675, on the left) and nano-gouge (AE 757, on the right). A - B) Overview of the principal slip zone (PSZ) and the lower deactivated sintered layer showing a sintering gradient (SG). SG in micro-gouge extends to the cylinder grooving where coarse original grains are preserved (white star in A). The non-sintered volume in nano-gouge appear poorly polished (white star in B). C - D) Ultramylonitic PSZ showing smaller grain size than the one in the outer, sintered layers (SG). E – F) brittle damage showing clear reworking at dynamic (tilting and embricate structures) and static (split PSZ boundaries) conditions. Brittle damage is more pervasive in experiments that achieved lower temperatures in the PSZ (e.g. VF 675, which was performed at lower velocity).*

gouges is less pervasive than in micro-gouges, probably due to the lower temperature achieved in the PSZ. Its extension is visible from cross-section where the poorly sintered material outside SG is easily removed during the polishing procedure (Fig. 4.11 B, white star).

4.7. Discussion

4.7.1. Microstructures reveal deformation mechanisms evolution during the weakening history

Acoustic emissions provided with some indirect evidence of a polyphasic evolution of deformation mechanisms throughout the weakening history of samples deformed at seismic slip rates (1 ms^{-1}). In the previous chapter, four different stages were individuated in micro-gouge experiments, each corresponding to a particular microstructure. Here is a brief recap to ease the subsequent discussion.

During Stage I, slip hardening is associated to grain size reduction by cataclasis (brittle deformation), first distributed across the whole thickness of the sample and then localised into a single cataclastic principal slip zone (PSZ). At the beginning of Stage II, the PSZ has well-defined boundaries, marked by wavy patches of incipient sintered material in the outer layers. These wavy patches form embryonic mirror-like surfaces (MS). The PSZ rapidly evolves throughout Stage II by becoming less porous, homogeneous in grain size and decreasing its thickness by multiple localisation steps. This process has been described as "migration" of the MSs, as the old sintered boundary is every time deactivated and left as a characteristic microstructure in the outer layers.

At the end of Stage II, the PSZ has homogeneous thickness, grain size and very low porosity, and its textures closely resemble those of natural and experimental ultramylonites, i.e. rocks that deform in a ductile fashion. This evidence suggests that a major change in rheology has happened throughout Stage II. During Stage III, the PSZ maintains a steady-state thickness while grain size slowly increases with temperature. This equilibrium is broken during Stage IV, when deceleration of the sample and

subsequent temperature drop promote embrittlement of the PSZ. At this stage, it is speculated that the most prominent brittle damage exposes the shiny MSs as they are seen in hand samples.

4.7.2. The AE signature of micro- and nano-gouges during dynamic weakening

Overall, AE recorded during micro-gouge experiments proved to be less informative than those recorded during runs on nano-gouge, especially during the dynamic stages of deformation. Micro-gouge AE have low, almost homogeneous amplitudes and are continuously emitted throughout the dynamic part of the experiment (Stages I-IV). Their spectral signature is not varying substantially with time, and no characteristic changes are observed at the transition between the deformation stages. However, some information emerges from the cumulative hit count, but this should be evaluated with care due to the difficulty to set an accurate amplitude threshold. The highest AE activity is recorded during Stage II and the beginning of Stage III and again after the stop of the sample. The latter emissions during Stage V are discrete events that have higher amplitude than those recorded at dynamic conditions. Stage V AE activity decreases with time as shown by the slope of the cumulative hit count. Even if this stage is clearly correlated to the logarithmic decay of temperature, the spectral signature of events is not very informative.

Conversely, AE signal from nano-gouge experiments requires less amplification and has a better resolution throughout the deformation Stages. This may find a speculative explanation in the different initial distribution of grainsize compared to that of micro-gouges. The signals emitted from the actively deforming PSZ (localized towards the top cylinder) must travel through the deactivated sintered layers, towards the sensors placed in the lower cylinder. In the case of micro-gouges, these layers are heterogeneous, porous and crossed by oblique shear zones (Riedel shears). Grainsizes range between the initial grain size (63-90 μm, preserved especially in the grooving of the cylinders) and few tens of nanometres (along localised shear zones). AE travelling across the deactivated layers are affected by such heterogeneity and may experience

scattering and attenuation of the signal. On the other hand, nano-gouges have more homogeneous SG layers, due to the already comminute initial grainsize, in the range of that produced during Stage I in the PSZ of the micro-gouges. This may represent an explanation about why a clearer signal emerges from nano-gouges experiments, which allows the observation of variations in the spectral signatures of energetic events, even if the signal was less amplified (compare the sonograms of Figs. 4.5 and 4.7).

However, nano-gouge experiments do have some limitations as, in turn, do not benefit of a complete textural characterisation. Nonetheless, microstructures recovered after deformation to Stage III do not differ from those obtained in micro-gouge samples. We speculate that both materials, made of the same mineral, experience the same weakening history and are affected by the same weakening mechanisms, although the timing of the different processes may be affected by differences in the initial grainsize. In fact, in micro-gouge experiments, the formation of the viscous PSZ is strictly dependent on the formation of volumes of small particles during the precursor brittle deformation phase in Stage I. Extreme comminution eases the activation of thermally activated mechanisms (such as grain boundary sliding) and contributes to the rapid onset of weakening at rising temperatures. Nano-gouges would therefore favour early localisation processes and result in a shorter Stage II, the transient phase when purely brittle mechanisms give way to purely viscous deformation mechanisms.

4.7.3. Integrating acoustic emissions and microstructures to interpret the weakening history

With the premise that the microstructural evolution is comparable in both materials tested, here we discuss further independent evidences from AE activity in the context of the weakening history proposed from textural observations and mechanical data, already described in the previous chapter.

Nano-gouges experiments start almost silently, like in micro-gouges, and only towards the end of Stage I AE activity increases with progressively more energetic events (higher amplitude). Their frequency content is mostly represented below 200 kHz. Stage

I corresponds to the brittle phase of the experiments and increasing AE activity seems related to slip hardening. In fact, the most energetic events are recorded at peak fault strength. Arguably, AE recorded during Stage I unlikely relate to the fracturing of single grains during grain size reduction by cataclasis, as shown by widespread microstructural observations. First, grains in the range of 200 nm are unlike to fracture due to the low stresses produced during the experiments (e.g. Sammis and Ben-Zion, 2008), especially deforming rock powders where stress-concentration effects are limited. Second, sources with average dimension smaller than the initial grain size would produce peak frequencies that are well above the band width of the sensors ($v \sim 14$ GHz), according to Eq. 4.1 and using $V_p = 5800$ ms^{-1} (p-wave speed in porous limestone; Domenico, 1983). This also applies to micro-gouges, with frequencies $v > 32$ MHz. We speculate that Stage I AE activity recorded is related to localisation processes. Our explanation is that the onset of AEs during Stage I is due to the coalescence of multiple shear bands into a fast deforming Y-shear band, the brittle PSZ. In this scenario, AEs would generate due to the creation of larger fractures during distributed shear and slip events nucleated along Riedel shears (Fig. 4.12 C microstructures a-c).

AE recorded during the initial Stage II have high amplitude distributed on all frequency of the band width of the sensor. After ~70% of the total weakening, AE rapidly lose the low frequency content (< 200 kHz), with the lowest amplitudes in frequencies below 50 kHz. These AE during early Stage II are interpreted as due to the formation, evolution and migration of the sintered PSZ boundaries, the Mirror-like surfaces (MSs, see. Chapter 3). This is well supported by microstructural observations in micro gouge-experiments, which show that the first MSs are patchy, irregular and locally reworked and fractured (Fig. 4.12 C microstructure b). The deactivated layers observed above the PSZ contain numerous early, disrupted MSs, with an orientation that is not consistent with the shear direction in the PSZ (Fig. 4.12 C microstructure c). On the other hand, the latest MSs, observed close to the PSZ, are continuous and organized into shear-parallel arrays (see Ch. 3 Fig. 3.7 B). We infer that early Stage II deformation is associated to localisation processes that progressively destroy and abandon the old, irregular MSs (Fig. 4.12 C microstructure c). Brittle damage is progressively less intense with increasing temperature and homogenisation of the PSZ thickness. As a consequence, the low-
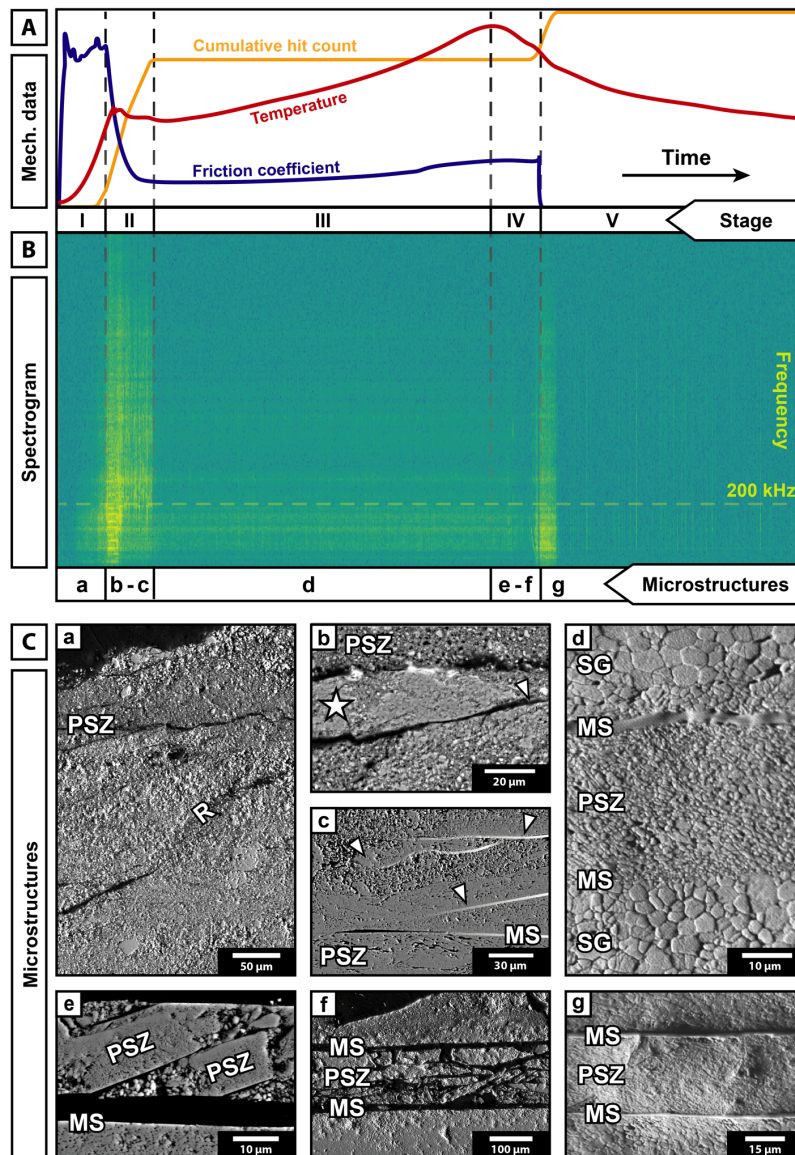
Fig 4.12 | *Summary of the main results: A) schematic of mechanical data and cumulative hit count of AE, experiment AE 943, v = 1 ms^{-1} and σ_n = 20 MPa; B) spectrogram and relative position of microstructures; C) representative microstructures. a) Stage I brittle principal slip zone (PSZ) and riedel shear bands (R) in the outer layers; b) Stage II PSZ showing patchy, sintered boundaries (white star), which display brittle, dynamic reworking (white arrow pointing to a Riedel-type fracture); c) Stage II relict PSZ boundaries (white arrows), reworked and preserved in the Stage III upper deactivated layer, the latter PSZ boundary is split open (MS); d) Stage III ultramylonitic PSZ bounded by the outer sintered layers (SG), the upper boundary is split and filled with epoxy; e) bits of PSZ with straight boundaries showing Stage IV brittle dynamic reworking (imbricated structure); f) stage IV and V brittle damage in lower velocity experiments; g) Stage V brittle damage exploiting the PSZ boundaries and revealing mirror-like surfaces (MS, see Ch. 3).*

frequency content of AE recorded during Stage II fades out when PSZ boundaries are no more reworked.

Energetic AE rapidly disappear when entering Stage III. This stage is homogeneous, characterised by a continuous background of AE with low amplitude, just above the ambient noise. This "silent behaviour" is in good agreement with the switch from a brittle to a viscous rheology, which was already supported by the ultramylonitic texture of the PSZ (Fig. 4.12 C microstructure d). The continuous background emission can be related to the formation of the sintering gradient (SG) in the deactivated layers.

Passelegue *et al.* (2016) performed similar high-velocity experiments where weakening was associated to the formation of a layer of melt, which deforms viscously. They argue that AE recorded during the weakening stage are emitted from the outer layers, where heat radiating from the PSZ promotes thermal cracking. Similarly, Stage III AE may be imputed to thermal cracking during grain growth, strongly anisotropic in calcite (Widhalm *et al.*, 1997; Yavuz *et al.*, 2010), in the SG layers. However, compared to cracking in Westerley granite (Passelègueet al., 2016), AE are far less energetic due to the monomineralic nature of the calcite aggregates tested in our experiments.

During late Stage IV, discrete events with higher amplitude in the low-frequency range (< 200 kHz) are recorded, similar to those events produced in concomitance with the formation and disruption of the early MSs. Microstructural evidence shows the brittle, synkinematic reworking within the PSZs, which easily split along their boundaries (Fig. 4.12 C microstructures e, f). These AE can therefore be associated to the progressive overprinting of brittle deformation in the PSZ caused by the decreasing temperature, well in agreement with the re-strengthening shown by the mechanical data.

Finally, AE recorded after the stop of the experiment show the effect of thermal cracking during rapid cooling occurring at static conditions. During early Stage V, the spectral signature shows again larger amplitudes in the low frequencies (< 200 kHz). The frequency range where peak amplitudes are observed in both stage IV and V is ν = 60 -

100 kHz. Within this interval, and using wave speed of 5800 ms^{-1}, eq. 1 yields a source length in the order of 50 – 30 mm. This range is compatible with the dimension of the split MS, which cover an area slightly smaller than the base of the metal cylinders, having an inner and outer radius of 12.5 and 5.25 mm, respectively. If the crack propagates along the PSZ boundaries following the shear sense, a path with length > 25 mm is expected for its complete rupture.

4.8. Summary and conclusions

The study of acoustic emission in high-velocity shear experiments allowed to document the evolution of deformation mechanisms at dynamic conditions. The method proved to be suitable for experiments with rock powders sheared in the rotary shear apparatus, which are underrepresented in literature. The heterogeneity of deformation observed in coarser grained material (micro-gouges) limits the applicability of the method, and further improvement on the sample assembly geometry is in order. In fact, similar experiments to those presented in chapter 3 yielded poor quality AE data when using microgouges. The issue was bypassed using finer calcite powder with nanometric grainsize (nano-gouges). This finer-grained material allowed to reduce inhomogeneities produced during the initial, brittle deformation stages. As a consequence, nano-gouge AE signal showed less attenuation and required less amplification. Micro- and nano-gouges share a similar weakening history and develop comparable microstructures. We therefore included in the analysis the evidences collected from both materials.

The AE-listener point of view has the advantage of being continuous in time, but does provide with an indirect measurement. AE were therefore interpreted in conjunction with mechanical data and microstructural observations. The integrated dataset shows that the weakening history of calcite gouges is composed of five distinct stages. During Stage I, slip hardening behaviour is associated to brittle deformation. Initially distributed deformation and cataclasis are relatively silent within the resonance spectrum of the sensors. Localisation of deformation into a narrow principal slip zone (PSZ) and

74

hardening behaviour can be associated to the increasing AE activity, whose most energetic emissions were recorded at peak strength conditions. The first sintered PSZ boundaries, i.e. embryonic mirror-like surfaces (MSs), form during early Stage II. These are initially irregular and prone to brittle reworking as observed in microstructures. PSZ boundaries become progressively more stable, during MSs migration. This evolution is coherent with AE amplitudes and signatures. The early, reworked MSs are associated to energetic events, with high amplitudes in the low-frequencies (< 200 kHz). Stabilisation of the MSs corresponds in turn with the rapid loss of the low-frequency content. The overall amplitude of Stage II events diminishes and remains close to the ambient noise throughout Stage III. This relatively silent stage supports the hypothesis of the viscous nature of deformation mechanisms in the PSZ. The continuous background of AE with low energy is possibly related to the anisotropic grain growth of calcite during the expansion of the sintering gradient in the deactivated layers outside the PSZ. AE activity rises once again during Stage IV, when the sample decelerates to stop. Events are recorded mostly towards the end of the Stage, when temperatures are rapidly diminishing and deformation is switching to brittle mechanisms once again. The high amplitudes recorded in the low frequencies range suggest that the brittle fracturing that exposes the MSs as they are observed in post-mortem samples occurs during this transient. Splitting along MSs is also enhanced after the stop of the sample, during early Stage V, due to thermal cracking from rapid cooling and small adjustments of the apparatus column. Further thermal damage introduced at smaller scale is revealed by subsequent discrete AE events fading in time.

I conclude that coseismic deformation of calcite in the experimental faults presented here is viscous. This hypothesis is supported not only by post-mortem microstructures but also by the "silent" nature of Stage III, when the recorded AE activity is extremely low. I also observe that the brittle nature of mirror-like surfaces is intimately related to the transition between different deformation styles and that it is enhanced by late thermal damage. Therefore, brittle mirror-like surfaces may represent the expression of the post-seismic strength recovery of the experimental fault and may not play an active role during dynamic weakening.

5. The architecture, structural evolution and deformation mechanisms of seismic carbonate principal slip zones.

5.1 Foreword

The evidences presented in chapters 3 and 4 show that coseismic weakening of carbonate gouges is operated by viscous processes, active at sub-melting temperatures. The microstructures produced in the principal slip zone are remarkably similar to those of natural and experimental ultramylonites, whose deformation is controlled by creep mechanisms. However, classic ultramylonites are believed to accommodate slow and aseismic creep deformation, and it is still poorly investigated whether the same deformation mechanisms can operate at coseismic – i.e. more than eight orders of magnitude higher – strain rates. Experimental data, associated microstructures and acoustic emissions do not allow to unambiguously reveal the specific deformation mechanisms that operate during coseismic viscous flow, which leads to the formation of mylonitic fabrics in the principal slip zones. In order to retrieve this kind of information, a further study is required to inspect deformation at sub-micron scale. This chapter will present an in-detail characterisation of the evolution of textures during coseismic deformation and associated deformation mechanisms using EBSD techniques. The analysis is performed with the aid of both scanning and transmission electron microscope.

The results and main findings of this chapter have also been published in Earth and Planetary Science Letters (Pozzi *et al.*, 2019), and a copy of the original Geology manuscript is included in the Appendix III.

5.2 Introduction

Faults are classically viewed as the main expression of brittle deformation in the upper crust. The macroscopic to microscopic fabrics of fault zones are known to evolve

76

with depth and temperature (Sibson, 1977; Faulkner et al., 2010). However, their rheology and fault rock development are also strongly determined by a wide range of strain rates such as in slow, creeping faults to fast, seismogenic ones (e.g. see the fault rock classification scheme of Spray, 2010). An example of this dependence of fault rocks on strain rate is given by pseudotachylytes (Sibson, 1977), which are found in natural faults where they form due to almost instantaneous frictional melting during the propagation of earthquakes. In particular, very large local strain rates can be attained during seismic slip and, as a consequence of shear heating, thermal activated processes, such as frictional melting, become a dominant factor in controlling the strength of the fault (Di Toro et al., 2006). Similarly, other thermally activated processes, such as flash heating (e.g. Goldsby and Tullis, 2011; Rice, 2006) and thermal pressurisation (e.g. Rice, 2006; Sibson, 1973) can take place and produce transient coseismic decreases in fault strength.

Recent experimental studies have also proposed that the onset of viscous deformation mechanisms in ultrafine grained fault rocks could also lead to coseismic dynamic weakening. In particular, in carbonate rocks, grain size sensitive (GSS) creep processes could become dominant, with textural and mechanical evidence pointing to the transient operation of grain boundary sliding (GBS) mechanisms (De Paola et al., 2015; Green et al., 2015). In the previous chapters we strengthened these hypotheses by showing that ultramylonite-like domains form during seismic slip in carbonate-hosted experimental faults (see also Smith et al., 2015) and that they localise most of the deformation

Ultramylonites are very fine-grained fault rocks produced by dynamic recrystallization and creep deformation mechanisms during high-T ductile deformation (Sibson, 1977). Such deformation mechanisms are known to accommodate viscous flow and aseismic behaviour in lower crustal and lithospheric mantle shear zones deforming at low strain rates ($<< 10^{-8}$ s^{-1}). Also, these deformation mechanisms have previously been observed at high strain rates for a range of nano-phase alloys (Chandra, 2002) and ceramics (Lankford, 1996) in association with superplastic behaviour. However, their role in controlling fault strength during deformation of fine- to ultrafine-grained

geological materials at high strain rates (> 10^2 s^{-1}) and sub-melting temperatures, characteristic of upper crustal seismic ruptures, is still poorly understood.

In this chapter we document the development of coseismic ultramylonites produced experimentally at ultra-high, seismic strain rates, and describe in detail their structures by analysing their crystallographic preferred orientation (CPO) fabrics and their microstructural evolution throughout the dynamic weakening history. We use these findings to infer how deformation mechanisms compete in controlling the fault strength at a nanograin scale during episodic seismic slip events.

5.3   Methods

5.3.1   Experimental procedure

Friction experiments were performed using a low to high velocity rotary shear apparatus at the Durham Rock Mechanics Laboratory using simulated fault gouge, which consists of fine grained (grainsize between 63 μm and 90 μm) calcite powder.

Experiments were run at room temperature and dry conditions (relative humidity ~ 40%). Samples (1 g of gouge) were first loaded up to the maximum axial pressure (parallel to the vertical rotation axis) σ_n = 25 MPa and were then sheared at tangential velocities of v = 1.4 ms^{-1} (calculated at the reference radius of 8.9 mm). A series of experiments were stopped after different amounts of displacement in order to document the microstructural evolution of recovered samples throughout the slip weakening history. Details for each experiment are reported in Appendix I.

After each run, samples were carefully removed to preserve the full layer thickness, were then embedded in epoxy and cut parallel to the slip direction at a distance equal to the reference radius. This procedure preserves an X-Z cross-section, where X is parallel to the slip direction and Z is perpendicular to the shear zone boundary (shear plane). The cut surface was then lapped with diamond paste down to 0.25 μm and polished using colloidal silica.

5.3.2 Microstructural analysis

Microstructural analysis was carried on polished cross-sections using a FEI Helios Dual Beam Nanolab 600 scanning electron microscope (SEM at the Department of Physics of Durham). SEM images were acquired in backscatter (BS), using the through-the-lens acquisition system, and forescattered (FS) modes. FS is operated on 70° tilted specimens using a 4 Quadrant KE Development FS imaging control detector. Electron back-scattered diffraction (EBSD) data were collected on uncoated tilted specimens using an Oxford Instruments Nordlys HKL detector (AZtec acquisition software, Oxford Instruments). For this technique, we used a working distance of 14-15 mm and a step size of 0.2 μm. Operating conditions were 10-20 kV of accelerating voltage and 1.4 nA current. EBSD data have been processed and analysed using CHANNEL5 software (HKL Technology, Oxford Instruments).

5.4 Experimental results and microstructural observations

5.4.1 Mechanical data

The experimental deformation of the calcite gouges displays a dynamic weakening history in agreement with many previous studies (e.g. Di Toro et al., 2011; Fondriest et al., 2013; De Paola et al., 2015; Siman-Tov et al., 2015; Smith et al., 2013, 2015). Under these conditions, the friction curve follows a characteristic four stage evolution (Fig. 5.1). During Stage I, strain hardening behaviour is observed with friction coefficients in the Byerlee's range (μ = 0.6 - 0.9). Stage II includes the onset of dynamic weakening, following the achievement of frictional peak values, and rapid decay of the fault strength to low friction coefficients. Stage III shows low friction values (μ = 0.1 - 0.2), which continuously decrease following a very shallow slope. Stage IV takes over upon deceleration of the apparatus when the fault strength recovers up to values of μ = 0.4 - 0.5.

5.4.2 Microstructure evolution throughout the weakening history

Each of the four main stages recorded throughout the weakening history is associated with characteristic fault/shear zone architecture. Here is a brief recap from Ch. 3.

Stage I slip hardening is associated with structures and microstructures typical of the brittle regime. Samples show numerous R, R' (Riedel) shears and a shear-parallel Y shear band (~200 μm thick) develops, which generally nucleates close to the top (rotating) cylinder (Fig. 5.2 A). Brittle deformation is distributed throughout the entire gouge layer, which shows pervasive brittle grain size reduction. Extreme strain localisation occurs in the Y-shear band where grain size reduction to a few tens of nm is observed.
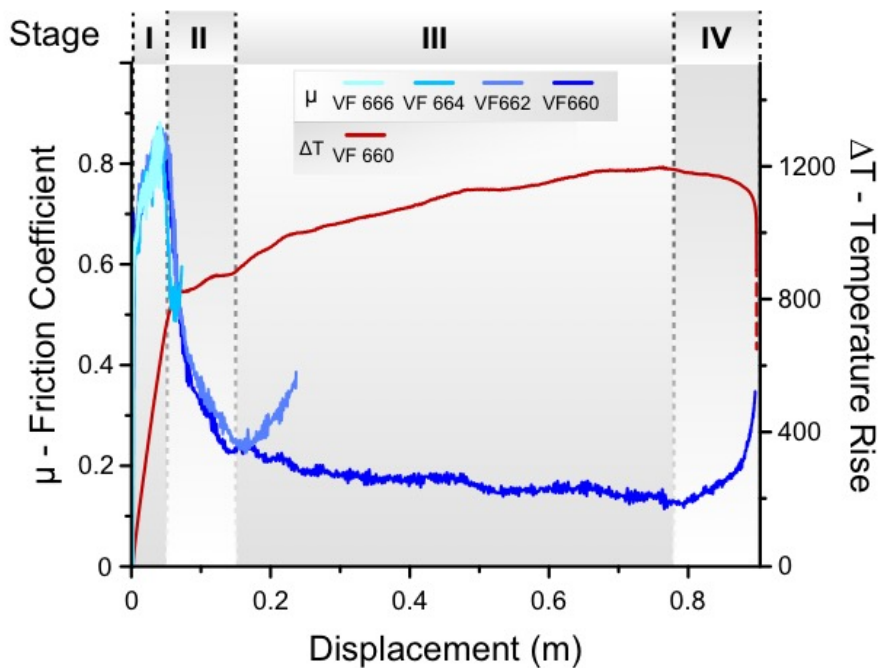
Figure 5.1 | *Mechanical data (v = 1.4 m s^{-1}, σ_n = 25 MPa): friction coefficient (μ, shown in blue) and estimated temperature rise (ΔT, shown red) curves are plotted versus displacement. The four stages of friction evolution are highlighted in the graph by the shaded areas.*

80

Following the achievement of peak friction, the Y shear band becomes a well-defined principal slip zone (PSZ) that becomes increasingly confined between sharp boundaries (Fig. 5.2 B). In its embryonic stage, patchy volumes of polygonal grains form in the low-strain domains outside the PSZ (Fig. 5.2 B). The recovered samples easily split along the PSZ boundaries revealing the reflective surface of the polygonal patches. These have been interpreted as the (embryonic) mirror-like surfaces (MSs) formed by sintering processes (Fondriest et al., 2013; Siman-Tov et al., 2013; Smith et al., 2013; see ch. 3). Inside the PSZ, the material is still porous and has an inhomogeneous grain size, with larger grains (~ 1 μm) embedded in a much finer matrix (Fig. 5.2 C). At the end of Stage II - early Stage III, the PSZ has thinned by up to an order of magnitude (~30 μm width) and shows parallel, fully developed sharp, sintered boundaries forming continuous, flat MSs (Figs. 5.2 D and 5.3 A). The localisation process appears to progressively abandon several (now relict) MSs in the outer deactivated layers, a process referred to here as "MSs migration" (ch. 3).

By Stage III, the PSZ is characterised by grains displaying triple junctions, very low porosity and homogeneous grainsize (~300 nm, Figs. 5.3 A, B). The crystals typically show a shape preferred orientation defining an oblique foliation, consistent with the shear sense. It is worth noting here that the texture of the PSZ itself is comparable to that of natural (Bestmann, Kunze and Matthews, 2000; Herwegh and Kunze, 2002) and experimental (Barnhoorn et al., 2004) ultramylonites. Hereafter, we refer to these textures as coseismic ultramylonite textures. The oblique foliation of the PSZ is interpreted to be the result of cycles of dynamic recrystallisation and passive rotation of nanograins. The volumes outside the PSZ have a much coarser grain size (up to 1-2 μm) and extend outward for several tens of μm forming a so-called 'sintering gradient (SG)' (Fig 5.2d). The latter is evident from the observed decrease of mean grainsize and increase of porosity moving away from the PSZ.

The architecture of the PSZ and the surrounding material does not change substantially throughout Stage III. The PSZ maintains a stable thickness while the sintering gradient expands away from the PSZ and becomes stronger (Figs. 5.2 E and 5.3 B). Significantly, the grainsize within the PSZ and in the sintered regions grows (700 nm and up to 3 - 4
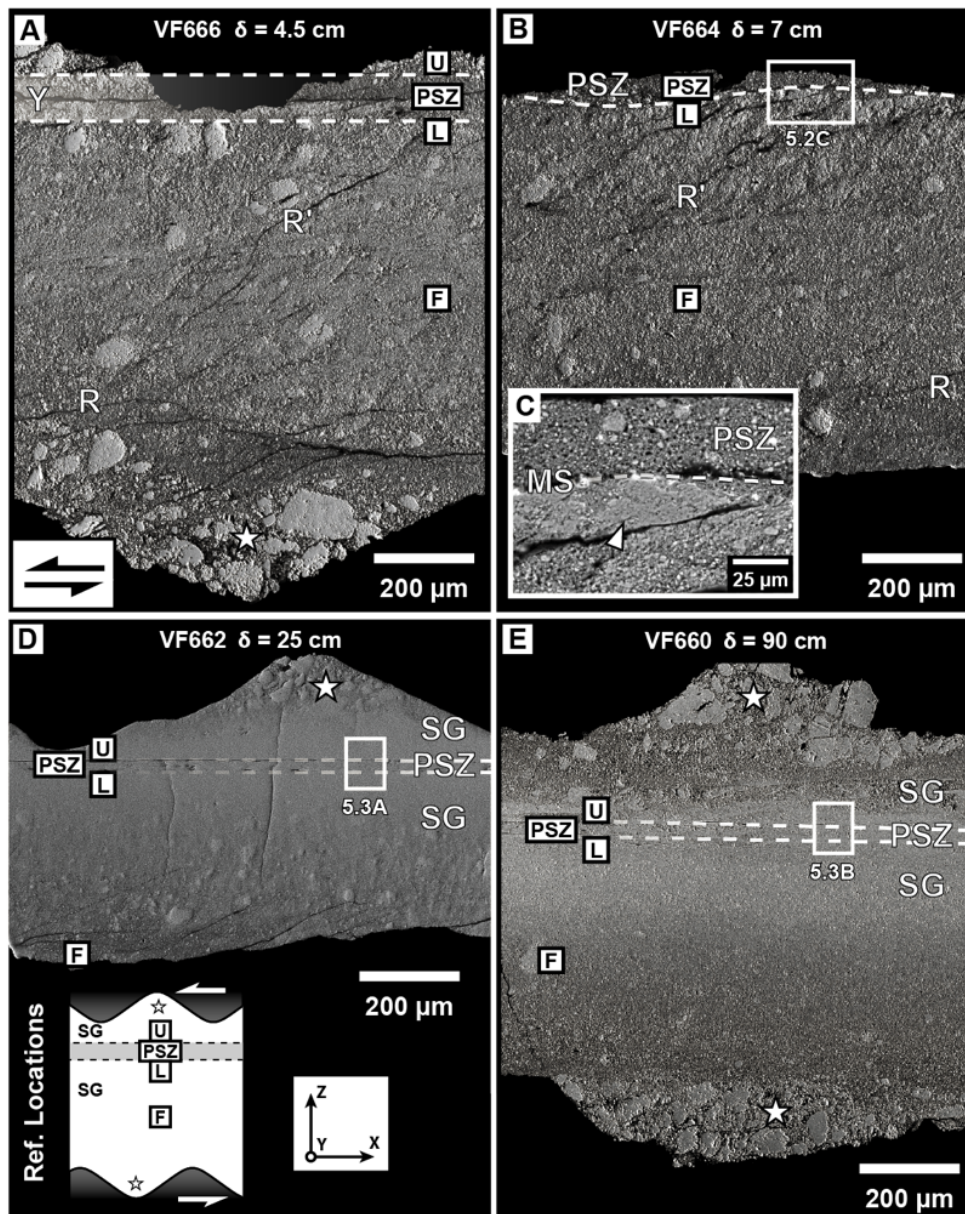
Figure 5.2 | *Backscattered electron images of sample cross sections obtained from the whole thickness of gouge layers cut at the reference radius. The fault displacement, δ, is shown for each microstructure. Relicts of the starting coarse-grained gouge are preserved in the grooves machined on the top and bottom cylinder surfaces, indicated with white stars. Shear sense is sinistral. a) Stage I: diffuse and localized deformation with Riedel shears (R, R') and a horizontal Y shear band (Y). b) Stage II: well-developed principal slip zone (PSZ) with patchy recrystallized boundary ("mirror-like surfaces", MSs). c) Close-up of area outlined in b) showing a polygonal sintered patch below an embryonic MS. d) Early Stage III: fully developed PSZ bounded by MSs and sintered, deactivated layers (sintering gradient, SG). e) Late Stage III: microstructure similar to that of early Stage III (Fig. 5.2 D) but the SG is wider and more strongly developed. The framed U, PSZ, L and F are the reference locations (see schematic inset in Fig. 5.2 D).*

μm, respectively, after 65 cm of slip) with displacement and inferred rise in temperature (Fig. 5.3 B).

Earlier formed microstructures are unavoidably overprinted, but not destroyed, by the latest stages of deformation that take place upon deceleration of the machine to arrest. The Stage IV PSZ is commonly reworked and fragmented due to the effects of embrittlement. Continuous MSs are typically well preserved at the PSZ boundaries (ch. 3).
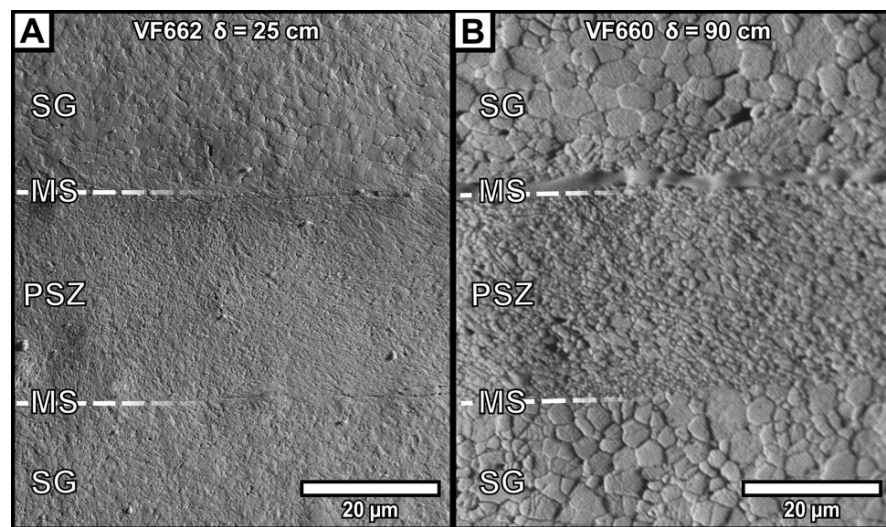
Figure 5.3 *| Forescattered electron images of A) Early Stage III and B) Late Stage III PSZ and surroundings. The PSZ maintains its thickness while grain size is observed to grow both within and outside the PSZ. Shear sense is top to the left.*

5.5   Characteristic textures of coseismic ultramylonites revealed by EBSD data

5.5.1   Methods

The nature and evolution of grain crystallographic orientation patterns can be investigated using electron back scattered diffraction (EBSD) analysis (e.g. Prior et al., 1999). This gives important quantitative insights into the nature and evolution of grain scale mechanisms, which can then be related to the other microstructural observations

and bulk mechanical data obtained during the experimental deformation of calcite micro-gouges reported here.

We performed EBSD analysis on the same polished cross sections (X-Z plane) used for the microstructural characterization. In particular, four critical moments of the deformation history are investigated: i) Stage I, ii) early Stage II, iii) early Stage III and iv) late Stage III (Figs. 5.1 and 5.2). Four distinct reference locations are selected in the samples, each preserving the characteristic deformation features of these stages (Fig. 5.2 and inset of Fig. 5.2 D). One is located within the PSZ (which correspond to the Y-shear band formed during Stage I) and two lie immediately outside its boundaries, in the upper (e.g. U, towards the rotating cylinder) and lower (e.g. L, towards the stationary cylinder) outer SG layers (Figs. 5.2 D, 5.5 and 5.6). Note that U and L positions are not fixed as the active PSZ boundaries migrate during localization. The fourth location, F, is chosen halfway between the lower PSZ boundary and the stationary cylinder. This reference location is fixed and never lies close to the PSZ at any of the four deformation stages. Given their frail nature, samples were polished with particular care. However, as it is difficult to completely remove the grain topography, this makes the indexation of EBSD data variable, ranging from a minimum of 20% of Stage I gouges successfully measured up to 95% in the sintered layers of Stage III.

The EBSD data were processed to visualise the crystallographic orientation of calcite grains using orientation maps (Fig. 5.4, coloured using IPF-Y gradient), to analyse the orientation of relevant crystallographic elements with pole figures (Fig. 5.5, using one point per grain and plotted on equal-area projections, upper hemisphere) and to perform misorientation analyses (Fig. 5.6). In our samples, two representative crystallographic directions in calcite (commonly used in literature) are selected: (0001) c-axis and <1120> <a> direction. Pole figures were contoured using the orientation distribution function (Bunge, 1981) calculated with a half width of 15°.

Misorientation analysis is used to quantify the overall distribution of crystal orientations and is utilised herein to investigate the deformation mechanisms responsible for each texture (Wheeler et al., 2001). The misorientation angle, MA, is the
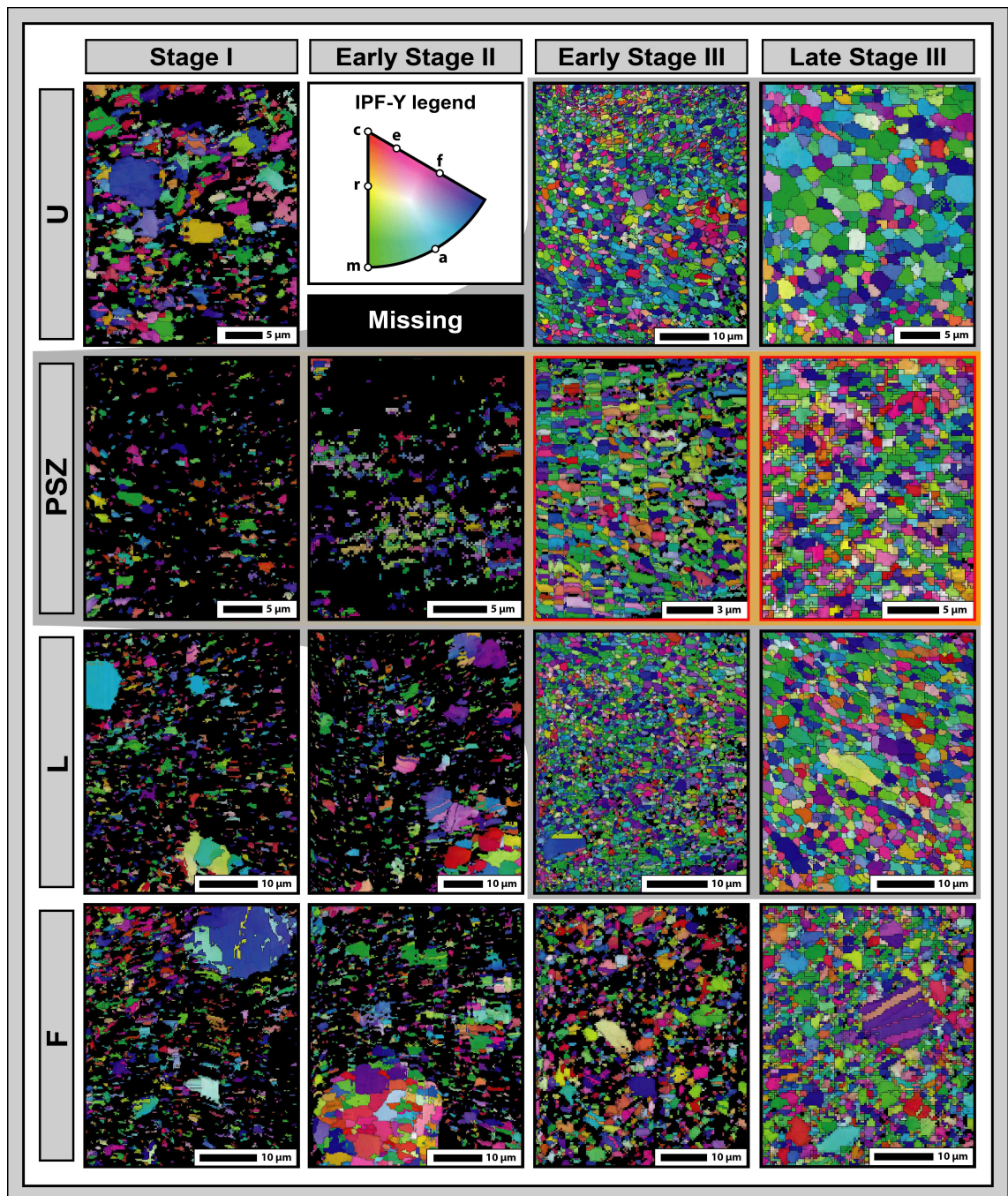
Figure 5.4 | *EBSD orientation maps coloured using IPF-Y gradients. The legend shows important crystallographic directions (including c-axis and a-direction) and their IPF-Y colour. Late Stage III U and L reference locations show that some of the larger grains are composed by coalescence of individuals sharing low MAs (< 10°, i.e. grains containing subdomains with slightly different shades of IPF colouring).*

minimum angle describing the difference of crystallographic orientation between two grains, and can be measured for neighbouring (grains sharing a boundary) or random (randomly picked grains) pairs. Measured MAs provide an indication of the grain lattice transformation – taking into account the symmetry – that lead to differently oriented grains. The relative frequency of MAs falling within an orientation range – binned here with a width of 5° - can be plotted for each orientation in a diagram producing correlated and uncorrelated MA distributions (MAD), respectively. MAs < 2° were discarded as these values lie close to the resolution of the measurements. The reference theoretical misorientation angle distribution for a random distribution (TRD) of trigonal crystals (Wheeler et al., 2001) is shown along with the MAD data in Fig. 5.6.

5.5.2   Results

Deformation Stage I : During Stage I, the PSZ reference location is in the proto-PSZ (the Y-shear band) while U, L and F lie in the Riedel-shear dominated sample region (Figs. 5.2 A and 5.5 A). The latter areas typically show a strongly heterogeneous grainsize, with larger particles (>> 1µm) dispersed in a finer matrix; this contrasts with the more comminuted, but heterogeneous, PSZ (mean grainsize ~ 200nm). Stage I materials are poorly consolidated and porous, which hindered the polishing procedure. As a result of the topographic effects caused by the poor polish, data from loose nanoparticles could not be retrieved and large areas of non-indexed material (dark areas) dominate the EBSD maps at this stage (Fig. 5.4, Stage I). Hence, the interpretation of crystallographic data is necessarily restricted to detected grains, which are overall larger than 1 µm.

Pole figures show a relatively weak clustering of the calcite c-axes at a small angle to the Z direction, especially in the PSZ (Fig. 5.5 B). This produces a weak crystal preferred orientation (CPO), with multiple uniform distributions (m.u.d.) smaller than 3. Each of the four reference locations produces very similar misorientation plots (Fig. 5.6). The correlated MAD shows a strong maximum at low MAs (< 10°, MA used to separate between grain and sub-grain boundaries), with the highest intensity found in the PSZ. Another peak is located between 75°-80° MAs, the lowest of which occurs in the PSZ
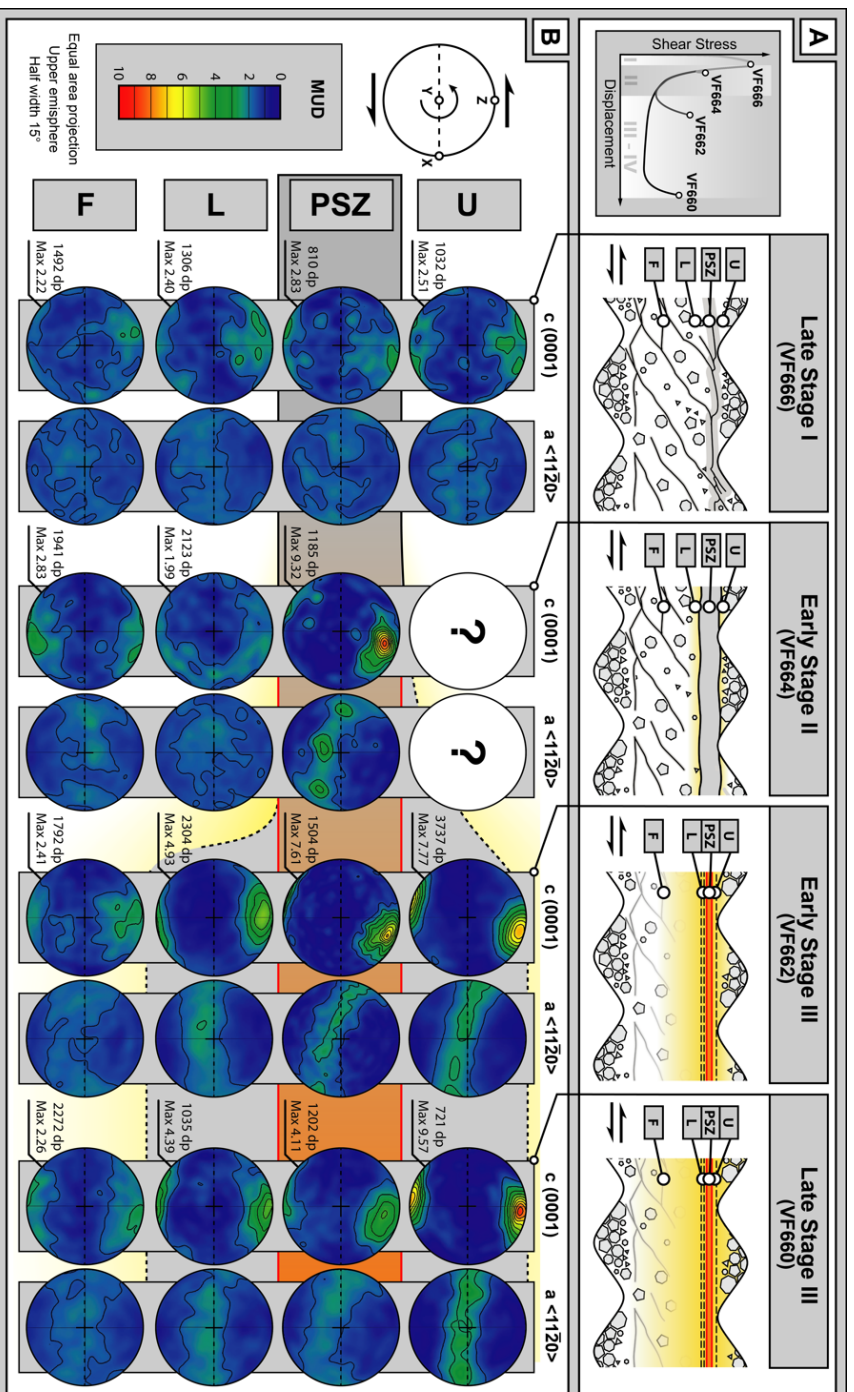
Figure 5.5 | A) Schematic representation of mechanical data, microstructures and locations of the four analysed reference areas (U, PSZ, L and F). Orange and yellow shading are used to highlight the viscous PSZ and the sintering gradient, respectively. B) EBSD pole figures for two selected crystallographic directions for calcite: c (0001) axis and a <112̄0> direction. Poles are plotted in an equal area projection on the upper hemisphere. Multiples of uniform density (MUD) colouring applies to all of the pole figures.

(Fig. 5.6). This peak is likely related to e-twinning of calcite (*e {01-18}*; e.g. Bestmann and Prior, 2003). The uncorrelated MAD matches almost perfectly the theoretical misorientation angle distribution for a random distribution (TRD) of trigonal crystals (TRD in Fig. 5.6).

Early Deformation Stage II : During early Stage II, when the material has started to weaken, clustering of c-axes produces a strong monoclinic CPO (m.u.d. = 9.32) within the PSZ domain, tilted clockwise – consistent with the sinistral shear sense – at a small angle with respect to Z (Fig. 5.5 B). a-axes form distinct maxima distributed every ~60° on the great circle laying at low angle to the XY plane (Fig. 5.5 B). This pattern is typical of simple shear deformation of calcite (e.g. Wenk et al., 1987). Within the PSZ, the uncorrelated MAD deviates from the TRD due to the development of the strong CPO. The e-twin peak disappears from the correlated MAD and the intensity of low MAs (< 10°) decreases (Fig. 5.6). In reference locations L and F, textures and crystallographic data do not differ substantially from Stage I. The U domain could not be retrieved due to the delicate nature of the samples. By the end of Stage II, localization processes have ended and PSZ has reached a steady state thickness of 30 µm (Fig. 5.3).

Early Deformation Stage III : During early Stage III, the PSZ is non-porous and shows a nanogranular ultramylonitic texture. The CPO is comparable to that of the Stage II PSZ, but is slightly weaker (m.u.d. of 7.61, Fig. 5.5 B). The dominant green and blue IPF-Y colouring indicates a prevalence of *<a>* and *m <10-10>* directions, respectively, parallel to the Y direction (Fig. 5.4). In the PSZ, the uncorrelated MAD is bell-shaped, centred on the MA bin between 55 and 60°, reflecting the distribution of *a*-maxima (Fig. 5.6). The correlated MAD is similar, but the peak at low angles has become weaker compared to previous stages.

Due to the narrowing of the PSZ (during Stage II), the U and L reference locations are now within the sintered gradient below and above the PSZ, respectively, containing the array of relict MSs (Figs. 5.2 D and 5.5 A). These reference locations are non-porous and their sintered texture is similar to that of the PSZ as well as their CPO, however, with a different intensity (Fig. 5.5 B). The U location shows a clear maximum at low MAs (< 10°, Fig. 5.6), while the L location has a CPO that is apparently orthorhombic, with the c-axes

88
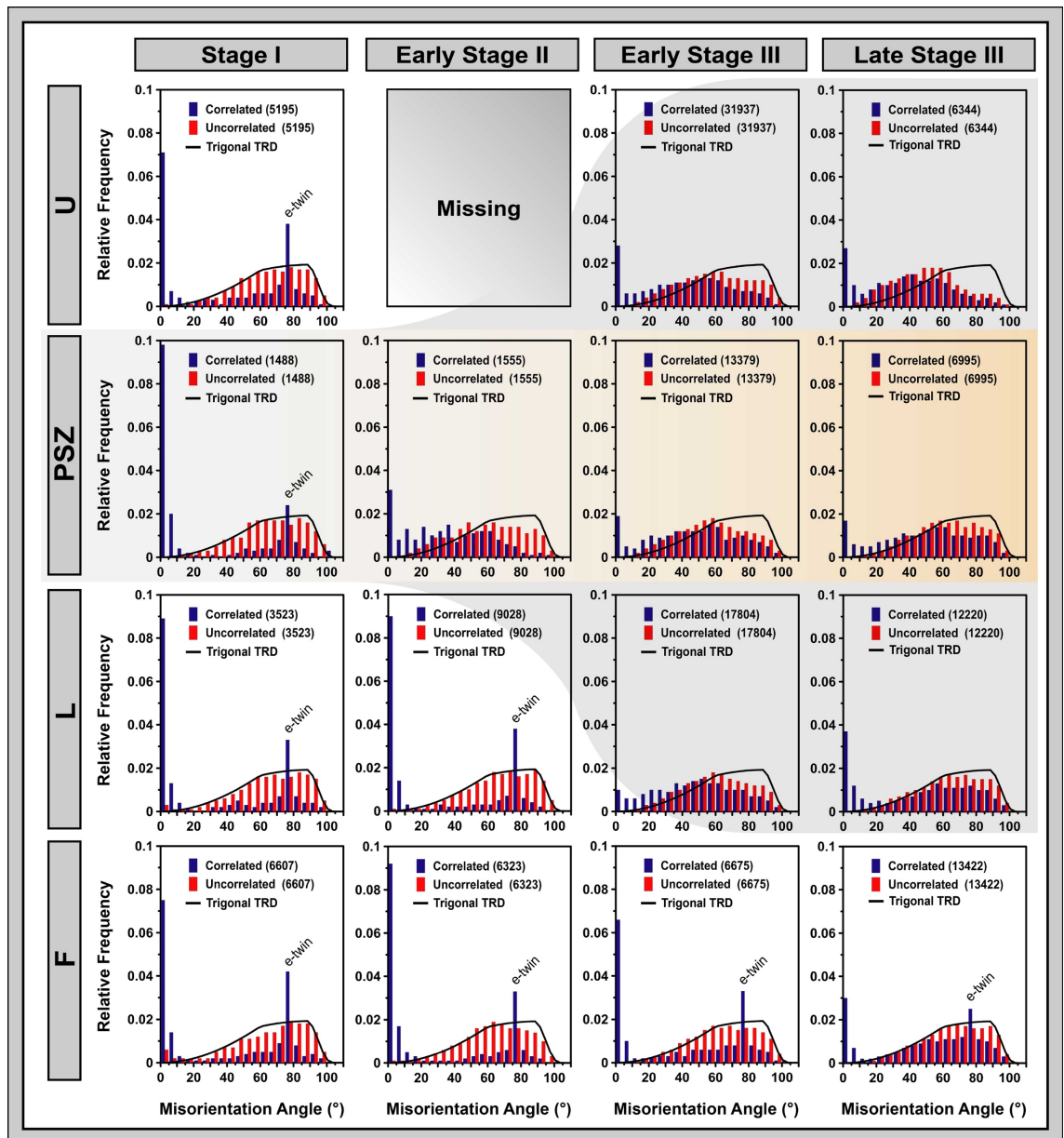
Figure 5.6 | *Misorientation analysis plots showing correlated MAD (blue bars), uncorrelated MAD (red bars) and theoretical random distribution (TRD) for trigonal crystals (black curve). The bin width of each misorientation angle (MA) group is 5°. MAs < 2° are disregarded as they lie within the resolution of measurement.*

parallel to Z (Fig. 5.5 B). At this stage, the F location is still porous, but shows incipient sintering (densification and recrystallization, Figs. 5.3 D and 5.4). Here the pole figure and MAD show no substantial evolution from the previous stages (Figs. 5.5 B and 5.6). However, the intensity of uncorrelated MAs is slightly reduced (Fig. 5.6).

Late Deformation Stage III : At late Stage III, after ~75 cm of slip, the PSZ CPO has weakened substantially (m.u.d. of 5.11, Fig. 5.5 B) and the girdle formed by *a*-axes is spread over a wider area. *a*-maxima have completely disappeared. The uncorrelated MAD distribution in the PSZ has shifted to the right towards the TRD (Fig. 5.6). No obvious change is observed in the correlated MAD. The CPO in the U reference location strengthens and shows clear monoclinic symmetry (Fig. 5.5 B). The CPO in the L reference location does not vary substantially and remains similar to previous stages and to the PSZ domain (Fig. 5.5 B). The uncorrelated MAD is also comparable to that of the PSZ (Fig. 5.6).

However, the peak at low correlated MA is now much higher. The F location is now fully sintered and it is possible to see porphyroclasts (> 5µm) inherited from Stage I embedded in a polygonal sintered matrix (Figs. 5.2 E and 5.4). Again, the pole figure has not substantially evolved (Fig. 5.5 B) despite becoming slightly weaker. This location also presents the same TRD-matching uncorrelated MAD, while in the correlated MAD, the two peaks (e-twin and low MAs) have substantially decreased (Fig. 5.6).

5.6 TEM imaging

Transmission Electron Microscope imaging was carried out in order to gain further insights into nanograin-scale processes. Two thin foil samples from the U and PSZ reference locations of experiment VF660 (Late Stage III) were prepared using focused ion beam (FIB) technique. Here, TEM imaging performed in scanning mode (S-TEM) reveals polygonal aggregates of slightly elongated crystals with mean aspect ratios of 1.37 and 1.62, respectively (Figs. 5.7 A, E).

The grains in the U location have fairly homogeneous grain size (mean D = 1.8 µm) and display well-defined triple junctions and sharp crystal boundaries (Fig. 5.7 B). These are generally straight, but locally display a slight curvature (Fig. 5.7 B, yellow arrow). Grains show, on average, a homogeneous distribution of dislocation densities (Figs. 5.7

90

B, C). Crystals appear fairly equant and weakly distorted (e.g. bend contours in Figs. 5.7 A-D) and rare cavitation is observed at triple junctions (Figs. 5.7 A, D). Dislocations are commonly elongate (hundreds of nm) and do not form large entanglements nor dislocation walls (Figs. 5.7 C, D). No subgrains are observed. Locally, some partially-healed triple junctions are found within grains (white arrow in Fig. 5.7 D).

Grains in the PSZ are more irregular, with a mean D ~ 700 nm (Fig. 5.7 E). Grains form triple junctions, and are commonly non-equiangular and cuspidate (Fig. 5.7f, white arrow), while grain boundaries are frequently curved (Fig. 5.7 F, yellow arrow). Diffuse
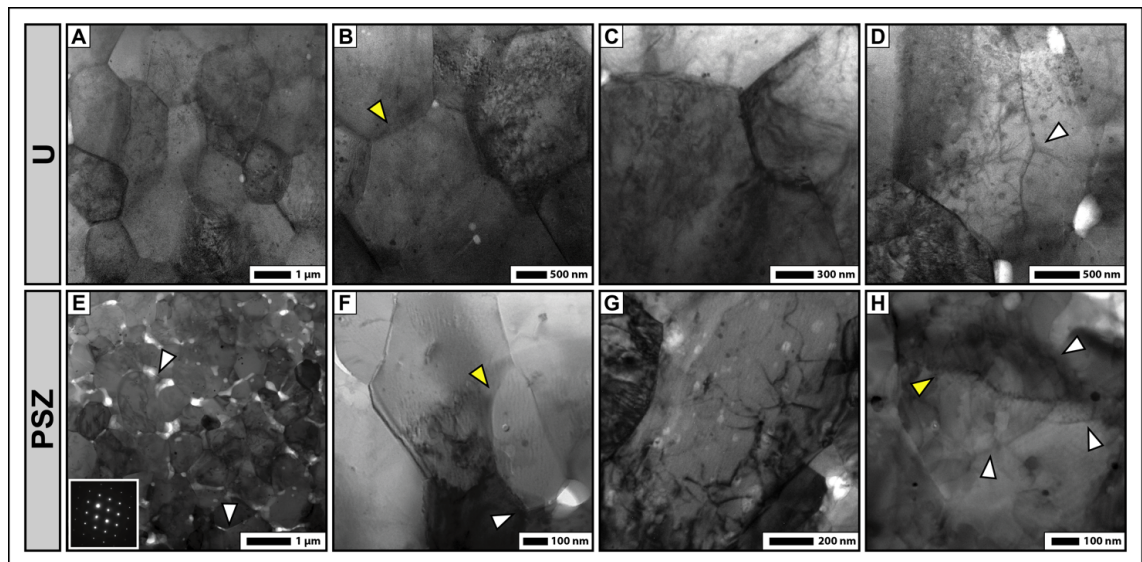
Figure 5.7 | *Bright field S-TEM images of the U (a-d) and PSZ (e-h) domains of experiment VF660 (δ = 90 cm, Late Stage III). A) Equant grains displaying tightly packed structure with well-defined triple junctions and rare cavitation; B) Slight curvature of the grain boundaries (yellow arrow); C) Crystals containing numerous dislocations but few bend contours; D) Partially healed triple junction (white arrow) within a grain and cavitation at triple junctions (white areas). E) Sub-equant grains displaying tightly packed structure with triple junctions, diffuse cavitation (white spots) and microcracking (e.g. white arrows), inset shows a clear diffraction pattern attesting the non-amorphous nature of grains in the PSZ; F) Curved boundaries (yellow arrow) and cuspidate triple junctions (white arrow); G) Dislocations in a grain; H) Subgrains (e.g. white arrows) bordered by well-organised dislocation walls (e.g. yellow arrow).*

cavitation, which was not resolvable with SEM imaging, is observed at triple junctions and at grain boundary-parallel microfractures (Fig. 5.7 E white arrows). Grains in the PSZ contain dislocations (Fig. 5.7 G) and neighbouring grains may have different dislocation densities (e.g. Fig. 5.7 F, compare the two grains in the centre of the picture). Curved grain boundaries are generally convex towards the most strained individual grain (Fig. 5.7 F). Furthermore, entanglements, dislocation walls (Fig. 5.7 H, yellow arrow) and subgrains (Fig. 5.7 H, white arrow) are observed within grains with higher density of dislocations.

5.7 Discussion

5.7.1 Low vs. high (coseismic) strain rate ultramylonites

The development of calcite mylonites and ultramylonites has been intensively studied at a range of high temperatures but only at relatively low strain rates ($< 10^{-3}$). Our new microstructural evidence and CPOs analyses show that coseismic ultramylonites can also form when initial calcite micro-gouges are sheared under extremely high strain rate coseismic slip conditions.

The textures of the coseismic ultramylonites described here are strikingly similar to those of ultramylonites obtained in high displacement torsion experiments carried out under elevated temperature conditions at much lower strain rates (Pieri et al., 2001; Barnhoorn et al., 2004), and predicted by theoretical studies (Wenk et al., 1987). Our mechanical data and microstructural observations show that the processes that control fault weakening of coseismic ultramylonites may not differ substantially from those observed in lower strain rate ultramylonites. However, coseismic ultramylonites must operate at the nanoscale in order to accommodate high seismic strain rates at sub-melting temperatures.

5.7.2 Evolution of the architecture and deformation mechanisms of coseismic ultramylonites during seismic slip propagation

During high velocity friction experiments on calcite gouge, mechanical data show that the strength of the material evolves dynamically with slip, and the friction curve follows a characteristic four stage evolution (Fig. 5.1). Our microstructural observations reveal a shear zone-like architecture where shear localizes within a PSZ from the very early stages of deformation. Hence, microstructural observations and EBSD data have been collected at four distinct reference locations: within the PSZ, in the sintered layers immediately outside the PSZ (U, L locations) and away from the PSZ (F location).

Our data show that each of the four main stages recorded throughout the weakening history is associated with characteristic structures in the PSZ and surrounding areas. Such observations are used below to propose a conceptual model describing the dynamic evolution of processes and deformation mechanisms associated with the development of nanometric grain size ultramylonites during seismic slip.

5.7.3   From gouge-cataclasites to nanometre grainsize ultramylonites

During high velocity friction experiments on calcite gouge, mechanical data show that the strength of the material changes dynamically with slip, as temperature rises due to frictional heating. This suggests that, during shear localization in the principal slipping zone, thermally activated weakening mechanisms must be dominant. Such hypotheses are supported by microstructural observations showing a transition from cataclastic shear band textures to nanoscale ultramylonites, with rising temperature during seismic slip.

Slip hardening behaviour during cataclastic flow (Deformation Stage I) : During Stage I, when the deforming gouge displays slip hardening behaviour, deformation is mainly brittle preserving evidence of widespread grainsize reduction and localisation into a proto-PSZ (Y-shear band, Fig. 5.2 A). At this stage, the material is still porous and only

Figure 5.8 | *Conceptual model for the dynamic evolution of deformation mechanisms in the PSZ constrained using microstructural evidence, including EBSD. A) Conceptual partitioning of shear strain rates (γ̇) accommodated by brittle (blue), grain size insensitive creep (GSI, red) and grain size sensitive creep (GSS, green) during the different Stages (I-IV) of deformation. It is assumed that at any moment, they sum to 100% of the total strain rate in the PSZ (See text for details). B) Schematic evolution of stress (τ) and temperature (T) during a high velocity experiment. C) Deformation path experienced by the PSZ in a schematic deformation mechanism map. Dashed lines represent the grain size piezometric equilibrium at different moments during Stage III, where grain size is directly related to the stress state by a temperature-dependent piezometric law. Circled numbers link to the position of the event in Fig. 5.8a.*

slightly cohesive. Uncorrelated MAD of the grains plots close to the trigonal TRD, suggesting that crystal orientations are only weakly influenced by the directionality of the stress field (Fig. 5.6). This is consistent with what is predicted to occur during cataclastic shear flow, when particles are continuously rearranged in a random fashion with increased mobility of the finer grainsizes (e.g. Hutter and Rajagopal, 1994, and references therein).

The correlated MAD reveals that two coeval plastic mechanisms take place during cataclasis. The first, e-twinning of calcite (peak at MA = 75°-80°, Fig. 5.6), is typical of low temperature deformation regimes and is intimately related to stress concentration effects along grain contacts (Wenk et al., 1973; Schmid et al., 1987; De Bresser and

Spiers, 1997). e-twinning is unable to accommodate large amounts of strain (Schmid et al., 1987; Burkhard, 1990) and we suggest that it happens at the very beginning of deformation. This process produces rotation of the calcite c-axes toward the maximum stress axis (σ') within its surrounding 26° small circle (Schmid et al., 1987), a mechanism possibly responsible for the weak CPO seen for Stage I in all domains in the deforming gouge layer. Alternatively, the strong peak at low MAs could be related to the activity of plastic processes such as subgrain rotation recrystallization (MAs < 10°).

Subgrains with dimensions (<200 nm) comparable to those of the nanograins formed during Stage I are also found in the Stage III PSZ. Such evidence supports the hypothesis that mechanisms such as shock-like stress release processes (Sammis and Ben-Zion, 2008; Spagnuolo et al., 2015) and brittle failure aided by intragranular crystal plasticity (Siman-Tov et al., 2013; De Paola et al., 2015) produce the extreme grainsize reduction measured in the shear bands within the samples. Thus, we conclude that during Stage I the dominant strain-accommodating mechanism is brittle (Figs. 5.8 A, C).

Transient strength decay to quasi steady-state low strength (Deformation Stage II) : By Stage II, the bulk temperature rise, due to frictional heating, is such that other plastic processes become competitive in accommodating strain in the PSZ. In fact, at this temperature (> 700°C) and strain (>> 10), e-twinning is no longer efficient (De Bresser and Spiers, 1997), and so its peak completely disappears from the correlated MAD through recovery (Fig. 5.6). Its disappearance is also consistent with the observed pervasive grainsize reduction - below the dimension of the twins (Rowe and Rutter, 1990) - operating in the PSZ.

The deformed material becomes less porous due to yielding of nanoparticles and progressive grainsize homogenization. The observed strong c-max CPO in the PSZ (Fig. 5.5 B) is explained by the operation of grain size insensitive, GSI, creep mechanisms, such as subgrain rotation (MAS < 10° in Fig. 5.6), which operate during dynamic recrystallization processes (dislocation creep, Figs. 5.8 A, C). By the end of Stage II, the PSZ is fully localised and does not substantially change its thickness throughout Stage III.

Viscous flow during slip at quasi steady-state low strength (Deformation Stage III) :

During Stage III, the PSZ hosts an ultramylonite with a fairly homogeneous grainsize, triple junctions and oblique foliation (Fig. 5.3). The strong CPO developed during Stage II is observed to progressively weaken throughout Stage III, as shown by the uncorrelated MAD that migrates toward the trigonal TRD (Fig. 5.5 B). A progressive attenuation of the CPO in the PSZ could be explained by the increasing activity of diffusion creep, which is enhanced by the reduction of grainsize and temperature rise (Bestmann and Prior, 2003). Wheeler (2009) showed with his model that a transition to a diffusion-creep-dominated regime will weaken, but not destroy the CPO (see also Rutter et al., 1994). This effect is sustained by grain rotation and especially grain growth, which is observed in samples sheared throughout Stage III (Fig. 5.3).

However, it should be noted that the correlated MAD in the PSZ is almost identical during both the early and late Stage III (Fig. 5.5 B). Therefore, we suggest that the major switch in rheology happens during Stage II while a quasi- steady-state regime is maintained throughout Stage III (Fig. 5.8a, c). At the beginning of Stage III, a piezometric equilibrium – i.e. between grain size reduction operated by GSI mechanisms (e.g. see subgrains in Fig. 5.7 H) and grain growth driven by thermal processes – is reached within the ultramylonitic PSZ (Figs. 5.8 A, C). At equilibrium conditions, the grain size should be directly related to the stress state, following a temperature-dependent piezometric law (e.g. De Bresser et al., 2001, 1998; Fig. 5.8 C). Importantly, we observe that during Stage III, the mean grain size grows with slip within the PSZ (Figs. 5.3 A, B), suggesting that grain size is directly related to the rising temperatures (Fig. 5.8 C; De Bresser et al., 1998, 2001).

Our microstructural observations suggest that, during Stage III, a combination of grain size sensitive (GSS) and insensitive (GSI) creep mechanisms are active within the ultramylonitic PSZ (Figs. 5.8 A, C). The combined operation of GSI (e.g. dislocation creep) and GSS (e.g. diffusion creep) creep mechanisms is capable of explaining not only the microstructural and topological features observed, but also the low measured stress levels (see ch. 3 and De Paola et al., 2015).

In their pioneering work, Ashby and Verrall (1973) recognized that, although GSI and GSS creep mechanisms are described by two independent flow mechanisms, they are likely to occur simultaneously in nature. In this case, the overall creep rate is given, to a sufficient approximation, by the sum of their relative contribution (Fig. 5.8 A). The interplay between GSI and GSS creep mechanisms is well known in material sciences from observations, theory (e.g. Ashby and Verrall, 1973; Nieh et al., 1996) and modelling (Bower and Wininger, 2004; Cipoletti et al., 2011) of GBS-accommodated superplasticity. However, modelling diffusion creep coupled to intracrystalline plasticity has been an intractable problem in geoscience, leading to generic uncertainties with flow laws which combine these processes.

Therefore, we conclude that the dynamic weakening of nanometre aggregates in seismic ultramylonites involves competition between multiple and evolving temperature-dependent mechanisms, whose quantification remains so far difficult.

PSZ ultramylonite embrittlement and fault restrengthening during slip deceleration (Deformation stage IV) : During the experiments, there is always a fourth stage of deformation during sample deceleration to arrest, when the fault strength is partially recovered. The most prominent damage produced during this stage is the embrittlement of the PSZ ultramylonite, leading to splitting along the MSs (ch. 4). The post-mortem PSZ is a cataclasite confined between the two last active MSs. S-TEM images show embrittlement in the PSZ due to cavitation and micro-fractures (Fig. 5.7 E), which are interpreted to form when the PSZ material moves out of piezometric equilibrium as the temperature falls. These interpretations can help explaining the restrengthening observed during Stage IV. In most cases, the reworking of the PSZ is modest and the ultramylonitic structure is rarely completely destroyed (Fig. 5.3).

5.7.4 Shear localization by ultramylonite boundary migration during seismic slip

Microstructures suggest that the PSZ localises during Stage II with its width reducing from 200 μm to 30 μm (Figs. 5.2 A-C). This process appears to occur by the inward migration of the PSZ boundaries – MSs – in discrete, non-continuous events. Each

localisation step deactivates a portion of the PSZ forming a new PSZ boundary that migrates inwards. The deactivated boundary is left in the SG domain as a relict MS. These layers, when deactivated, dramatically change their deformation regime, as they show substantial grain growth while accommodating limited amounts of deformation. This is supported by the S-TEM microstructural observations of low grain aspect ratios, straight grain boundaries and low distortion of the lattice (Figs. 5.7 A-D).

If these hypotheses hold, the U and L locations found in the SG, and containing the abandoned MSs, should "freeze" the PSZ CPO at different moments in its evolution during Stage II. SEM images show that relict and reworked MSs are present within the U locations, but are absent within the L locations, during early Stage II (Fig. 5.2 C). These observations show that shear localization occurred with an asymmetric migration of the upper and lower PSZ boundaries, where the upper U location deactivated prior to the lower L location (Ch. 3). This interpretation is strongly supported by the observation that the U location has a stronger CPO than the L location (Fig. 5.5 B), as the latter was active longer in the PSZ, witnessing a weaker activity of the GSI creep (e.g. dislocation creep).

The grains in these deactivated regions in the SG show a grain size which is an order of magnitude larger compared to that observed in the PSZ (Figs. 5.2 and 5.3). Also, no outstanding variation of CPO is observed during Stage III in the L location, while the CPO in the U location has slightly strengthened (Fig. 5.5 B). The inherited strong CPO in the U location, compared to L location, may aid sintering processes by facilitating the coalescence of slightly misaligned neighbouring grains (e.g. not fully-healed triple junctions seen in some grains in Fig. 5.4 and Fig. 5.7 D, yellow arrow). Overall, our observations suggest that grain growth in the SG locations, which occurs in less than a second, is not influenced by dynamic recrystallization (i.e. the same GSI and GSS creep processes operating in the PSZ no longer act in the SG region) and thus can be considered to be quasi-static. The operation of a quasi-static sintering in the SG region is also supported by the evidence of: (i) low amounts of lattice distortion in the grains (Figs. 5.7 A-C); (ii) low dislocation entanglements (Figs. 5.7 B-D); (iii) equant grainsize (Fig. 5.7 A); and (iv) straight grain boundaries connected by well-defined triple junctions (Figs. 5.7 A-C). However, the increase of the low MAs (< 10°) peak observed within the L location (Fig 5.6) and microstructural evidence of intracrystalline plasticity within the

U location (Figs. 5.7 B-D) suggest that a relatively small degree of plastic deformation is still accommodated in the deactivated regions during Stage III and that it is coeval with sintering.

Away from the PSZ, the Riedel-populated F location is no longer sheared after Stage I, and becomes overprinted by the expanding sintering front. Its correlated MAD does not change shape throughout the four stages, but shows recovery processes driven by static recrystallization (Fig. 5.5 B) as illustrated by the progressive lowering of both e-twin and low MAs peaks (Fig. 5.6).

5.7.5   Implications for natural faults

Our experimental work has shown that ultramylonites can develop and have a significant role in controlling fault strength during seismogenic slip under upper crustal conditions. However, in nature, the mylonitic PSZ would experience a more protracted deceleration phase than in the experiments (with lower velocity rate), as the velocity profile of seismic slip along faults follows that of a modified Yoffe function (Fukuyama and Mizoguchi, 2010 and references therein). Hence, it is expected that the lower cooling rates and higher re-strengthening of the fault may produce more brittle damage than observed during the experiments (Stage IV), potentially overprinting/obliterating the coseismic ultramylonite fabric within the PSZ. Liao et al. (2014) show that slow deceleration of the apparatus brings the experimental fault back to friction values in the Byerlee range (> 0.6), which are observed during the cataclastic flow of Stage I.

Arrays of parallel MSs and MSs-bounded cataclasites in seismic natural faults have been described in the published literature (Collettini et al., 2014; Tesei et al., 2013; Siman-Tov et al., 2013). Other authors who performed similar experiments have also suggested that reflective, nanograin decorated surfaces found in exhumed carbonate-hosted faults might form during earthquakes (Fondriest et al., 2013; Siman-Tov et al., 2013; Smith et al., 2013). These microstructures are indeed observed to form in our and their samples (MSs) after high velocity shear deformation. Importantly, other authors have shown that similar microstructures can form even at subseismic slip rates and thus

that cannot be used in isolation as reliable seismic proxies (Verberne et al., 2013; Tesei et al., 2017).

We argue in ch. 4 that MSs are formed during the late stage embrittlement of the PSZ boundaries. It is shown that deceleration of the system produces a pervasive brittle (and possibly plastic) overprint, which is enhanced at lower temperatures (i.e. as seen in lower velocity experiments). In this scenario, it is the hardened sintered layer outside the PSZ which would stand a better chance of being preserved in natural seismic faults. Our results have shown that the sintered layers below the MSs contain important information about the ultramylonite deformation history. In particular, EBSD analysis have been shown to be a powerful tool that can be used to extract further information from microstructures (see also Kim *et al.*, 2018) that may otherwise have been overlooked in previous studies of natural fault rocks. This technique can usefully be employed in the analysis of natural MSs and it may be possible to discriminate whether they formed due to their seismic or aseismic slip, as the EBSD characteristics and patterns of the surrounding sintered regions should show a different slip history in response to different conditions in the PSZ.

5.8 Conclusions

The integration of mechanical data with microstructural observations and EBSD analyses shows that coseismic ultramylonites form in carbonate-hosted faults and follow a complex weakening path. In particular, the weakening of initial calcite micro-gouges when sheared at earthquake slip rates is controlled by the competition between brittle (e.g. cataclastic flow) and viscous creep deformation mechanisms. Therefore, we conclude that:

- Thermally activated grain size sensitive (GSS) and insensitive (GSI) creep mechanisms lead to the formation of coseismic ultramylonites when initial calcite micro-gouges are sheared at extremely high strain rate conditions. Compared to ultramylonites which form deeper in the Earth under lower strain rate conditions, coseismic ultramylonites are only able to form at the nanoscale in order to

accommodate high seismic strain rates at elevated (sub-melting) temperatures generated by frictional heating during slip.

- The combined and simultaneous action of GSI and GSS mechanisms may lead to a grain size piezometric equilibrium in the coseismic ultramylonite PSZ, due to cycles of grain size reduction due to the operation of GSI mechanisms and grain growth driven by thermal processes. The interplay between GSI and GSS creep mechanisms is well known in material sciences from observations, theory and modelling, but modelling diffusion creep coupled to intracrystalline plasticity has been an intractable problem in geoscience, leading to generic uncertainties with flow laws which combine these processes.

- The crystallographic orientations of transient microstructures are preserved in the narrow deactivated layers close to the principal slip zone. Hence, EBSD techniques can usefully be employed in the analysis of microstructures associated with natural mirror-like surfaces, which are preserved in both experimental and exhumed natural faults.

6. Viscous earthquakes: a general constitutive law for the coseismic lubrication of faults

6.1. Foreword

In the previous chapters we have investigated coseismic weakening and associated weakening mechanisms in calcite gouges. However, there is overwhelming evidence that coseismic weakening occurs in experimental faults in many different rock materials. Nevertheless, a general constitutive law is yet missing. Instead, many different deformation mechanisms have been proposed to explain the observed coseismic weakening of experimental faults, most of which are material-dependent. In this chapter we try to tackle this problem using the same experimental approach adopted for calcite gouge experiments to investigate coseismic weakening in a range of common rock-forming materials. Our main aim is to explore whether a unifying constitutive law, describing thermally-activated weakening mechanisms, can be found to account for the coseismic lubrication of faults.

6.2. A generalisation problem

The partitioning of energy during earthquakes plays a dominant role in controlling the propagation of the rupture (Kanamori and Rivera, 2006; Nielsen *et al.*, 2016). Frictional heating produced during fast, seismic sliding along the fault can promote the onset of thermally activated weakening mechanisms that, in turn, contribute to reduce its strength. Fast, efficient weakening occurring in the sliding portion of seismic faults can release elastic strain energy and reduce dissipated energy, promoting slip acceleration and rupture propagation (Nielsen *et al.*, 2016; Kanamori and Rivera, 2006). Therefore, the characterisation and quantification of weakening mechanisms associated with the faulting process has become a crucial study subject in seismology.

Among different theories, flash heating (Rice, 1999; Goldsby and Tullis, 2011) emerges thanks to its general formulation, which specifically considers the energy budget of seismic sliding at the asperity-scale contacts. However, the physics behind this mechanism is related to the concept of load-bearing asperities and does not account for their evolution during slip. At increasing displacements (i.e. large earthquakes), pressures and temperatures, flash heating is likely overcome by other thermally-controlled processes (Di Toro *et al.*, 2011; Goldsby and Tullis, 2011) such as frictional melting (common in silicate rocks; Di Toro *et al.*, 2006) or thermal pressurisation (in presence of fluids initially present in the fault or released by thermal decomposition processes; Rice, 2006). An alternative weakening mechanism has been recently described in seismic shear experiments in carbonate gouges. Microstructural investigations have revealed the development of a narrow (< 100 µm) shear zone made of uniformly fine grained (< 1 µm) rock, which deforms in a ductile fashion by creep mechanisms (Green *et al.*, 2015; De Paola *et al.*, 2015; Pozzi *et al.*, 2018). However, a unifying law describing the ubiquitous thermal weakening observed for different rock types during coseismic slip is still lacking.

6.3.   Experimental procedure and results

Twenty-one friction tests were performed on a low to high velocity shear apparatus at Durham University (see Ch. 2.1). We have chosen to test powders of both silicate and non-silicate, anhydrous rock materials commonly found in upper crustal settings and showing different types of crystalline bonds: calcite and dolomite (carbonates), anhydrite (sulphate), sodium halide (chloride, an ionic compound) and olivine (silicate). Our goal here is to characterize their weakening mechanisms other than frictional melting, which is already known to follow an Arrhenius-type formulation (Nielsen *et al.*, 2008). The experiments were run at conditions that are less favourable to flash heating and thermal pressurization. Deformation within finely powdered fault rocks (gouges), which are a common occurrence in natural fault cores (Sibson, 1977), is known to diminish the efficiency of flash heating processes (Goldsby and Tullis, 2011; Brantut and Platt, 2017). In fact, the weakening velocity is directly proportional to the number of
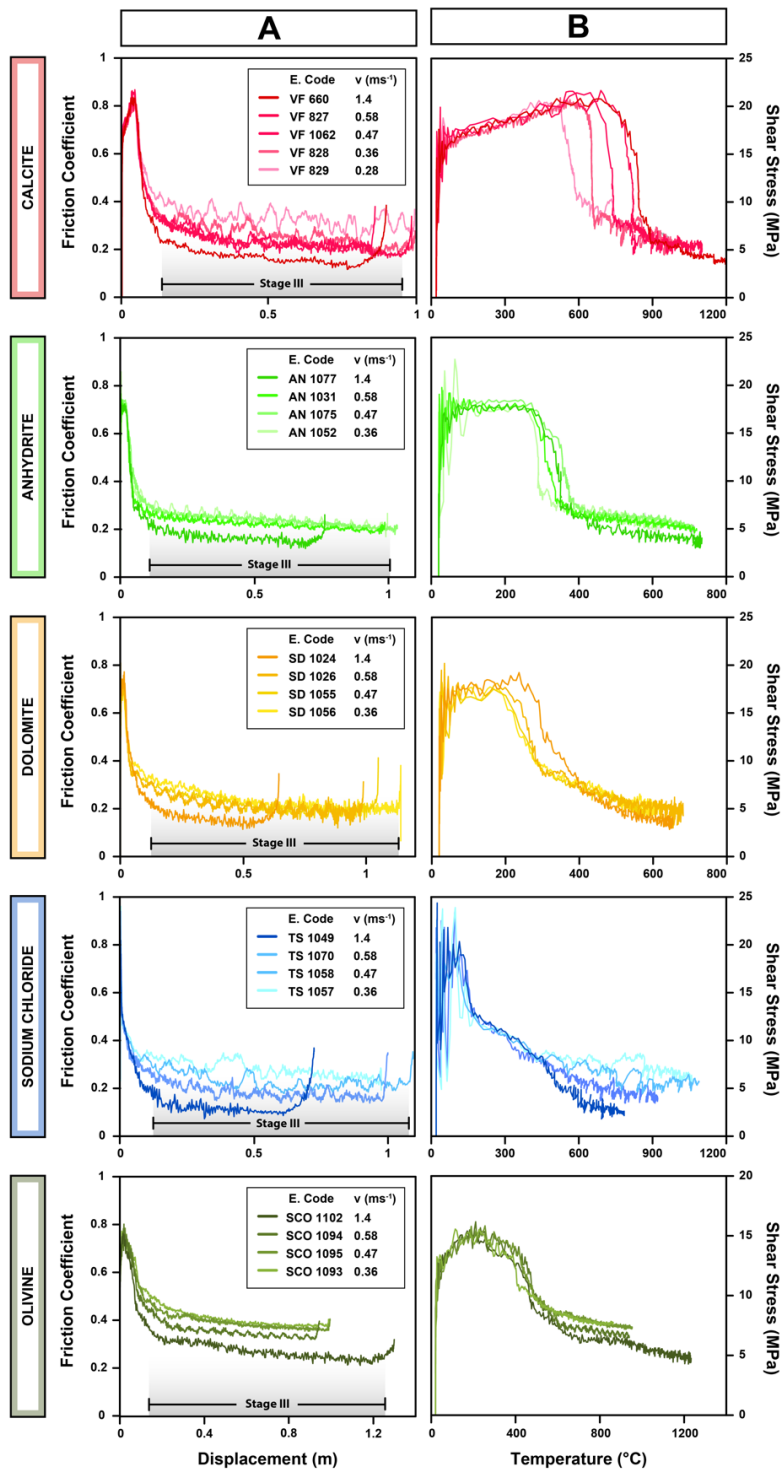
Figure 6.1 *|A) Friction coefficient evolving with displacement during Stages I - IV (see text for details). During Stage III, friction coefficient values are lower in experiments run at higher velocities. Each experiment terminates with partial re-strengthening during deceleration to arrest. B) Shear stress plotted against calculated temperature (up to stage III). Notably, the Stage III mechanical data of calcite, dolomite and anhydrite plot collapse on the single material-characteristic curve. Sodium chloride curves overlap up to a temperature of ~440° C.*

contacts mobilised across the gouge (see Ch. 1.3.2). Similarly, the tests were performed at room humidity conditions and for small amounts of slip, to diminish the efficiency of thermal pressurization by minimising fluids present or released in the gouges by thermal decomposition of the initial materials (De Paola *et al.*, 2015; Pozzi *et al.*, 2018).

A normal stress of σ_n = 25 MPa (20 MPa for olivine) was applied to the samples, and held constant throughout the tests. The samples were then sheared at different seismic velocities (0.36 to 1.4 ms^{-1}) for ~1 m of total slip per run. Details for each experiment are reported in Appendix I. This method allowed sufficient displacement to observe fault evolution beyond the stage of active flash heating (Goldsby and Tullis, 2011), but still not large enough to produce significant thermal decomposition, frictional melting and other physical changes in the rocks (De Paola *et al.*, 2011; Pozzi *et al.*, 2018).

For each experiment, the friction coefficient μ (i.e. the shear stress normalised by the normal stress) follows a classic weakening profile (Fig. 6.1 A; Pozzi *et al.*, 2018). Initial slip hardening in the Byerlee's range (Stage I; μ = 0.6-0.9) – almost absent in sodium chloride – is followed by an abrupt decay of fault strength to low friction values (Stage II; μ < 0.4). Friction then remains low at dynamic conditions and constant velocity, showing a slow decay with slip (Stage III in Fig. 6.1 A). Partial re-strengthening is associated with the final deceleration and arrest of the sample (Stage IV). The bulk temperature in the principal slip zone (PSZ) cannot be measured during the experiment, and is obtained using an equation for one-dimensional thermal diffusion (Rice, 2006; See Ch. 2.4 for details). Estimated temperature values are plotted against shear stress values in Fig. 6.1 B. For all tested materials, the segments corresponding to the low stress values attained during Stage III of each experiment collapse on the same material-dependent curve (Fig. 6.1 B).

6.4. Microstructures

After each run, samples were carefully recovered and cross-sections were prepared for microstructural analysis. Fig. 6.2 shows SEM images (using fore- and back-scattered modes) of four selected experiments. In all experiments, we observe a principal slip zone
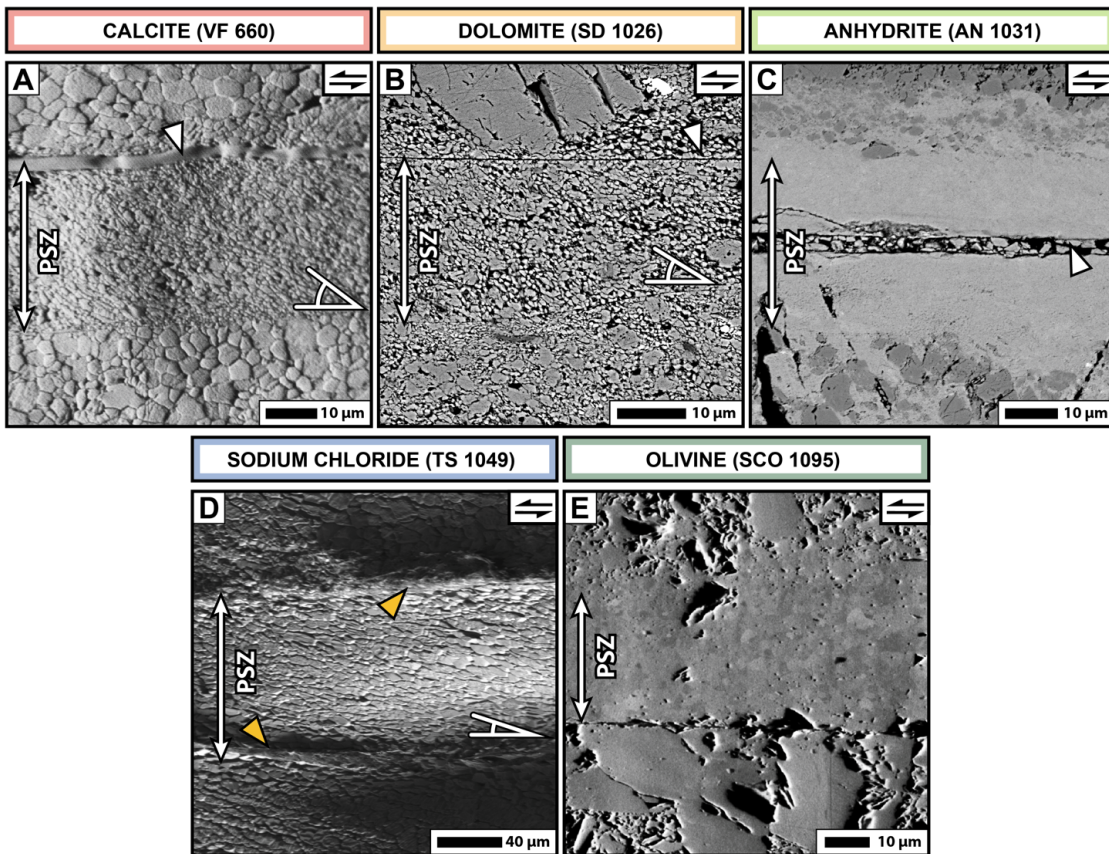
Figure 6.2 | *Fore-scattered (A,E) and back-scattered (B-D) SEM images of sample principal slip zones (PSZ) in polished cross sections cut parallel to the slip direction. In a, b and d the oblique (white angle) ultramylonitic foliation is visible. White arrows point to the splitting of the sample after the experiments along the mirror-like surfaces at the boundary of the PSZ (Pozzi et al., 2018). Such fractures are locally exploited by the impregnating agent used for preparation (white arrow in panel A). Yellow arrows highlight melt patches (ridges) at the margins of the PSZ in sodium chloride. Shear sense is top-to-the-left in all images.*

(PSZ) with a finite thickness of a few tens of microns (Fig. 6.2). The PSZs are characterised by extremely low porosity, fairly homogeneous grain size, grains displaying triple junction type contacts and oblique foliation (Pozzi *et al.*, 2018). Notably, these textures are similar to those of some natural (Trouw *et al.*, 2010) and experimental monomineralic ultramylonites. Recent analysis of PSZs in calcite gouges revealed that deformation during Stage III slip is controlled by grain size sensitive creep mechanisms,

106

most likely diffusion-accommodated grain boundary sliding (De Paola *et al.*, 2015; Green *et al.*, 2015; Pozzi *et al.*, 2018). Importantly, microstructural observations from all other materials tested here support the hypothesis that co-seismic deformation is accommodated by viscous processes at sub-melting temperatures. Sodium chloride additionally shows the onset of melting with the formation of small melt patches overprinting the ductile texture (yellow arrows in Fig. 6.2 D).

6.5. Discussion

Microstructural analyses on calcite experiments (Pozzi *et al.*, 2018) suggest that the PSZ accommodates almost all of the shear deformation, and it does not vary in thickness throughout Stage III. Therefore, at this stage, each experiment can be considered to run at constant strain rate. The curves shown in Fig. 6.1 B can be replotted in an Arrhenius space as the natural logarithm of shear stress versus the inverse values of temperature (Fig. 6.3 B). Stage III segments form – to a good approximation – straight lines which share the same trend (thick dark lines in Fig 6.3 B).

Exponential regression allows the calculation of Stage III fault strength dependence on temperature, which can be rearranged to follow the equation

$$ln(\tau) = A\frac{1}{T} + B \qquad (6.1)$$

where A and B are best-fit constants. The specific equations for each material and the material-dependent curves are reported in Fig. 6.3 B. Creep mechanisms typical of ductile deformation share a similar exponential relationship following the constitutive equation (Kohlstedt, 2007)

$$\dot{\gamma} = C^* \frac{\tau^n}{D^m} e^{-\frac{Q}{RT}} \qquad (6.2)$$

where $\dot{\gamma}$ is the strain rate, C^* is the pre-exponential constant, D is the mean grain size, n and m are the stress and grain size exponents, respectively, Q is the activation energy and R is the gas constant. Eq. 6.2 can be rearranged to

$$ln\ (\tau) = \left[\frac{Q}{nR}\right]\frac{1}{T} + \left[\frac{1}{n}\ ln\left(\dot{\gamma}\ \frac{D^m}{C^*}\right)\right] \quad (6.3)$$

which is directly comparable to Eq. 6.1.

The slope A in Eq. 6.1 is then a function of the stress exponent *n* and the activation energy *Q* (Eq. 6.3). In our case, quantification of the parameters *Q* and *n* from the temperature dependence of strain rate at constant stress (Poirier, 1985) is not possible. This is due to the fact that strain rate, stress and temperature cannot be independently controlled by the operator during the experiments, although they can be calculated. At the same temperature and stress conditions (Fig. 6.3), different velocities are associated with completely different strain rates. In fact, the measured thickness of the PSZ (W_{PSZ}) is smaller at higher velocities (see Ch. 3; Pozzi *et al.*, 2018), implying higher strain rates, as $\dot{\gamma}_{PSZ} = v/2W_{PSZ}$. Although the stress exponent *n* cannot be inferred from the best fit line as a consequence, it will have positive correlation with the activation energy *Q*. From the literature it consistently emerges that lower values of *n* in creep of polycrystalline calcite aggregates correspond to lower activation energies Q (in the range of 200 and 300 kJ; De Paola *et al.*, 2015; Schmid *et al.*, 1977).

The intercept B in Eq. 6.1, contains geometric variables such as strain rate (dependent on the velocity and width of the PSZ) and grainsize, which can be measured in post-mortem samples. However, the term *B* cannot be used to quantify the grain size exponent *m* and pre-exponential factor *C**, which are intimately linked in the formulation. In fact, at constant strain rate during Stage III, the grain size in the PSZ is observed to grow with temperature while stress is slowly decreasing (Pozzi *et al.*, 2018). However, grain size and stress are positively correlated and thus other variables (*C**, *m* and *n*) must change as well during the experiment.

These observations collectively suggest that the fault stress is mainly controlled by the temperature according to an Arrhenius type law, while the interplay and relative dominance of creep mechanisms with different nature (Ch. 5) adjust to the evolving conditions. The result is the co-variance of the bulk parameters (e.g. activation energy and stress exponent), which represent the macroscopic and averaged effect of all mechanisms involved. Therefore, Eq. 6.2, originally formulated for creep at low strain

rates in which parameters are essentially constant, fails to describe high-strain rate, coseismic deformation. Linear fit of experimental data and microstructural observations point out to a mixed rheology of the rocks at high strain rates, in which the bulk geometrical and thermodynamic parameters are interdependent and strongly modulated by the local temperature.

Slightly different behaviour may be observed with olivine experiments (Fig. 6.3), where a slope change is observed when temperatures exceed 900°C (Fig. 6.3 B, best fit olivine 2). It is interesting to note that such temperatures values correspond to the homologues temperature T = 0.5 Tm of forsterite (Poirier, 1985), where the melting temperature of fosterite Fo$_{100}$ T_m = 1896 °C (Wang et $al.$, 2016). The homologues temperature of a crystalline material has been widely used to compare the creep strength of crystalline materials (Poirier, 1985). This may suggest that during the early
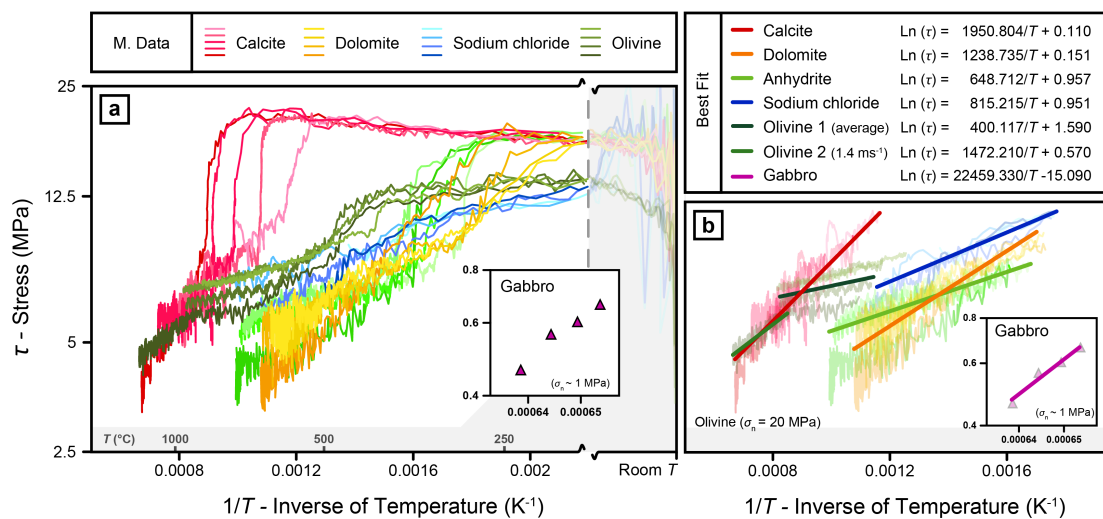

Figure 6.3 | (Previous Page) A) Data presented in Fig. 6.1 is rearranged here in an Arrhenius space (natural logarithm of shear stress vs the inverse of temperature). B) When the fault strength is weak, the mechanical data of each experiment falls on a material-dependent, characteristic straight line. The best fit equation is reported on the graph for each material.

stages of weakening in olivine gouges, when T < 0.5 T$_m$, deformation is not purely accommodated by creep processes but also by temperature insensitive brittle mechanisms, such as such as dilatancy in granular flows (Hutter and Rajagopal, 1994). This mechanism is dominant when temperature is low (e.g. stage I to stage II; De Paola *et al.*, 2015; Smith *et al.*, 2015; Pozzi *et al.*, 2018) and may still affect the mechanical response during stage III of materials with slower creep kinetics such as olivine (Thieme *et al.*, 2018) and dolomite.

We propose that during co-seismic slip, the PSZ properties are controlled by grain-scale deformation processes that allow for minimisation of the power dissipation, i.e. the total rate of viscous strain energy dissipated within the fault. This is similar to what postulated for heterogeneous slip in natural mylonites of ductile, aseismic shear zones active in the lower crust. If deformation is entirely accommodated in the PSZ, the power dissipation (per unit fault area) will be $\dot{E}_{tot} \cong \tau\,\dot{\gamma}_{PSZ}$. Therefore, localisation processes and stress drops – affecting the viscosity – are likely controlled by a balance between heat production by viscous dissipation and removal by thermal diffusion and endothermal processes. As demonstrated by our experiments, stress monotonically decrease with increasing temperature and steady state conditions would then be achieved only when a stable temperature profile is set across the fault, similar to the case of frictional melting in pseudotachylytes (Nielsen *et al.*, 2008).

6.6. Conclusions

To summarize, different materials commonly found in natural rocks in the crust – calcite, dolomite, anhydrite, halite and olivine – were tested in shear experiments performed at seismic slip velocities. Each material shows dramatic weakening to low friction values, which remain low as long as high-velocity slip is maintained. Weakening is associated to the development of a well-defined PSZ, with finite thickness, and displaying textures typical of sub-solidus viscous flow. These texture are similar to those found in natural ultramylonites of aseismic, ductile shear zones. During this stage, the strength of the experimental fault follows an Arrhenius-type temperature dependence,

which is material-specific and can be characterized using the general Eq. 6.1. Affinity with the classic constitutive flow law for creep (rearranged in Eq. 6.3) and microstructural evidence suggest that weakening is controlled by creep mechanisms. Eq. 6.3 cannot be used to quantify the creep variables due to the non-steady state conditions of the PSZ. However, we suggest that the macroscopic strain rate, grain size and creep exponents – which are the expression of the interplay and the evolution of multiple creep mechanisms – are subordinate to the effect of temperature. We propose that they adjust conjunctly to contribute to an energetic balance within the PSZ, evolving toward the minimization of power dissipation and achievement of steady-state values.

In conclusion, coseismic lubrication of faults appears to be controlled by sub-solidus viscous processes, according to a material-dependent, Arrhenius-type constitutive equation. The affinity of sub-solidus viscous flow with melt lubrication, common in silicate rocks, strengthens the hypothesis that most rocks behave similarly, and independently of their composition, when strongly dissipative processes are involved.

I believe that these results offer an alternative, quantitative viewpoint of fault friction-controlling processes, and might open new frontiers for the study of overlooked, ubiquitous ductile processes active along faults at seismic strain rates.

7. Discussion and Conclusions

7.1. Coseismic weakening: towards a unifying approach?

The coseismic weakening of faults is a fundamental process that controls the energy partitioning during earthquake propagation (Kanamori and Rivera, 2006; Nielsen et al., 2016). The drop in strength in the slipping portion of the fault allows the transfer of elastic stress from the faulted body to the very rupture tip, thus enhancing the efficiency of coseismic rupture propagation (Fig. 7.1). Reduced friction coefficients have been measured in every rock deformed in shear experiments at high, seismic velocities (> 0.1 ms^{-1}, Di Toro *et al.*, 2011).
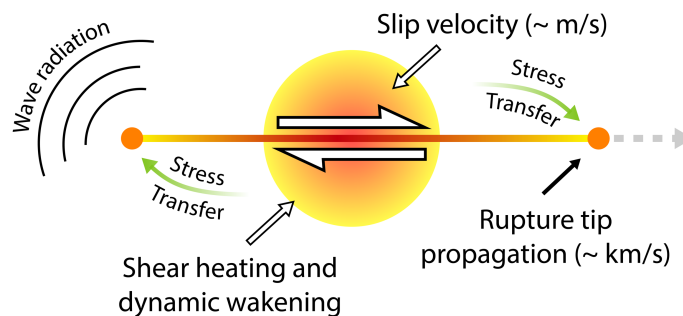
Figure 7.1 | *Schematic representation of the relationships between the actively slipping portion of a fault and rupture propagation at its tip. Coseismic temperature rise, due to shear heating in the slipping zone, can activate dynamic weakening mechanisms and cause fault lubrication. This eases rupture tip propagation.*

It has been argued that the ubiquity of the weakening behaviour of experimental faults is of thermal origin (Rice, 2006), and almost all of the dynamic weakening proposed are controlled by the temperature rise due to frictional heating. Indeed, temperature rises significantly (often higher than 1000 °C) during earthquakes due to

frictional heating, especially during the initial stages of deformation when the rock is still strong. As a consequence, friction is reduced almost to zero when slip velocities approach those typical of natural earthquakes (> $1ms^{-1}$, Di Toro *et al.*, 2011). Despite this being a convenient factuality that is directly applied to, for instance, large-scale modelling of geodynamic processes, the intrinsic nature of such behaviour remains somewhat still debated and poorly understood.

In the previous literature (as well as in the first part of this thesis) a great variety of physical and conceptual models have been proposed to explain the past decade of experimental work, and different weakening mechanisms have been proposed for different rock types. For instance, the physics of melt lubrication mechanisms (e.g. in silicate rocks) enjoy solid mathematical treatise (Nielsen et al., 2008), as well as being well constrained by evidences from natural seismic faults (Di Toro *et al.*, 2006a), while the physics of powder lubrication mechanisms (e.g. in carbonate rocks) is poorly understood beyond simplistic conceptual models (Reches and Lockner, 2011), which are based mostly on microstructural observations (Han *et al.*, 2010). Furthermore, some lithologies such as carbonate rocks have received lots of attention with a variety of mechanisms proposed to explain the same observed weakening behaviour during experiments (see Ch. 1).

In this thesis I tried to explore the case study of coseismic weakening of calcite gouges, by integrating direct measurements of mechanical data with microstructural observations and EBSD analyses on post-mortem samples, with indirect acoustic emission datasets recorded during the experiments. Then, my findings were extended to case studies of other rock-forming minerals. The final aim was to bring new experimental evidence able to shed some light on the common controls, if any, which govern the physics of coseismic weakening.

7.2.   From cataclasis to viscous flow during earthquakes

The main body of evidence in this thesis focuses on the systematic study of coseismic weakening of calcite gouges sheared during high velocity friction experiments. As in

113

previous studies, gouges were prepared and mounted in a rotary shear apparatus, sheared, and then samples were removed carefully for microstructural analysis (see Ch. 2). The link between mechanical data and microstructures, which are recovered from experiments run at different amounts of slip, has allowed investigating the evolution of the mechanisms during fault weakening. In previous studies, some authors have discussed the role played by thermal decomposition and powder lubrication (Han *et al.*, 2010), flash weakening or even crystal plasticity (e.g. Kim *et al.*, 2010; Siman-Tov *et al.*, 2015; Smith *et al.*, 2015), including ductile processes such as diffusion assisted grain boundary sliding (Green *et al.*, 2015; De Paola *et al.*, 2015). Indeed, the prominent characteristic observed by each previous author is the formation of reflective surfaces, also referred to as "mirror-like surfaces" (MSs), along which the sample easily splits (see Ch. 3, Fig. 3.9 A). Analyses from previous authors were then mostly performed on one of the two halves of the sample, which were decorated on one side by MSs. MSs were then interpreted as frictional sliding surfaces or principal slip surfaces (e.g. Siman-Tov et al., 2015; Smith et al., 2015). It must be noted that observation of MSs are rather common in natural exhumed faults (Hancock and Barka, 1987; Siman-Tov et al., 2013), and these features have been also linked to/interpreted as evidence of past seismic slip (Siman-Tov, 2013; Smith et al., 2015; Fondriest et al., 2013).

Compared to previous studies, in my work, microstructural observations were collected from sample whose full thickness was recovered after the experiments (e.g. containing both the top and bottom imprints of the roughened steel cylinder of the sample assembly). My observations show that, after weakening has been achieved, deformation is mostly accommodated within a principal slip zone (PSZ) with finite thickness, separated from the surrounding layers by sharp boundaries. These boundaries are marked by a sharp textural transition from the fine-grained PSZ and the coarse, sintered outer layers. Frequently, the sintered layers show brittle damage and tend to split revealing a grooved MS. To a close inspection, the outer layers host several generations of sub-parallel PSZ boundaries, which suggest successive steps of localisation. The PSZ preserves characteristics of ductile flow, as shown by tightly packed structure, homogeneous grainsize, oblique foliation (Fig. 7.2 A). Such microstructures
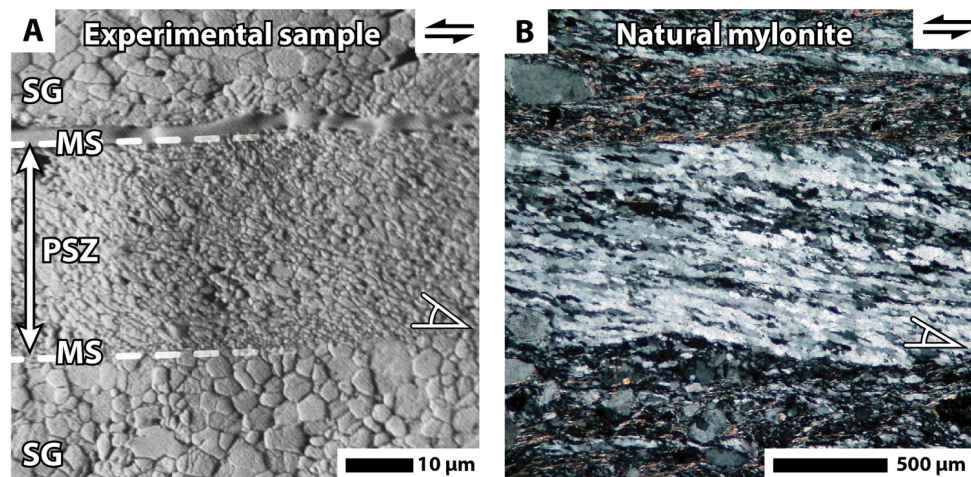
Figure 7.2 | A) *Forescattered electron image of the principal slip zone (PSZ) produced in calcite gouges sheared at high velocity (VF 660, v = 1.4 ms^{-1}, σ_n = 25 MPa, δ = 90 cm). PSZ displays tightly packed structure, fairly homogeneous grain size (~700 nm) and oblique foliation (white angle). Sharp grain-size transition is observed at the PSZ boundaries. Outside the PSZ, sintered layers (SG) have a coarser grainsize (> 3µm). Textures inside and outside the PSZ are clearly asymmetric with respect to the mirror-like surfaces (dashed lines, MS) found along the PSZ boundaries. B) Natural quartz ultramylonite (Trouw et al., 2010) displaying textures typical of sub-solidus ductile flow: tightly-packed structure, fairly homogeneous grainsize and oblique foliation (white angle).*

are typically found in natural (e.g. Fig. 7.2 B) and experimental ultramylonites (e.g. Herwegh and Kunze, 2002; Barnhoorn et al., 2004; Trouw *et al.*, 2010), which were believed to be exclusive of high-temperature and low-strain rates deformation regimes.

Some novel microstructural observations show the presence of a textural asymmetry across the PSZ boundaries (e.g. MSs), as the grainsize is much smaller in the material located in the PSZ than in the material located in the adjacent sintered layer on the other side of the MSs (Fig. 7.2 A). These observations conflict with the hypothesis that MSs are frictional sliding surfaces, as sintered layers of coarse grainsize should develop on both sides of the sliding MSs, due to frictional heating. On the other hand, the observations of sintered outer layers on both sides of the PSZ and the PSZ textures itself suggest that deformation is mostly accommodated within the PSZ finite thickness, i.e. a discrete volume, not a surface. These interpretations are also supported by the activity of

acoustic emissions (AE) recorded throughout the experiments (see Ch. 4). In fact, the experimental fault stays relatively "silent" when its strength is low, while peaks of acoustic emissions are recorded during the latest stages of re-strengthening to stop and successive rapid cooling. These regimes can be associated respectively to the viscous nature of the PSZ (aseismic) and successive embrittlement causing the typical brittle overprint during the latest, decelerating stages of deformation and during the post-sliding cooling phase. Since it is observed that grainsize is homogeneous and small within the PSZ (Fig. 7.2 A), we also suggest that the material is deforming by grainsize sensitive creep processes, in good agreement with previous interpretations in De Paola *et al.* (2015) and Green *et al.* (2015).

Crucial for the evolution of a ductile PSZ is the pre-localisation processes observed during the initial stages of deformation. Soon after the onset of slip, when the fault is strong and shows slip-hardening behaviour, the PSZ starts forming as a thin brittle shear band, where extreme cataclastic comminution reduces the grainsize while local temperatures are rising. The onset of weakening by viscous flow is then facilitated in the pre-comminuted, hot medium. Indeed, the relevance of brittle precursors to ductile shear bands is well known from natural (e.g. Guermani and Pennacchioni, 1998; Mancktelow and Pennacchioni, 2005) and experimental examples (e.g. Tullis *et al.*, 1990).

To summarize, coseismic weakening in calcite-hosted faults is achieved throughout a complex weakening history where a brittle precursor of the PSZ evolves rapidly, but gradually, to become a ductile PSZ, dominated by grainsize sensitive creep processes. The evolution from brittle cataclasis to viscous flow is critical to the understanding of the onset of dynamic weakening processes observed in experimental seismic faults in calcite gouges. I believe that another outstanding observation is that the PSZ will not continue to localise, but instead will achieve a steady-state thickness after a certain amount of slip and related temperature rise. This information has given a fundamental clue about the operation of subsolidus viscous deformation weakening mechanisms, which may control the strength of seismic faults.

7.3. Coseismic ultramylonites

Microstructures found in the ductile PSZ do not differ substantially from those found in natural ultramylonites (Fig. 7.2, e.g. Herwegh and Kunze, 2002; Trouw *et al.*, 2010), i.e. textures developed in shear zones deforming mainly by sub-solidus viscous processes. However, the question whether the same mechanisms are viable ones to accommodate deformation at such extreme coseismic strain rates, which can exceed values of 10^4 s^{-1}, raises spontaneously. Mylonites are in fact considered to be exclusive of deep settings, where aseismic slow deformation is accommodated by strain rate-, temperature- and grainsize-dependent viscous mechanisms (e.g. dislocation and diffusion creep). In order to investigate the weakening mechanisms operating in the PSZ of my experiments, we performed textural analysis using electron microscopy techniques. Electron backscattered diffraction (EBSD) at the scanning electron microscope (SEM) allows to measure the preferred orientation of grains (CPO) within the rock samples and to assess its relationship with the stress field. Transmission electron microscopy (TEM) allows to investigate the sub-crystalline structure affected by deformation processes.

The results obtained from EBSD analyses well match the multistage weakening history reconstructed from microstructural analysis. It is observed the evolution of textures from brittle cataclasis, corresponding to almost random orientation of grains (extremely weak CPO), to the onset of weakening, corresponding to a highly ordered (strong CPO) texture within the PSZ (Fig. 7.3). Textures then evolve to a lower grade of ordering, when the PSZ microstructure has homogenised (Fig. 7.3). Outstandingly, such textures are well known to occur in experiments performed at much lower strain rates (Barnhoorn et al., 2004), in natural mylonites (Bestmann et al., 2000) and are also predicted by theoretical studies (Wenk et al., 1987). The integration of our results and those form various previous studies suggests that an initial brittle regime was followed by viscous deformation dominated initially by grain size insensitive creep (GSI, i.e. dislocation-creep) and, then, by grain size sensitive creep (GSS, i.e. diffusion assisted grain boundary sliding) mechanisms (Fig. 7.3). TEM analysis corroborates these interpretations by showing the activity of dislocations within the tightly-packed grains of the PSZ.
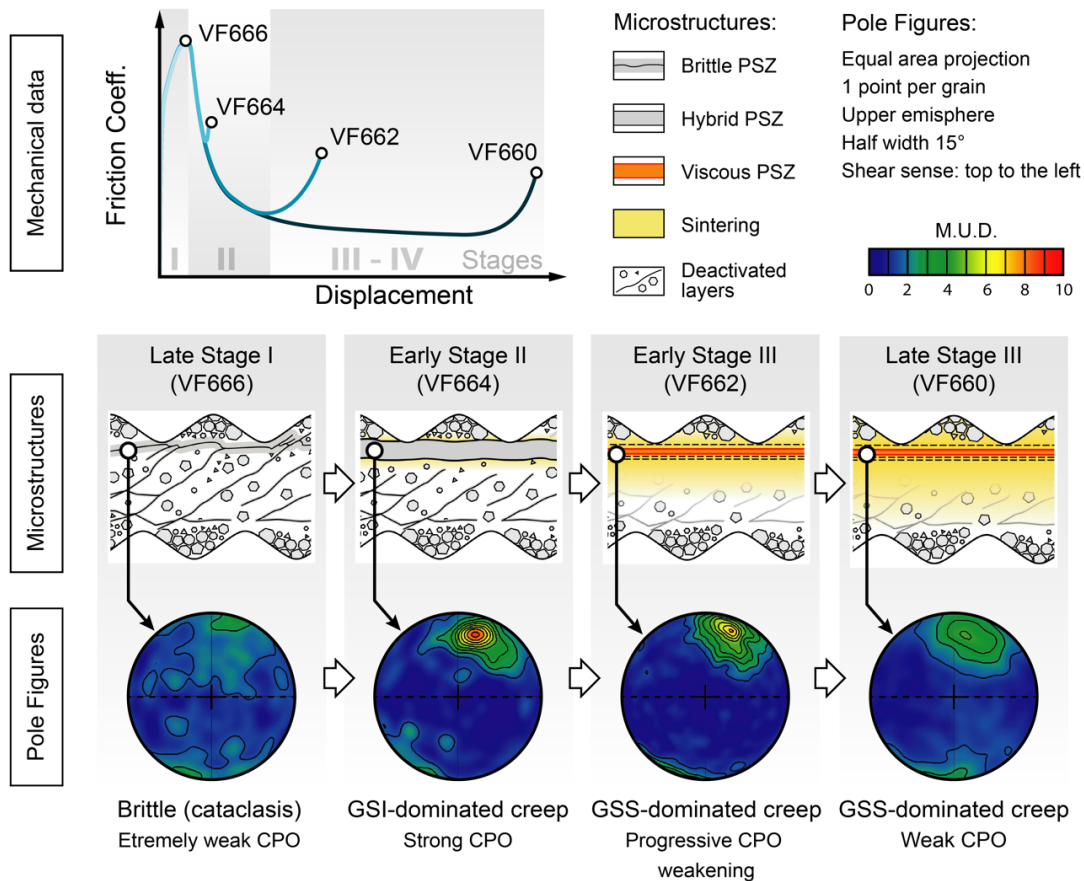
Figure 7.3 *| Schematic diagram of the evolution of mechanical data, microstructures and preferred orientation of grains in the PSZ, observed in high-velocity shear experiments of calcite gouges (σ_n = 25 MPa and v = 1.4 ms^{-1}). Pole figures of the calcite c axis show the evolution of the crystal preferred orientation (CPO) throughout the weakening history (see Ch. 5). Higher M.U.D. values (orange to red) correspond to a highly ordered texture, i.e. strong CPO. A strong CPO is related to the activity of grainsize insensitive creep (GSI) mechanisms (e.g. dislocation creep) while a weak CPO can be related to brittle granular flow (e.g. cataclasis) or, in case of progressive weakening, to the activity of grainsize sensitive creep (GSS) mechanisms (e.g. diffusion-assisted grain boundary sliding). Stages I-IV are described in detail in chapters 3 to 5.*

Such deformation style, again, is similar to that observed at much lower strain rates, and suggests that the coseismic PSZ is indeed a (ultra-) mylonite. Our evidences suggest that fault strength is controlled at dynamic conditions by the competition between (at least) three mechanisms: (i) dilatant and temperature-independent granular flow (i.e. brittle deformation, dominant at the beginning of the experiment), (ii) GSS creep and

118

(iiI) GSI creep, which concur in determining the textural characteristics observed in the principal slip zone.

In conclusion, I show evidence that the PSZ material deformed during my experiments at seismic slip rates is an extremely fine-grained (grainsize < µm) ultramylonite, suggesting that processes occurring during seismic slip might not be that different from those observed at much lower strain rate in aseismic shear zones active in the lower crust. However, the main difference could be that deformation processes in coseismic ultramylonites must operate at the nanoscale and produce extremely localised, comminuted textures.

7.4. Viscous Earthquakes

In the first chapters of this thesis, we have shown that subsolidus viscous deformation can be a viable dynamic weakening mechanism of calcite gouges. In the last chapter, however, we wanted to broaden our findings by characterising the dynamic weakening mechanisms of other relevant rock-forming minerals.

The experimental observation in Di Toro *et al*. (2011) that fault strength drops toward zero for each rock tested at seismic slip rates, has been so far ascribed to the role played by shear heating in activating a variety of material-dependent weakening mechanisms. Indeed, grain size sensitive creep proposed to explain the dynamic weakening of calcite gouges is a temperature-controlled mechanism. The evolution of shear stress measured during my calcite gouge experiments show a clear dependence to local PSZ temperatures and can be easily fitted using an Arrhenius-type equation. Frictional melting mechanisms enjoy a similar Arrhenius-tupe dependence (Nielsen *et al.,* 2008; Philpotts and Ague, 2009). It is worth noting that Arrhenius type processes are widespread in nature, and it should come with no surprise that, in an environment characterised by fast temperature rise, either sub-solidus (mylonites) or super-solidus (pseudotachylytes) viscous flow can lubricate seismic faults. However, beside this parallelism found with calcite gouges sheared at seismic slip rates, can these findings be applied to other materials?

We explored this hypothesis by performing a set of experiments following the same procedure as for calcite gouge experiments. Powders of five rock-forming minerals were chosen, belonging to different mineralogical classes: carbonates (calcite and dolomite), sulphates (anhydrite), halides (halite) and silicates (olivine). Each mineralogical class is characterised by different atomic bonds, hardness and chemical behaviour. We decided to avoid hydrated phases and to keep the experiments as short as possible to minimise the kick-in of buffering reactions (such as dehydration and decarbonation), which would affect our temperature estimate. With little surprise, the fault strength dropped to low, shear-rate dependent values for all of the tested materials. However, it was very interesting to note that the evolution of the shear strength with temperature (when the fault is weak) showed a clear linear trend in the Arrhenius space (Fig. 7.4). The outcome of these results is that the coseismic strength of each of the tested materials is controlled by weakening mechanisms with Arrhenius-type dependency to temperature.
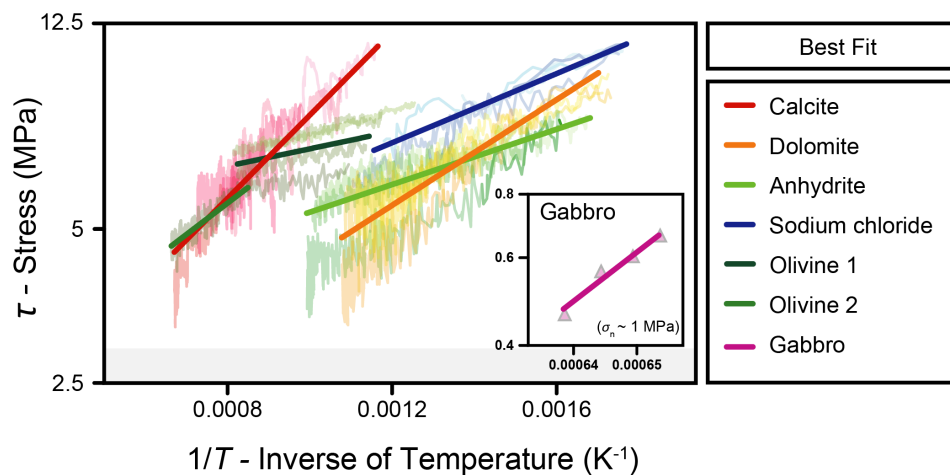

Figure 7.4 *| This Arrhenius-type graph shows the evolution with temperature (increasing to the left) of shear stress values measured during high-velocity shear experiments in a range of different materials. The best fit of data collected when the fault is weak produces straight lines.*

120

The next question to ask is whether the observed weakening is due to a single, unifying mechanism or to multiple weakening mechanisms characteristic of each material? Microstructural analysis reveals that each material develops a clearly defined PSZ with finite thickness. Again, deformation is not accommodated along a single sliding surface, but rather in a well-defined shear zone with more or less well-developed ductile textures (i.e. reduced porosity and oblique foliation). If the behaviour is then similar to that inferred for calcite, shear localisation does not reduce the PSZ to a singularity, i.e. a sliding surface. Therefore, PSZ thickness and shear stress determine the viscosity of the deforming material and evolve to achieve steady state conditions. The dynamic equilibrium towards which the system evolves is driven by the minimisation of the dissipated strain energy, achieved through the balance between heat production and dissipation. This concept was developed for ductile flow in natural mylonites (Handy, 1994), where shear localisation plays a foremost role.

Furthermore we observed that, independently of the PSZ width (directly related to the strain rate) and grain size, the dynamic fault strength seems dominantly controlled by temperature. This suggests that, as long as textures are allowed to evolve without external constraints (i.e. spontaneous localisation), creep mechanisms evolve conjointly to favour energetic balance within the PSZ.

Our results show that the first approach to the analysis of deformation mechanisms at extreme strain rates yields an almost naive message: the system evolves to minimise the dissipation of energy and spontaneously moves towards thermal equilibrium.

7.5. Concluding remarks

In this thesis I conducted an experimental study of the coseismic weakening of simulated fault gouges, starting from carbonate-hosted faults and extending the approach to the generalised case of other natural materials. I have found that the fundamental relationship that links shear stress to temperature, the main controlling

parameter, has an Arrhenius-type formulation. Despite the similar Arrhenius-type behaviour shown at high slip rates, the rate of weakening appear to be material-dependent. Owing to this observation and evidences from microstructural analyses, we suggest that the nature of coseismic deformation is viscous, accommodated by either sub-solidus or super-solidus viscous mechanisms.

The findings from our case study can be further extended during future research, which should aim at exploring the quantification of the described processes. However, we have shown that careful removal of microstructures may become a game changer for this purpose since fundamental variables such as strain rate, grain size and porosity are "easily" accessible. The next step is therefore a more reliable quantification of stress and temperature values, which have been not measured but calculated so far.

Once obtained, the physical variables can be used to tune a model for viscous deformation at high strain rates where different creep mechanisms conjointly affect the bulk rheological response of the deforming PSZ. This approach might also provide a new tool to model deformation of faults and earthquakes in a continuum using rigorous and non-empirical constitutive, physical laws.

References

Abercrombie, R. E., McGarr, A., Di Toro, G. and Kanamori, H. (2013) Earthquakes: Radiated Energy and the Physics of Faulting, Earthquakes: Radiated Energy and the Physics of Faulting. Edited by R. Abercrombie, A. McGarr, H. Kanamori, and G. Di Toro. Washington, D. C.: American Geophysical Union (Geophysical Monograph Series). doi: 10.1029/GM170.

Amato, A., Azzara, R., Chiarabba, C., Cimini, G. B., Cocco, M., Di Bona, M., Margheriti, L., Mazza, S., Mele, F., Selvaggi, G., Basili, A., Boschi, E., Courboulex, F., Deschamps, A., Gaffet, S., Bittarelli, G., Chiaraluce, L., Piccinini, D. and Ripepe, M. (1998) 'The 1997 Umbria-Marche, Italy, earthquake sequence: A first look at the main shocks and aftershocks', Geophysical Research Letters. John Wiley & Sons, Ltd, 25(15), pp. 2861–2864. doi: 10.1029/98GL51842.

Archard, J. F. (1959) 'The temperature of rubbing surfaces', Wear, 2(6), pp. 438–455. doi: 10.1016/0043-1648(59)90159-0.

Ashby, M. F. and Verrall, R. A. (1973) 'Diffusion-accommodated flow and superplasticity', Acta Metallurgica, 21(2), pp. 149–163. doi: 10.1016/0001-6160(73)90057-6.

Avouac, J. P., Meng, L., Wei, S., Wang, T. and Ampuero, J. P. (2015) 'Lower edge of locked Main Himalayan Thrust unzipped by the 2015 Gorkha earthquake', Nature Geoscience. Nature Publishing Group, 8(9), pp. 708–711. doi: 10.1038/ngeo2518.

Barnhoorn, A., Bystricky, M., Burlini, L. and Kunze, K. (2004) 'The role of recrystallisation on the deformation behaviour of calcite rocks: Large strain torsion experiments on Carrara marble', Journal of Structural Geology, 26(5), pp. 885–903. doi: 10.1016/j.jsg.2003.11.024.

Beeler, N. M., Tullis, T. E. and Goldsby, D. L. (2008) 'Constitutive relationships and physical basis of fault strength due to flash heating', Journal of Geophysical Research: Solid Earth, 113(1), p. B01401. doi: 10.1029/2007JB004988.

Bestmann, M., Kunze, K. and Matthews, A. (2000) 'Evolution of a calcite marble shear zone complex on Thassos Island, Greece: Microstructural and textural fabrics and their kinematic significance', Journal of Structural Geology, 22(11–12), pp. 1789–1807. doi: 10.1016/S0191-8141(00)00112-7.

Bestmann, M., Pennacchioni, G., Mostefaoui, S., Göken, M. and de Wall, H. (2016) 'Instantaneous healing of micro-fractures during coseismic slip: Evidence from microstructure and Ti in quartz geochemistry within an exhumed pseudotachylyte-bearing fault in tonalite', Lithos, 254–255, pp. 84–93. doi: 10.1016/j.lithos.2016.03.011.

Bestmann, M. and Prior, D. J. (2003) 'Intragranular dynamic recrystallization in naturally deformed calcite marble: Diffusion accommodated grain boundary sliding as a result of subgrain rotation recrystallization', Journal of Structural Geology, 25(10), pp. 1597–1613. doi: 10.1016/S0191-8141(03)00006-3.

Biswas, S. K. and Vijayan, K. (1992) 'Friction and wear of PTFE - a review', Wear. Elsevier, 158(1–2), pp. 193–211. doi: 10.1016/0043-1648(92)90039-B.

Bizzarri, A. and Cocco, M. (2006a) 'A thermal pressurization model for the spontaneous dynamic rupture propagation on a three-dimensional fault: 1. Methodological approach', Journal of Geophysical Research: Solid Earth, 111(5), p. B05303. doi: 10.1029/2005JB003862.

Bizzarri, A. and Cocco, M. (2006b) 'A thermal pressurization model for the spontaneous dynamic rupture propagation on a three-dimensional fault: 2. Traction evolution and dynamic parameters', Journal of Geophysical Research: Solid Earth. John Wiley & Sons, Ltd, 111(B5), p. n/a-n/a. doi: 10.1029/2005JB003864.

Bowden, F. P. and Thomas, F. H. (1954) 'The surface temperature of sliding solids', Proceedings of the Royal Society of London. Series A. Mathematical and Physical Sciences, 223(1152), p. 29 LP-40. doi: 10.1098/rspa.1954.0098.

Bower, A. F. and Wininger, E. (2004) 'A two-dimensional finite element method for simulating the constitutive response and microstructure of polycrystals during high temperature plastic deformation', Journal of the Mechanics and Physics of Solids. Pergamon, 52(6), pp. 1289–1317. doi: 10.1016/J.JMPS.2003.11.004.

Brantut, N., Han, R., Shimamoto, T., Findling, N. and Schubnel, A. (2011) 'Fast slip with inhibited temperature rise due to mineral dehydration: Evidence from experiments on gypsum', Geology, 39(1), pp. 59–62. doi: 10.1130/G31424.1.

Brantut, N. and Platt, J. D. (2017) 'Dynamic weakening and the depth dependence of earthquake faulting', Fault Zone Dynamic Processes: Evolution of Fault Properties During Seismic Rupture, pp. 171–194. doi: 10.1002/9781119156895.ch9.

Brantut, N., Schubnel, A., Rouzaud, J. N., Brunet, F. and Shimamoto, T. (2008) 'High-velocity frictional properties of a clay-bearing fault gouge and implications for earthquake mechanics', Journal of Geophysical Research: Solid Earth, 113(10), p. B10401. doi: 10.1029/2007JB005551.

Brune, J. N., Henyey, T. L. and Roy, R. F. (1969) 'Heat flow, stress, and rate of slip along the San Andreas Fault, California', Journal of Geophysical Research. Wiley-Blackwell, 74(15), pp. 3821–3827. doi: 10.1029/JB074i015p03821.

Bullock, R. J., De Paola, N., Holdsworth, R. E. and Trabucho-Alexandre, J. (2014) 'Lithological controls on the deformation mechanisms operating within carbonate-hosted faults during the seismic cycle', Journal of Structural Geology, 58, pp. 22–42. doi: 10.1016/j.jsg.2013.10.008.

Bunge, H. J. (1981) 'Fabric analysis by orientation distribution functions', Tectonophysics. Elsevier, 78(1–4), pp. 1–21. doi: 10.1016/0040-1951(81)90003-2.

Burchfiel, B. C., Nakov, R., Dumurdzanov, N., Papanikolaou, D., Tzankov, T., Serafimovski, T., King, R. W., Kotzev, V., Todosov, A. and Nurce, B. (2008) 'Evolution and dynamics of the Cenozoic tectonics of the South Balkan extensional system', Geosphere. GeoScienceWorld, 4(6), p. 919. doi: 10.1130/GES00169.1.

Burkhard, M. (1990) 'Ductile deformation mechanisms in micritic limestones naturally deformed at low temperatures (150-350°C)', Geological Society, London, Special Publications. Geological Society of London, 54(1), pp. 241–257. doi: 10.1144/GSL.SP.1990.054.01.23.

124

Byerlee, J. (1978) 'Friction of rocks', Pure and Applied Geophysics PAGEOPH, 116(4–5), pp. 615–626. doi: 10.1007/BF00876528.

Carslaw, H. S. and Jaeger, J. C. (1986) Conduction of Heat in Solids. 2nd edition. Clarendon Press.

Chandra, N. (2002) 'Constitutive behavior of superplastic materials', International Journal of Non-Linear Mechanics, 37(3), pp. 461–484. doi: 10.1016/S0020-7462(01)00021-X.

Chester, F. M. and Chester, J. S. (1998) 'Ultracataclasite structure and friction processes of the Punchbowl fault, San Andreas system, California', Tectonophysics, 295(1–2), pp. 199–221. doi: 10.1016/S0040-1951(98)00121-8.

Chester, F. M., Evans, J. P. and Biegel, R. L. (1993) 'Internal structure and weakening mechanisms of the San Andreas Fault', Journal of Geophysical Research, 98(B1), pp. 771–786. doi: 10.1029/92JB01866.

Chester, F. M., Rowe, C., Ujiie, K., Kirkpatrick, J., Regalla, C., Remitti, F., Moore, J. C. and Toy, V. (2013) '2011 Tohoku-Oki Earthquake', (December), pp. 1208–1212.

Chester, J. S., Chester, F. M. and Kronenberg, A. K. (2005) 'Fracture surface energy of the Punchbowl fault, San Andreas system', Nature, 437(7055), pp. 133–136. doi: 10.1038/nature03942.

Chiaraluce, L. (2012) 'Unravelling the complexity of Apenninic extensional fault systems: A review of the 2009 L'Aquila earthquake (Central Apennines, Italy)', Journal of Structural Geology. Pergamon, pp. 2–18. doi: 10.1016/j.jsg.2012.06.007.

Cipoletti, D. E., Bower, A. F. and Krajewski, P. E. (2011) 'A microstructure-based model of the deformation mechanisms and flow stress during elevated-temperature straining of a magnesium alloy', Scripta Materialia. Pergamon, 64(10), pp. 931–934. doi: 10.1016/J.SCRIPTAMAT.2010.12.033.

Clauser, C. and Huenges, E. (2013) 'Thermal Conductivity of Rocks and Minerals', in. American Geophysical Union (AGU), pp. 105–126. doi: 10.1029/RF003p0105.

Collettini, C., Carpenter, B. M., Viti, C., Cruciani, F., Mollo, S., Tesei, T., Trippetta, F., Valoroso, L. and Chiaraluce, L. (2014) 'Fault structure and slip localization in carbonate-bearing normal faults: An example from the Northern Apennines of Italy', Journal of Structural Geology, 67(PA), pp. 154–166. doi: 10.1016/j.jsg.2014.07.017.

Collettini, C., Viti, C., Tesei, T. and Mollo, S. (2013) 'Thermal decomposition along natural carbonate faults during earthquakes', Geology, 41(8), pp. 927–930. doi: 10.1130/G34421.1.

De Bresser, J. H. P., Ter Heege, J. H. and Spiers, C. J. (2001) 'Grain size reduction by dynamic recrystallization: can it result in major theological weakening?', International Journal of Earth Sciences. Springer-Verlag, 90(1), pp. 28–45. doi: 10.1007/s005310000149.

De Bresser, J. H. P., Peach, C. J., Reijs, J. P. J. and Spiers, C. J. (1998) 'On dynamic recrystallization during solid state flow: Effects of stress and temperature', Geophysical Research Letters, 25(18), pp. 3457–3460. doi: 10.1029/98GL02690.

De Bresser, J. H. P. and Spiers, C. J. (1997) 'Strength characteristics of the r, f, and c slip systems in calcite', Tectonophysics, 272(1), pp. 1–23. doi: 10.1016/S0040-1951(96)00273-9.

Deer, W. A. (William A., Howie, R. A. (Robert A. and Zussman, J. (1992) An introduction to the rock-forming minerals. doi: 0-582-30094-0.

De Paola, N., Collettini, C., Faulkner, D. R. and Trippetta, F. (2008) 'Fault zone architecture and deformation processes within evaporitic rocks in the upper crust', Tectonics, 27(4), pp. 1–21. doi: 10.1029/2007TC002230.

De Paola, N., Chiodini, G., Hirose, T., Cardellini, C., Caliro, S. and Shimamoto, T. (2011a) 'The geochemical signature caused by earthquake propagation in carbonate-hosted faults', Earth and Planetary Science Letters. Elsevier B.V., 310(3–4), pp. 225–232. doi: 10.1016/j.epsl.2011.09.001.

De Paola, N., Hirose, T., Mitchell, T., Di Toro, G., Viti, C. and Shimamoto, T. (2011b) 'Fault lubrication and earthquake propagation in thermally unstable rocks', Geology. ICE Publishing Ltd., 39(1), pp. 35–38. doi: 10.1130/G31398.1.

De Paola, N., Holdsworth, R. E., Viti, C., Collettini, C. and Bullock, R. (2015) 'Can grain size sensitive flow lubricate faults during the initial stages of earthquake propagation?', Earth and Planetary Science Letters. Elsevier B.V., 431, pp. 48–58. doi: 10.1016/j.epsl.2015.09.002.

Di Bucci, D. and Mazzoli, S. (2003) 'The October-November 2002 Molise seismic sequence (southern Italy): an expression of Adria intraplate deformation', Journal of the Geological Society, 160(4), pp. 503–506. doi: 10.1144/0016-764902-152.

Di Toro, G., Goldsby, D. L. and Tullis, T. E. (2004) 'Friction falls towards zero in quartz rock as slip velocity approaches seismic rates', Nature, 427(6973), pp. 436–439. doi: 10.1038/nature02249.

Di Toro, G., Hirose, T., Nielsen, S., Pennacchioni, G. and Shimamoto, T. (2006a) 'Natural and experimental evidence of melt lubrication of faults during earthquakes', Science. American Association for the Advancement of Science, 311(5761), pp. 647–649. doi: 10.1126/science.1121012.

Di Toro, G., Hirose, T., Nielsen, S. and Shimamoto, T. (2006b) 'Relating high-velocity rock-friction experiments to coseismic slip in the presence of melts', in Geophysical Monograph Series, pp. 121–134. doi: 10.1029/170GM13.

Di Toro, G., Han, R., Hirose, T., De Paola, N., Nielsen, S., Mizoguchi, K., Ferri, F., Cocco, M. and Shimamoto, T. (2011) 'Fault lubrication during earthquakes', Nature. Nature Publishing Group, 471(7339), pp. 494–499. doi: 10.1038/nature09838.

Domenico, S. N. (1983) 'Sandstone and limestone porosity determination from shear and compressional wave velocity', Exploration Geophysics, 14(4), p. 81. doi: 10.1071/EG983081.

Durand, B., Geological Society of London. and Integrated Basin Studies Project. (1999) The Mediterranean basins : tertiary extension within the Alpine Orogen. Geological Society.

Faulkner, D. R., Jackson, C. A. L., Lunn, R. J., Schlische, R. W., Shipton, Z. K., Wibberley, C. A. J. and Withjack, M. O. (2010) 'A review of recent developments concerning the structure, mechanics and fluid flow properties of fault zones', Journal of Structural Geology. (Fault Zones), 32(11), pp. 1557–1575. doi: 10.1016/j.jsg.2010.06.009.

Fondriest, M. (2014) Structure and mechanical properties of seismogenic fault zones in carbonates. Available at: http://paduaresearch.cab.unipd.it/6586/1/Fondriest_PhD_thesis_2014.pdf (Accessed: 16 August 2016).

Fondriest, M., Smith, S. A. F., Candela, T., Nielsen, S. B., Mair, K. and Toro, G. Di (2013) 'Mirror-like faults and power dissipation during earthquakes', Geology, 41(11), pp. 1175–1178. doi: 10.1130/G34641.1.

Fondriest, M., Smith, S. A. F., Di Toro, G., Zampieri, D. and Mittempergher, S. (2012) 'Fault zone structure and seismic slip localization in dolostones, an example from the Southern Alps, Italy', Journal of Structural Geology. (Fault zone structure, mechanics and evolution in nature and experiment), 45, pp. 52–67. doi: 10.1016/j.jsg.2012.06.014.

Fukuyama, E. and Mizoguchi, K. (2010) 'Constitutive parameters for earthquake rupture dynamics based on high-velocity friction tests with variable sliprate', International Journal of Fracture. Springer Netherlands, 163(1–2), pp. 15–26. doi: 10.1007/s10704-009-9417-5.

Goldsby, D. L. and Tullis, T. E. (2011) 'Flash heating leads to low frictional strength of crustal rocks at earthquake slip rates', Science, 334(6053), pp. 216–218. doi: 10.1126/science.1207902.

Green, H. W., Shi, F., Bozhilov, K., Xia, G. and Reches, Z. (2015) 'Phase transformation and nanometric flow cause extreme weakening during fault slip', Nature Geoscience, 8(6), pp. 448–489. doi: 10.1038/NGEO2436.

Guermani, A. and Pennacchioni, G. (1998) 'Brittle precursors of plastic deformation in a granite: an example from the Mont Blanc massif (Helvetic, western Alps)', Journal of Structural Geology. Pergamon, 20(2–3), pp. 135–148. doi: 10.1016/S0191-8141(97)00080-1.

Han, R., Hirose, T. and Shimamoto, T. (2010) 'Strong velocity weakening and powder lubrication of simulated carbonate faults at seismic slip rates', Journal of Geophysical Research: Solid Earth, 115(3), p. B03412. doi: 10.1029/2008JB006136.

Han, R., Shimamoto, T., Hirose, T., Ree, J. H. and Ando, J. I. (2007) 'Geophysics: Ultralow friction of carbonate faults caused by thermal decomposition', Science, 316(5826), pp. 878–881. doi: 10.1126/science.1139763.

Hancock, P. L. and Barka, A. A. (1987) 'Kinematic indicators on active normal faults in Western Turkey', Journal of Structural Geology. Pergamon, 9(5–6), pp. 573–584. doi: 10.1016/0191-8141(87)90142-8.

Heaton, T. H. (1990) 'Evidence for and implications of self-healing pulses of slip in earthquake rupture', Physics of the Earth and Planetary Interiors, 64(1), pp. 1–20. doi: 10.1016/0031-9201(90)90002-F.

Herwegh, M. and Kunze, K. (2002) 'The influence of nano-scale second-phase particles on deformation of fine grained calcite mylonites', Journal of Structural Geology, 24(9), pp. 1463–1478. doi: 10.1016/S0191-8141(01)00144-4.

Hickman, S. H. (1991) 'Stress in the lithosphere and the strength of active faults', Reviews of Geophysics, 29(April 1991), pp. 759–775. doi: 10.1016/j.amjcard.2007.12.014.

Hirose, T. and Bystricky, M. (2007) 'Extreme dynamic weakening of faults during dehydration by coseismic shear heating', Geophysical Research Letters, 34(14), p. L14311. doi: 10.1029/2007GL030049.

Hirose, T. and Shimamoto, T. (2005) 'Growth of molten zone as a mechanism of slip weakening of simulated faults in gabbro during frictional melting', Journal of Geophysical Research. John Wiley & Sons, Ltd, 110(B5), p. B05202. doi: 10.1029/2004JB003207.

Hobbs, B. and Ord, A. (2014) Structural Geology: The Mechanics of Deforming Metamorphic Rocks, Structural Geology: The Mechanics of Deforming Metamorphic Rocks. Elsevier. doi: 10.1016/C2012-0-01215-X.

Hutter, K. and Rajagopal, K. R. (1994) 'On flows of granular materials', Continuum Mechanics and Thermodynamics. Springer-Verlag, 6(2), pp. 81–139. doi: 10.1007/BF01140894.

Ide, S., Baltay, A. and Beroza, G. C. (2011) 'Shallow dynamic overshoot and energetic deep rupture in the 2011 Mw9.0 Tohoku-Oki earthquake', Science, 332(6036), pp. 1426–1429. doi: 10.1126/science.1207020.

Jackson, J. and McKenzie, D. (1999) 'A hectare of fresh striations on the Arkitsa fault, central Greece', Journal of Structural Geology. Pergamon, 21(1), pp. 1–6. doi: 10.1016/S0191-8141(98)00091-1.

Kanamori, H. and Rivera, L. (2006) 'Energy partitioning during an earthquake', in Geophysical Monograph Series, pp. 3–13. doi: 10.1029/170GM03.

Kim, J.-W., Ree, J.-H., Han, R. and Shimamoto, T. (2010) 'Experimental evidence for the simultaneous formation of pseudotachylyte and mylonite in the brittle regime', Geology, 38(12), pp. 1143–1146. doi: 10.1130/G31593.1.

Kim, S., Ree, J.-H., Han, R., Kim, N. and Jung, H. (2018) 'Fabric transition with dislocation creep of a carbonate fault zone in the brittle regime', Tectonophysics. Elsevier, 723, pp. 107–116. doi: 10.1016/J.TECTO.2017.12.008.

Kohlstedt, D.L., (2007), 'Properties of Rocks and Minerals – Constitutive Equations , Rheological Behavior , and Viscosity of Rocks', Treatise on Geophysics, v. 2, p. 389–417, doi: 10.1016/B978-044452748-6.00043-2.

Lachenbruch, A. H. (1980) 'Frictional heating, fluid pressure, and the resistance to fault motion.', Journal of Geophysical Research, 85(B11), pp. 6097–6112. doi: 10.1029/JB085iB11p06097.

Lankford, J. (1996) 'High strain rate compression and plastic flow of ceramics', Journal of Materials Science Letters, 15(9), pp. 745–750. doi: 10.1007/BF00274593.

Liao, Z., Chang, J. C. and Reches, Z. (2014) 'Fault strength evolution during high velocity friction experiments with slip-pulse and constant-velocity loading', Earth and Planetary Science Letters, 406, pp. 93–101. doi: 10.1016/j.epsl.2014.09.010.

Lin, A., Katayama, S., Rao, G. and Kubota, Y. (2015) 'Structural analysis of a previously unknown active fault that triggered the 2013 M_w 5.8 Awajishima earthquake, Southwest Japan', Bulletin of the Seismological Society of America, 105(3), pp. 1502–1516. doi: 10.1785/0120140122.

Lockner, D. (1993) 'The role of acoustic emission in the study of rock fracture', International Journal of Rock Mechanics and Mining Sciences and. Pergamon, 30(7), pp. 883–899. doi: 10.1016/0148-9062(93)90041-B.

Lockner, D. A., Naka, H., Tanaka, H., Ito, H. and Ikeda, R. (2000) 'Permeability and strength of core samples from the Nojima fault of the 1995 Kobe earthquake', GSJ Internal Report No. EQ/00/1, Proceedings of the Internal Workshop on Nojima Fault Core and Borehole Date Analysis, pp. 147–157. doi: 10.1016/j.ijggc.2010.08.005.

Mancktelow, N. S. and Pennacchioni, G. (2005) 'The control of precursor brittle fracture and fluid-rock interaction on the development of single and paired ductile shear zones', Journal of Structural Geology. Pergamon, 27(4), pp. 645–661. doi: 10.1016/j.jsg.2004.12.001.

Mase, C. W. and Smith, L. (1984) 'Pore-fluid pressures and frictional heating on a fault surface', Pure and Applied Geophysics PAGEOPH, 122(2–4), pp. 583–607. doi: 10.1007/BF00874618.

Miller, S. A., Collettini, C., Chiaraluce, L., Cocco, M., Barchi, M. and Kaus, B. J. P. (2004) 'Aftershocks driven by a high-pressure CO_2 source at depth', Nature. Nature Publishing Group, 427(6976), pp. 724–727. doi: 10.1038/nature02251.

Mitchell, T. M., Smith, S. A. F., Anders, M. H., Di Toro, G., Nielsen, S., Cavallo, A. and Beard, A. D. (2015) 'Catastrophic emplacement of giant landslides aided by thermal decomposition: Heart Mountain, Wyoming', Earth and Planetary Science Letters, 411, pp. 199–207. doi: 10.1016/j.epsl.2014.10.051.

Mizoguchi, K., Hirose, T., Shimamoto, T. and Fukuyama, E. (2007) 'Reconstruction of seismic faulting by high-velocity friction experiments: An example of the 1995 Kobe earthquake', Geophysical Research Letters, 34(1), p. L01308. doi: 10.1029/2006GL027931.

Mo, Y., Turner, K. T. and Szlufarska, I. (2009) 'Friction laws at the nanoscale', Nature, 457(7233), pp. 1116–1119. doi: 10.1038/nature07748.

Mogi, K. (1972) 'Fracture and flow of rocks', Tectonophysics. Elsevier, 13(1–4), pp. 541–568. doi: 10.1016/0040-1951(72)90037-6.

Moresi, L. and Solomatov, V. (1998) 'Mantle convection with a brittle lithosphere: throughts on the global tectonic styles of the Earth and Venus', Geophysical Journal International, 133(3), pp. 669–682. doi: 10.1046/j.1365-246X.1998.00521.x.

Nieh, T. G., Wadsworth, J. and Sherby, O. D. (1997) Superplasticity in metals and ceramics. Cambridge University Press.

Nielsen, S., Spagnuolo, E., Violay, M., Smith, S., Di Toro, G. and Bistacchi, A. (2016) 'G: Fracture energy, friction and dissipation in earthquakes', Journal of Seismology, 20(4), pp. 1187–1205. doi: 10.1007/s10950-016-9560-1.

Nielsen, S., Di Toro, G., Hirose, T. and Shimamoto, T. (2008) 'Frictional melt and seismic slip', Journal of Geophysical Research: Solid Earth, 113(1), p. B01308. doi: 10.1029/2007JB005122.

Ning, J. G., Chu, L. and Ren, H. L. (2014) 'A quantitative acoustic emission study on fracture processes in ceramics based on wavelet packet decomposition', Journal of Applied Physics. AIP Publishing LLC, 116(8), p. 084901. doi: 10.1063/1.4893723.

Noda, H. and Lapusta, N. (2013) 'Stable creeping fault segments can become destructive as a result of dynamic weakening', Nature. Nature Publishing Group, 493(7433), pp. 518–521. doi: 10.1038/nature11703.

Noda, H. and Shimamoto, T. (2005) 'Thermal pressurization and slip-weakening distance of a fault: An example of the Hanaore fault, southwest Japan', Bulletin of the Seismological Society of America, 95(4), pp. 1224–1233. doi: 10.1785/0120040089.

Passelègue, F. X., Spagnuolo, E., Violay, M., Nielsen, S., Di Toro, G. and Schubnel, A. (2016) 'Frictional evolution, acoustic emissions activity, and off-fault damage in simulated faults sheared at seismic slip rates', Journal of Geophysical Research: Solid Earth, 121(10), pp. 7490–7513. doi: 10.1002/2016JB012988.

Philpotts, A. R. (Anthony R. and Ague, J. J. (2009) Principles of igneous and metamorphic petrology. Cambridge University Press.

Pieri, M., Kunze, K., Burlini, L., Stretton, I., Olgaard, D. L., Burg, J.-P. and Wenk, H.-R. (2001) 'Texture development of calcite by deformation and dynamic recrystallization at 1000 K during torsion experiments of marble to large strains', Tectonophysics. Elsevier, 330(1–2), pp. 119–140. doi: 10.1016/S0040-1951(00)00225-0.

Platt, J. D., Rudnicki, J. W. and Rice, J. R. (2014) 'Stability and localization of rapid shear in fluid-saturated fault gouge: 2. Localized zone width and strength evolution', Journal of Geophysical Research: Solid Earth, 119(5), pp. 4334–4359. doi: 10.1002/2013JB010711.

Poirier, J.-P. (1985) Creep of crystals. , High-temperature deformation processes in metals, ceramics and minerals. Cambridge: Cambridge University Press. doi: 10.1007/978-0-387-09751-0_26.

Prior, D. J., Boyle, A. P., Brenker, F., Cheadle, M. C., Day, A., Lopez, G., Peruzzo, L., Potts, G. J., Reddy, S., Spiess, R., Timms, N. E., Trimby, P., Wheeler, J. and Zetterström, L. (1999) 'The application of electron backscatter diffraction and orientation contrast imaging in the SEM to textural problems in rocks', American Mineralogist, 84, pp. 1741–1759.

Reches, Z. and Lockner, D. A. (2010) 'Fault weakening and earthquake instability by powder lubrication', Nature, 467(7314), pp. 452–455. doi: 10.1038/nature09348.

Rempel, A. W. (2006) 'The Effects of Flash-Weakening and Damage on the Evolution of Fault Strength and Temperature', in Abercrombie, R., McGarr, A., Toro, G. Di, and Kanamori, H. (eds) Earthquakes: Radiated Energy and the Physics of Faulting. American Geophysical Union, pp. 263–270. doi: 10.1029/170GM26.

Rempel, A. W. and Rice, J. R. (2006) 'Thermal pressurization and onset of melting in fault zones', Journal of Geophysical Research: Solid Earth, 111(9), p. B09314. doi: 10.1029/2006JB004314.

Rice, J. R. (1999) 'Flash heating at asperity contacts and rate-dependent friction', Eos Trans. AGU, 80(46), Fa(46), p. F6811. Available at: https://ci.nii.ac.jp/naid/10024495537/#cit (Accessed: 16 November 2018).

Rice, J. R. (2006) 'Heating and weakening of faults during earthquake slip', Journal of Geophysical Research: Solid Earth, 111(5), p. B05311. doi: 10.1029/2005JB004006.

Rice, J. R., Rudnicki, J. W. and Platt, J. D. (2014) 'Stability and localization of rapid shear in fluid-saturated fault gouge: 1. Linearized stability analysis', Journal of Geophysical Research: Solid Earth, 119(5), pp. 4311–4333. doi: 10.1002/2013JB010710.

Rivera, L. and Kanamori, H. (2005) 'Representations of the radiated energy in earthquakes', Geophysical Journal International, 162(1), pp. 148–155. doi: 10.1111/j.1365-246X.2005.02648.x.

Rockwell, T. K. and Ben-Zion, Y. (2007) 'High localization of primary slip zones in large earthquakes from paleoseismic trenches: Observations and implications for earthquake physics', Journal of Geophysical Research: Solid Earth, 112(10), p. B10304. doi: 10.1029/2006JB004764.

Rowe, K. J. and Rutter, E. H. (1990) 'Palaeostress estimation using calcite twinning: experimental calibration and application to nature', Journal of Structural Geology, 12(1), pp. 1–17. doi: 10.1016/0191-8141(90)90044-Y.

Rutter, E. H., Casey, U. K. M. and Burlini, L. (1994) 'Preferred crystallographic orientation development during the plastic and superplastic flow of calcite rocks', Pergamon Journal of Structural Geology, 16(10), pp. 1431–1446.

Sammis, C. G. and Ben-Zion, Y. (2008) 'Mechanics of grain-size reduction in fault zones', Journal of Geophysical Research: Solid Earth, 113(2), p. B02306. doi: 10.1029/2006JB004892.

Sause, M. G. R. (2011) 'Investigation of pencil-lead breaks as acoustic emission sources', Journal of Acoustic Emission. Journal of Acoustic Emission, 29, pp. 184–196. doi: http://www.ndt.net/article/jae/papers/29-184.pdf.

Sammis, C. G. and King, G. C. P. (2007) 'Mechanical origin of power law scaling in fault zone rock', Geophysical Research Letters. Wiley-Blackwell, 34(4), p. L04312. doi: 10.1029/2006GL028548.

Schmid, S. M., Panozzo, R. and Bauer, S. (1987) 'Simple shear experiments on calcite rocks: rheology and microfabric', Journal of Structural Geology, 9(5), pp. 747–778. doi: 10.1016/0191-8141(87)90157-X.

Scholz, C. H. (2002) The Mechanics of Earthquakes and Faulting. Cambridge University Press.

Schubnel, A., Walker, E., Thompson, B. D., Fortin, J., Guéguen, Y. and Young, R. P. (2006) 'Transient creep, aseismic damage and slow failure in Carrara marble deformed across the brittle-ductile transition', Geophysical Research Letters. John Wiley & Sons, Ltd, 33(17), p. L17301. doi: 10.1029/2006GL026619.

Shimamoto, T. and Tsutsumi, A. (1994) 'A new rotary-shear high-speed frictional testing machine: its basic design and scope of research', Journal of the Tectonic Research Group, Japan, 39, pp. 65–78. doi: 10.1016/j.jcis.2012.09.080.

Sibson, R. H. (1973) 'Interactions between Temperature and Pore-Fluid Pressure during Earthquake Faulting and a Mechanism for Partial or Total Stress Relief', Nature Physical Science, 243(126), pp. 66–68. doi: 10.1038/physci243066a0.

Sibson, R. H. (1975) 'Generation of Pseudotachylyte by Ancient Seismic Faulting', Geophysical Journal of the Royal Astronomical Society, 43(3), pp. 775–794. doi: 10.1111/j.1365-246X.1975.tb06195.x.

Sibson, R. H. (1977) 'Fault rocks and fault mechanisms', Journal of the Geological Society, 133(3), pp. 191–213. doi: 10.1144/gsjgs.133.3.0191.

Sibson, R. H. (2003) 'Thickness of the seismic slip zone', Bulletin of the Seismological Society of America, 93(3), pp. 1169–1178. doi: 10.1785/0120020061.

Siman-Tov, S., Aharonov, E., Boneh, Y. and Reches, Z. (2015) 'Fault mirrors along carbonate faults: Formation and destruction during shear experiments', Earth and Planetary Science Letters, 430, pp. 367–376. doi: 10.1016/j.epsl.2015.08.031.

Siman-Tov, S., Aharonov, E., Sagy, A. and Emmanuel, S. (2013) 'Nanograins form carbonate fault mirrors', Geology, 41(6), pp. 703–706. doi: 10.1130/G34087.1.

Smith, D. D. (1976) 'Thermal conductivity of halite using a pulsed laser', doi:10.2172/7228316.

Smith, S. A. F., Billi, A., di Toro, G. and Spiess, R. (2011) 'Principal Slip Zones in Limestone: Microstructural Characterization and Implications for the Seismic Cycle (Tre Monti Fault, Central Apennines, Italy)', Pure and Applied Geophysics, 168(12), pp. 2365–2393. doi: 10.1007/s00024-011-0267-5.

Smith, S. A. F., Nielsen, S. and Di Toro, G. (2015) 'Strain localization and the onset of dynamic weakening in calcite fault gouge', Earth and Planetary Science Letters, 413, pp. 25–36. doi: 10.1016/j.epsl.2014.12.043.

Smith, S. A. F., Di Toro, G., Kim, S., Ree, J. H., Nielsen, S., Billi, A. and Spiess, R. (2013) 'Coseismic recrystallization during shallow earthquake slip', Geology, 41(1), pp. 63–66. doi: 10.1130/G33588.1.

Spagnuolo, E., Plümper, O., Violay, M., Cavallo, A. and Di Toro, G. (2015) 'Fast-moving dislocations trigger flash weakening in carbonate-bearing faults during earthquakes', Scientific Reports. Nature Publishing Group, 5, pp. 1–11. doi: 10.1038/srep16112.

Spray, J. G. (1987) 'Artificial generation of pseudotachylyte using friction welding apparatus: simulation of melting on a fault plane', Journal of Structural Geology. Pergamon, 9(1), pp. 49–60. doi: 10.1016/0191-8141(87)90043-5.

Spray, J. G. (1993) 'Viscosity determinations of some frictionally generated silicate melts: implications for fault zone rheology at high strain rates', Journal of Geophysical Research, 98(B5), pp. 8053–8068. doi: 10.1029/93JB00020.

Spray, J. G. (2010) 'Frictional Melting Processes in Planetary Materials: From Hypervelocity Impact to Earthquakes', Annual Review of Earth and Planetary Sciences. Annual Reviews, 38(1), pp. 221–254. doi: 10.1146/annurev.earth.031208.100045.

Su, C., Liu, Y., Song, W., Fan, D., Wang, Z. and Tang, H. (2018) 'Thermodynamic properties of San Carlos olivine at high temperature and high pressure', Acta Geochimica. Science Press, 37(2), pp. 171–179. doi: 10.1007/s11631-018-0261-z.

Sulem, J. and Famin, V. (2009) 'Thermal decomposition of carbonates in fault zones: Slip-weakening and temperature-limiting effects', Journal of Geophysical Research, 114(B3), p. B03309. doi: 10.1029/2008JB006004.

Tarling, M. S., Smith, S. A. F., Viti, C. and Scott, J. M. (2018) 'Dynamic earthquake rupture preserved in a creeping serpentinite shear zone', Nature Communications. Nature Publishing Group, 9(1), p. 3552. doi: 10.1038/s41467-018-05965-0.

Tesei, T., Carpenter, B. M., Giorgetti, C., Scuderi, M. M., Sagy, A., Scarlato, P. and Collettini, C. (2017) 'Friction and scale-dependent deformation processes of large experimental carbonate faults', Journal of Structural Geology. Pergamon, 100, pp. 12–23. doi: 10.1016/j.jsg.2017.05.008.

Tesei, T., Collettini, C., Viti, C. and Barchi, M. R. (2013) 'Fault architecture and deformation mechanisms in exhumed analogues of seismogenic carbonate-bearing thrusts', Journal of Structural Geology. Pergamon, 55, pp. 167–181. doi: 10.1016/j.jsg.2013.07.007.

Thieme, M., Demouchy, S., Mainprice, D., Barou, F., and Cordier, P., (2018), 'Stress evolution and associated microstructure during transient creep of olivine at 1000–1200 °C', Physics of the Earth and Planetary Interiors, v. 278, p. 34–46, doi: 10.1016/j.pepi.2018.03.002.

Tinti, E., Scognamiglio, L., Michelini, A. and Cocco, M. (2016) 'Slip heterogeneity and directivity of the ML6.0, 2016, Amatrice earthquake estimated with rapid finite-fault inversion', Geophysical Research Letters. Wiley-Blackwell, 43(20), p. 10,745-10,752. doi: 10.1002/2016GL071263.

Tisato, N., Di Toro, G., De Rossi, N., Quaresimin, M. and Candela, T. (2012) 'Experimental investigation of flash weakening in limestone', Journal of Structural Geology. (Physico-Chemical Processes in Seismic Faults), 38, pp. 183–199. doi: 10.1016/j.jsg.2011.11.017.

Townend, J. and Zoback, M. D. (2000) 'How faulting keeps the crust strong', Geology, 28(5), pp. 399–402. doi: 10.1130/0091-7613(2000)028<0399:HFKTCS>2.3.CO;2.

Trouw, R.A.J. (Rudolph A.J.., Passchier, C.W. (Cees W., and Wiersma, D.J., 2010, 'Atlas of mylonites and related microstructures', Springer, 322 p.

Tullis, J., Dell'Angelo, L. and Yund, R. A. (1990) 'Ductile shear zones from brittle precursors in feldspathic rocks: The role of dynamic recrystalli-zation', in. American Geophysical Union (AGU), pp. 67–81. doi: 10.1029/GM056p0067.

Twiss, R. J. and Moores, E. M. (2007) Structural geology. W.H. Freeman. Available at: https://books.google.it/books?id=aXvmQwAACAAJ&dq=twiss+and+moores+2nd&hl=it&sa=X&ved=0ahUKEwiP9Yi21YTfAhVH_aQKHcUXCDgQ6AEIKTAA (Accessed: 3 December 2018).

Verberne, B. A., de Bresser, J. H. P., Niemeijer, A. R., Spiers, C. J., de Winter, D. A. M. and Plümper, O. (2013) 'Nanocrystalline slip zones in calcite fault gouge show intense crystallographic preferred orientation: Crystal plasticity at subseismic slip rates at 18-150 °C', Geology, 41(8), pp. 863–866. doi: 10.1130/G34279.1.

Verberne, B. A., Plümper, O., De Winter, D. A. M. and Spiers, C. J. (2014) 'Superplastic nanofibrous slip zones control seismogenic fault friction', Science, 346(6215), pp. 1342–1344. doi: 10.1126/science.1259003.

Verberne, B. A., Spiers, C. J., Niemeijer, A. R., De Bresser, J. H. P., De Winter, D. A. M. and Plümper, O. (2013) 'Frictional Properties and Microstructure of Calcite-Rich Fault Gouges Sheared at Sub-Seismic Sliding Velocities', Pure and Applied Geophysics, 171(10), pp. 2617–2640. doi: 10.1007/s00024-013-0760-0.

Vernon, R. H. (2004) A Practical Guide to Rock Microstructure. Cambridge University Press.

Viti, C. (2011) 'Exploring fault rocks at the nanoscale', Journal of Structural Geology, 33(12), pp. 1715–1727. doi: 10.1016/j.jsg.2011.10.005.

Viti, C., Brogi, A., Liotta, D., Mugnaioli, E., Spiess, R., Dini, A., Zucchi, M. and Vannuccini, G. (2016) 'Seismic slip recorded in tourmaline fault mirrors from Elba Island (Italy)', Journal of Structural Geology. Pergamon, 86, pp. 1–12. doi: 10.1016/j.jsg.2016.02.013.

Viti, C. and Hirose, T. (2010) 'Thermal decomposition of serpentine during coseismic faulting: Nanostructures and mineral reactions', Journal of Structural Geology, 32(10), pp. 1476–1484. doi: 10.1016/j.jsg.2010.09.009.

Wang, L., Blaha, S., Pintér, Z., Farla, R., Kawazoe, T., Miyajima, N., Michibayashi, K., and Katsura, T., 2016, 'Temperature dependence of [100](010) and [001](010) dislocation mobility in natural olivine', Earth and Planetary Science Letters, v. 441, p. 81–90, doi: 10.1016/J.EPSL.2016.02.029.

Wenk, H. R., Takeshita, T., Bechler, E., Erskine, B. G. and Matthies, S. (1987) 'Pure shear and simple shear calcite textures. Comparison of experimental, theoretical and natural data', Journal of Structural Geology. doi: 10.1016/0191-8141(87)90156-8.

Wenk, H. R., Venkitasubramanyan, C. S., Baker, D. W. and Turner, F. J. (1973) 'Preferred orientation in experimentally deformed limestone', Contributions to Mineralogy and Petrology. Springer-Verlag, 38(2), pp. 81–114. doi: 10.1007/BF00373875.

Wheeler, J. (2009) 'The preservation of seismic anisotropy in the Earth's mantle during diffusion creep', in Geophysical Journal International. Oxford University Press, pp. 1723–1732. doi: 10.1111/j.1365-246X.2009.04241.x.

Wheeler, J., Prior, D., Jiang, Z., Spiess, R. and Trimby, P. (2001) 'The petrological significance of misorientations between grains', Contributions to Mineralogy and Petrology, 141(1), pp. 109–124. doi: 10.1007/s004100000225.

Widhalm, C., Tschegg, E. and Eppensteiner, W. (1997) 'Acoustic Emission and Anisotropic Expansion when Heating Marble', Journal of Performance of Constructed Facilities, 11(1), pp. 35–40. doi: 10.1061/(ASCE)0887-3828(1997)11:1(35).

Wilson, B., Dewers, T., Reches, Z. and Brune, J. (2005) 'Particle size and energetics of gouge from earthquake rupture zones', Nature, 434(7034), pp. 749–752. doi: 10.1038/nature03433.

Xu, Y., Shankland, T. J., Linhardt, S., Rubie, D. C., Langenhorst, F. and Klasinski, K. (2004) 'Thermal diffusivity and conductivity of olivine, wadsleyite and ringwoodite to 20 GPa

and 1373 K', Physics of the Earth and Planetary Interiors. Elsevier, 143–144, pp. 321–336. doi: 10.1016/J.PEPI.2004.03.005.

Yao, L., Ma, S., Platt, J. D., Niemeijer, A. R. and Shimamoto, T. (2016) 'The crucial role of temperature in high-velocity weakening of faults: Experiments on gouge using host blocks with different thermal conductivities', Geology, 44(1), pp. 63–66. doi: 10.1130/G37310.1.

Yavuz, H., Demirdag, S. and Caran, S. (2010) 'Thermal effect on the physical properties of carbonate rocks', International Journal of Rock Mechanics and Mining Sciences. Pergamon, 47(1), pp. 94–103. doi: 10.1016/J.IJRMMS.2009.09.014.

Zoback, M. D. and Healy, J. H. (1992) 'In situ stress measurements to 3.5 km depth in the Cajon Pass Scientific Research Borehole: Implications for the mechanics of crustal faulting', Journal of Geophysical Research: Solid Earth, 97(B4), pp. 5039–5057. doi: 10.1029/91JB02175.

Appendix I : Summary table of experiments

Compendium of mechanical data for all experiments discussed in this thesis.

Symbols: D is the grain size range or mean grain size, v is the slip rate, δ is the total displacement for the reliable part of the experiment, δ_{tr} is the displacement to the onset of weakening, σ_n is the normal stress, τ_P is the peak shear stress, τ_{ss} is the minimum shear stress during stage III, μ_{ss} is the minimum friction coefficient during stage III and T_W is the calculated PSZ bulk temperature at the onset of weakening (room T = 20°C).

Chapter	Exp. #	Material	D (μm)	v (ms⁻¹)	δ (m)	δ_{tr} (cm)	σ_n (MPa)	τ_P (MPa)	τ_{ss} (MPa)	μ_{ss}	T_W (°C)
3, 5, 6	VF 666	Calcite	63-90	1.4	0.04	4.7	25.0	20.1	3.8	0.15	751
	VF 664				0.07						
	VF 695				0.26						
	VF 662				0.26						
	VF 693				0.26						
	VF 660				0.90						
	VF 793				3.24						
	VF 827	Calcite	63-90	0.58	1.00	4.7	25.0	21.2	5.6	0.22	735
	VF 828	Calcite	63-90	0.36	1.00	4.7	25.0	20.1	6.8	0.27	604
	VF 829*	Calcite	63-90	0.25	0.60	4.7	25.0	20.0	~8.6	~0.34	487
	VF 680	Calcite	63-90	0.14	0.08	6.4	25.0	21.4	~10.5	~ 0.42	474
	VF 675				0.23						
	VF 679*				0.26						
	VF 677*				0.29						
	VF 676*				0.37						
	VF 803*				0.39						
	VF 834*	Calcite	63-90	0.077	0.15	9	25.0	-	-	-	445
	VF 831*	Calcite	63-90	0.046	0.20	12	25.0	-	-	-	410
	VF 833*	Calcite	63-90	0.031	0.22	20	25.0	-	-	-	420
	VF 672*	Calcite	63-90	0.014	0.13	27	25.0	-	-	-	334
	VF 673*				0.18						
	VF 824*				0.32						
	VF 670	Calcite	63-90	0.0014	0.07	-	25.0	-	-	-	-
	VF 823*				0.32						
4	VF 954	Calcite	63-90	1	1.01	4.7	20.0	15.2	3.6	0.18	520
	VF 902*			0.1	0.36	7.2		17.0	~11.5	~0.58	345
	VF 907*			0.001	0.71	-		-	-	-	-
	AE 943			1	1.00	2.7	20.0	11.8	2.6	0.13	285
	AE 904	Calcium Carbonate	0.2	0.1	1.00	3.8	20.0	12.3	3.8	0.19	198
	AE 944			0.001	1.00	33.4	20.0	13.8	5.4	0.27	205
6	VF 1062	Calcite	63-90	0.47	0.86	4.7	25.0	21.0	5.5	0.22	624
	AN 1077			1.4	0.76	2	25.0	17.6	3.9	0.16	248
	AN 1031	Anhydrite	63-90	0.58	0.99	2.2	25.0	17.4	4.9	0.20	268
	AN 1075			0.47	1.03	2.2	25.0	18.1	5.4	0.22	270
	AN 1052			0.36	1.00	2.3	25.0	17.5	5.1	0.20	251
	SD 1024			1.4	0.65	1.8	25.0	18.4	3.6	0.14	211
	SD 1026	Dolomite	63-90	0.58	0.99	1.6	25.0	17.8	4.5	0.18	169
	SD 1055			0.47	1.00	1.5	25.0	17.3	4.7	0.19	151
	SD 1056			0.36	1.14	1.4	25.0	17.8	5.1	0.20	146
	TS 1049			1.4	0.72	0.4	25.0	19.6	2.6	0.10	226
	TS 1070	Sodium Chloride	63-90	0.58	1.00	0.4	25.0	18.9	4.2	0.17	230
	TS 1058			0.47	1.09	0.4	25.0	18.7	5.2	0.21	195
	TS 1057			0.36	0.98	0.4	25.0	20.0	6.0	0.24	197
	SCO 1102			1.4	1.30	1.8	20.0	15.0	4.6	0.23	202
	SCO 1094	Olivine (Fo91)	63-90	0.58	0.95	1.9	20.0	15.7	6.7	0.34	251
	SCO 1095			0.47	0.99	2.1	20.0	15.4	7.5	0.38	223
	SCO 1093			0.36	0.99	1.9	20.0	14.9	7.7	0.39	197

THE GEOLOGICAL SOCIETY
OF AMERICA®

A new interpretation for the nature and significance of mirror-like surfaces in experimental carbonate-hosted seismic faults

Giacomo Pozzi[1], Nicola De Paola[1], Stefan B. Nielsen[1], Robert E. Holdsworth[1], and Leon Bowen[2]
[1]Department of Earth Sciences, Rock Mechanics Laboratory, Durham University, Durham, DH1 3LE, UK
[2]Department of Physics, Durham University, Durham, DH1 3LE, UK

ABSTRACT

Highly reflective, continuous smooth surfaces, known as "mirror-like surfaces" (MSs), have been observed in experimental carbonate-hosted faults, which were sheared at both seismic and aseismic velocities. MSs produced during high-velocity friction experiments (>0.1 m s⁻¹) are typically interpreted to be frictional principal slip surfaces, where weakening mechanisms are activated by shear heating. We re-examined this model by performing friction experiments in a rotary shear apparatus on calcite gouge, at seismic velocities up to $v = 1.4$ m s⁻¹ and normal stress $\sigma_n = 25$ MPa, to analyze the evolution of microstructures as displacement increases. After the onset of dynamic weakening, when the friction coefficients are low ($\mu \ll 0.6$), sheared gouges consistently develop a well-defined, porosity-free principal slip zone (PSZ) of constant finite thickness (a few tens of micrometers) composed of nanometric material, which displays polygonal grain shapes. MSs occur at both boundaries of the PSZ, where they mark a sharp contrast in grain size with the sintered, much coarser material on either side of the PSZ. Our observations suggest that, with the onset of dynamic weakening, MSs partition the deformation by separating strong, sintered wall rocks from a central weak, actively deforming viscous PSZ. Therefore, the MSs do not correspond to frictional slip surfaces in the classical sense, but constitute sharp rheological boundaries, while, in the PSZ, shear is enhanced by thermal and grain-size–dependent mechanisms.

INTRODUCTION

Highly reflective smooth surfaces, known as "mirror-like surfaces" (MSs), have long been found and described along natural exhumed faults. More recently, it has been proposed that they may represent a possible microstructural proxy for past seismic activity in carbonate-hosted fault zones (Siman-Tov et al., 2013). Several authors have since demonstrated that continuous MSs develop in carbonate gouges and rocks when sheared at seismic velocities (> 0.1 m s⁻¹)—in situations where frictional weakening is also observed—and have proposed different interpretations of their role in the weakening process (e.g., Smith et al., 2013, 2015; Siman-Tov et al., 2015; Green et al., 2015; De Paola et al., 2015). Other authors, however, have produced patchy MSs during lower-velocity experiments (0.1–10 μm s⁻¹), and therefore questioned their reliability as seismic markers (e.g., Verberne et al., 2013).

When dynamic fault weakening is observed, MSs are typically interpreted to be principal slip surfaces developed within and/or at the boundary of a slip zone. It has been argued that weakening during shear along the MSs can be driven by flash heating (Smith et al., 2015) or by thermal runaway at dynamic asperities (Siman-Tov et al., 2015). In support of these models, there is also evidence of temperature-activated crystal plasticity in the immediately adjacent rock volumes. Other authors have suggested that grain-size–sensitive creep mechanisms, occurring in a narrow (<100-μm-thick), ultrafine-grained shear zone, can cause coseismic weakening (Green et al., 2015; De Paola et al., 2015). However, the role played by MSs throughout the weakening history of carbonate gouges is still uncertain, as is the partitioning of strain between presumed sliding along MSs and bulk deformation by grain boundary sliding and/or crystal plasticity within the main slip zone.

Here, we integrate mechanical data and microstructural observations to develop a new conceptual model concerning the role and significance of MSs throughout the weakening history of calcite gouges sheared at seismic velocities.

MECHANICAL DATA

We performed friction experiments on simulated calcite gouge (grain size: 63–90 μm) in a low- to high-velocity rotary shear apparatus (De Paola et al., 2015). A sample assembly with two hollow cylinders made of a titanium-vanadium alloy (Ti-alloy, Ti90Al6V4; Yao et al., 2016) was used to sandwich a layer of gouge (weight of 1 g and initial thickness ~1.4 mm), which was confined using a Teflon outer ring and an inner Teflon cylinder (see Section DR1 in the GSA

Data Repository[1]). All experiments were run at room temperature and humidity conditions; normal stress, σ_n, of ~25 MPa; and slip rates up to $v = 1.4$ m s⁻¹ calculated at the reference radius of ~8.9 mm. Experiments were arrested at different displacements (up to 1 m, for a duration <1 s) to analyze the evolution of microstructures of samples throughout their weakening path.

Dynamic weakening was observed in experiments run at $v > 0.1$ m s⁻¹, in good agreement with values typical of seismic slip rates (Smith et al., 2013). The evolution of strength of the experimental fault follows a characteristic weakening profile characterized by four distinct phases (Fig. 1; axial shortening data are reported in Section DR3). During Stage I, Byerlee's friction values of $\mu > 0.6$ were attained, and slip-hardening up to peak values of $\mu = 0.9$ is observed (Fig. 1). Experiments consistently showed the onset of weakening after an amount of slip of δ ~6.4 cm and δ ~4.7 cm for target velocities of $v = 0.14$ m
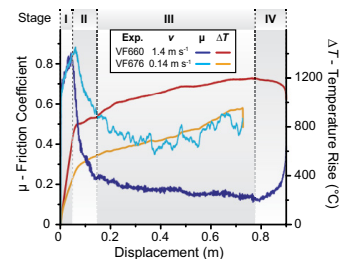

Figure 1. Mechanical data for two representative experiments (Exp.; $v = 1.4$ and $v = 0.14$ m s⁻¹): friction coefficient (μ, shown in cold colors [blues]) and estimated temperature rise (ΔT, shown in warm colors [orange, red]) curves are plotted versus displacement. The four stages of friction evolution are highlighted by the shaded areas.

s^{-1} and $v \geq 0.25$ m s^{-1}, respectively (Stages I and II in Fig. 1). During Stage II, the material weakens in an exponential fashion to low, rate-dependent friction values, $\mu = 0.5$–0.4 at $v = 0.14$ m s^{-1} and $\mu = 0.2$–0.15 at $v = 1.4$ m s^{-1}, which then remain low throughout Stage III (Fig. 1). During Stage IV, material strengthens up to friction values $\mu = 0.4$–0.5 upon deceleration of the motor to arrest (Fig. 1).

We use a simple mono-dimensional thermal diffusion model (Rice, 2006) to calculate the bulk temperature rise associated with the development of a thin slip zone (Section DR2). Due to the high angular strains ($\gamma \gg 10$) and strain rates ($\dot{\gamma} > 10^3$) attained during the experiments, it is reasonable to assume that, to a first approximation, all of the deformation energy in the deforming slip zone is dissipated as heat (Hobbs and Ord, 2014, and references therein). The estimated temperature at the onset of weakening, T_w (beginning of Stage II) is rate-dependent, with $T_w \sim 470$ °C and $T_w \sim 750$ °C for $v = 0.14$ m s^{-1} and $v = 1.4$ m s^{-1}, respectively. Repeated runs show a consistent evolution in the mechanical data, proving good reproducibility of the experimental results (Section DR3).

MICROSTRUCTURAL OBSERVATIONS

After the experiments, sample chips were carefully removed from the rotary assembly and embedded in epoxy to preserve the whole thickness of the gouge layer (Fig. 2). We used a FEI Helios Nanolab 600 electron microscope to acquire backscattered and forescattered electron images on polished cross sections, which were cut parallel to the slip direction and perpendicular to the gouge layer boundaries, at the reference radius (~8.9 mm). The values of grain size and slip zone thickness reported here refer to samples sheared at $v = 1.4$ m s^{-1}.

Gouge samples recovered at the end of Stage I are porous, slightly cohesive, and show the effect of widespread brittle grain-size reduction (Fig. 2A). During this stage, deformation is mostly accommodated by Riedel shears (R and R′) and is within an ~100-µm-thick Y-shear zone (Fig. 2A), where extreme grain-size reduction occurs (down to a few tens of nanometers). Microstructures change during Stage II, from the onset of weakening, when the Y-shear zone evolves to a well-defined principal slip zone (PSZ) with sharp boundaries and inhomogeneous grain size, with larger clasts (<1 µm) dispersed within a finer-grained matrix (mean grain size ~100 nm; Figs. 2B and 2C). Volumes of low-porosity sintered material, with thicknesses of ~20 µm, form outside the PSZ (Fig. 2C) and their surfaces bound the PSZ, forming discontinuous MSs.

At the end of the transient stage of decay from peak to low friction values (Stage II) and throughout Stage III, the PSZ becomes a discrete, porosity-free volume of fine, polygonally recrystallized material with constant thickness (~30 µm; Figs 2D, 3A, and 3B). The internal structure of the PSZ shows fairly homogeneous grain size, triple junctions, and oblique foliation, marked by a shape-preferred orientation of the crystals, consistent with the overall (sinistral) sense of shear (Fig. 3B; Section DR5, Fig. DR17). This texture is similar to that observed in some natural (Bestmann et al., 2000; Herwegh and Kunze, 2002) and experimental (Barnhoorn et al., 2004) calcite ultramylonites.

PSZ grain size increases from an average of ~300 nm at the beginning of Stage III to ~700 nm (Fig. 3B) after ~0.75 m of slip (Section DR5, Fig. DR17). The texture observed in proximity to, but outside, the PSZ is similar to that observed inside the PSZ, but shows an abrupt increase in

grain size of approximately one order of magnitude (>1 µm; Fig. 3B). Such marked grain-size decoupling produces sharp planar boundaries on either side of the PSZ: the MSs (Fig. 3B; Section DR5, Fig. DR7). In the outer layers, away from and on both sides of the PSZ, porosity gradually increases as recrystallization becomes less pervasive, forming what we term here a 'sintering gradient' (SG; Fig. 2D). In these regions, an array of relict subparallel MSs is observed (white lines in Fig. 3A). The younger MSs are straight and smooth, and show a homogeneous grain size along them (Figs. 3A and 3B). Another set of more irregular MSs is also observed (Fig. 3A), and interpreted to represent older MSs due to their similarity to the patchy ones formed during the early Stage II (Fig. 2C). These are locally reworked and may truncate larger clasts (e.g., Fondriest et al., 2013) during formation and localization of the early PSZ.

During Stage IV, brittle dilatant fracturing occurs and appears to be consistently restricted to the PSZ (e.g., Fig. 2E). It includes splitting along the MSs (exploited by epoxy during sample preparation; Fig. 3B), which exposes shiny MSs visible in recovered samples (Section DR5, Fig. DR7A). These structures always unavoidably overprint—but do not obliterate—microstructures developed during Stage III.

Similar to findings discussed by De Paola et al. (2015), our microstructural and mineralogical observations revealed that, during Stage III and IV, the PSZ is composed of crystalline calcite. This confirms that decarbonation reactions were not quantitatively significant during our experiments.

DISCUSSION

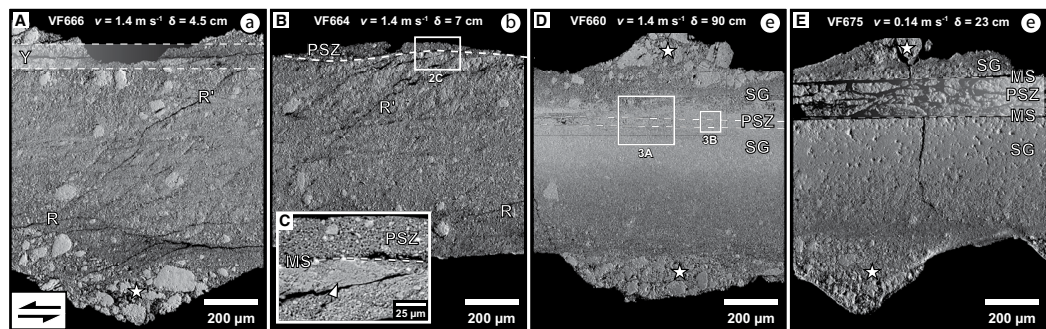With its finite volume, parallel boundaries, and textural decoupling with the outer layers, we

Figure 2. Backscattered electron images of sample cross sections obtained from the whole thickness of gouge layer (see the coarse-grained gouges filling the grooves machined on the top and bottom sample assembly cylinders, indicated with white stars) cut at the reference radius. Shear sense is sinistral. A: Stage I: diffuse and localized deformation with Riedel shear bands (R, R′) and a horizontal Y shear band (Y). B: Stage II: well-developed principal slip zone (PSZ) with patchy recrystallized boundary ("mirror-like surface", MS). C: Close-up of area outlined in B. D,E: Stages III and IV: fully developed PSZ bounded by MSs and sintered deactivated layers (sintering gradient, SG) of experiments run at $v = 1.4$ m s^{-1} and $v = 0.14$ m s^{-1}, respectively. Stage IV damage in the PSZ is more evident in the lower-velocity experiment. Lowercase letters link to microstructural sketches shown in Figure 4A.
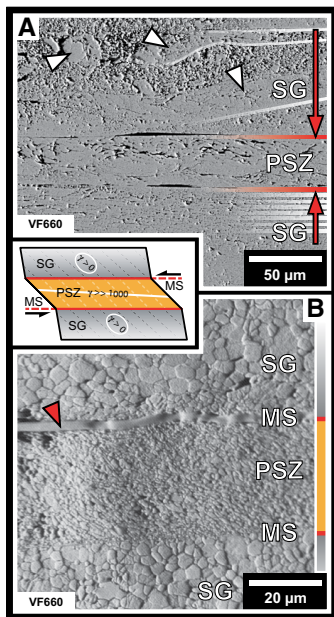
Figure 3. Close-up scanning electron microscopy images of Stages III and IV principal slip zone (PSZ) cross sections (same sample as in Fig. 2D, v = 1.4 m s⁻¹, δ = 90 cm). A: Backscattered electron image showing relict (highlighted with white lines) and the last active (red lines) "mirror-like surfaces" (MSs); white arrows indicate the older, irregular, reworked MSs; red arrows indicate direction of migration of the PSZ boundaries during localization. SG—sintering gradient. B: Forescattered electron image of PSZ displaying oblique foliation, sharp grain-size transition at the boundaries, and MSs locally split and filled with epoxy during sample preparation (red arrow). Textures inside and outside the PSZ are clearly asymmetric with respect to MSs. In the inset, a schematic model of simple shear is compared to the microstructures. γ—angular strain.

can reasonably assume that the PSZ corresponds to a zone of finite simple shear strain (inset of Fig. 3), where grain-size–sensitive processes are active (e.g., De Paola et al., 2015; Green et al., 2015). We define W_{PSZ} as the thickness of the PSZ, evolving throughout every stage of the weakening path. W_{PSZ} is constrained by microstructural observations (Figs. 2 and 3). We propose a conceptual model where W_{PSZ} is compared to a theoretical thickness W_T (Fig. 4B). W_T is here defined as the minimum thickness, for a given velocity ($W_T = v / (2\dot\gamma_{max})$ where $\dot\gamma_{max}$ is the maximum strain rate), of an ideal viscous shear zone deforming by grain-size–sensitive creep. W_T is therefore a function of grain size (D), temperature (T) and shear stress (τ), i.e., $W_T = f(D, T^{-1}, \tau^{-1})$ (Poirier, 1985).

During Stage I, brittle deformation, which is initially distributed within the entire gouge-layer thickness, localizes after a small amount of slip into a Y shear band (Figs. 2A and 4B). With increasing displacement, this band becomes a well-defined discrete PSZ, where extreme comminution (D << 1 µm) and increasing bulk temperature occur. Nanometric particles are formed in the PSZ, possibly by shock-like stress release processes (Sammis and Ben-Zion, 2008; Spagnuolo et al., 2015) and brittle failure aided by intragranular crystal plasticity (Siman-Tov et al., 2013; De Paola et al., 2015). At this stage, the PSZ temperature is still relatively low (Fig. 4C) and, consequently, $W_T \gg W_{PSZ}$ (Fig. 4B), which means that the dominant strain rate is still controlled by brittle processes (e.g., Smith et al., 2015).

At the beginning of Stage II, as the temperature rises, we infer that the viscous strain rate increases and begins to compete with the brittle one, leading to a rapid decay in friction to the low friction values of Stage III (Figs. 4B and 4C). During Stage II, the PSZ grain size homogenizes and porosity reduces due to plastic yielding of nanograins. The heat diffusing from the PSZ boundaries promotes grain-size growth in the outer regions on either side of the PSZ. During this stage, the PSZ becomes confined between two sharp sintered boundaries, and its thickness reduces as the temperature rises (migration of MSs; see below). When $W_T = W_{PSZ}$, the viscous strain rate becomes dominant, and at this point, the grain-size–sensitive creep controls the strength of the fault (Fig. 4B). The increase in temperature due to viscous shear heating will

decrease W_T and can lead to further localization of the PSZ (Fig. 4B), before the achievement of the low friction values of Stage III. As the PSZ narrows, the old boundaries are deactivated and are preserved as closely spaced planar discontinuities (relict MSs) in the coarse-grained sintered layer (Fig. 3A). A similar microstructure has also been observed in natural faults (Tesei et al., 2013; Collettini et al., 2014).

By Stage III, the PSZ has reached steady-state thickness and strain rate, with low, slowly evolving shear stress (viscosity) and grain size (Fig. 4B). We interpret that the oblique foliation formed in the PSZ during Stage III is a steady-state foliation, achieved through cycles of passive rotation and resetting through dynamic recrystallization (e.g., Barnhoorn et al., 2004, and references therein). Thus, it does not reflect the total strain in the PSZ. Following the method of De Paola et al. (2015), a good agreement is found between the shear stresses measured during Stage III and those calculated using existing flow laws for grain-size–sensitive grain boundary sliding in calcite (Section DR4, Fig. DR6).

We propose that throughout Stages II and III, heat produced by shear heating within the PSZ diffuses into regions immediately adjacent to and outside the PSZ, where the strain rate is lower. The dissipated heat leads to the development of sintering gradients (SGs) by quasi-static grain growth and densification in the materials outside the PSZ. At the same time, viscous deformation maintains a homogeneous, nanometric grain size inside the PSZ. These interpretations are supported by our microstructural observations showing a sharp textural contrast
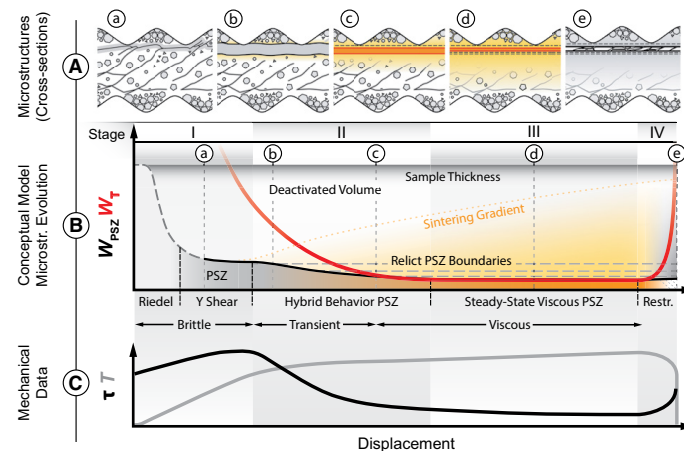

Figure 4. Graphical representation of the conceptual model with increasing displacement. A: Interpretation of microstructural evolution in the sample. B: Conceptual model comparing the thickness of the actively deforming volume (W_{PSZ}; PSZ—principal slip zone) with the theoretical thickness (W_T) and evolution of microstructures with increasing displacement. C: Schematics of shear stress (τ) and temperature (T) during experiments.

between the material in the PSZ and that in the SG domains (Fig. 3B). Therefore, the MSs evolve to become strain compatibility boundaries, separating a fine-grained, weak, viscously deforming PSZ (with $\dot{\gamma} > 10^3$), from coarser-grained and sintered volumes. These are passively heated and deform slowly on both sides of the PSZ (also proposed by Smith et al., 2015). If slip (and frictional heating) did localize on the MS, rather than inside the PSZ, the microstructural evidence of the temperature gradient (SG) would be symmetrical with respect to the MS, which it is not (Fig. 3B). MSs are therefore *not* frictional sliding surfaces, as they are commonly interpreted, but instead, they mark sharp rheological contrasts between highly strained (PSZ) and much lower-strained (SG) regions. We interpret that grooves seen on the MSs parallel to slip direction, down to the nanometer scale (Section DR5, Fig. DR7A; De Paola et al., 2015; Smith et. al, 2015), are corrugations of the PSZ boundary. We speculate that they may reflect small local variations in PSZ thickness, in a direction orthogonal to slip; i.e., they are not formed due to abrasive wear. This might be inherited from the irregularity of older MSs (Fig. 3A), formed during Stage II, when the PSZ grain size was less homogeneous (Fig. 2C).

During Stage IV, upon deceleration of the sample to arrest, the PSZ temperature drops, affecting its rheological behavior (Fig. 4C). At this stage, the theoretical thickness is $W_T > W_{PSZ}$ (Fig. 4B). We interpret that the actively deforming PSZ, which is unable to thicken due to its now coarser-grained sintered boundaries, rapidly strengthens and eventually undergoes embrittlement and reworking (Figs. 2D and 2E). Thermal cracking due to fast undercooling and damage during unloading may also enhance the splitting of the sample along preexisting textural discontinuities, such as the MSs, which are then exposed in extracted samples (Section DR5, Fig. DR7A). During the fast (<1 s) cooling stage after the experiments, grain growth due to static recrystallization is very limited, both within and on either side of the PSZ (see De Paola et al., 2015).

CONCLUSIONS

A simple conceptual model for coseismic weakening in calcite gouges is developed, integrating experimental data, microstructural analysis, and theoretical arguments. We propose that weakening is driven by thermally induced grain-size–sensitive mechanisms active within a PSZ, whose finite thickness is controlled by grain size, temperature, and shear stress.

Careful recovery of the samples has allowed a quantitative characterization of the entire PSZ thickness, which is on the order of a few tens of microns, comparable to the thickness of those found in natural seismic faults in carbonates.

According to our conceptual model, MSs mark rheological contrasts across which an extremely sharp strain gradient is observed. They partition the deformation between the weak, viscously deforming PSZ and the stronger and sintered outer layers. Thus, our observations suggest that MSs are not frictional slip surfaces in the classical sense. Whether their preservation in natural carbonate-hosted fault zones remains indicative of past seismogenic behavior is open to debate. However, seismic slip velocities and coincident shear heating make their formation more likely.

REFERENCES CITED
Barnhoorn, A., Bystricky, M., Burlini, L., and Kunze, K., 2004, The role of recrystallisation on the deformation behaviour of calcite rocks: large strain torsion experiments on Carrara marble: Journal of Structural Geology, v. 26, p. 885–903, https://doi.org/10.1016/j.jsg.2003.11.024.
Bestmann, M., Kunze, K., and Matthews, A., 2000, Evolution of a calcite marble shear zone complex on Thassos Island, Greece: Microstructural and textural fabrics and their kinematic significance: Journal of Structural Geology, v. 22, p. 1789–1807, https://doi.org/10.1016/S0191-8141(00)00112-7.
Collettini, C., Carpenter, B.M., Viti, C., Cruciani, F., Mollo, S., Tesei, T., Trippetta, F., Valoroso, L., and Chiaraluce, L., 2014, Fault structure and slip localization in carbonate-bearing normal faults: An example from the Northern Apennines of Italy: Journal of Structural Geology, v. 67, p. 154–166, https://doi.org/10.1016/j.jsg.2014.07.017.
De Paola, N., Holdsworth, R.E., Viti, C., Collettini, C., and Bullock, R., 2015, Can grain size sensitive flow lubricate faults during the initial stages of earthquake propagation?: Earth and Planetary Science Letters, v. 431, p. 48–58, https://doi.org/10.1016/j.epsl.2015.09.002.
Fondriest, M., Smith, S.A.F., Candela, T., Nielsen, S.B., Mair, K., and Di Toro, G., 2013, Mirror-like faults and power dissipation during earthquakes: Geology, v. 41, p. 1175–1178, https://doi.org/10.1130/G34641.1.
Green, H.W., II, Shi, F., Bozhilov, K., Xia, G., and Reches, Z., 2015, Phase transformation and nanometric flow cause extreme weakening during fault slip: Nature Geoscience, v. 8, p. 484–489, https://doi.org/10.1038/ngeo2436.

Herwegh, M., and Kunze, K., 2002, The influence of nano-scale second-phase particles on deformation of fine grained calcite mylonites: Journal of Structural Geology, v. 24, p. 1463–1478, https://doi.org/10.1016/S0191-8141(01)00144-4.
Hobbs, B., and Ord, A., 2014, Structural Geology: The Mechanics of Deforming Metamorphic Rocks: Amsterdam, Elsevier, 665 p., https://doi.org/10.1016/C2012-0-01215-X.
Poirier, J.-P., 1985, Creep of Crystals: Cambridge, UK, Cambridge University Press, 260 p., https://doi.org/10.1017/CBO9780511564451.
Rice, J.R., 2006, Heating and weakening of faults during earthquake slip: Journal of Geophysical Research: Solid Earth, v. 111, B05311, https://doi.org/10.1029/2005JB004006.
Sammis, C.G., and Ben-Zion, Y., 2008, Mechanics of grain-size reduction in fault zones: Journal of Geophysical Research: Solid Earth, v. 113, B02306, https://doi.org/10.1029/2006JB004892.
Siman-Tov, S., Aharonov, E., Boneh, Y., and Reches, Z., 2015, Fault mirrors along carbonate faults: Formation and destruction during shear experiments: Earth and Planetary Science Letters, v. 430, p. 367–376, https://doi.org/10.1016/j.epsl.2015.08.031.
Siman-Tov, S., Aharonov, E., Sagy, A., and Emmanuel, S., 2013, Nanograins form carbonate fault mirrors: Geology, v. 41, p. 703–706, https://doi.org/10.1130/G34087.1.
Smith, S.A.F., Nielsen, S., and Di Toro, G., 2015, Strain localization and the onset of dynamic weakening in calcite fault gouge: Earth and Planetary Science Letters, v. 413, p. 25–36, https://doi.org/10.1016/j.epsl.2014.12.043.
Smith, S.A.F., Di Toro, G., Kim, S., Ree, J.-H., Nielsen, S., Billi, A., and Spiess, R., 2013, Coseismic recrystallization during shallow earthquake slip: Geology, v. 41, p. 63–66, https://doi.org/10.1130/G33588.1.
Spagnuolo, E., Plümper, O., Violay, M., Cavallo, A., and Di Toro, G., 2015, Fast-moving dislocations trigger flash weakening in carbonate-bearing faults during earthquakes: Scientific Reports, v. 5, p. 1–11, https://doi.org/10.1038/srep16112.
Tesei, T., Collettini, C., Viti, C., and Barchi, M.R., 2013, Fault architecture and deformation mechanisms in exhumed analogues of seismogenic carbonate-bearing thrusts: Journal of Structural Geology, v. 55, p. 167–181, https://doi.org/10.1016/j.jsg.2013.07.007.
Verberne, B.A., Spiers, C.J., Niemeijer, A.R., De Bresser, J.H.P., De Winter, D.A.M., and Plümper, O., 2013, Frictional properties and microstructure of calcite-rich fault gouges sheared at sub-seismic sliding velocities: Pure and Applied Geophysics, v. 171, p. 2617–2640, https://doi.org/10.1007/s00024-013-0760-0.
Yao, L., Ma, S., Platt, J.D., Niemeijer, A.R., and Shimamoto, T., 2016, The crucial role of temperature in high-velocity weakening of faults: Experiments on gouge using host blocks with different thermal conductivities: Geology, v. 44, p. 63–66, https://doi.org/10.1130/G37310.1.

Coseismic ultramylonites: An investigation of nanoscale viscous flow and fault weakening during seismic slip

Giacomo Pozzi [a],*, Nicola De Paola [a], Robert E. Holdsworth [a], Leon Bowen [b], Stefan B. Nielsen [a], Edward D. Dempsey [c]

[a] Department of Earth Sciences, Rock Mechanics Laboratory, University of Durham, Durham, DH1 3LE, UK
[b] Department of Physics, University of Durham, Durham, DH1 3LE, UK
[c] School of Environmental Sciences, University of Hull, Hull, HU6 7RX, UK

ARTICLE INFO

ABSTRACT

Faults weaken during the propagation of earthquakes due to the onset of thermally-activated mechanisms, which vary depending on the rock type. Recent experimental work suggests that carbonate-hosted faults are lubricated by viscous flow in nano-granular aggregates having ultramylonitic textures. However, their frail nature has often hindered unbiased characterisation of the textures and deformation mechanisms operating at such extreme conditions (strain rates as high as 10^4), which remain so far poorly investigated and understood.

We explore the formation, evolution and deformation mechanisms of coseismic ultramylonites in carbonate-hosted faults generated during high velocity (1.4 m s^{-1}), displacement-controlled shear experiments in a rotary apparatus. Microstructures were analysed using integrated SEM and TEM imaging while detailed crystallographic fabrics were investigated using the electron back-scattered diffraction (EBSD) technique.

Mechanical data show that the strength of the experimental fault decays dynamically with slip, according to a characteristic four stage evolution; each stage is associated with characteristic textures. Microstructural observations show that brittle processes dominate when the fault is strong (friction coefficients >0.6). Cataclasis, aided by twinning and crystal plasticity, operates forming an extremely comminuted shear band (mean grain size ~200 nm). As the fault starts weakening, shear localises within a well-defined principal slip zone. Here, thermally-activated grain size sensitive (GSS) and insensitive (GSI) creep mechanisms compete with brittle processes in controlling fault strength. GSI mechanisms produce strong monoclinic crystallographic preferred orientations in the slip zone, while textures and crystallographic orientations in adjacent locations do not evolve from the previous deformation stage. By the end of the transient weakening stage, the slip zone has reached a steady state thickness (30 μm) and shows a nanogranular ultramylonitic texture. The intensity of the crystallographic preferred orientation in the coseismic ultramylonite is reduced compared to the previous stage, due to grainsize sensitive creep mechanisms becoming gradually more dominant. As the experimental fault re-strengthens, upon deceleration to arrest, the ultramylonite may be partially reworked by brittle deformation.

Our findings show that the crystallographic orientations of transient microstructures are preserved in the slip zone of coseismic ultramylonites and in narrow, adjacent deactivated layers, where mirror-like surfaces are located. This shows that EBSD techniques can usefully be employed to determine the deformation mechanisms of coseismic ultramylonites and their evolution during earthquake slip in both experimental and, potentially, natural faults.

Crown Copyright © 2019 Published by Elsevier B.V. This is an open access article under the CC BY license (http://creativecommons.org/licenses/by/4.0/).

1. Introduction

Faults are classically viewed as the main expression of brittle deformation in the upper crust. The macroscopic to microscopic fabrics of fault zones are known to evolve with depth and tem-

* Corresponding author.
    E-mail address: giacomo.pozzi@durham.ac.uk (G. Pozzi).

perature (Sibson, 1977; Faulkner et al., 2010). However, their rheology and fault rock development are also strongly determined by a wide range of strain rates such as in slow, creeping faults to fast, seismogenic ones (e.g. Spray, 2010). An example of this dependence of fault rocks on strain rate is given by pseudotachylytes (Sibson, 1977), which are found in natural faults where they form due to almost instantaneous frictional melting during the propagation of earthquakes. In particular, very large local strain

rates can be attained during seismic slip and, as a consequence of shear heating, thermal activated processes, such as frictional melting, become a dominant factor in controlling the strength of the fault (Di Toro et al., 2006). Similarly, other thermally activated processes, such as flash heating (e.g. Goldsby and Tullis, 2011; Rice, 2006) and thermal pressurisation (e.g. Rice, 2006; Sibson, 1973) can take place and produce transient coseismic decreases in fault strength.

Recent experimental studies have also proposed that the onset of viscous deformation mechanisms in ultrafine grained fault rocks could also lead to coseismic dynamic weakening (Green et al., 2015; De Paola et al., 2015; Pozzi et al., 2018). In particular, in carbonate rocks, grain size sensitive (GSS) creep processes could become dominant, with textural and mechanical evidence pointing to the transient operation of grain boundary sliding (GBS) mechanisms (De Paola et al., 2015; Green et al., 2015). It has been shown that ultramylonite-like domains may form during seismic slip in carbonate-hosted experimental faults (Smith et al., 2015) and that they localise most of the deformation (Pozzi et al., 2018).

Ultramylonites are very fine-grained fault rocks produced by dynamic recrystallisation and creep deformation mechanisms during high-T ductile deformation (Sibson, 1977). Such deformation mechanisms are known to accommodate viscous flow and aseismic behaviour in lower crustal and lithospheric mantle shear zones deforming at low strain rates ($\ll 10^{-8}$ s^{-1}). Also, these deformation mechanisms have previously been observed at high strain rates for a range of nano-phase alloys (Chandra, 2002) and ceramics (Lankford, 1996) in association with superplastic behaviour. However, their role in controlling fault strength during deformation of fine- to ultrafine-grained geological materials at high strain rates ($>10^2$ s^{-1}) and sub-melting temperatures, characteristic of upper crustal seismic ruptures, is still poorly understood.

In this paper we document the development of coseismic ultramylonites produced experimentally at ultra-high, seismic strain rates, and describe in detail their structures by analysing their crystallographic preferred orientation (CPO) fabrics and their microstructural evolution throughout the dynamic weakening history. We use these findings to infer how deformation mechanisms compete in controlling fault strength at a nanograin scale during episodic seismic slip events.

2. Methods

2.1. Experimental procedure

Friction experiments were performed using a low to high velocity rotary shear apparatus at the Durham Rock Mechanics Laboratory using simulated fault gouge, which consists of fine grained (grainsize between 63 μm and 90 μm) calcite powder. The apparatus and sample assembly are described in detail in the work of De Paola et al. (2015) (see also Hirose and Shimamoto, 2005; Pozzi et al., 2018).

Experiments were run at room temperature and dry conditions (relative humidity ~40%). Samples (1 g of gouge) were first loaded up to the maximum axial pressure $\sigma_n = 25$ MPa and then sheared at velocities of $v = 1.4$ m s^{-1} (calculated at the reference radius of 8.9 mm). A series of experiments were stopped after different amounts of displacement (4.5, 7, 25 and 90 cm at the reference radius) in order to document the microstructural evolution of recovered samples throughout the slip weakening history.

After each run, samples were carefully removed to preserve the full layer thickness, embedded in epoxy and cut parallel to the slip direction at a distance equal to the reference radius. This procedure preserves an X-Z cross-section, where X is parallel to the slip direction and Z is perpendicular to the shear zone boundary. The
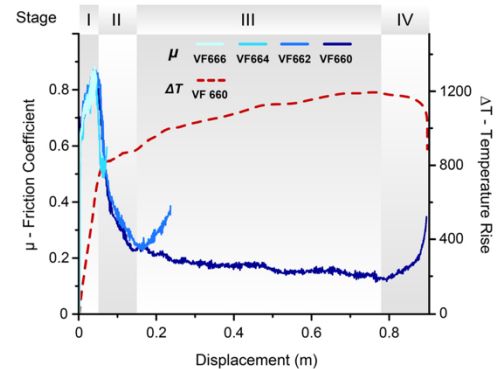

Fig. 1. Mechanical data ($v = 1.4$ m s^{-1}, $\sigma_n = 25$ MPa): friction coefficient (μ, solid lines) and estimated temperature rise in the principal slip zone (ΔT, dashed line) curves are plotted versus displacement. Temperature is calculated using a simple mono-dimensional thermal diffusion model (e.g. Rice, 2006; see also Supplementary Material I). The four stages of friction evolution are highlighted in the graph by the shaded areas. (For interpretation of the colours in the figure(s), the reader is referred to the web version of this article.)

cut surface was then lapped with diamond paste down to 0.25 μm and polished using colloidal silica.

2.2. Microstructural analysis

Microstructural analysis was carried out on polished cross-sections using a FEI Helios Dual Beam Nanolab 600 scanning electron microscope (SEM at the Department of Physics of Durham). SEM images were acquired in backscatter (BS), using the through-the-lens acquisition system, and forescattered (FS) modes. FS is operated on 70° tilted specimens using a 4 Quadrant KE Development FS imaging control detector. Electron back-scattered diffraction (EBSD) data were collected on uncoated tilted specimens using an Oxford Instruments Nordlys HKL detector (AZtec acquisition software, Oxford Instruments). For this technique, we used a working distance of 14-15 mm and a step size of 0.2 μm. Operating conditions were 10-20 kV of accelerating voltage and 1.4 nA current. EBSD data have been processed (including initial data cleaning) and analysed using CHANNEL5 software (HKL Technology, Oxford Instruments). Grain boundaries were defined at misorientation angles $\geq 10°$. Grains with less than 5 data points (pixels) were discarded (i.e. with an equivalent diameter below ~0.45 μm).

3. Experimental results and microstructural observations

3.1. Mechanical data

The experimental deformation of the calcite gouges displays a dynamic weakening history in agreement with many previous studies (e.g. Di Toro et al., 2011; Fondriest et al., 2013; De Paola et al., 2015; Siman-Tov et al., 2015; Smith et al., 2013, 2015; Pozzi et al., 2018). The friction curve follows a characteristic four stage evolution (Fig. 1). During Stage I, strain hardening behaviour is observed with friction coefficients in the Byerlee's range ($\mu = 0.6$-0.9). Stage II includes the onset of dynamic weakening, following the achievement of frictional peak values, and rapid decay of the fault strength to low friction coefficients. Stage III shows low friction values ($\mu = 0.1$-0.2), which continuously decrease following a very shallow slope. Stage IV takes over upon deceleration of the apparatus when the fault strength recovers up to values of
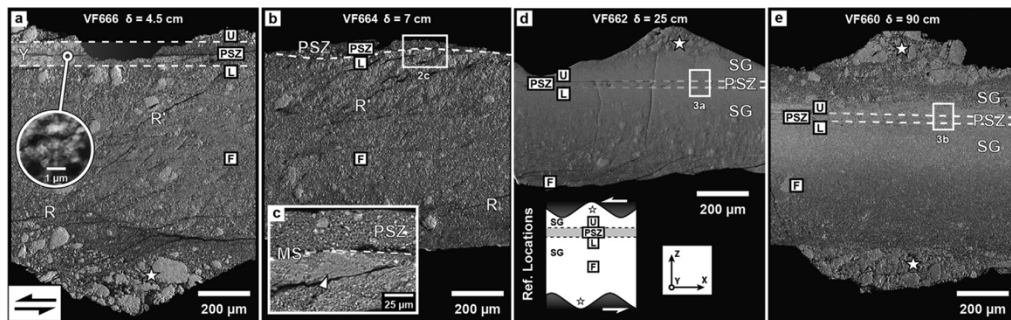
Fig. 2. Backscattered electron images of sample cross sections obtained from the whole thickness of gouge layers cut at the reference radius. The fault displacement, δ, is shown for each microstructure. Relicts of the starting coarse-grained gouge are preserved in the grooves machined on the top and bottom cylinder surfaces, indicated with white stars. Shear sense is sinistral. U, PSZ, L and F squares indicate the locations where EBSD analysis has been performed (see text for details). a) Stage I: diffuse and localised deformation with Riedel shears (R, R′) and a horizontal Y shear band (Y). In the inset, close-up showing the extreme grainsize reduction within the Y shear band. b) Stage II: well-developed principal slip zone (PSZ) with patchy recrystallised boundary ("mirror-like surfaces", MSs). c) Close-up of area outlined in b) showing a polygonal sintered patch below an embryonic MS. d) Early Stage III: fully developed PSZ bounded by MSs and sintered, deactivated layers (sintering gradient, SG). e) Late Stage III: microstructure similar to that of early Stage III (Fig. 2d) but the SG is wider and more strongly developed. The framed U, PSZ, L and F are the reference locations (see schematic inset in Fig. 2d).

$\mu = 0.4$-0.5. The local temperature rise (Fig. 1, red line) is calculated using a simple mono-dimensional thermal diffusion model (e.g. Rice, 2006; see Supplementary Material I).

3.2. Microstructure evolution throughout the weakening history

Each of the four main stages recorded throughout the weakening history is associated with a characteristic fault/shear zone architecture (Pozzi et al., 2018).

Stage I slip hardening is associated with structures and microstructures typical of the brittle regime. Samples show numerous R, R′ (Riedel) shears and a shear-parallel Y shear band (∼200 μm thick), which generally nucleates close to the top (rotating) cylinder (Fig. 2a). Brittle deformation is distributed throughout the entire gouge layer, which shows pervasive brittle grain size reduction. Extreme strain localisation occurs in the Y-shear band where grain size reduction even down to few tens of nm is observed (inset of Fig. 2a).

Following the achievement of peak friction, the Y shear band becomes a well-defined principal slip zone (PSZ) that becomes increasingly confined between sharp boundaries (Fig. 2b). In its embryonic stage, patchy volumes of polygonal grains form in the low-strain domains outside the PSZ (Fig. 2c). The recovered samples easily split along the PSZ boundaries revealing the reflective surface of the polygonal patches. These have been interpreted as the (embryonic) mirror-like surfaces (MSs) formed by sintering processes (Fondriest et al., 2013; Siman-Tov et al., 2013; Smith et al., 2013; full details in Pozzi et al., 2018). Inside the PSZ, the material is still porous and has an inhomogeneous grain size (Fig. 2c), with larger grains (∼1 μm) embedded in a much finer matrix (∼200 nm). At the end of Stage II - early Stage III, the PSZ has thinned by up to an order of magnitude (∼30 μm width) and shows parallel, sharp, sintered boundaries forming continuous, flat MSs (Figs. 2d and 3a). The localisation process appears to progressively abandon several (now relict) MSs in the outer deactivated layers, a process referred to here as "MSs migration".

By Stage III, the PSZ is characterised by polygonal grains, very low porosity and homogeneous grainsize (∼300 nm, Fig. 3a). The crystals typically show a shape preferred orientation defining an oblique foliation, consistent with the shear sense. The texture of the PSZ itself is comparable to that of natural (Bestmann et al., 2000; Herwegh and Kunze, 2002) and experimental (Barnhoorn et

al., 2004) ultramylonites. Hereafter, we refer to these textures as 'coseismic ultramylonite' textures. The oblique foliation of the PSZ is interpreted to be the result of cycles of dynamic recrystallisation and passive rotation of grains (e.g. Barnhoorn et al., 2004, and references therein). The volumes outside the PSZ have a much coarser grain size (up to 1-2 μm) and extend outward for several tens of μm forming a so-called 'sintering gradient' (SG; Fig. 2d; Pozzi et al., 2018). The latter is evident from the observed decrease of mean grainsize and increase of porosity moving away from the PSZ.

The architecture of the PSZ and the surrounding material does not change substantially throughout Stage III. The PSZ maintains a stable thickness while the sintering gradient expands away from the PSZ and becomes stronger (Figs. 2e and 3b). Significantly, the grainsizes within the PSZ and in the sintered regions grow (700 nm and up to 3-4 μm, respectively, after 65 cm of slip) with displacement and inferred rise in temperature (Fig. 3b).

Earlier formed microstructures are overprinted, but not destroyed, by the latest stages of deformation that take place upon deceleration of the machine to arrest. The Stage IV PSZ is commonly reworked and fragmented due to the effects of embrittlement. Continuous MSs are typically well preserved at the PSZ boundaries (Pozzi et al., 2018). At all stages in the experiments, the PSZ is composed exclusively of crystalline calcite showing that thermally-driven decarbonation reactions were not quantitatively significant (De Paola et al. 2015; Pozzi et al., 2018).
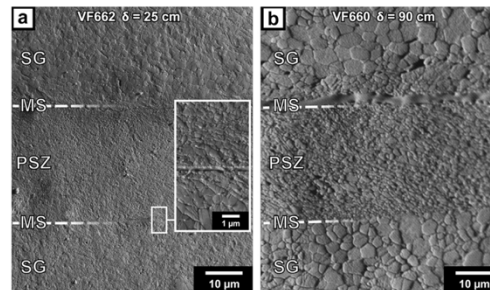

Fig. 3. Forescattered electron images of a) Early Stage III (close-up in the inset) and b) Late Stage III PSZ and surroundings. The PSZ maintains its thickness while grain size is observed to grow both within and outside the PSZ. Shear sense is sinistral.
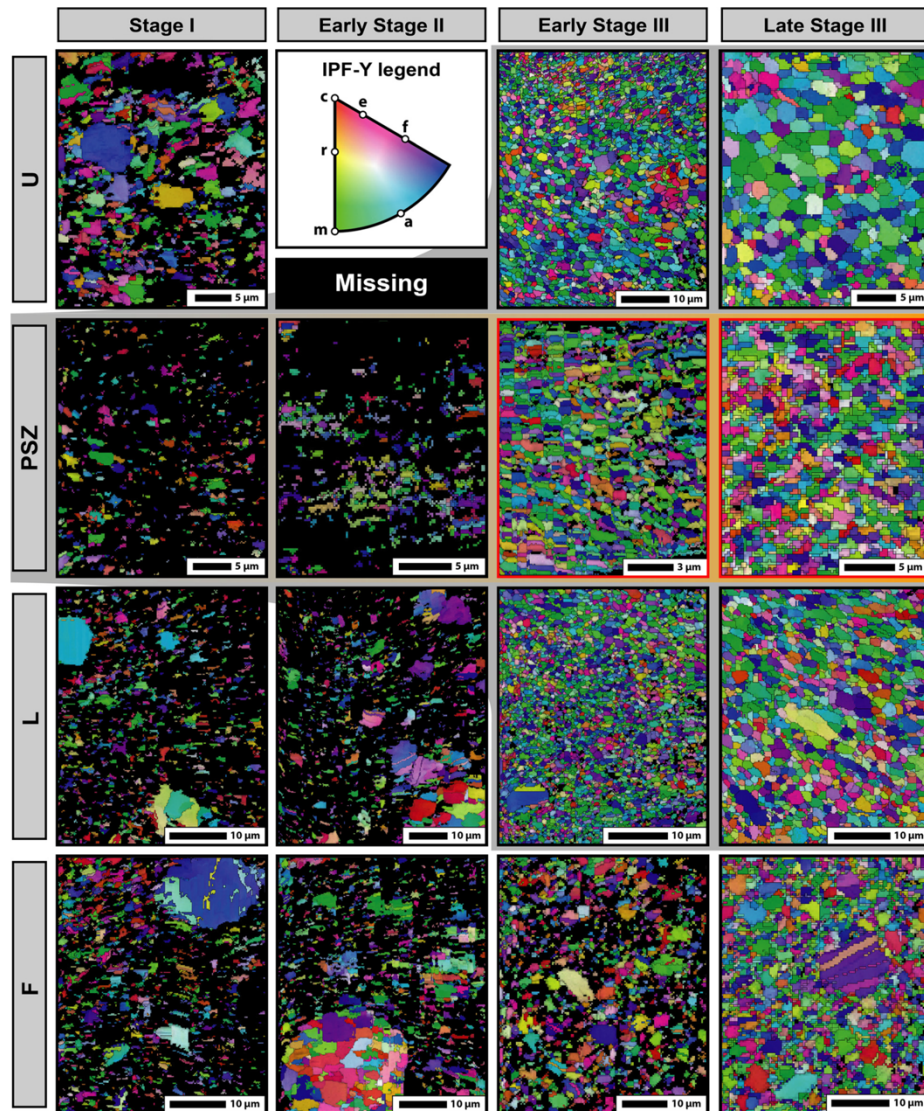
144

Fig. 4. EBSD orientation maps coloured using IPF-Y gradients. The legend shows important crystallographic directions (including c-axis and a-direction) and their IPF-Y colour. Grain boundaries (misorientation angles MAs $\geq 10°$) are contoured in black (better seen in Fig. SM3 in Supplementary Material III). Late Stage III U and L reference locations show that some of the larger grains are composed by coalescence of individuals sharing low MAs ($<10°$, i.e. grains containing subdomains with slightly different shades of IPF colouring). (For interpretation of the colours in the figure(s), the reader is referred to the web version of this article.)

4. Characteristic textures of coseismic ultramylonites revealed by EBSD data

4.1. Methods

The nature and evolution of grain crystallographic orientation patterns can be investigated using electron back scattered diffrac-

tion (EBSD) analysis (e.g. Prior et al., 1999). This gives important quantitative insights into the nature and evolution of grain scale mechanisms, which can then be related to the other microstructural observations and bulk mechanical data obtained during the experimental deformation of calcite microgouges reported here.

We performed EBSD analysis on the same polished cross sections (X-Z plane) used for the microstructural characterisation. In
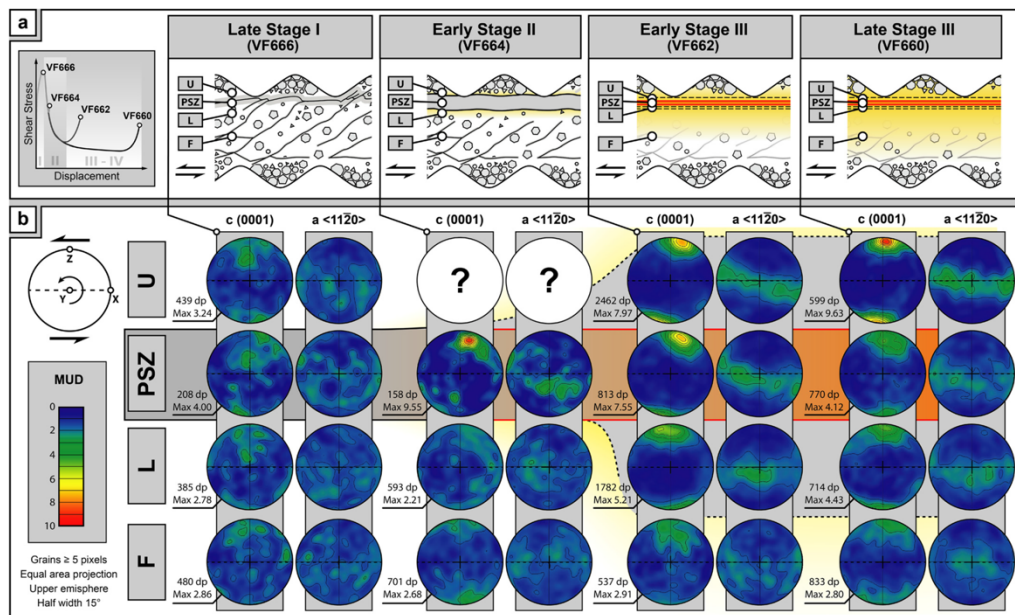
Fig. 5. a) Schematic representation of mechanical data, microstructures and locations of the four analysed reference areas (U, PSZ, L and F). Orange and yellow shading are used to highlight the viscous PSZ and the sintering gradient, respectively. b) EBSD pole figures (one pixel per grain, for grains ≥5 pixels) for two selected crystallographic directions for calcite: c-axis plane, (0001), and a-axis-direction, <11-20>. Poles are plotted in an equal area projection on the upper hemisphere. Multiples of uniform density (MUD) colouring applies to all of the pole figures. (For interpretation of the colours in the figure(s), the reader is referred to the web version of this article.)

particular, four critical moments of the deformation history are investigated: i) Stage I, ii) early Stage II, iii) early Stage III and iv) late Stage III (Figs. 1–2). Four distinct reference locations are selected in the samples, each preserving the characteristic deformation features of these stages (Fig. 2 and inset of Fig. 2d). One is located within the PSZ (which correspond to the Y-shear band formed during Stage I) and two lie immediately outside its boundaries, in the upper (i.e. U, towards the rotating cylinder) and lower (e.g. L, towards the stationary cylinder) outer SG layers (Figs. 2d, 5 and 6). Note that U and L positions are not fixed as the active PSZ boundaries migrate during localisation. The fourth location, F, is chosen halfway between the lower PSZ boundary and the stationary cylinder. This reference location is fixed and never lies close to the PSZ at any of the four deformation stages. Given their frail nature, samples were polished with particular care. However, as it is difficult to completely remove the grain topography, this makes the indexing of EBSD data variable, ranging from a minimum of 20% of Stage I gouges successfully measured up to 95% in the sintered layers of Stage III.

The EBSD data were processed to visualise the crystallographic orientation of calcite grains using orientation maps (Fig. 4, coloured using IPF-Y gradient), to analyse the orientation of relevant crystallographic elements with pole figures (Fig. 5, using one point per grain and plotted on equal-area projections, upper hemisphere) and to perform misorientation analyses (Fig. 6). In our samples, two representative crystallographic directions are selected: (0001) c-axis plane and <11-20> a-axis direction. Results for other directions and planes can be found in the Supplementary Material (section IV). Pole figures were contoured using the orientation distribution function (Bunge, 1981) calculated with a half width of 15°. This value is chosen for consistency reasons with some of the cited articles (e.g. Bestmann et al., 2000; Pieri et al., 2001; Barnhoorn et al., 2004).

Due to the extremely small grain size observed locally in the samples (<450 nm), we also report in Supplementary Material V pole figures that include grains containing less than 5 pixels. These pole figures do not differ substantially from those reported (Fig. 5), but include information from small grains that might have been lost.

Misorientation analysis is used to quantify the overall distribution of crystal orientations and is utilised herein to investigate the deformation mechanisms responsible for each texture (Wheeler et al., 2001). The misorientation angle, MA, is the minimum angle describing the difference in crystallographic orientation between two grains, and can be measured for neighbouring (grains sharing a boundary) or random (randomly picked grains) pairs. Measured MAs provide an indication of the grain lattice transformation – taking into account the symmetry – that lead to differently oriented grains. The relative frequency of MAs falling within an orientation range (bins having a width of 5° in this work) can be plotted in a diagram for each selected range (e.g. 22 bins between 0° to 110°), thus producing neighbour-pair and random-pair MA distributions (MAD), respectively. MAs < 2° were discarded as these values lie close to the resolution of the measurements. The reference theoretical misorientation angle distribution for a random distribution (TRD) of trigonal crystals (Wheeler et al., 2001) is shown along with the MAD data in Fig. 6.
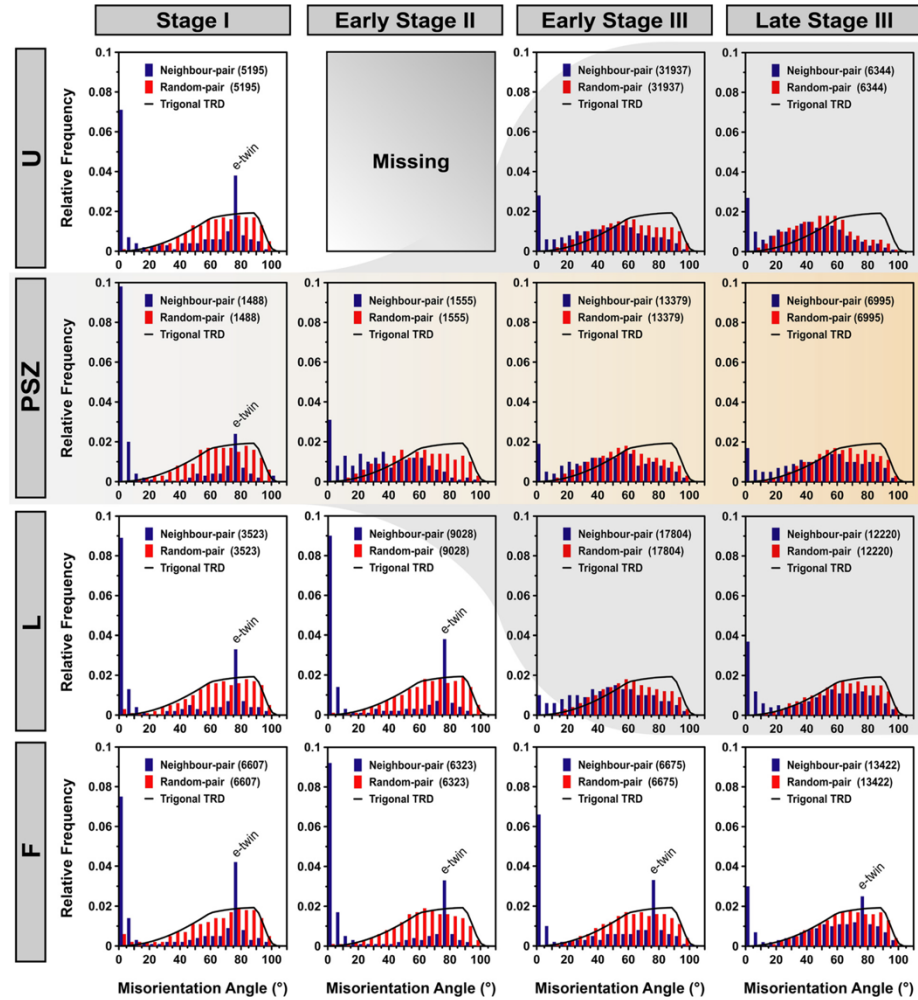
Fig. 6. Misorientation analysis plots showing neighbour-pair MAD (blue bars), random-pair MAD (red bars) and theoretical random distribution (TRD) for trigonal crystals (black curve). The bin width of each misorientation angle (MA) group is 5°. MAs <2° are disregarded as they lie within the resolution of measurement. (For interpretation of the colours in the figure(s), the reader is referred to the web version of this article.)

4.2. Results

4.2.1. Deformation Stage I

During Stage I, the PSZ reference location is in the proto-PSZ (the Y-shear band) while U, L and F lie in the Riedel-shear dominated sample region (Figs. 2a and 5a). The latter areas typically show a strongly heterogeneous grainsize, with larger particles (≫1 μm) dispersed in a finer matrix; this contrasts with the more comminuted – but still heterogeneous grainsize – PSZ (mean grainsize ∼200 nm). Stage I materials are poorly consolidated and porous, which hindered the polishing procedure. As a result of the topographic effects caused by the poor polish, data from loose nanoparticles could not be retrieved and large areas of

non-indexed material (dark areas) dominate the EBSD maps at this stage (Fig. 4, Stage I). Hence, the interpretation of crystallographic data is necessarily restricted to detected grains, which are overall larger than 1 μm.

Pole figures show a relatively weak clustering of the calcite c-axes at a small angle to the Z direction, especially in the PSZ (Fig. 5b). This produces a weak crystal preferred orientation (CPO), with multiple uniform distributions (m.u.d.) smaller than 4. Each of the four reference locations produces very similar misorientation plots (Fig. 6). The neighbour-pair MAD shows a strong maximum at low MAs (<10°, MA used to separate between grain and sub-grain boundaries), with the highest frequency found in the PSZ. Another peak is located between 75°-80° MAs, the lowest of which occurs

in the PSZ (Fig. 6). This peak is likely related to e-twinning of calcite (e {01-18}; e.g. Bestmann and Prior, 2003). The random-pair MAD deviates slightly (especially in L and F locations at the low MAs, <10°) from the theoretical misorientation angle distribution for a random distribution (TRD) of trigonal crystals (TRD in Fig. 6). This is consistent with the presence of the weak CPO in all locations (Fig. 5).

4.2.2. Early Deformation Stage II

During early Stage II, when the material has started to weaken, clustering of c-axes produces a strong monoclinic CPO (m.u.d. = 9.55) within the PSZ domain, tilted clockwise – consistent with the sinistral shear sense – at a small angle with respect to Z-direction (Fig. 5b). The a-axes form distinct maxima (better seen in Fig. SM8, Supplementary Material V) on the great circle lying at a low angle to the XY plane (Fig. 5b). This pattern is typical of simple shear deformation of calcite (e.g. Wenk et al., 1987). Within the PSZ, the random-pair MAD deviates from the TRD due to the development of the strong CPO. The e-twin peak disappears from the neighbour-pair MAD and the frequency of low MAs (<10°) decreases (Fig. 6). In reference locations L and F, textures and crystallographic data do not differ substantially from Stage I. The U domain could not be retrieved due to the delicate nature of the samples.

By the end of Stage II, localisation processes have ended and PSZ has reached a steady state thickness of 30 μm (Fig. 3).

4.2.3. Early Deformation Stage III

During early Stage III, the PSZ is non-porous and shows a nanogranular ultramylonitic texture. The CPO is comparable to that of the Stage II PSZ, but is slightly weaker (m.u.d. of 7.55, Fig. 5b). The dominant green and blue IPF-Y colouring indicates a prevalence of a-axis and m <10-10> directions, respectively, parallel to the Y direction (Fig. 4). In the PSZ, the random-pair MAD is bell-shaped, centred on the MA bin between 55 and 60°, reflecting the distribution of a-maxima (Fig. 6 and Fig. SM8 in Supplementary material V). The neighbour-pair MAD is similar, but the peak at low angles has become weaker compared to previous stages.

Due to the narrowing of the PSZ (during Stage II), the U and L reference locations are now within the sintered gradient below and above the PSZ, respectively, containing the array of relict MSs (Figs. 2d and 5a). These reference locations are non-porous and their sintered texture is similar to that of the PSZ as well as their CPO, but with a different intensity (Fig. 5b). The U location shows a clear maximum at low MAs (<10°, Fig. 6), while the L location has a CPO that is apparently orthorhombic, with the c-axes parallel to Z (Fig. 5b). At this stage, the F location is still porous, but shows incipient sintering (densification and recrystallisation, Figs. 3d and 4). Here the pole figure and MAD show no substantial evolution from the previous stages (Figs. 5b, 6). However, the frequency of neighbour-pair low MAs (<10°) is slightly reduced (Fig. 6).

4.2.4. Late Deformation Stage III

At late Stage III, after ~75 cm of slip, the PSZ CPO has weakened substantially (m.u.d. of 4.12, Fig. 5b) and the girdle formed by a-axes is spread over a wider area. The a-maxima have completely disappeared. The random-pair MAD distribution in the PSZ has become closer to the TRD with an increase of the frequency of 70°-90° MAs (Fig. 6). No obvious change is observed in the neighbour-pair MAD.

The CPO in the U reference location strengthens and shows a clear monoclinic symmetry (Fig. 5b). The CPO in the L reference location does not vary substantially and remains similar to previous stages and to the PSZ domain (Fig. 5b). The random-pair MAD is also comparable to that of the PSZ (Fig. 6). However, the peak at low neighbour-pair MA is now much higher. The F location is now fully sintered and it is possible to see porphyroclasts

(>5 μm) inherited from Stage I embedded in a polygonal sintered matrix (Figs. 2e and 4). Again, the pole figure has not substantially evolved (Fig. 5b) despite becoming slightly weaker. This location also maintains a similar random-pair MAD close to the TRD, while in the neighbour-pair MAD, the two peaks (e-twin and low MAs) have substantially decreased (Fig. 6).

5. TEM imaging

Transmission Electron Microscope imaging was carried out on a JEOL 2100F FEG TEM (Department of Physics of Durham) in order to gain further insights into nanograin-scale processes. Two thin foil samples from the U and PSZ reference locations of experiment VF660 (Late Stage III) were prepared using focused ion beam (FIB) technique. Here, TEM imaging performed in scanning mode (S-TEM) reveals polygonal aggregates of slightly elongated crystals with mean aspect ratios of 1.37 and 1.62, respectively (Fig. 7a, e).

The grains in the U location have fairly homogeneous grain sizes (mean $D = 1.8$ μm) and display well-defined triple junctions and sharp crystal boundaries (Fig. 7b). These are generally straight, but locally display a slight curvature (Fig. 7b, black arrow). Grains show, on average, a homogeneous distribution of dislocation densities (Fig. 7b, c). Crystals appear fairly equant and weakly distorted (e.g. bend contours in Fig. 7a-d) and rare cavitation is observed at triple junctions (Fig. 7a, d). Dislocations are commonly elongated (hundreds of nm) and do not form large entanglements or dislocation walls (Fig. 7c, d). No subgrains are observed. Locally, some partially-healed triple junctions are found within grains (white arrow in Fig. 7d).

Grains in the PSZ are more irregular, with a mean D ~700 nm (Fig. 7e). Grains form triple junctions, and are commonly non-equiangular and cuspidate (Fig. 7f, white arrow), while grain boundaries are frequently curved (Fig. 7f, black arrow). Diffuse cavitation, which was not resolvable with SEM imaging, is observed at triple junctions and at grain boundary-parallel microfractures (Fig. 7e, white arrows). Grains in the PSZ contain dislocations (Fig. 7g) and neighbouring grains may have substantially different dislocation densities (e.g. Fig. 7f, compare the two grains in the centre of the picture). Curved grain boundaries are generally convex towards the most strained individual grain (Fig. 7 f). Furthermore, entanglements, dislocation walls (Fig. 7h, black arrow) and subgrains (Fig. 7h, white arrow) are observed within grains with higher density of dislocations.

6. Discussion

6.1. Low vs. high (coseismic) strain rate ultramylonites

The development of calcite mylonites and ultramylonites has been intensively studied (e.g. Schmid et al., 1987; Pieri et al., 2001; Barnhoorn et al., 2004; and references therein) at a range of high temperatures, but only at relatively low strain rates (<10^{-3}). Our new microstructural evidence and CPOs analyses show that coseismic ultramylonites can also form when initial calcite microgouges are sheared under extremely high strain rate coseismic slip conditions.

The textures of the coseismic ultramylonites described here are strikingly similar to those of ultramylonites obtained in high displacement torsion experiments carried out under elevated temperature conditions at much lower strain rates (Pieri et al., 2001; Barnhoorn et al., 2004), and predicted by theoretical studies (Wenk et al., 1987). Our mechanical data and microstructural observations show that the processes that control fault weakening of coseismic ultramylonites may not differ substantially from those observed in lower strain rate ultramylonites. However, coseismic ultramylonites must operate at the nanoscale in order to accommodate high seismic strain rates at sub-melting temperatures.
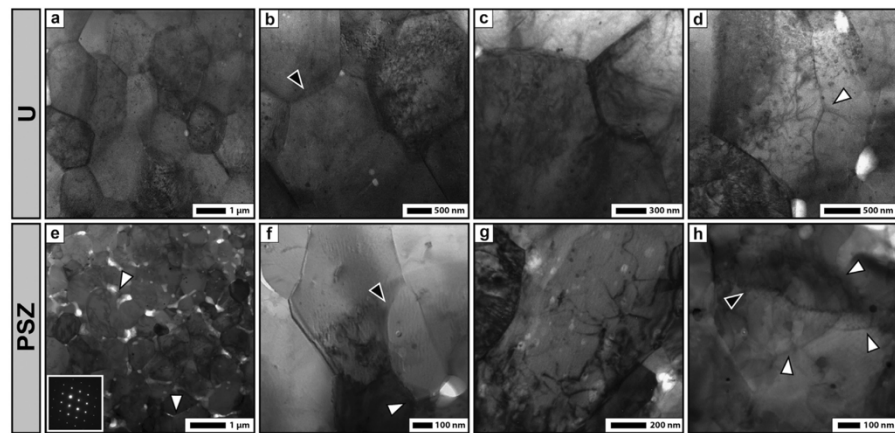
Fig. 7. Bright field S-TEM images of the U (a-d) and PSZ (e-h) domains of experiment VF660 (δ = 90 cm, Late Stage III). a) Equant grains displaying tightly packed structure with well-defined triple junctions and rare cavitation; b) Slight curvature of the grain boundaries (black arrow); c) Crystals containing numerous dislocations but few bend contours; d) Partially healed triple junction (white arrow) within a grain and cavitation at triple junctions (white areas). e) Sub-equant grains displaying tightly packed structure with triple junctions, diffuse cavitation (white spots) and microcracking (e.g. white arrows), inset shows a clear diffraction pattern attesting the non-amorphous nature of grains in the PSZ; f) Curved boundaries (black arrow) and cuspidate triple junctions (white arrow); g) Dislocations in a grain; h) Subgrains (e.g. white arrows) bordered by well-organised dislocation walls (e.g. black arrow).

6.2. Evolution of the architecture and deformation mechanisms of coseismic ultramylonites during seismic slip propagation

During high velocity friction experiments on calcite gouge, mechanical data show that the strength of the material evolves dynamically with slip, and the friction curve follows a characteristic four stage evolution (Fig. 1). Our microstructural observations reveal a shear zone-like architecture where shear localises within a PSZ from the very early stages of deformation. Hence, microstructural observations and EBSD data have been collected at four distinct reference locations: within the PSZ, in the sintered layers immediately outside the PSZ (U, L locations) and away from the PSZ (F location).

Our data show that each of the four main stages recorded throughout the weakening history is associated with characteristic microstructures in the PSZ and surrounding areas. Such observations are used below to propose a conceptual model describing the dynamic evolution of processes and deformation mechanisms associated with the development of nanometric grain size ultramylonites during seismic slip.

6.2.1. From gouge-cataclasite to nanometre grainsize ultramylonite

During high velocity friction experiments on calcite gouge, mechanical data show that the strength of the material changes dynamically with slip, as temperature rises due to frictional heating. This suggests that, during shear localisation in the principal slipping zone, thermally activated weakening mechanisms must be dominant. Such hypotheses are supported by microstructural observations showing a transition from cataclastic shear band textures to nanoscale ultramylonites, with rising temperature during seismic slip.

- *Slip hardening behaviour during cataclastic flow* (*Deformation Stage I*)

During Stage I, when the deforming gouge displays slip hardening behaviour, deformation is mainly brittle preserving evidence of widespread grainsize reduction and localisation into a proto-PSZ

(Y-shear band, Fig. 2a). At this stage, the material is still porous and only slightly cohesive. Random-pair MAD of the grains plots close to the trigonal TRD, suggesting that crystal orientations are only weakly influenced by the directionality of the stress field (Fig. 6). This is consistent with what is predicted to occur during cataclastic shear flow, when particles are continuously rearranged in a random fashion with increased mobility of the finer grainsizes (e.g. Hutter and Rajagopal, 1994, and references therein).

The neighbour-pair MAD reveals that two coeval plastic mechanisms take place during cataclasis. The first, e-twinning of calcite (peak at MA = 75°-80°, Fig. 6), is typical of low temperature deformation regimes and is intimately related to stress concentration effects along grain contacts (Wenk et al., 1973; Schmid et al., 1987; De Bresser and Spiers, 1997). e-twinning is unable to accommodate large amounts of strain (Schmid et al., 1987; Burkhard, 1990) and we suggest that it happens at the very beginning of deformation. This process produces rotation of the calcite c-axes toward the maximum stress axis (σ') within its surrounding 26° small circle (Schmid et al., 1987), a mechanism possibly responsible for the weak CPO seen for Stage I in all domains in the deforming gouge layer. Alternatively, the strong peak at low MAs could be related to the activity of plastic processes such as subgrain rotation recrystallisation (MAs < 10°). This is supported by the fact that MAs below 10° measured in the compressed gouge (pre-shear material) are far less frequent than those observed in all reference locations during Stage I (Supplementary Material II, Fig. SM1 c).

Subgrains with dimensions (<200 nm) comparable to those of the nanograins formed during Stage I (inset of Fig. 2a) are also found in the Stage III PSZ. Such evidence supports the hypothesis that mechanisms such as shock-like stress release processes (Sammis and Ben-Zion, 2008; Spagnuolo et al., 2015) and brittle failure aided by intragranular crystal plasticity (Siman-Tov et al., 2013; De Paola et al., 2015) produce the extreme grainsize reduction measured in the shear bands within the samples.

Thus, we conclude that during Stage I, the dominant strain-accommodating mechanism is brittle (Fig. 8a, c).
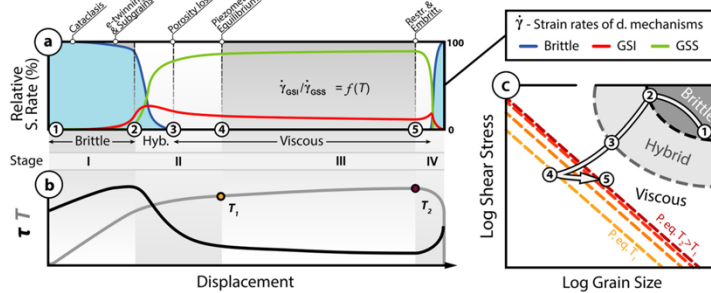
149

Fig. 8. Conceptual model for the dynamic evolution of deformation mechanisms in the PSZ constrained using microstructural evidence, including EBSD. a) Conceptual partitioning of shear strain rates ($\dot{\gamma}$) accommodated by brittle (blue), grain size insensitive creep (GSI, red) and grain size sensitive creep (GSS, green) during the different Stages (I–IV) of deformation. It is assumed that at any moment, they sum to 100% of the total strain rate in the PSZ (see text for details). b) Schematic evolution of stress (τ) and temperature (T) during a high velocity experiment. c) Deformation path experienced by the PSZ in a schematic deformation mechanism map. Dashed lines represent the grain size piezometric equilibrium at different moments during Stage III, where grain size is directly related to the stress state by a temperature-dependent piezometric law. Circled numbers link to the position of the event in (a). (For interpretation of the colours in the figure(s), the reader is referred to the web version of this article.)

- *Transient strength decay to quasi steady-state low strength* (*Deformation Stage II*)

By Stage II, the bulk temperature rise, due to frictional heating, is such that other plastic processes become competitive in accommodating strain in the PSZ. In fact, at this temperature ($>700\,^\circ$C) and strain ($\gg10$), e-twinning is no longer efficient (De Bresser and Spiers, 1997), and so its peak completely disappears from the neighbour-pair MAD through recovery (Fig. 6). Its disappearance is also consistent with the observed pervasive grainsize reduction – below the dimension of the twins (Rowe and Rutter, 1990) – operating in the PSZ.

The deformed material becomes less porous due to yielding of nanoparticles and progressive grainsize homogenisation. The observed strong c-axis CPO in the PSZ (Fig. 5b) is explained by the operation of grain size insensitive, GSI, creep mechanisms, such as subgrain rotation (MAS $< 10^\circ$ in Fig. 6), which operate during dynamic recrystallisation processes (dislocation creep, Fig. 8a, c).

By the end of Stage II, the PSZ is fully localised and does not substantially change its thickness throughout Stage III.

- *Viscous flow during slip at quasi steady-state low strength* (*Deformation Stage III*)

During Stage III, the PSZ hosts an ultramylonite with a fairly homogeneous grainsize, triple junctions and oblique foliation (Fig. 3). The strong CPO developed during Stage II is observed to progressively weaken throughout Stage III, as shown by the random-pair MAD that migrates toward the trigonal TRD (Fig. 5b). A progressive attenuation of the CPO in the PSZ could be explained by the increasing activity of diffusion creep, which is enhanced by the reduction of grainsize and temperature rise (Bestmann and Prior, 2003). Wheeler (2009) showed with his model that a transition to a diffusion-creep-dominated regime will weaken, but not destroy the CPO (see also Rutter et al., 1994). This effect is sustained by grain rotation and especially grain growth, which is observed in samples sheared throughout Stage III (Fig. 3).

However, it should be noted that the neighbour-pair MAD in the PSZ is almost identical during both the early and late Stage III (Fig. 5b). Therefore, we suggest that the major switch in rheology happens during Stage II while a quasi-steady-state regime is maintained throughout Stage III (Fig. 8a, c). At the beginning of Stage III, a piezometric equilibrium – i.e. between grain size reduction operated by GSI mechanisms (e.g. see subgrains in Fig. 7h)

and grain growth driven by thermal processes – is reached within the ultramylonitic PSZ (Fig. 8a, c). At equilibrium conditions, the grain size should be directly related to the stress state, following a temperature-dependent piezometric law (e.g. De Bresser et al., 2001, 1998; Fig. 8c). Importantly, we observe that during Stage III, the mean grain size grows with slip within the PSZ (Fig. 3a and 3b, Pozzi et al., 2018), suggesting that grain size is directly related to the rising temperatures (Fig. 8c; De Bresser et al., 1998, 2001).

Our microstructural observations suggest that, during Stage III, a combination of grain size sensitive (GSS) and insensitive (GSI) creep mechanisms are active within the ultramylonitic PSZ (Fig. 8a, c). In their pioneering work, Ashby and Verrall (1973) recognised that, although GSI and GSS creep mechanisms are described by two independent flow mechanisms, they are likely to occur simultaneously in nature. In this case, the overall creep rate is given, to a sufficient approximation, by the sum of their relative contribution (Fig. 8a). The interplay between GSI and GSS creep mechanisms is well known in material sciences from observations, theory (e.g. Ashby and Verrall, 1973; Nieh et al., 1997) and modelling (Bower and Wininger, 2004; Cipoletti et al., 2011) of grain boundary sliding accommodated superplasticity. However, modelling diffusion creep coupled to intracrystalline plasticity has been an intractable problem in geoscience, leading to generic uncertainties with flow laws which combine these processes.

Therefore, we conclude that the dynamic weakening of nanometre aggregates in seismic ultramylonites involves competition between multiple and evolving temperature-dependent mechanisms, whose quantification remains so far difficult.

- *PSZ ultramylonite embrittlement and fault restrengthening during slip deceleration* (*Deformation Stage IV*)

During the experiments, there is always a fourth stage of deformation during sample deceleration to arrest, when the fault strength is partially recovered. The most prominent damage produced during this stage is the embrittlement of the PSZ ultramylonite, leading to splitting along the MSs (Pozzi et al., 2018). The post-mortem PSZ is a cataclasite confined between the two last active MSs. S-TEM images show embrittlement in the PSZ due to cavitation and micro-fractures (Fig. 7e), which are interpreted to form when the PSZ material moves out of piezometric equilibrium as the temperature falls. These interpretations can help explaining the restrengthening observed during Stage IV. In most cases, the

reworking of the PSZ is modest and the ultramylonitic structure is rarely completely destroyed (Fig. 3).

6.2.2. Shear localisation by ultramylonite boundary migration during seismic slip

Microstructures suggest that the PSZ localises during Stage II with its width reducing from 200 μm to 30 μm (Fig. 2a-c). This process appears to occur by the inward migration of the PSZ boundaries – MSs – in discrete, non-continuous events. Each localisation step deactivates a portion of the PSZ forming a new PSZ boundary that migrates inwards. The deactivated boundary is left in the SG domain as a relict MS. These layers, when deactivated, dramatically change their deformation regime, as they show substantial grain growth while accommodating limited amounts of deformation. This is supported by the S-TEM microstructural observations of low grain aspect ratios, straight grain boundaries and low distortion of the lattice (Fig. 7a-d).

If these hypotheses hold, the U and L locations found in the SG, and containing the abandoned MSs, should "freeze" the PSZ CPO at different moments in its evolution during Stage II. SEM images show that relict and reworked MSs are present within the U locations, but are absent within the L locations, during early Stage II (Fig. 2c). These observations show that shear localisation occurred with an asymmetric migration of the upper and lower PSZ boundaries, where the upper U location deactivated prior to the lower L location (Pozzi et al., 2018). This interpretation is strongly supported by the observation that the U location has a stronger CPO than the L location (Fig. 5b), as the latter was active longer in the PSZ, witnessing a weaker activity of the GSI creep (e.g. dislocation creep). The asymmetric migration of PSZ boundaries can be related to the fact that the U location is closer to the upper metal cylinder than the L location. Despite the cylinders having thermal properties close to those of rocks (Supplementary Materials I), they may act as more efficient heat sinks. This would promote inward (towards L) localisation of the PSZ, away from the major heat sink, where the higher temperature is found. Such asymmetric conditions are not expected to be representative of natural faults.

The grains in these deactivated regions in the SG show a grain size which is an order of magnitude larger compared to that observed in the PSZ (Figs. 2–3). Also, no outstanding variation of CPO is observed during Stage III in the L location, while the CPO in the U location has slightly strengthened (Fig. 5b). The inherited strong CPO in the U location, compared to the L location, may aid sintering processes by facilitating the coalescence of slightly misaligned neighbouring grains (e.g. partially healed triple junctions seen in some grains in Fig. 4 and Fig. 7d, black arrow). Overall, our observations suggest that grain growth in the SG locations is not influenced by dynamic recrystallisation (i.e. the same GSI and GSS creep processes operating in the PSZ no longer act in the SG region) and thus can be considered to be quasi-static. The operation of a quasi-static sintering in the SG region is also supported by the evidence of: (i) low amounts of lattice distortion in the grains (Fig. 7a-c); (ii) low dislocation entanglements (Fig. 7b-d); (iii) equant grainsize (Fig. 7a); and (iv) straight grain boundaries connected by well-defined triple junctions (Fig. 7a-c). However, the increase of the low MAs (<10°) peak observed within the L location (Fig. 6) and microstructural evidence of intracrystalline plasticity within the U location (Fig. 7b-d) suggest that a relatively small degree of plastic deformation is still accommodated in the deactivated regions during Stage III and that it is coeval with sintering.

Away from the PSZ, the Riedel-populated F location is no longer sheared after Stage I, and becomes overprinted by the expanding sintering front. Its neighbour-pair MAD does not change shape throughout the four stages, but shows recovery processes driven by static recrystallisation (Fig. 5b) as illustrated by the progressive lowering of both e-twin and low MAs peaks (Fig. 6).

6.3. Implications for natural faults

Our experimental work has shown that ultramylonites can develop and have a significant role in controlling fault strength during seismogenic slip under upper crustal conditions. However, in nature, the mylonitic PSZ would experience a more protracted deceleration phase than in the experiments (with lower velocity rate), as the velocity profile of seismic slip along faults follows that of a modified Yoffe function (Fukuyama and Mizoguchi, 2010 and references therein). Hence, it is expected that the more protracted re-strengthening of the fault may produce more brittle damage than observed during the experiments (Stage IV), potentially overprinting/obliterating the coseismic ultramylonite fabric within the PSZ. Liao et al. (2014) show that slow deceleration of the apparatus brings the experimental fault back to friction values in the Byerlee range (>0.6), which are observed during the cataclastic flow of Stage I.

Arrays of parallel MSs and MSs-bounded cataclasites in seismic natural faults have been described in the published literature (Collettini et al., 2014; Tesei et al., 2013; Siman-Tov et al., 2013). Other authors who performed similar experiments have also suggested that reflective, nanograin decorated surfaces found in exhumed carbonate-hosted faults might form during earthquakes (Fondriest et al., 2013; Siman-Tov et al., 2013; Smith et al., 2013). These microstructures are indeed observed to form in our and their samples (MSs) after high velocity shear deformation. Importantly, other authors have shown that similar microstructures can form even at subseismic slip rates and thus that cannot be used in isolation as reliable seismic proxies (Verberne et al., 2013; Tesei et al., 2017).

Pozzi et al. (2018) argue that MSs are formed during the late stage embrittlement of the PSZ boundaries. It is shown that deceleration of the system produces a pervasive brittle overprint, which is enhanced at lower temperatures (i.e. as seen in lower velocity experiments).

In this scenario, it is the hardened sintered layer outside the PSZ which would stand a better chance of being preserved in natural seismic faults. Our results have shown that the sintered layers below the MSs contain important information about the ultramylonite deformation history. In particular, EBSD analysis has been shown to be a powerful tool that can be used to extract further information from microstructures that may otherwise have been overlooked in previous studies of natural fault rocks. This technique can usefully be employed in the analysis of natural MSs and it may be possible to discriminate whether they formed due to their seismic or aseismic slip, as the EBSD characteristics and patterns of the surrounding sintered regions should show a different slip history in response to different conditions in the PSZ.

7. Conclusions

The integration of mechanical data with microstructural observations and EBSD analyses shows that coseismic ultramylonites form in carbonate-hosted faults and follow a complex weakening path. In particular, the weakening of initial calcite microgouges when sheared at earthquake slip rates is controlled by the competition between brittle (e.g. cataclastic flow) and viscous creep deformation mechanisms. Therefore, we conclude that:

- Thermally activated grain size sensitive (GSS) and insensitive (GSI) creep mechanisms lead to the formation of coseismic ultramylonites when calcite gouges are sheared at extreme strain rate conditions. Compared to ultramylonites which form

deeper in the Earth under lower strain rate conditions, co-seismic ultramylonites must form at the nanoscale in order to accommodate high seismic strain.

- The combined and simultaneous action of GSI and GSS mechanisms may lead to a grain size piezometric equilibrium in the coseismic ultramylonite PSZ, due to cycles of grain size reduction due to the operation of GSI mechanisms and grain growth driven by thermal processes.
- The crystallographic orientations of transient microstructures are preserved in the narrow deactivated layers close to the principal slip zone. Hence, EBSD techniques can usefully be employed in the analysis of microstructures associated with natural mirror-like surfaces, which are preserved in both experimental and exhumed natural faults.

Acknowledgements

Appendix A. Supplementary material

Supplementary material related to this article can be found online at https://doi.org/10.1016/j.epsl.2019.03.042.

References

Ashby, M.F., Verrall, R.A., 1973. Diffusion-accommodated flow and superplasticity. Acta Metall. 21 (2), 149–163. https://doi.org/10.1016/0001-6160(73)90057-6.

Barnhoorn, A., Bystricky, M., Burlini, L., Kunze, K., 2004. The role of recrystallisation on the deformation behaviour of calcite rocks: large strain torsion experiments on Carrara marble. J. Struct. Geol. 26, 885–903. https://doi.org/10.1016/j.jsg.2003.11.024.

Bestmann, M., Kunze, K., Matthews, A., 2000. Evolution of a calcite marble shear zone complex on Thassos Island, Greece: microstructural and textural fabrics and their kinematic significance. J. Struct. Geol. 22 (11–12), 1789–1807. https://doi.org/10.1016/S0191-8141(00)00112-7.

Bestmann, M., Prior, D.J., 2003. Intragranular dynamic recrystallization in naturally deformed calcite marble: diffusion accommodated grain boundary sliding as a result of subgrain rotation recrystallization. J. Struct. Geol. 25 (10), 1597–1613. https://doi.org/10.1016/S0191-8141(03)00006-3.

Bower, A.F., Wininger, E., 2004. A two-dimensional finite element method for simulating the constitutive response and microstructure of polycrystals during high temperature plastic deformation. J. Mech. Phys. Solids 52 (6), 1289–1317. https://doi.org/10.1016/J.JMPS.2003.11.004.

Bunge, H.J., 1981. Fabric analysis by orientation distribution functions. Tectonophysics 78 (1–4), 1–21. https://doi.org/10.1016/0040-1951(81)90003-2.

Burkhard, M., 1990. Ductile deformation mechanisms in micritic limestones naturally deformed at low temperatures (150-350 °C). Special Publications. Geological Society of London, vol. 54(1). Geological Society, London, pp. 241–257.

Chandra, N., 2002. Constitutive behavior of superplastic materials. Int. J. Non-Linear Mech. 37 (3), 461–484. https://doi.org/10.1016/S0020-7462(01)00021-X.

Cipoletti, D.E., Bower, A.F., Krajewski, P.E., 2011. A microstructure-based model of the deformation mechanism and flow stress during elevated-temperature straining of a magnesium alloy. Scr. Mater. 64 (10), 931–934. https://doi.org/10.1016/J.SCRIPTAMAT.2010.12.033.

Collettini, C., Carpenter, B.M., Viti, C., Cruciani, F., Mollo, S., Tesei, T., Trippetta, F., Valoroso, L., Chiaraluce, L., 2014. Fault structure and slip localization in carbonate-bearing normal faults: an example from the Northern Apennines of Italy. J. Struct. Geol. 67 (Part A), 154–166. https://doi.org/10.1016/j.jsg.2014.07.017.

De Bresser, J.H.P., Spiers, C.J., 1997. Strength characteristics of the r, f, and c slip systems in calcite. Tectonophysics 272 (1), 1–23. https://doi.org/10.1016/S0040-1951(96)00273-9.

De Bresser, J.H.P., Peach, C.J., Reijs, J.P.J., Spiers, C.J., 1998. On dynamic recrystallization during solid state flow: effects of stress and temperature. Geophys. Res. Lett. 25 (18), 3457–3460. https://doi.org/10.1029/98GL02690.

De Bresser, J.H.P., Ter Heege, J.H., Spiers, C.J., 2001. Grain size reduction by dynamic recrystallization: can it result in major rheological weakening? Int. J. Earth Sci. 90 (1), 28–45. https://doi.org/10.1007/s005310000149.

De Paola, N., Holdsworth, R.E., Viti, C., Collettini, C., Bullock, R., 2015. Can grain size sensitive flow lubricate faults during the initial stages of earthquake propagation? Earth Planet. Sci. Lett. 431, 48–58. https://doi.org/10.1016/j.epsl.2015.09.002.

Di Toro, G., Han, R., Hirose, T., De Paola, N., Nielsen, S., Mizoguchi, K., Ferri, F., Cocco, M., Shimamoto, T., 2011. Fault lubrication during earthquakes. Nature 471 (7339), 494–498. https://doi.org/10.1038/nature09838.

Di Toro, G., Hirose, T., Nielsen, S., Pennacchioni, G., Shimamoto, T., 2006. Natural and experimental evidence of melt lubrication of faults during earthquakes. Science 311 (5761), 647–649. https://doi.org/10.1126/science.1121012.

Faulkner, D.R., Jackson, C.A.L., Lunn, R.J., Schlische, R.W., Shipton, Z.K., Wibberley, C.A.J., Withjack, M.O., 2010. A review of recent developments concerning the structure, mechanics and fluid flow properties of fault zones. J. Struct. Geol. 32 (11), 1557–1575. https://doi.org/10.1016/j.jsg.2010.06.009.

Fondriest, M., Smith, S.A.F., Candela, T., Nielsen, S.B., Mair, K., Toro, Di, G., 2013. Mirror-like faults and power dissipation during earthquakes. Geology 41 (11), 1175–1178. https://doi.org/10.1130/G34641.1.

Fukuyama, E., Mizoguchi, K., 2010. Constitutive parameters for earthquake rupture dynamics based on high-velocity friction tests with variable sliprate. Int. J. Fract. Mech. 163 (1–2), 15–26. https://doi.org/10.1007/s10704-009-9417-5.

Goldsby, D.L., Tullis, T.E., 2011. Flash heating leads to low frictional strength of crustal rocks at earthquake slip rates. Science 334 (6053), 216–218. https://doi.org/10.1126/science.1207902.

Green II, H.W., Shi, F., Bozhilov, K., Xia, G., Reches, Z., 2015. Phase transformation and nanometric flow cause extreme weakening during fault slip. Nat. Geosci. 8 (6), 484–489. https://doi.org/10.1038/ngeo2436.

Herwegh, M., Kunze, K., 2002. The influence of nano-scale second-phase particles on deformation of fine grained calcite mylonites. J. Struct. Geol. 24 (9), 1463–1478. https://doi.org/10.1016/S0191-8141(01)00144-4.

Hirose, T., Shimamoto, T., 2005. Growth of molten zone as a mechanism of slip weakening of simulated faults in gabbro during frictional melting. J. Geophys. Res., Solid Earth 110 (B5), B05202. https://doi.org/10.1029/2004JB003207.

Hutter, K., Rajagopal, K.R., 1994. On flows of granular materials. Contin. Mech. Thermodyn. 6 (2), 81–139. https://doi.org/10.1007/BF01140894.

Lankford, J., 1996. High strain rate compression and plastic flow of ceramics. J. Mater. Sci. Lett. 15 (9), 745–750. https://doi.org/10.1007/BF00274593.

Liao, Z., Chang, J.C., Reches, Z., 2014. Fault strength evolution during high velocity friction experiments with slip-pulse and constant-velocity loading. Earth Planet. Sci. Lett. 406, 93–101. https://doi.org/10.1016/j.epsl.2014.09.010.

Nieh, T.G., Wadsworth, J., Sherby, O.D., 1997. Superplasticity in Metals and Ceramics. Cambridge University Press.

Pieri, M., Kunze, K., Burlini, L., Stretton, I., Olgaard, D.L., Burg, J.-P., Wenk, H.-R., 2001. Texture development of calcite by deformation and dynamic recrystallization at 1000 K during torsion experiments of marble to large strains. Tectonophysics 330 (1–2), 119–140. https://doi.org/10.1016/S0040-1951(00)00225-0.

Pozzi, G., De Paola, N., Nielsen, S.B., Holdsworth, R.E., Bowen, L., 2018. A new interpretation for the nature and significance of mirror-like surfaces in experimental carbonate-hosted seismic faults. Geology 46 (7), 583–586. https://doi.org/10.1130/G40171.1.

Prior, D.J., Boyle, A.P., Brenker, F., Cheadle, M.C., Day, A., Lopez, G., Peruzzo, L., Potts, G.J., Reddy, S., Spiess, R., Timms, N.E., Trimby, P., Wheeler, J., Zetterström, L., 1999. The application of electron backscatter diffraction and orientation contrast imaging in the SEM to textural problems in rocks. Am. Mineral. 84, 1741–1759.

Rice, J.R., 2006. Heating and weakening of faults during earthquake slip. J. Geophys. Res., Solid Earth 111 (B5), B05311. https://doi.org/10.1029/2005JB004006.

Rowe, K.J., Rutter, E.H., 1990. Palaeostress estimation using calcite twinning: experimental calibration and application to nature. J. Struct. Geol. 12 (1), 1–17. https://doi.org/10.1016/0191-8141(90)90044-Y.

Rutter, E.H., Casey, U.K.M., Burlini, L., 1994. Preferred crystallographic orientation development during the plastic and superplastic flow of calcite rocks. J. Struct. Geol. 16 (10), 1431–1446.

Sammis, C.G., Ben-Zion, Y., 2008. Mechanics of grain-size reduction in fault zones. J. Geophys. Res., Solid Earth 113 (B2), B02306. https://doi.org/10.1029/2006JB004892.

Schmid, S.M., Panozzo, R., Bauer, S., 1987. Simple shear experiments on calcite rocks: rheology and microfabric. J. Struct. Geol. 9 (5), 747–778. https://doi.org/10.1016/0191-8141(87)90157-X.

Sibson, R.H., 1973. Interactions between temperature and pore-fluid pressure during earthquake faulting and a mechanism for partial or total stress relief. Nature 243, 66–68. https://doi.org/10.1038/physci243066a0.

Sibson, R.H., 1977. Fault rocks and fault mechanisms. J. Geol. Soc. 133 (3), 191–213. https://doi.org/10.1144/gsjgs.133.3.0191.

Siman-Tov, S., Aharonov, E., Sagy, A., Emmanuel, S., 2013. Nanograins form carbonate fault mirrors. Geology 41 (6), 703–706. https://doi.org/10.1130/G34087.1.

Siman-Tov, S., Aharonov, E., Boneh, Y., Reches, Z., 2015. Fault mirrors along carbonate faults: formation and destruction during shear experiments. Earth Planet. Sci. Lett. 430, 367–376. https://doi.org/10.1016/j.epsl.2015.08.031.

Smith, S.a.F., Di Toro, G., Kim, S., Ree, J.-H., Nielsen, S., Billi, A., Spiess, R., 2013. Co-seismic recrystallization during shallow earthquake slip. Geology 41 (1), 63–66. https://doi.org/10.1130/G33588.1.

Smith, S.A.F., Nielsen, S., Di Toro, G., 2015. Strain localization and the onset of dynamic weakening in calcite fault gouge. Earth Planet. Sci. Lett. 413, 25–36. https://doi.org/10.1016/j.epsl.2014.12.043.

Spagnuolo, E., Plümper, O., Violay, M., Cavallo, A., Di Toro, G., 2015. Fast-moving dislocations trigger flash weakening in carbonate-bearing faults during earthquakes. Sci. Rep. 5, 1–11. https://doi.org/10.1038/srep16112.

Spray, J.G., 2010. Frictional melting processes in planetary materials: from hypervelocity impact to earthquakes. Annu. Rev. Earth Planet. Sci. 38 (1), 221–254. https://doi.org/10.1146/annurev.earth.031208.100045.

Tesei, T., Collettini, C., Viti, C., Barchi, M.R., 2013. Fault architecture and deformation mechanisms in exhumed analogues of seismogenic carbonate-bearing thrusts. J. Struct. Geol. 55, 167–181. https://doi.org/10.1016/j.jsg.2013.07.007.

Tesei, T., Carpenter, B.M., Giorgetti, C., Scuderi, M.M., Sagy, A., Scarlato, P., Collettini, C., 2017. Friction and scale-dependent deformation processes of large experimental carbonate faults. J. Struct. Geol. 100, 12–23. https://doi.org/10.1016/J.JSG.2017.05.008.

Verberne, B.A., Spiers, C.J., Niemeijer, A.R., De Bresser, J.H.P., De Winter, D.A.M., Plümper, O., 2013. Frictional properties and microstructure of calcite-rich fault gouges sheared at sub-seismic sliding velocities. Pure Appl. Geophys. 171 (10), 2617–2640. https://doi.org/10.1007/s00024-013-0760-0.

Wenk, H.R., Venkitasubramanyan, C.S., Baker, D.W., Turner, F.J., 1973. Preferred orientation in experimentally deformed limestone. Contrib. Mineral. Petrol. 38 (2), 81–114. https://doi.org/10.1007/BF00373875.

Wenk, H.R., Takeshita, T., Bechler, E., Erskine, B.G., Matthies, S., 1987. Pure shear and simple shear calcite textures. Comparison of experimental, theoretical and natural data. J. Struct. Geol. 9 (5–6), 731–745. https://doi.org/10.1016/0191-8141(87)90156-8.

Wheeler, J., 2009. The preservation of seismic anisotropy in the Earth's mantle during diffusion creep. Geophys. J. Int., 1723–1732. https://doi.org/10.1111/j.1365-246X.2009.04241.x.

Wheeler, J., Prior, D., Jiang, Z., Spiess, R., Trimby, P., 2001. The petrological significance of misorientations between grains. Contrib. Mineral. Petrol. 141 (1), 109–124. https://doi.org/10.1007/s004100000225.

The - less formal - acknowledgments

I wish to express here my deepest gratitude to the people who made this work possible. To those who strengthened my scientific knowledge. To those who lifted my spirit.

To Ines, my most wonderful friend, the one I truly shared my thoughts with and the one who truly listened.

To Chiara, age-old friend, the one who shares with me countless memories and many to come.

To Mikaela, whose talk is a secure haven, a welcoming companion for a dinner, for a film, for a walk.

To Luca, Simon and Alberto, exceptional minds and unique friends, the ones I had shared my science with, along a mountain path or in front of a pint of beer.

To Telemaco, extraordinary scientist and friend, the one that grew my knowledge and evergreen source of enthusiastic new research.

To Andrea and Giacomo, to whom I owe mind-free days and many memorable nights spent on nerdy stuff.

To Chris, my messy flatmate, colleague and friend, who rocked and brightened life at home as well as in the lab.

To my parents, Emanuela and Alberto, and especially to my sister Giulia, who always supported me, even just with the most sincere smile and brightest eyes.

To C, who binds and shapes the clouds where my mind wanders about.